

Loughborough University
Wolfson School of Mechanical, Electrical
and Manufacturing Engineering

Plasma-Assisted Organic Synthesis of Epoxides Using Carbon Dioxide as a Precursor

Prateep Ganesh Kasinathan

1st March 2025

Contents

1	Introduction	1
1.1	Contribution to knowledge	4
2	Plasma Overview	5
2.1	DC Discharge	6
2.1.1	Breakdown	6
2.1.2	Characteristics	8
2.1.3	Discharge Sources	11
2.2	AC Discharge	14
2.2.1	Breakdown and Characteristics	14
2.2.2	Discharge Sources	16
3	Carbon Dioxide Splitting	23
3.1	Traditional Process	23
3.2	Plasma-assisted CO ₂ Splitting	27

4 The Split Ring Resonator	35
4.1 Overview	36
4.2 Production	38
4.2.1 Simulations	38
4.2.2 Design	45
4.3 Testing	49
4.3.1 Scattering Parameters	49
4.3.2 Experimental Setup	50
4.3.3 Device Performance	52
4.3.4 Pressure Drop across Orifice	55
4.4 Flow of gases	61
4.4.1 Helium only	61
4.4.2 Helium with Carbon Dioxide	63
5 Gas recirculation	75
5.1 Control System with Helium only	75
5.1.1 Pressure in the SRR chamber	79
5.1.2 Flow rate to the SRR	90
5.1.3 Complete control system	92
5.2 Control System with Helium and Carbon Dioxide	94
5.2.1 Controlling carbon dioxide concentration	96
5.2.2 Carbon monoxide concentrations	107

5.3 Overall Control System performance	109
6 Epoxidation Process	113
6.1 Investigation the role of solvent	113
6.2 Developing the plasma reactor	121
6.2.1 Designing the main reactor housing	121
6.2.2 Removing the acetonitrile vapours	124
6.2.3 Complete setup design	126
6.3 Characterising the plasma reactor	129
6.3.1 Evaluating impact of flow rate and reaction distance	131
6.3.2 Evaluating impact of CO ₂ concentration	136
6.3.3 Evaluating impact of temperature	138
6.3.4 Evaluating the impact of inert gas used	141
6.3.5 Comparison with the COST jet reactor	144
6.4 Recirculating the feed gas for the reactor	150
6.5 Cost analysis of recirculating the feed gas	156
7 Conclusion	159
A Particle-in-Cell Simulations	160
A.1 Particle Mover	162
A.2 Charge and Current Deposition	165
A.3 Field Solver	166

A.4	Field Interpolation	169
A.5	Monte-Carlo Collisions	170
B	Simulation Software	173
B.1	Overview	173
B.1.1	Remote Server	174
B.1.2	Input Files	175
B.2	Improvements	176
B.2.1	Motivation	176
B.2.2	Methodology	178
B.2.3	Validation	183
B.2.4	Future Work	189
Bibliography		190

List of Tables

4.1	Simulation parameters of SRR in XOOPIIC.	39
4.2	Comparison of pressure drop across single-hole and multi-hole SRR orifices across different flow rates.	58
4.3	Parameters used in equation 4.14.	59
4.4	The effect of flow rate on the light intensity of the He plasma.	62
5.1	Name and description of equipment used for recirculation of helium only.	77
5.2	Average rate of change of pressure measured for flow rates between 10-50 sccm.	81
5.3	Measured lag time across various flow rates of CO ₂ gas.	100
5.4	Best fit rate of change of FTIR absorbance across various flow rates.	102
6.1	Comparison of trans-Stilbene epoxide produced across flow rates of 100 sccm to 1 slm and reaction distance of 12 mm to 24 mm.	132
6.2	GC-MS results of periodic samples taken from the wet plasma system running in the open and closed gas loop configurations.	152
A.1	Determining the type of collision based on the value of R [108].	171
B.1	Circuit boundary variables for cartesian geometry.	182

B.2	Circuit boundary variables for cylindrical geometry.	183
B.3	Parameters for test case of Circuit boundary without particles.	184
B.4	Parameters for test case of Circuit boundary with particles.	187

List of Figures

1.1	Global greenhouse gas emissions by sector for the year 2016 [3].	2
2.1	Paschen curve for Helium, Neon, Argon, Hydrogen, and Nitrogen gases [10]. . .	7
2.2	Circuit diagram with a DC voltage (V_s) and variable resistor (R) to control the current through a discharge region [13].	8
2.3	Depiction of the current-voltage relationship across three discharge regions [14].	9
2.4	Schematic highlighting the regions present in a DC glow discharge [15]. The cathode is on the left and the grounded anode is on the right. On the vertical axes, V is the potential and ε denotes the electric field distribution. CDS is the cathode dark space, NG is the negative glow, and AZ is the anode dark space. .	10
2.5	A DC plasma from molecular emission detector on chip [16].	11
2.6	A simplified illustration of a hollow cathode design [18].	12
2.7	A comparison of the voltage vs current curve for a hollow cathode geometry (solid line) and a typical parallel plate geometry (dashed line)[20].	13
2.8	Paschen curve for AC discharge across various frequencies [30].	15
2.9	Illustration of a capacitively coupled plasma (CCP) experimental setup [32]. . .	16
2.10	Cycle averaged electron temperature in a CCP reactor [33].	17

2.11 Schematic of inductively coupled plasma (ICP) torches [36].	18
2.12 Comparison of plasma parameters between CCP and ICP reactor [37]. The two left most graphs (a, c) are the results from a CCP reactor, while the two right most graphs (b, d) are the results of the ICP reactor. The top two graphs (a, b) show the radial distribution of electron temperatures for a CCP and ICP reactor respectively. The bottom two graphs (c, d) show the distribution of electron density for a CCP and ICP reactor respectively.	19
2.13 Examples of different Dielectric Barrier Discharge (DBD) designs [41]. The left most (a) and right most (c) drawings show at least one dielectric on the electrodes, while the middle (b) illustrates a dielectric in the discharge gap, but not touching the electrodes.	20
2.14 Schematic of a surface wave discharge plasma source [44].	21
2.15 Schematic of an electron cyclotron resonance plasma source [44].	21
2.16 Examples of different types of microstrip plasma sources [21]. The top three designs (a, b, c) are linear microstrip resonators, while (d) shows a microstrip split-ring resonator, and (e) illustrates a coaxial resonator.	22
3.1 Gibbs free energy of formation for different chemicals based on data from the NIST database. [50]	24
3.2 Thermal conversion and energy efficiency of CO ₂ splitting as a function of temperature. [51]	25
3.3 Comparison of conversion and energy efficiencies for various CO ₂ splitting plasma reactors [51].	29
3.4 Schematic of microwave reactors for CO ₂ splitting [51].	31
3.5 Photograph of COST jet [74].	33
3.6 Schematic of experimental setup by Xu et al [75].	34

4.1 Schematic (left) and photo (right) of SRR [77].	36
4.2 A cross section comparison of SRR simulation domain without a hole (a) and with hole (b) in gap.	39
4.4 A comparison of the number of particles diagnostic between a simulation potential difference of 150V (a) causing a voltage breakdown and one with a potential difference of 100V (b) which does not cause a breakdown.	41
4.5 Simulation breakdown voltages across the various tested discharge gap widths. .	42
4.7 PCB schematic of SRR panels in the KiCad software suite.	47
4.8 SRR gap designs with multiple holes (a, c) versus single holes (b, d). The designs in the lower two subfigures (c, d) have the presence of ‘finger-like’ copper pours next to the holes.	48
4.9 Reflection coefficient (S_{11}) of SRR in dB.	50
4.10 Schematic of experimental setup.	51
4.11 Photograph of plasma discharge in the gap of the SRR.	52
4.12 Ignition power of SSR, in W, across a pressure range of 5 Torr to 850 Torr. . . .	53
4.13 Pressure drop across an orifice visualised. [81]	55
4.14 Schematic of setup used to determine the pressure drop through orifice.	58
4.15 Comparison of true and predicted results for pressure drop across SRR with single hole orifice.	59
4.16 Schematic of setup used for He feed gas to ignite SRR.	61
4.17 Schematic for Ocean Optics spectrometer [84].	62
4.18 Optical emission spectra of He plasma with SRR.	63
4.19 Schematic of setup used for He-CO ₂ gas mixture to ignite SRR.	63

4.20 Comparison of optical emission spectra of He only plasma and (1%) CO ₂ -Helium plasma.	65
4.21 Photograph of carbon deposits on SRR.	65
4.22 Schematic of Fourier-transform infrared spectroscopy (FTIR) interferometer.	66
4.23 3D CAD model of gas viewing chamber for FTIR.	68
4.24 Snapshots of raw light data from FTIR across the span of 3.5 hours.	69
4.25 The change of the second moment of area over the span of 3.5 hours.	70
4.26 Output signals from FTIR preprocessing steps.	71
4.27 Test measured transmittance at 2360 cm ⁻¹ across CO ₂ concentrations between 1-2%.	72
4.28 Absorbance across CO ₂ concentrations between 0-5%.	74
5.1 Schematic of control system with helium feed gas.	76
5.2 Splitting control system into chamber pressure control (a) and target flow rate control (b).	78
5.3 Rate of change of pressure in main chamber for flow rates between 10-50 sccm.	80
5.4 Relationship between rate of change of pressure and flow rate.	81
5.5 Basic schematic of control system.	82
5.6 Illustration of control system.	83
5.7 Evaluation of proportional controller for test cases 1 (a), 2 (b), and 3 (c).	84
5.8 Illustration of control system.	86
5.9 Comparison of offset introduced by the actuator and sensor error.	87
5.10 Illustration of integral windup for PI controller ($K_p = 5$, $K_i = 0.01$).	88

5.11 Evaluation of PI controller for test cases 1 (a), 2 (b), and 3 (c).	89
5.12 Comparison between the performance of the modelled and real PI controllers.	90
5.13 Flow chart of Helium only recirculation control system.	93
5.14 Schematic of control system with helium feed gas and carbon dioxide.	94
5.15 Time series response of the system without a CO ₂ controller various flow rates of CO ₂ gas.	98
5.16 Illustration of process used to determine the lag time of the system.	99
5.17 The inversely proportional relationship between flow rate and lag time.	100
5.18 Rate of change of CO ₂ concentration for CO ₂ flow rates between 0.3-1.0 sccm.. .	101
5.19 Rate of change of CO ₂ concentration for CO ₂ flow rates between 0.3-1.0 sccm.. .	102
5.20 Modelled CO ₂ gas control system in Simulink.	103
5.21 Comparison between the (real) measured characterisation data and modelled data for the flow rate $Q_c = 0.5$ sccm.	104
5.22 Difference between real and modelled data for all flow rates tested.	105
5.23 Time series response of system (without a CO ₂ controller) for larger flow rates. .	105
5.24 Comparison between the modelled and real proportional controllers for regulat- ing CO ₂ concentrations.	107
5.25 Comparison CO ₂ and CO absorption in the FTIR spectra.	108
5.26 Optical spectra between pure Argon plasma and Argon plasma with CO ₂	109
5.27 Time series plot of the mass flow controller and FTIR traces of the control system operating over a 24 hours.	110
5.28 “Top-up” interval (a) and gas volume (b) of the system.	112

6.1 Environmental assessment of 26 of the most common organic solvents used done by Capello et al [].	115
6.2 A schematic diagram of the gas chromatography method [92].	117
6.3 A schematic diagram of the mass spectrometry method [93].	117
6.4 A wide (a) and close-up (b) illustration of the GC-MS results from testing the reaction of atomic oxygen with trans-Stilbene dissolved in different solvents.	119
6.5 A wide (a) and close-up (b) illustration of the GC-MS results from testing an open and closed container of the reaction of trans-Stilbene in acetonitrile. Note, the naphthalene peak was due to its introduction as an internal standard.	120
6.6 An illustration of the schematic design (a) and finished SRR jet reactor build (b). . .	123
6.7 An illustration of the schematic design of the direct-contact condenser (a) and the finalised direct-contact condenser with a nichrome heating element (b).	127
6.8 An illustration of the completed SSR jet reactor schematic used as the experimental setup.	128
6.9 The calibration curve of trans-Stilbene for molar concentrations between 10 mM to 0.5 mM (a) and trans-Stilbene epoxide for molar concentrations between 10 mM to 0.0125 mM (b).	130
6.10 The concentration of trans-Stilbene used and trans-Stilbene epoxide produced across a feed flow rate of 250 sccm to 2 slm.	133
6.11 The percentage yield of trans-Stilbene epoxide produced and the CO ₂ efficiency across a feed flow rate of 250 sccm to 2 slm.	135
6.12 The concentration of trans-Stilbene used and trans-Stilbene epoxide produced across a He-CO ₂ mixture between 0.5 to 2.5%.	136
6.13 The percentage yield of trans-Stilbene epoxide produced and the CO ₂ efficiency of the reaction across a He-CO ₂ mixture between 0.5 to 2.5%	137

6.14 The concentration of trans-Stilbene used and trans-Stilbene epoxide produced across range of cooling bath temperatures of -40 °C to 20 °C, along with the epoxide yields produced.	139
6.15 Thermal images of the reactor reservoir at ambient temperature (a), with an ice bath (b), and in a dry ice bath with acetonitrile (c).	140
6.16 A comparison of the concentration of trans-Stilbene used and of trans-Stilbene oxide produced in a helium plasma (a) and an argon plasma (b).	142
6.17 Comparison of the optical spectra of a pure Ar and pure He plasma.	143
6.18 Comparison of the optical spectra of a pure Ar and a 1% CO ₂ +Ar plasma. . . .	144
6.19 Comparison of the optical spectra of a pure He and a 1% CO ₂ +He plasma. . . .	144
6.20 A comparison of the concentration of trans-Stilbene used and of trans-Stilbene oxide produced between the COST jet and the SRR jet with equal flow rate (1 slm) and reaction distances (24 mm).	145
6.21 A comparison of the concentration of trans-Stilbene used and of trans-Stilbene oxide produced between the COST jet and the SRR jet with equal flow rates (1 slm) but with optimum reaction distances (10 mm for COST jet, 24 mm for SRR jet).	146
6.22 A comparison of the concentration of trans-Stilbene used and of trans-Stilbene oxide produced between the COST jet and the SRR jet with equal reaction distances but velocity normalised flow rates (1.67 slm for COST jet, 250 sccm for SRR jet).	148
6.23 An illustration of the schematic design (a) and the prototype (b) of an inverted SRR jet reactor which was scrapped.	149

6.24 The time evolution comparison between the open gas loop and closed gas loop configurations, showing the measured sample concentrations and the corrected concentrations.	154	
6.25 A comparison between pure carbon deposition (a) and potentially organic solvent deposition (b) on the SRR electrodes.	155	
A.1 Process flow of PIC simulations.		161
A.2 Illustration of forward-difference and central-difference form [100].		163
A.3 Visualisation of velocity rotation from the Boris algorithm [101].		164
A.4 Interpolation from the grid to the particles [103].		165
A.5 Illustration of ADI method [105].		168
A.6 Addition of null collision to produce a constant collision frequency across all energies [108].		171
B.1 Illustration of circuit boundary.		177
B.2 Voltage-current relationship of circuit boundary.		178
B.3 Illustration of a circuit boundary along a fixed grid.		179
B.4 Illustration of test case for Circuit boundary without particles.		184
B.5 Comparison between the analytical solution and XOOPIIC, where $\Delta t = 10$ ps. . .		185
B.6 Comparison between the analytical solution and XOOPIIC, where $\Delta t = 1$ ns. . .		185
B.7 Comparison of the error from XOOPIIC when $\Delta t = 10$ ps and $\Delta t = 1$ ns. . .		186
B.8 Illustration of test case for Circuit boundary without particles.		186
B.9 Illustration of test case for Circuit boundary without particles.		189

Chapter 1

Introduction

Anthropogenic climate change represents a significant and pressing global challenge, described by the Intergovernmental Panel on Climate Change (IPCC) as “a threat to human well-being and the health of the planet” [1]. The driving force behind climate change has to do with the emissions of green house gases into the atmosphere. Data from the United States Environmental Protection Agency indicate that carbon dioxide (CO_2) accounts for nearly three-quarters of those greenhouse emissions [2].

As seen in figure 1.1, global greenhouse emissions originate from a diverse array of sources and processes. Hence, concentrating mitigation efforts exclusively within certain sectors, such as transport or electricity generation, are insufficient. While the current progress of reducing humanity’s reliance on fossil fuels through the adoption of renewable energy sources and the transition to electric vehicles is an important step forward, achieving the mark of net-zero emissions necessitate innovations across various other sectors. At present, there is no one solution to climate change.

One promising technology for addressing residual emissions and progressing toward net-zero targets is carbon capture and storage (CCS). It should be stressed that CCS alone cannot fully solve the climate crisis, instead it should be viewed as an indispensable component in a broad and comprehensive strategy to achieve net-zero emissions.

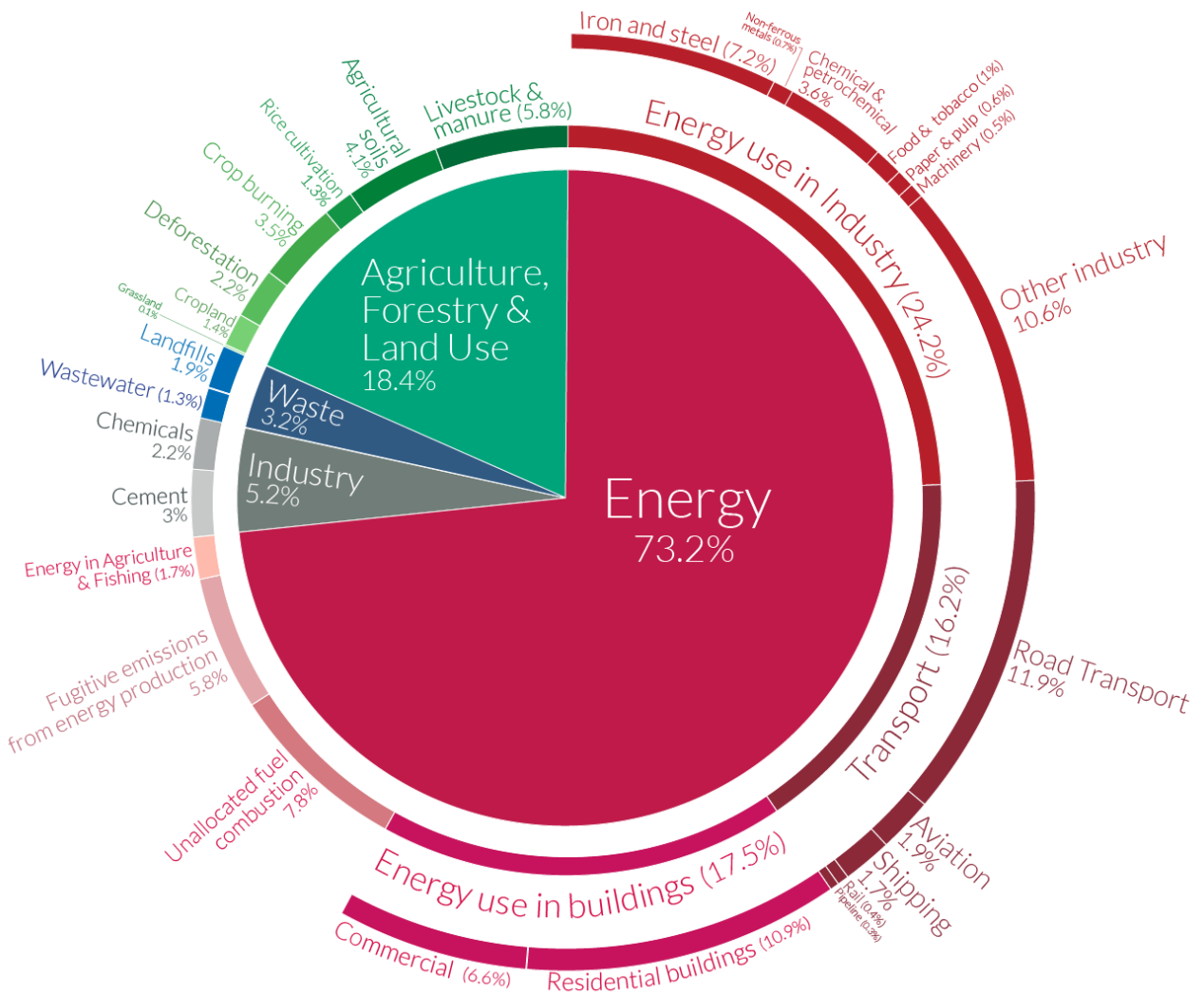


Figure 1.1: Global greenhouse gas emissions by sector for the year 2016 [3].

CCS represents a suite of processes that focus on either preventing the release of CO₂ into the environment or removing existing CO₂ in the atmosphere. The captured CO₂ would first be compressed, then transported for storage. The CO₂ storage typically entails injecting the gas into deep underground rock formations which essentially function as a geological reservoir [4].

The quintessential application of CCS lies in sectors that are otherwise challenging to decarbonise, such as the manufacturing of cement. Here, the CO₂ released stems from the chemical process, i.e. the conversion of calcium carbonate (CaCO₃) to calcium oxide (CaO), rather than through combustion. While the ambitions to implement CCS in this sector has been slow, in 2025 Norway is set to bring the world's first cement factory with CCS online [5].

The other approach to CCS would be using direct air capture (DAC) technologies, which extract

the CO₂ from the ambient air in one of two methods. Solvent-based approaches trap the CO₂ in a liquid chemical, then rely on heating to release the CO₂ gas [6]. Sorbent-based approaches use solid filters that bind with the CO₂, then with the use of low pressure, the desorption CO₂ molecules from the filters can occur [6]. Nonetheless, because the CO₂ concentration in the air is proportionally tiny, DAC should preferably be used as one of the methods to address legacy emissions already accumulated in the atmosphere.

While conventional CCS methods primarily focus on the sequestration of CO₂ for long-term storage, the captured of CO₂ itself can serve as a valuable feedstock for industrial applications. This is known as carbon capture and utilisation (CCU), and aims to recycle CO₂ into useful chemical products for industry. Several viable pathways exist for CO₂ utilisation, including thermal decomposition, electro-catalysis, and with the use plasmas [7]. However, each of these approaches presents distinct challenges.

Thermal decomposition requires high temperatures, leading to significant energy consumption and reduced overall efficiency. Similarly, electro-catalytic conversion typically relies on noble metal catalysts which can be quite expensive and are often times not environmentally friendly [7]. In contrast, plasma-assisted CO₂ conversion - also referred to as plasma-assisted CO₂ splitting - has emerged as a promising method, as it operates at low temperatures and atmospheric pressures, without the need for catalysts.

To generate and sustain the plasma, inert feed gases (typically argon or helium) are commonly employed due to their chemical non-reactivity. This inert behaviour minimises the likelihood of unwanted reactions with co-reactants, which would be CO₂ in this context. Furthermore, CO₂ is known as a molecular gas (similar to nitrogen and oxygen), thus possess vibrational and rotational energy levels. As a result, it can absorb and dissipate energy to heat loss, rather than sustaining the ionisation of the plasma. In comparison, inert gases lack these energy levels, reducing energy dissipation via quenching and allowing the plasma to be sustained for longer durations.

However, the major drawback of using inert gases is their high cost. Current CO₂ conversion techniques often involve venting waste gases (including both the inert gas and unconverted

CO₂) directly into the atmosphere. While this approach is feasible in a laboratory setting, its economic viability becomes increasingly untenable at an industrial scale. As such this research aims to investigate the feasibility of recycling the vented gases, which would should drastically improve the cost savings associated with this carbon utilisation technique.

With that in mind, the remainder of this report is structured as follows. Chapter 2 introduces the concept of plasma discharges, outlining the fundamental principles and some examples of discharge sources. Chapter 3 provides an overview of the CO₂ splitting process, presenting the relevant background information and detailing the particular process chosen for this research. Chapter 4 describes the design and manufacturing of the plasma discharge source used, including some preliminary tests with the feed gas and CO₂. Chapter 5 presents the engineering and development of the closed system designed for the recycling of gases. Chapter 6 describes the plasma reactor design utilised to facilitate organic synthesis from the CO₂ splitting process. Finally, the conclusion summarises the key findings of this research, discusses the implications, and elaborates on the future work required to scale this process to industrial applications.

1.1 Contribution to knowledge

TODO: Once finalised the conclusion

Chapter 2

Plasma Overview

Plasma is a fundamental state of matter, along with solid, liquid, and gas. They have a similar characteristics to gases, in that they are compressible and expand to fill a container they occupy. However, the key difference is that plasmas are highly electrically conductive, even capable of producing their own magnetic field. This is because plasmas contain a large number of positive ions that interact in a ‘sea’ of free-moving electrons.

There are several methods to generate plasma, one of which is via the extreme heating of gases. In such a method, the gas atoms gain enough kinetic energy so that upon collisions, electrons can escape the electromagnetic force of the nucleus. The most obvious example this type of plasma is in stars where the temperatures observed are between 2,000 to 33,000 K [8]. Another method for generating plasmas is with the aid of lasers, aptly called laser-induced plasmas. These rely on an intense pulse from the laser to rapidly excite, ionise, and atomise the target material into a plasma plume [9]. Laser-induced plasmas are commonly used for material processing, in a process called pulsed laser deposition.

Finally, plasmas can be formed when a gas exposed to a large electric field, which was the method used in this report. The details regarding the formation of this type of plasma are discussed in the rest of this chapter. An everyday example of this is lightning, where charges build up between the clouds and the ground, which in turn causes the potential difference between the two to grow until the air in between breaks down.

2.1 DC Discharge

2.1.1 Breakdown

The voltage necessary to break down a gas is given by *Paschen's law*. It states that the breakdown voltage is a function of two parameters [10]: the pressure of the gas and the distance between the electrodes (referred to as the gap length). Specifically, the breakdown voltage is a function of the product of these two parameters.

In order for breakdown to initiate, there needs to be a small number of seed electrons already present in the gas. These can be present due to previous discharges, or generated by highly energetic cosmic rays entering the gas chamber. Then when subjected to an electric field, these electrons gain energy creating other electrons via ionising collisions with the background gas. When more electrons are generated from the collisions than are lost, an avalanche is created, which causes the gas breakdown.

The breakdown voltage can be expressed by the following equation [10]:

$$V_B = \frac{Bpd}{\ln(Apd) - \ln[\ln(1 - \frac{1}{\gamma_{se}})]} \quad (2.1)$$

where V_B is the breakdown voltage, p is the pressure of the gas, d is the gap length, A and B are constants for a given gas that are determined experimentally, and γ_{se} is the coefficient for secondary-electron emission.

The phenomenon of *secondary-electron emissions* occur when either electrons or ions (and metastables) from the plasma collide with the cathode surface with sufficient energy, causing the release of secondary electron [11, 12]. As such, the coefficient can simply be thought as the frequency of this occurrence, and it is a key factor that allows a plasma to be self-sustaining.

Figure 2.1 illustrates the voltage breakdown curves for various gases. Each curve is slightly different, however all of them do exhibit a convex shape with a minimum between 1 to 10

Torr cm. Note that the unit *Torr* is a unit of pressure, and is defined as 1/760 of standard atmospheric pressure.

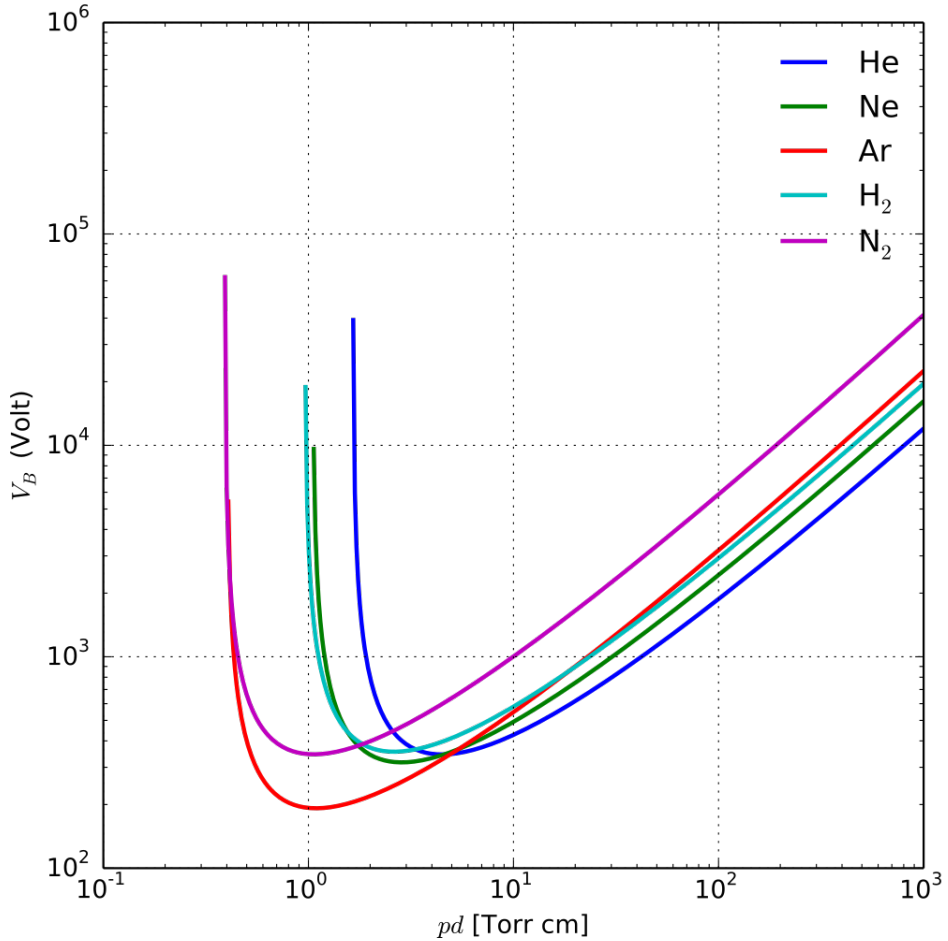


Figure 2.1: Paschen curve for Helium, Neon, Argon, Hydrogen, and Nitrogen gases [10].

A physical explanation of Paschen's law is as follows:

- **Consider the gap length remains constant.** Starting with a large pressure, the mean free path of an electron within the gas is quite short, meaning it does not have sufficient time in between collisions for it to gain enough energy to cause an ionising collision with the background gas. As the pressure is then reduced, the mean free path increases, making it easier for the electrons to gain sufficient energy to undergo ionising collisions; until a certain critical pressure (which was the aforementioned pd between 1 to 10 Torr cm). Beyond this, decreasing the pressure further causes the mean free path of the electron lengthen to a point that is comparable to the gap length, therefore this decreases the

likelihood of an electron colliding with a neutral gas particle and the breakdown voltage increases.

- Now consider that the pressure remains constant. When the gap length is very small, electrons are accelerated by a large electric field but are collected by the electrodes without undergoing collisions with the background gas. Increasing this gap length to a certain point gives the electrons the opportunity to collide with the background gas, producing ionising collisions. However, as the gap length continues to be increased, the strength of the electric field between the electrodes decreases, hence the electrons gain less energy between the collisions resulting in fewer ionising collisions with the background gas.

2.1.2 Characteristics

Consider a circuit as seen in figure 2.2. Two parallel electrodes with a DC voltage applied, and a plasma contained within a chamber. As the resistance of the variable resistor is decreased, the current through the plasma increases and one would observe three distinct discharge regions [13], shown in figure 2.3.

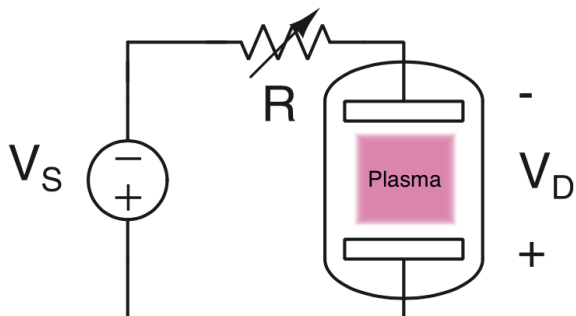


Figure 2.2: Circuit diagram with a DC voltage (V_s) and variable resistor (R) to control the current through a discharge region [13].

The first of these regions, is the dark discharge (or sometime referred to as the Townsend discharge) region. Initially when the voltage between the electrodes builds up, the only current through the gap is caused by pre-existing electrons, say from a previous discharge. However, this current quickly saturates (A-B in figure 2.3). Then, once the seed electrons gain sufficient

energy, they begin ionising the background gas to produce additional electrons in a process called the *Townsend avalanche* (B-D in figure 2.3). Once this avalanche is self-sustaining, where enough new electrons are produced to compensate for electrons lost (either to the electrodes or chamber walls), the voltage breakdown of the gas is reached (point D in figure 2.3).

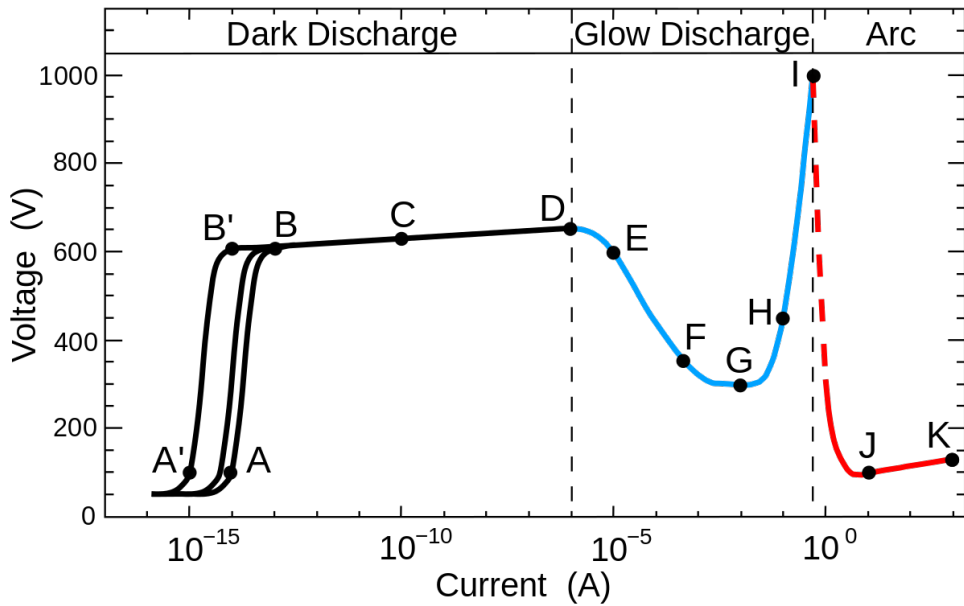


Figure 2.3: Depiction of the current-voltage relationship across three discharge regions [14].

After the breakdown, the plasma is said to be in a glow discharge region. Here, the voltage across the plasma decreases since a transition from a gas to plasma state causes a decrease in resistance, implying that the ionisation process from the avalanche is more efficient (D-G in figure 2.3). This efficiency arises due to the high charge densities created by the plasma that perturb the applied electric field. This results in a stronger electric field near the cathode. This region of negative resistance is known as the subnormal glow.

At first, ion bombardment on the surface of the cathode is non-uniform but as the current generated from this increases, it eventually stabilises and the distribution of the plasma (and thus the ions) across the cathode become more uniform. This is referred to as *subnormal glow* and *normal glow* respectively. As the current is increased further, ion bombardment across the cathode becomes saturated as it covers the entire surface of the cathode (seen from region G-I in figure 2.3). This is referred to as *abnormal glow*, and increasing the current further causes the glow discharge to become an arc (at point I in figure 2.3).

In the arc discharge region, the ion bombardment onto the cathode causes the cathode to heat up to a point where electrons are generated via thermionic emission. This significantly reduces the resistance of the plasma, causing a very large drop of the voltage (seen from region I-J in figure 2.3).

For the purposes of this project, the arc discharge region will be avoided because operating under arc conditions increases the electrode sputtering rate. *Sputtering* is the ejection of atoms from the electrode caused by the bombardment of energetic particles. While useful for processes such as ion etching [10], sputtering would not be desirable as the consumption of the electrode material is something to be avoided. Sputtering has the additional downside of potentially contaminating the plasma composition as ejected atoms could end up reacting with other plasma species.

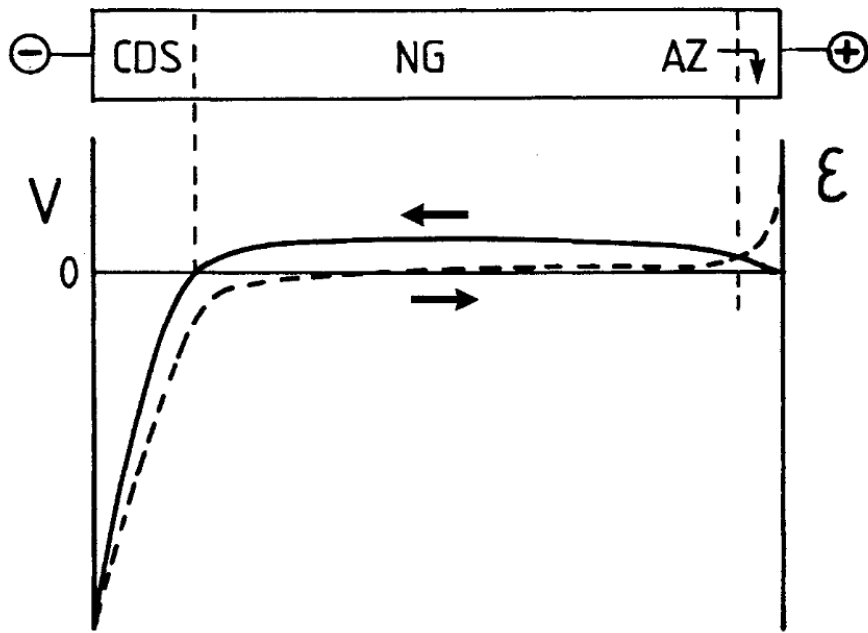


Figure 2.4: Schematic highlighting the regions present in a DC glow discharge [15]. The cathode is on the left and the grounded anode is on the right. On the vertical axes, V is the potential and ϵ denotes the electric field distribution. CDS is the cathode dark space, NG is the negative glow, and AZ is the anode dark space.

In a glow discharge there are typical three spatial regions present. These include a *cathode dark space* (CDS), a *negative glow* (NG) region, and the *anode dark space* (AZ) [13, 15]. This can be observed in figure 2.4, that shows the potential in each region. As the distance between the electrodes is increased, additional regions may develop, however these three regions will always

persist [13]. The dark space regions are called *sheaths* while the negative glow region is known as the *bulk plasma*. Generally, the sheaths on the cathode will be much larger than that of the anode, as it corresponds to the region where electrons are being accelerated before gaining sufficient energy to cause ionising collisions. In contrast, the anode sheaths form to limit the electron current to the anode, maintaining current continuity over the discharge. Finally, the bulk plasma is the quasi-neutral region that contains the ions and electrons of the plasma.

2.1.3 Discharge Sources

Parallel Plate Designs

The simplest form of a DC plasma source is the *parallel plate design*. As the name suggests, this design involves an anode and a cathode which are separated by a gap in which the plasma is formed. This is the design shown in figure 2.2.

An example of a device using this design can be seen in figure 2.5 of a molecular emission detector by Eijkel et al[16]. The plasma breakdown behaviour of such a design is simply governed by Paschen's law.

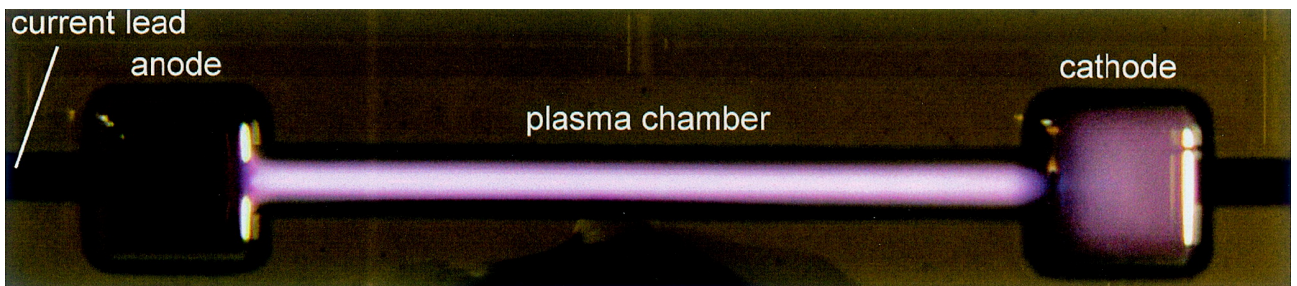


Figure 2.5: A DC plasma from molecular emission detector on chip [16].

Typically, parallel plate designs are favoured when simplicity and low cost are top priorities. There are some use cases such as plasma immersion ion implantation [17] and optical emission detectors [16] where this design proves useful. However, in most scenarios this design is fundamentally flawed due to erosion of the electrode. This erosion is caused by the ion bombardment, which is a necessary process to generate secondary emission electrons; a required mechanism

to sustain the plasma discharge. As such, electrode erosion limits the lifetime of a device with such a design.

Hollow Cathode Designs

The *hollow cathode design* is a commonly used alternative to the basic parallel plate geometry. Hollow cathodes are typically cylindrical in nature, where the anode remains the same but the cathode has been replaced with cup-like shape that is hollow in the centre (hence the name). An illustration of this can be seen in figure 2.6.

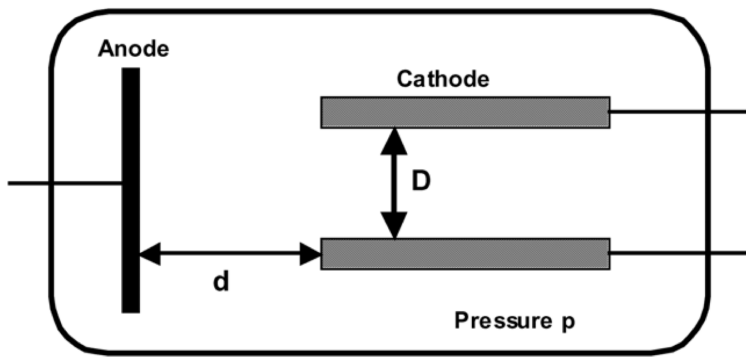


Figure 2.6: A simplified illustration of a hollow cathode design [18].

Such a design is favourable over the parallel plate geometry because of a phenomenon known as the *hollow cathode effect*. There are multiple factors that contribute to the hollow cathode effect. However, it is generally agreed upon that the primary mechanism is caused by the pendulum motion of electrons. Electrons generated via secondary-emissions from the cathode will tend to oscillate back and forth between the cathode walls, whilst slowly drifting towards the anode. This motion of electrons increases the likelihood that any given one will undergo an ionising collision with a neutral gas atom before reaching the anode [19].

While the hollow cathode geometry does obey Paschen's law, an additional parameter needs to be taken into account. This new parameter is the diameter of the aperture of the cathode, shown in figure 2.6 as D . A general rule of thumb is that the product of the pressure and cathode aperture (pD) should be in the range of 1-10 Torr cm [20]. When the pD value is too large, the pendulum effect of the electrons is lost since they undergo many collisions before

reaching the opposite end of the cathode. In contrast, when the pD value is too small, the plasma tends to form outside the hollow cathode structure as the diameter of the aperture is comparable to the Debye length [21].

Because of this, hollow cathodes have several benefits compared to their parallel plate counterparts. The most notable is that they have a lower breakdown voltage, particularly at lower gas pressures [22, 23]. Additionally, they generally produce a higher current density for a given operating voltage [22, 24], as illustrated in figure 2.7.

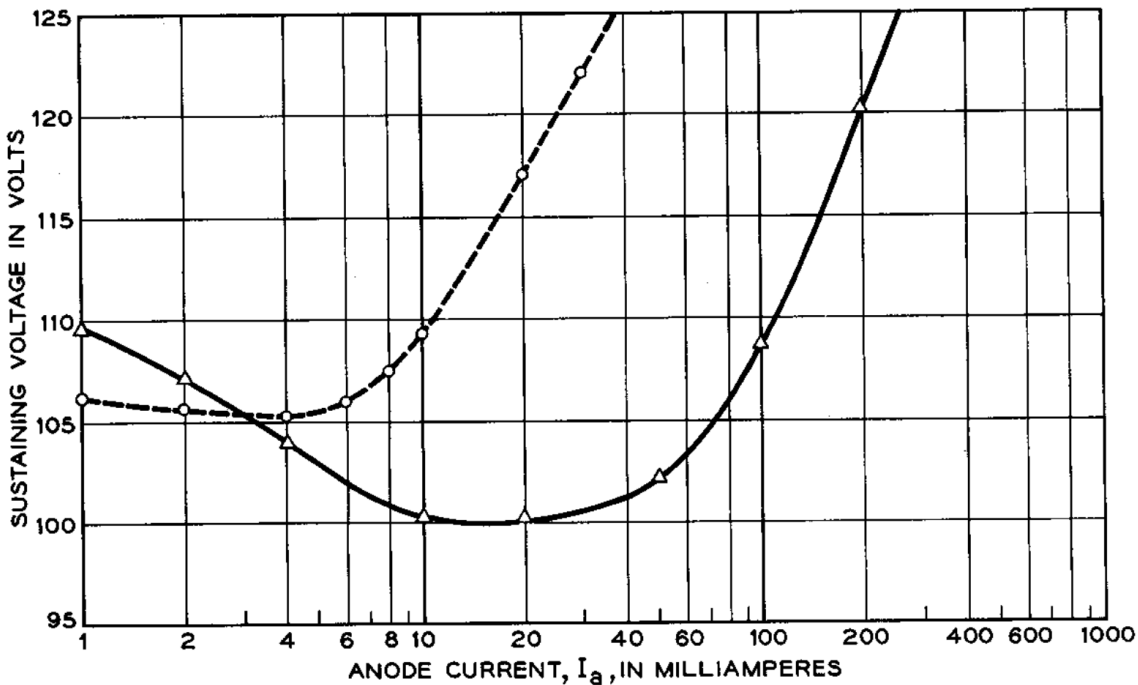


Figure 2.7: A comparison of the voltage vs current curve for a hollow cathode geometry (solid line) and a typical parallel plate geometry (dashed line)[20].

However, there are still several drawbacks to the hollow cathode. Despite their higher density, the vast majority of charged particle interactions are still collisionless. This means that there is greater bombardment of the cathode, thus leading to faster erosion. Another issue is with regards to the higher current densities, meaning that a power supply that is capable of supplying the necessary current without failure is required.

Despite this, advancements and developments of the hollow cathode geometry have mitigated this by extending the life and reliability of the cathode. As such, hollow cathode designs are found in research areas such as electron beam guns [25, 26] for welding and 3D printing of

metals, and electrostatic propulsion [27] for spacecraft thrusters.

2.2 AC Discharge

2.2.1 Breakdown and Characteristics

If the voltage source in the circuit of figure 2.2 were to be replaced with a low frequency AC source, the discharge behaviour would be almost identical to that of the DC discharge, provided that the half period of an AC cycle is larger than the time required for ions and electrons to move across the gap [15]. With such a case, the only difference compared to a DC discharge is that the electrons would move across in one direction (e.g. from left to right) in the first half period of the AC cycle, then in reverse (from right to left) in the second half period. This is because the position of the cathode and anode alternate.

However, as the frequency of the AC source is increased, typically to the region of radio or microwave frequencies, there is an asymmetry between the movement of the ions and electrons. The electrons are capable of responding to the change in the electric fields relatively quickly; however, due to the ions being significantly heavier than electrons, they have a much slower response time that is restricted by their inertia [28].

Since the ions cannot respond to the changing electric field quick enough, they respond to the time-averaged field thus are accelerated against both electrodes cross the sheath. On the other hand, the electrons begin accelerating through the bulk plasma towards the anode during the first half period of the AC signal. Then as the direction of the electric field reverses in the second half period of the signal, the positions of the anode and cathode flip, and any electron that has not collided with the original anode (which is now the cathode), gets accelerated through the bulk plasma towards the new anode. This oscillating behaviour confines the electrons, resulting in an increased likelihood of ionising collisions with the neutral background gas. This mechanism is similar to the pendulum effect of the electrons in hollow cathode DC discharges. As the frequency of the AC source is increased, more electrons become trapped in this regime,

hence it is no surprise that the breakdown voltage of the plasma decreases [29]. This can be seen in figure 2.8

Astute readers may notice the minimal role of the secondary emission of electrons plays in the AC discharge. This is because the ions do not need to be accelerated to high energies to induce secondary electron emissions. Thus in AC discharges, there is less erosion on the electrodes, which increases its overall lifetime.

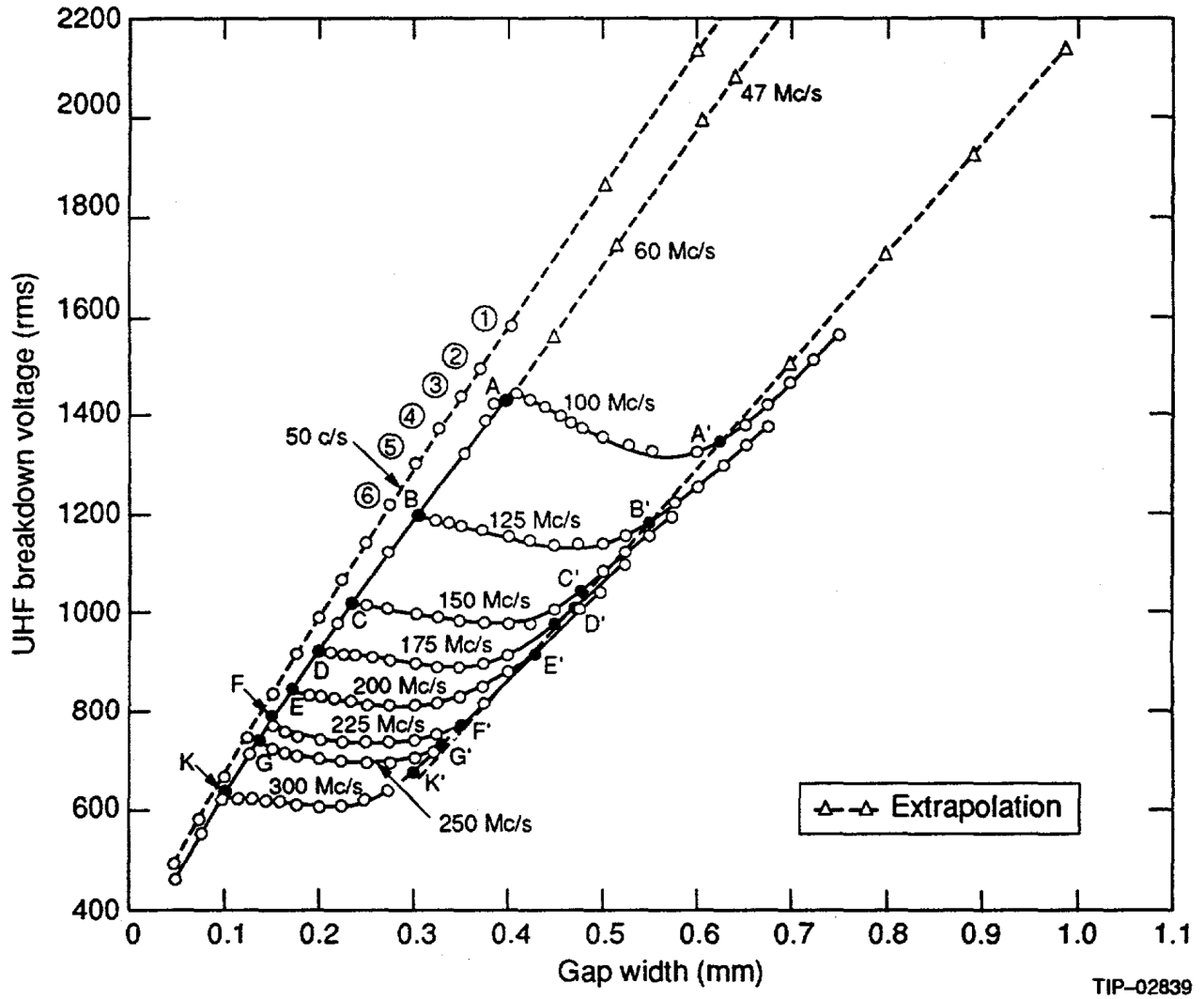


Figure 2.8: Paschen curve for AC discharge across various frequencies [30].

2.2.2 Discharge Sources

Capacitively Coupled Plasma Designs

Capacitively coupled plasma (CCP) reactors are one of the simpler designs for AC discharges. The design is very similar to the parallel plate geometry seen in figure 2.2, however rather than a DC power supply, one or more radio frequency (RF) sources are used. It is common to see the addition of a capacitor in such circuits as well. This would typically be used to block DC currents introduced by the source or additional matching networks. This can also be deliberately introduced to add a DC bias, which in some applications (such a material processing) is used to accelerate ions against the target or substrate.

An example of a CCP design can be seen in figure 2.9. These reactors typically operate at the approved ISM frequency of 13.56 MHz, however frequencies up to 100 MHz have been used as demonstrated by Sharma et al [31].

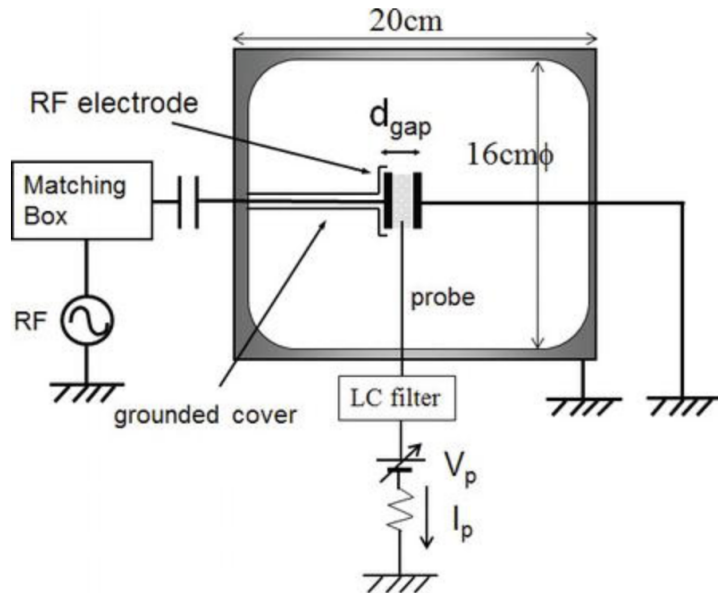


Figure 2.9: Illustration of a capacitively coupled plasma (CCP) experimental setup [32].

CCP sources are primarily used in the semiconductor industry for thin film deposition and etching. This is due to the simple design which can be scaled fairly inexpensively. Another benefit of CCPs is that the electron temperature is fairly uniform across the entire reactor, as seen in figure 2.10.

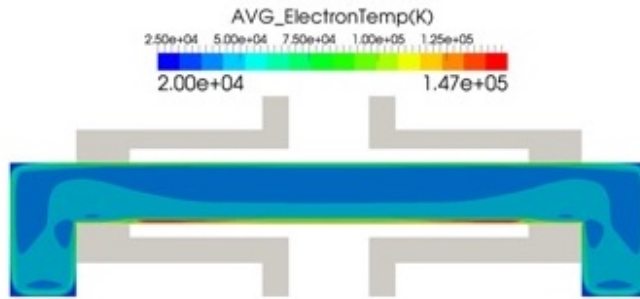


Figure 2.10: Cycle averaged electron temperature in a CCP reactor [33].

However, the biggest drawback with CCP designs has to do with the limited plasma density, typically on the order of 10^9 to 10^{10} cm $^{-3}$ [34]. Simply increasing the input power does not translate to an increased plasma density due to energy loss by ions in the sheaths [21].

Solutions for this include dual frequency driven CCPs such as the ones by Lee and Hong [35]. The idea behind such a design is that the higher frequency source controls the plasma density while the lower frequency source controls the energy of the ions bombarding the target. Other solutions including adding magnets and incorporating a hollow cathode shaped electrode to CCPs to confine the energetic electrons near the electrode [32].

Inductively Coupled Plasma Designs

Another type of AC discharge source is the *inductively coupled plasma* (ICP) design. The mechanism for plasma formation is different when comparing CCP and ICP designs. In CCPs, the plasma is formed by the RF voltage across a pair of parallel electrodes. However in ICPs, the plasma is generated using induction coils, relying on the phenomenon of electromagnetic induction. The RF current through the coils create a time-varying magnetic field, which in turn induces an electric field within the plasma chamber. An example of an ICP design is seen in figure 2.11.

Because the electric field in CCPs are perpendicular to the electrodes, the electrodes experience erosion due to ion bombardment. However in ICPs, the induced electric field is parallel to the walls of the reactor, thus such designs do not experience as much electrode erosion from ion

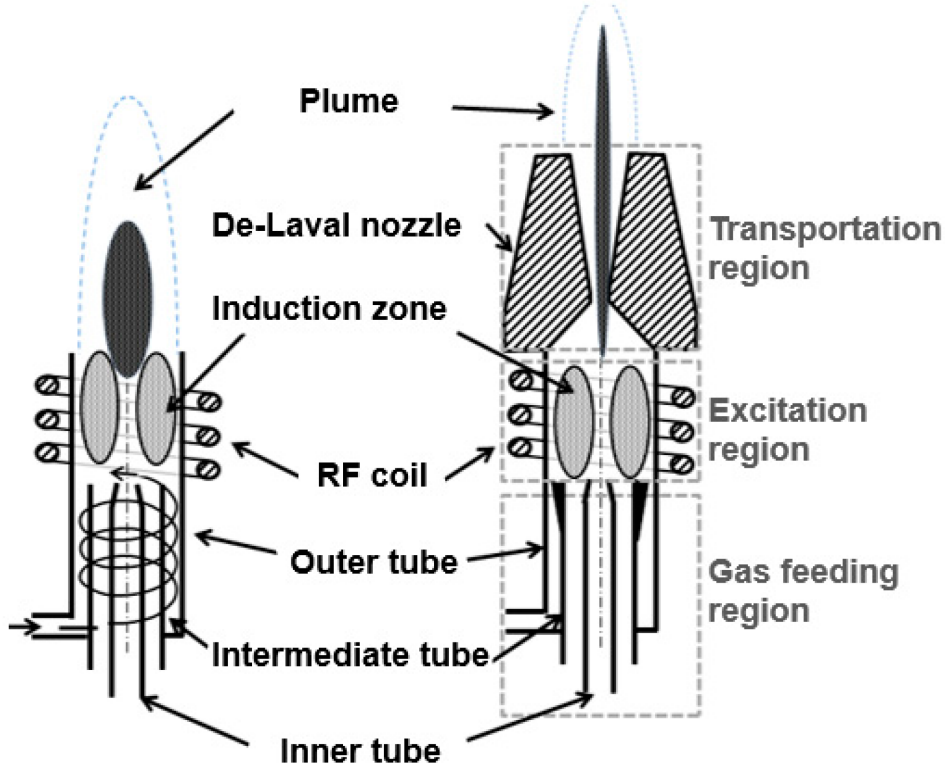


Figure 2.11: Schematic of inductively coupled plasma (ICP) torches [36].

bombardment or contamination of feed gas from sputtering as CCPs. Another advantage of the ICP design is that when compared to CCPs, they tend to generate a higher plasma density, especially at lower pressures. A comparison of ICP and CCP properties was done by Sakamoto et al [37], seen in figure 2.12. The results show that the electron density of ICPs were an order of magnitude greater than that of CCPs, though this did come with a drop in electron temperature.

However, it has been observed that this advantage of plasma density does not necessarily continue as the size of ICPs are miniaturised. This is because the rate of decrease of inductance of the coil is much higher the coil resistance [38]. Another downside is that ICPs are only viable at lower pressures. This is because the current in the coil required to sustain the plasma is quite high at atmospheric pressures, thus pressures between 0.1–10 Torr are typically used [39].

Much like CCP reactors, ICP reactors are also used in the semiconductor industry, however they each serve different functions. For example, ICPs are used for etching of conductors whereas CCPs are used for the etching of dielectrics [40].

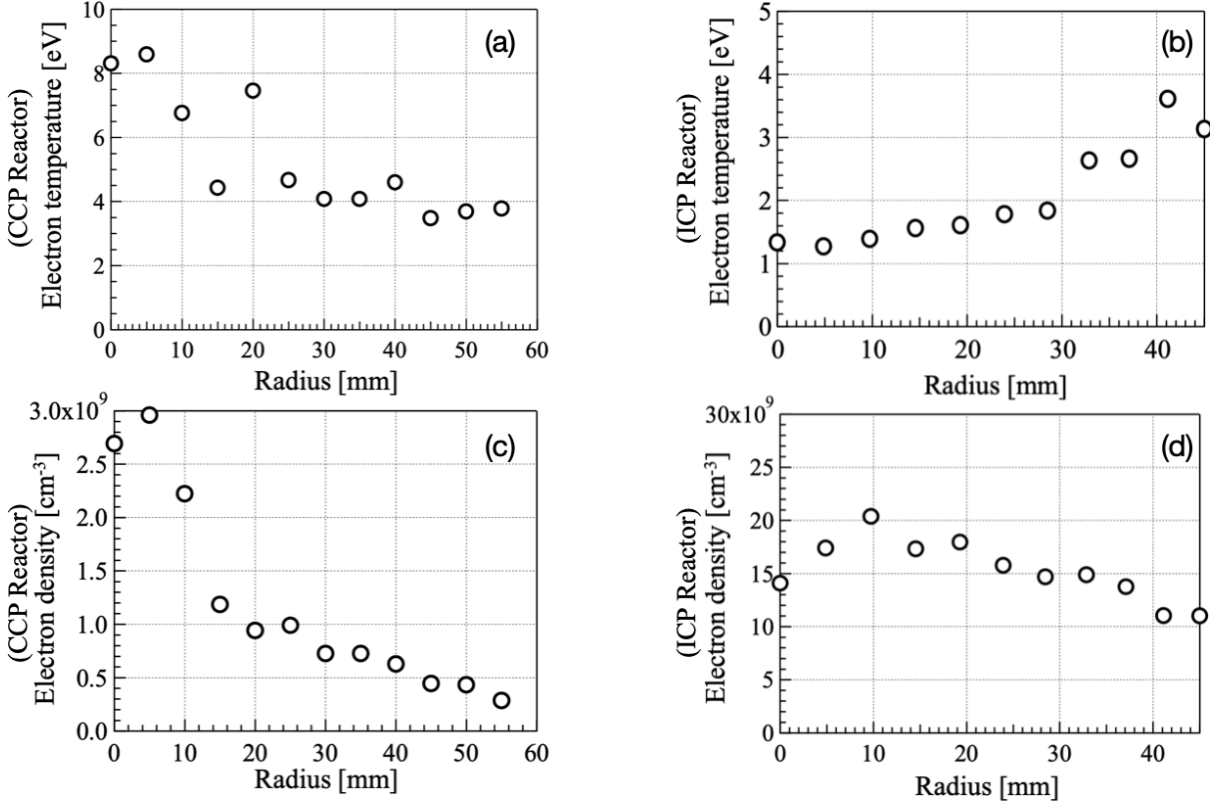


Figure 2.12: Comparison of plasma parameters between CCP and ICP reactor [37]. The two left most graphs (a, c) are the results from a CCP reactor, while the two right most graphs (b, d) are the results of the ICP reactor. The top two graphs (a, b) show the radial distribution of electron temperatures for a CCP and ICP reactor respectively. The bottom two graphs (c, d) show the distribution of electron density for a CCP and ICP reactor respectively.

Dielectric Barrier Discharge Designs

Dielectric barrier discharge (DBD), sometimes referred to as silent discharge, is a fairly common design used on a large industrial scale. Various DBD designs can be seen in figure 2.13. Much like the parallel plate discharge, there are two electrodes, however DBD designs require the presence of at least one dielectric material in the discharge gap.

Due to the dielectric being an insulator, no conduction current can flow between the electrodes, strictly limiting DBDs to AC operation. This layer of dielectric performs two functions. The first is that it protects the electrodes from ion bombardments, preventing their erosion. Secondly, the dielectric plays a role in limiting the average current density of the discharge, thus behaving as a ballast to prevent the transition of glow discharge to arc discharge [41].

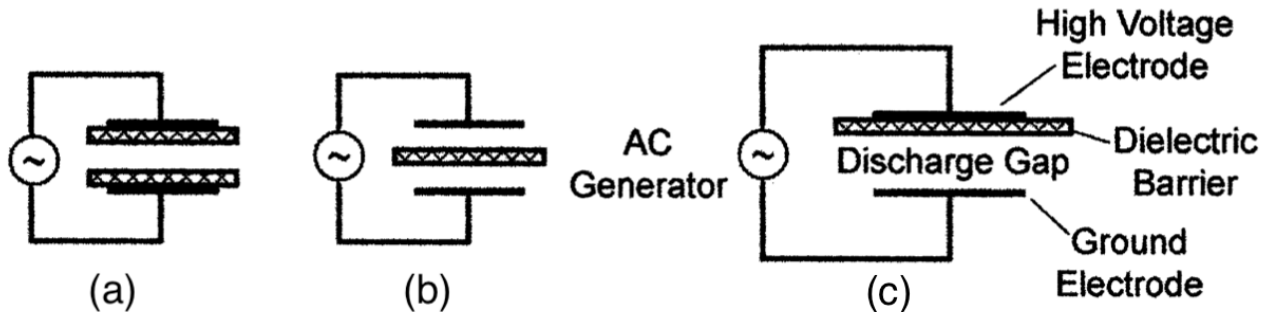


Figure 2.13: Examples of different Dielectric Barrier Discharge (DBD) designs [41]. The left most (a) and right most (c) drawings show at least one dielectric on the electrodes, while the middle (b) illustrates a dielectric in the discharge gap, but not touching the electrodes.

Most DBD devices operate in the kHz frequency range but experiments have been performed for reactors up to approximately the 10 MHz range [42]. This is because the dielectric constant of the substrate decreases at high frequencies, making it less effective at limiting the current [41].

DBD designs were frequently used in plasma display panels, which were fairly ubiquitous in televisions until about a decade ago. Nonetheless, DBD reactors still have applications ranging from surface treatment of materials to ozone generation [43].

Microwave Discharge Designs

All previous examples of AC discharges discussed so far have operated in the RF region of the electromagnetic (EM) spectrum. While there are various standard for radio bands set by agencies such as the International Telecommunication Union (ITU) or the Institute of Electrical and Electronics Engineers (IEEE), it is convention to class frequencies above 300 MHz as microwave.

The microwave plasma sources commonly used in industry tend to be fairly large devices. One of the most common of these devices generate the plasma via *surface wave discharge* where the microwaves are propagated by a wave guide [44], shown in figure 2.14. The waveguides channel the microwaves to a quartz tube containing the feed gas, which when excited by the microwaves generate the plasma.

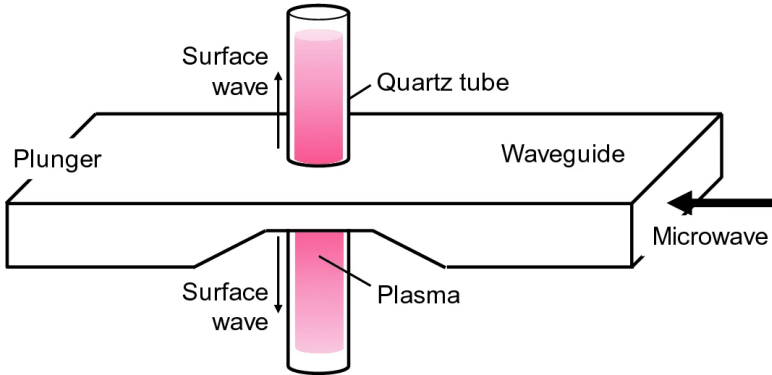


Figure 2.14: Schematic of a surface wave discharge plasma source [44].

Yet another type of microwave source is the *electron cyclotron resonance* plasma reactor that combine the microwaves source with a strong magnetic field [44]. The applied magnetic field for the electrons to move in a spiral trajectory due to the Lorentz force, and the frequency of this circular motion is called the *cyclotron frequency*. Typically, the microwave frequency is fixed, thus an appropriate magnetic flux is selected to achieve the desired cyclotron frequency.

Then, a microwave frequency is selected to match this cyclotron frequency, inducing a resonance in the electrons, which in turn increase their kinetic energy. An illustration of this reactor type can be seen in figure 2.15.

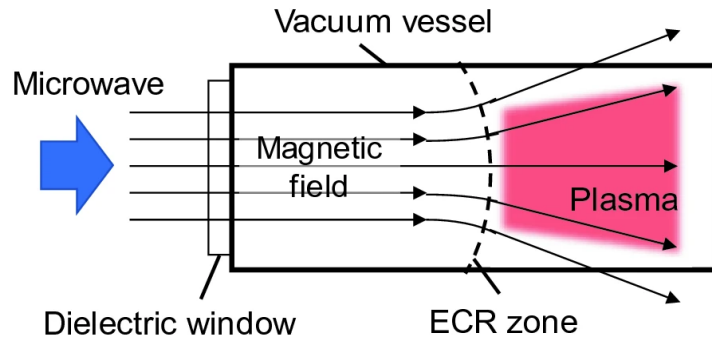


Figure 2.15: Schematic of an electron cyclotron resonance plasma source [44].

While these larger microwave plasma reactors produce plasmas with high densities and electron energies, they tend to be quite bulky and expensive (especially in the case of electron cyclotron resonance plasma sources). Smaller microwave plasma source designs aim to bring higher plasma densities seen with the larger devices, with the benefit of reduced power consumption and potentially lower costs. These smaller sources have the added benefit of portability and the ability to integrate such sources into subsystems in close proximity to other components,

with minimal electromagnetic interference.

However, miniaturising the two aforementioned designs are unfeasible. This is simply due to the fact that the size of the device determines the frequency of operation. For example a source that is approximately 1 cm would require a power supply capable of operating at around 30 GHz. Instead, these smaller plasma sources have been developed that utilise stripline and microstrip technologies that are capable of generating plasma using RF and microwave frequencies [45, 46]. Examples of these plasma sources can be seen in figure 2.16.

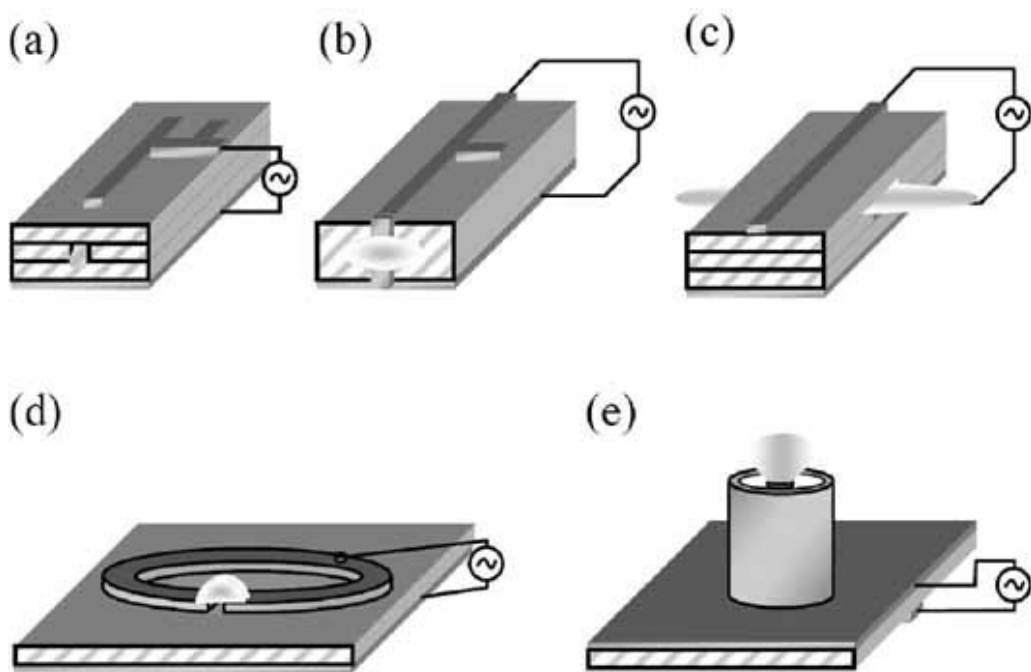


Figure 2.16: Examples of different types of microstrip plasma sources [21]. The top three designs (a, b, c) are linear microstrip resonators, while (d) shows a microstrip split-ring resonator, and (e) illustrates a coaxial resonator.

Since dimensions of the plasma formed by these microstrip sources are much smaller than the excitation wavelength, they can essentially be modelled as a CCP source. Since these microstrip sources operate at microwave frequencies, they are able to take advantage of the efficiency gains obtained by operating at higher frequencies as shown in figure 2.8, and have also been shown to produce higher density plasmas [47].

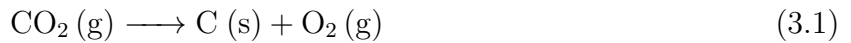
These microstrip sources have potential applications such as portable sterilisation devices [48] and chemical analysis in optical and mass spectrometry [49]. This research intends to extend its feasibility for chemical organic synthesis.

Chapter 3

Carbon Dioxide Splitting

3.1 Traditional Process

Before understanding the process of plasma-assisted CO₂ splitting, it would be useful to briefly explain the traditional thermally driven process. An ideal form of the decomposition would simply be the reverse of the coal burning process, shown in equation 3.1. This is similar to the process of methane (CH₄) pyrolysis, a method of generating hydrogen gas that has been successfully done in industry. The reaction for CH₄ pyrolysis is shown in equation 3.2.



However, such ideals are not currently feasible due to the incredible stability of the CO₂ molecule, with a Gibbs free energy of formation (ΔG°) of -394 kJ mol⁻¹. This is significantly higher than most other common gases as illustrated in figure 3.1. As such, there is limited successful research on a viable process.

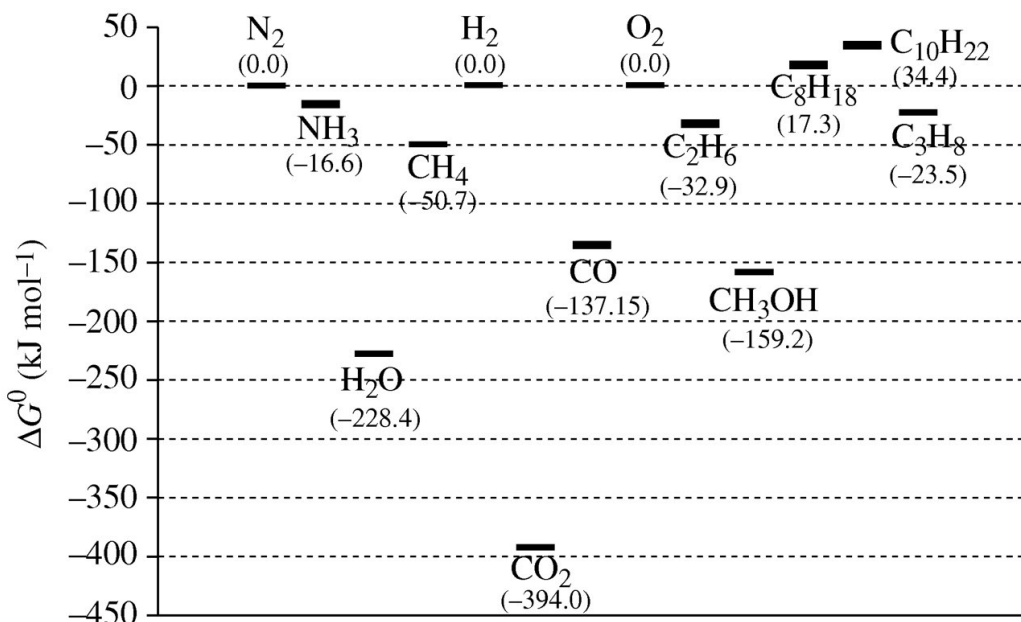
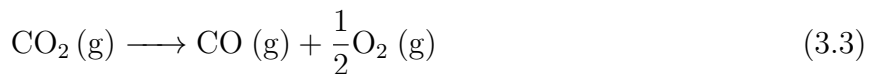


Figure 3.1: Gibbs free energy of formation for different chemicals based on data from the NIST database. [50]

Instead, current CO₂ splitting processes in the literature typically involves splitting the molecule into carbon monoxide (CO) and atomic oxygen (O). This reaction is slightly more viable than the ideal decomposition process, with an enthalpy change of $\Delta H = 283 \text{ kJ mol}^{-1}$. This reaction is shown in equation 3.3.



In the thermally driven process, CO₂ dissociated into CO begins at around 2000, forming primarily oxygen gas; but can also from atomic O at around 2300K [51, 52]. Figure 3.2 highlights this conversion based on temperature, along with its corresponding energy efficiency. For reference, converting the remaining CO to pure carbon via the Boudouard catalytic disproportionation reaction requires around 6300K [52].

It is no surprise why CO₂ splitting is greatly benefited with the use of catalysts, though this also increase the costs and complexity. The former is self explanatory, but the reason for increased complexity is that oxygen tends to remain on the catalyst surface, thus reducing its activity over time [53].

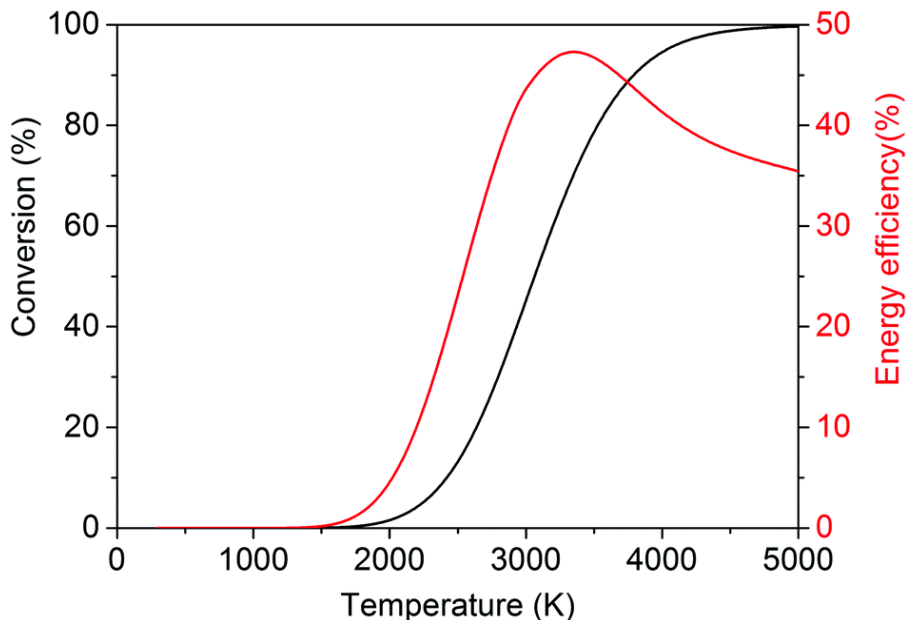


Figure 3.2: Thermal conversion and energy efficiency of CO₂ splitting as a function of temperature. [51]

As a result, it is oftentimes more practical to include the use of a co-reactant to undergo the decomposition process. Ideally, this is done using a co-reactant with a higher Gibbs free energy (i.e. a less negative value) [50]. In the literature, the most common co-reactants for CO₂ splitting are CH₄ ($\Delta G^\circ = -50.7 \text{ kJ mol}^{-1}$) and hydrogen gas (H₂, $\Delta G^\circ = 0.0 \text{ kJ mol}^{-1}$). A brief overview of both these co-reactant processes are detailed below.

CH₄ is fairly abundant, and one common use of it is for the process of steam methane reforming (involving CH₄ + H₂O) to produce syngas (CO + H₂). Syngas is typically intermediary for the production of ammonia, however is also used to produce liquid hydrocarbons via the Fischer–Tropsch process. Hence, it is no surprise why there has been research into investigating CO₂ reformation of CH₄. This process is known as the dry reforming of methane, which is an endothermic reaction requiring $\Delta H = 247.3 \text{ kJ mol}^{-1}$.



To push the equation to the right, high temperatures (between 1000-1300 K) are required and typically done in the presence of a catalysts [54]. Many different catalyst have been looked at, including the use of noble metals such as Rhodium (Rh) and Ruthenium (Ru), which have

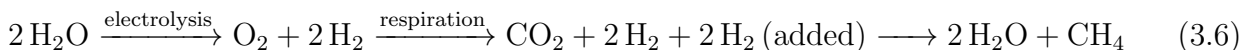
shown high activity and stability [55, 56]. However due to costs, most research has been into nickel (Ni) based catalysts which has been shown to have a similar activity to the noble metals [57]. Regardless of catalyst used, the big limitation with this process is the formation of soot on the catalyst, reducing the yields.

Besides the production of syngas, there are other uses for CH₄. The most common use of CH₄ by far is as a fuel source as it is the major constituent of natural gas. While not being particularly green in the long term, one viable use in the intermediary is to take excess electricity generated from renewable sources and convert them into synthetic CH₄. This is an example of the Sabatier reaction, and has been in operation at a power-to-gas plant in Germany for nearly a decade [58].



The benefit of this reaction is that is exothermic, with a $\Delta H = -165.3 \text{ kJ mol}^{-1}$, but it does require a catalyst in order to achieve high conversion yields. Nonetheless, there are two issues with this process. The first has to do with the fact that most of the world's supply of H₂ comes from the process of steam methane reforming, which uses CH₄ in the first place. The other issue is that unless water is the desired end product, a third of the H₂ used goes towards the creation of a waste product; not ideal when using this process at scale.

One case where water is the desired end product is on board the International Space Station, where NASA uses the Sabatier reaction to produce water for consumption by the astronauts [59]. The excess CH₄ is simply released into space. The reaction for this is expressed as:



Though even for this, half the hydrogen in the Sabatier reaction comes from resupply missions from Earth.

3.2 Plasma-assisted CO₂ Splitting

As highlighted above, there are several shortfalls with the traditional process of CO₂ splitting. This is where the use of plasma, specifically non-thermal plasmas (i.e. generated by electric means), can be beneficial. In these plasmas, electrons have a higher temperature than the ions or the background gas. Energetic electrons in the plasma can dissociate molecules, even highly stable ones such as CO₂ at standard temperatures and pressures [51].

Because of this behaviour, there is no need for heat and pressurised reactors, reducing the complexity (and thereby costs). This leads on to the second benefit, where the entire operation of such a reaction is described as a 'turn-key' process due to the ability to instantly turn the plasma on and off, with minimal stabilisation times. There is also no need for rare earth metals to be used as catalysts, and it has been shown that plasma reactors can have good scalability as shown by Kogelschatz in [60].

For the plasma assisted decomposition process, there are several pathways available for the reaction to take place. Just to note, all reactions will have the units eV, rather than kJ mol⁻¹, henceforth as it is the commonly used nomenclature in the literature. For reference, the CO₂ splitting reaction shown in equation 3.3 requires about 2.93 eV.

The dominant pathway is via electron-impact dissociation, with an energy threshold around 5.5 eV per molecule; which corresponds to the energy required to break the C=O bond [61];. This is often accompanied by the recombination of the oxygen atoms [62]. This is shown in equations 3.7 and 3.8 respectively.



Note that M is a particle from the background gas.

Though, it is also possible splitting to occur when vibrationally excited CO₂ molecules collide with the atomic oxygen or electrons, requiring around 0.3 eV and less than 1 eV per molecule respectively [62]. These are also shown in equations 3.9 and 3.10 respectively.



There are several different methods to generate plasma for CO₂ splitting in the literature, however the most common are: dielectric barrier discharges (DBD), gilding arc discharges (GA), and radio frequency (RF)/microwave (MW) discharges. These different processes used are typically characterised and evaluated by two main parameters: the *conversion efficiency* and the *energy efficiency*. The conversion efficiency (χ_{CO_2}) simply denotes the fraction of CO₂ used by the splitting process, and can be defined as:

$$\chi_{\text{CO}_2} = \frac{n_{\text{start}} - n_{\text{end}}}{n_{\text{start}}} \quad (3.11)$$

where n is the number of moles of CO₂. Though oftentimes, it is easier to determine the conversion efficiency based on the yields of the product.

On the other hand, energy efficiency (η_{CO_2}) corresponds to the fraction of input energy that went into splitting the CO₂ molecules. This can be expressed as:

$$\eta_{\text{CO}_2} = \frac{\chi_{\text{CO}_2} \Delta H_{\text{CO}_2, 298K}^\circ}{SEI} \quad (3.12)$$

where SEI is the specific energy input, which describes the average energy available per molecule in the plasma that contribute to plasma chemical reactions [63]. The SEI can be calculated as the ratio between the discharge power and the gas flow rate. The discharge power

is almost always measured in watts (W), however there are many different standard units for measuring flow rates of gases.

In this report, all flow rates are measured in standard cubic centimetres per minute (sccm). With discharge power (P) and flow rate (Q), the SEI (in eV molecule⁻¹) can be calculated as follows [64]:

$$SEI = \frac{P \text{ (Js}^{-1})}{Q \text{ (cm}^3 \text{ min}^{-1})} \times \frac{60 \text{ (s min}^{-1}) \times 6.24 \times 10^{18} \text{ (eV J}^{-1}) \times 24000 \text{ (cm}^3 \text{ mol}^{-1})}{6.022 \times 10^{23} \text{ (molecules mol}^{-1})} \quad (3.13)$$

Note that the value 24000 cm³mol⁻¹ is derived from the ideal gas law at atmospheric pressure and at 293K.

Snoeckx and Bogaerts compiled a list of various plasma reactors for CO₂ conversion, and evaluated their conversion and energy efficiencies [51]. An illustration of the result can be seen in figure 3.3.

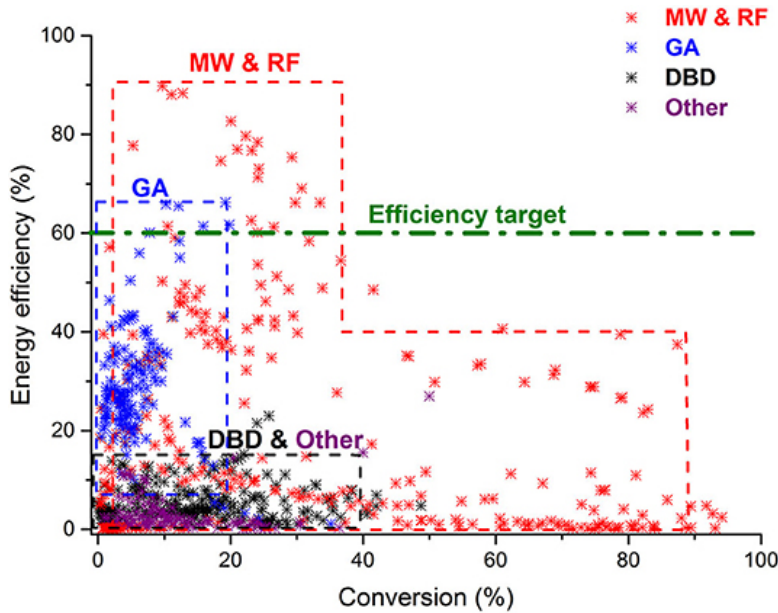


Figure 3.3: Comparison of conversion and energy efficiencies for various CO₂ splitting plasma reactors [51].

From the figure 3.3, it is evident that one of the most extensively studied processes for CO₂ splitting involved DBD reactors. This is not surprising given that DBD reactors have already

had industrial success in areas related to ozone production and VOC removal [41]. Nonetheless, they seem to have relatively poor performance, which makes it hard to justify them for industrial applications. GA plasma perform better than DBD reactors when it comes to energy efficiency. However, they struggle to get a conversion efficiency greater 20%, most likely due to the fact that the amount of gas passing through the the arc of plasma is minimal.

RF and MW plasmas by contrast appear to have a wide spectrum of results. From reactors that trade off low conversion for high energy efficiencies and vice versa, to designs that are located in the middle of both parameters. Though, a lot of these RF and MW plasma reviewed operated at sub-atmospheric pressure. Nevertheless, because of the promise shown by MW reactors, the rest of this chapter will highlight examples from the literature.

One final thing to note from figure 3.3 is the inclusion of an energy efficiency target of 60%. Snoeckx and Bogaerts believe that this values should be the target for plasma assisted splitting to be competitive and worthy alternative to traditional methods. The rational behind this number was two fold. First was a comparison to electrochemical water splitting, which have energy efficiencies of approximately 65-75%. The next was to couple CO₂ splitting with solar energy, to give a solar-to-fuel conversion efficiency around 20%, which was said to be competitive in industry.

Many experiments utilise a structure as seen in figure 3.4, called surface-wave discharges. Gas is typically fed through a tube (typically quartz), coupled with an external wave guide where the microwave discharge is generated. The typical frequencies in such experiments are 915 MHz or 2.45 GHz, which are comparable by the dimensions of the setup.

Bongers et al used such a reactor [65] at a frequency of 915 MHz at approximately 150 Torr. They were able to obtain an conversion efficiency of up to 23% at an energy efficiency of 36%, though were able to achieve an energy efficiency of 50% at lower powers which reduced the conversion. The downside of their setup was that it required a specialised configuration where the gas was supersonically expanded in the plasma.

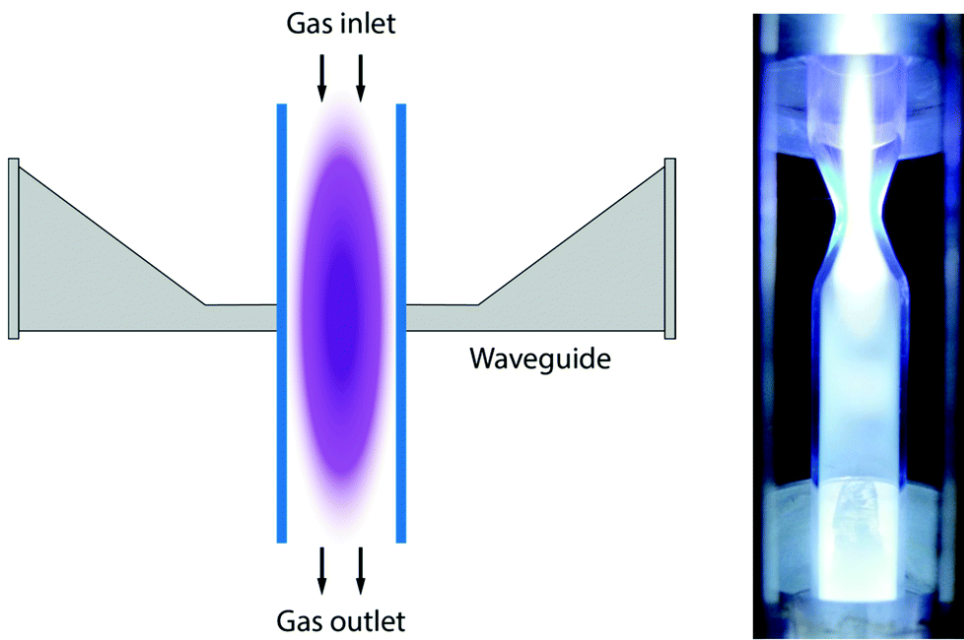


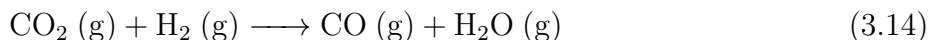
Figure 3.4: Schematic of microwave reactors for CO₂ splitting [51].

A more typical configuration was done by Silva et al [66], the experiment was operated at 2.45 GHz with a pulsed microwave generator, but it was operating at a very low pressure (between 1-10 Torr). They used a gas mixture of CO₂ with 5% nitrogen (N₂), and were able to get conversion efficiency of 80% with a steady energy efficiency of around 12%.

It is common to see co-reactants with plasma-assisted CO₂ splitting for the same reason as the thermally driven process, it becomes much easier for the reaction to take place because of thermodynamics. Generally, inert gases such as Argon (Ar) or Helium (He) are used. However, it is also common to see N₂ due to its abundance and cost effectiveness. The flaw with using N₂ is that the conversion of N₂ is more abundant than CO₂, resulting in the formation of undesirable gases such as NO₂, NO, and N₂O [67].

The rational for using inert gases is to function as an electron source, allowing for the plasma to be sustained more easily. It has also been shown that the breakdown voltage decreases when CO₂-Ar or CO₂-He mixtures are used [68], and that the electron density increases promoting more frequent collisions [67, 68]. When choosing between the two gas inert gases, Ar is cheaper than He. However, He has a higher ionising potential (of 24.6 eV) compared to that of Ar (of 15.8 eV), which explains why He plasmas have a higher electron temperature [67, 69].

Other gases have been used as co-reactants, such as H₂ by Chen et al [70]. They used a surface waveguide with a frequency of 915 MHz, at a pressure of around 30 Torr. The H₂ is actually first produced from the decomposition of water (H₂), then the following reaction takes place:



They were able to obtain a 22% conversion efficiency and a 52% energy efficiency. These efficiencies were obtained with the use of a (NiO/TiO) catalyst.

Additionally, CH₄ has been used co-reactants by Chun et al [71]. They used a plasma torch operating at 2.45 GHz, which has a similar structure to the surface waveguides shown in figure 3.4 but channels have been made within the quartz tube to allow the gas to swirl. With this, they were able to get conversion efficiencies of 68.4% for CO₂ and 96.8% for CH₄. No energy efficiency was given, but some rough calculations based on parameters used gives an efficiency of around 33%. The big advantage of this process had to do with the fact that it is one of the few processes that operates at atmospheric pressure (760 Torr).

So far all the previous examples include the use of gaseous reactants. It is also possible to for the co-reactants for the CO₂ decomposition process to be liquids. Research into this was limited due to the fact that these liquids are typically organic liquids which made them unsuitable at low pressure operations (as seen with many of the previous examples) due to vapor pressure limitations [72]. However, with the advances in microwave reactors operating at atmospheric pressure, these plasma–liquid systems have become a viable area of research. The obvious advantage is that this leads to even more possible reactions with CO₂ to produce desired end products. Additionally, if the end product is also a liquid, it allows for easier separation of the product from the waste reactants.

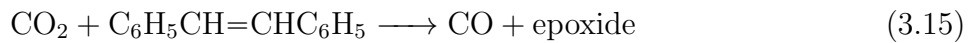
One example of research into plasma–liquid systems was done by Gorbanev et al [73]. They tested three different organic solutions (dehalogenation of iodoarenes, 5-exo-trig cyclisation, and trifluoromethylation with the Togni-II reagent) using a frequency of 24.9 kHz. The apparatus used was similar to that in figure 3.4, but because the frequency used was RF, the tube was

modified to include embedded electrodes. The feed gas included a CO₂-He mixture, with yields of up to 95% after 30 mins for the last test case. Though, there were a lot of variations in the results, and even the authors note that the results are only preliminary with more work required to optimise reaction efficiency.



Figure 3.5: Photograph of COST jet [74].

Another more recent development was developed by Xu et al [75]. The reactor used was a COST microplasma jet developed by Schulz-von der Gathen et al [?], a capacitively coupled reactor that operated at 13.56 MHz. A picture of the jet can be seen in figure 3.5, and the experimental setup by Xu et al is shown in figure 3.6. Their design also utilised a CO₂-He mixture, but with a co-reactant called *trans*-stilbene. The end product of this reaction was an epoxide (which is a popular compound use for detergents, adhesives, and plastics) and the waste gas CO. This reaction can be seen below:



The plasma jet had to be placed 4 mm above the surface of the liquid, and the authors were able to reliably get yield on epoxides of around 75%. The conversion efficiency was slightly lower at approximately 70%. The authors did not provide an energy efficiency, and its value

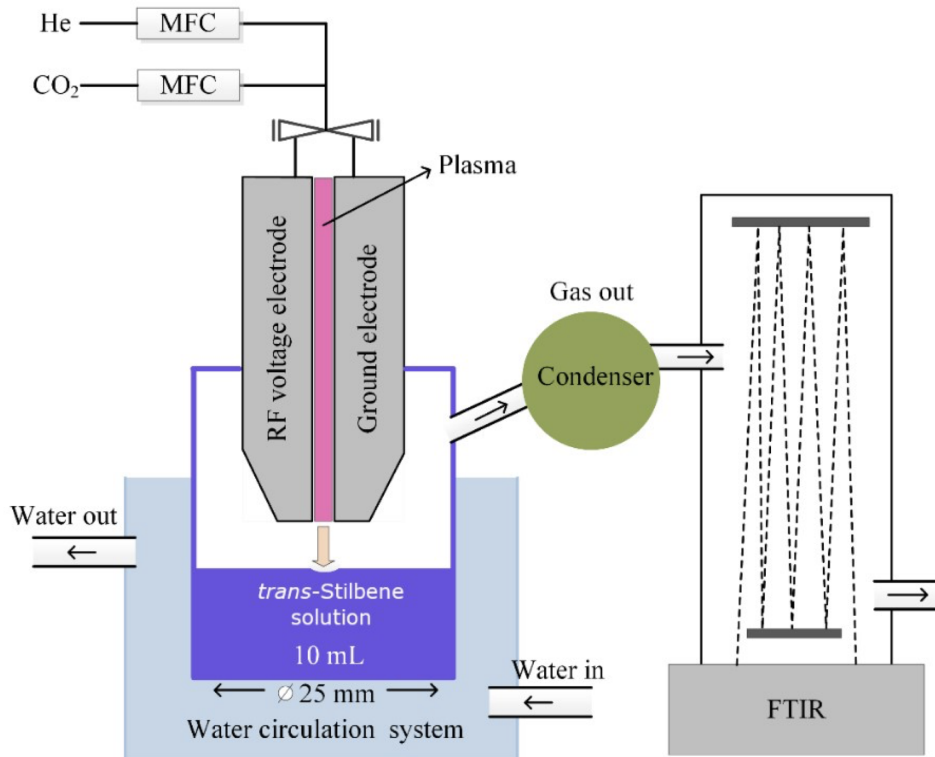


Figure 3.6: Schematic of experimental setup by Xu et al [75].

could not be determined as the details regarding the power of the reactor were not stated.

This approach seems quite feasible especially considering it was operating at atmospheric pressure. The only downside of this process was that temperature seems to play a role in the efficiency of the reaction, with the best performance at around 250K. Nonetheless, the reaction is still perfectly viable at room temperature, with the yields dropping by only 5%. As such, this will be the process that is emulated in this report.

Chapter 4

The Split Ring Resonator

In the work done by Xu et al [75], the plasma discharge was generated using a CCP jet, specifically a design by the European Cooperation in Science and Technology (COST) [76]. The COST plasma jet was originally developed for medical and biomedical applications, as such were developed to operate at the approved ISM frequency of 13.56 MHz. However, RF plasma sources are flawed in the sense that they have a limited plasma density, which could theoretically limit the rate of splitting of CO₂ molecules.

To improve upon this, the plasma discharge used for this project would use a microwave plasma, specifically a microstrip-based source called the *split ring resonator* (SRR). Using such a device will have two main benefits. First, the power efficiency of the microwave plasmas would allow for discharges would either allow for lower operating powers or greater electron densities at the same operating power. Additionally, the device would also be much smaller and cheaper to manufacture.

An illustration of an SRR can be seen in figure 4.1. The design of a SRR is quite simple, consisting of a conducting ring, usually made of copper, laid on top of a dielectric substrate. The bottom of the dielectric consist of a ground plane that covers the entirety of the surface. This has the added benefit of dispersing the heat generated from the SRR. As seen in figure 4.1, there is a small gap made on the top surface that breaks the copper ring, which is where the plasma discharge occurs.

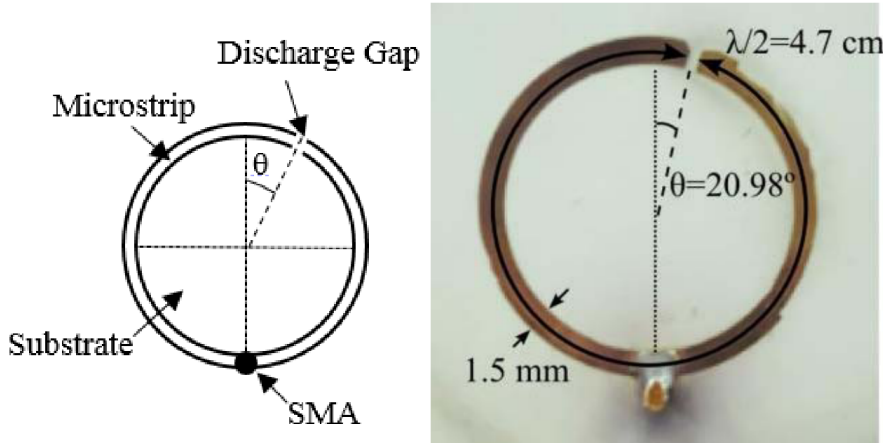


Figure 4.1: Schematic (left) and photo (right) of SRR [77].

4.1 Overview

In order to achieve a discharge, a high frequency (microwave) voltage is applied to the SRR via the SMA connector. The exact frequency to be used is governed by two factors: the mean circumference of the top conducting ring and the dielectric constant of the substrate used. The mean circumference is specifically designed to be half the wavelength corresponding to the desired frequency. The dielectric constant is required to determine the speed of light in the dielectric medium used. Thus, an equation for the frequency used for a given SRR is [77]:

$$f = \frac{c}{\lambda\sqrt{\epsilon_r}} \quad (4.1)$$

The reason why the mean circumference is designed to be half the desired wavelength is for power efficiency. Due to this design, the ends of the SRR (i.e. where the gap is) will be 180° out of phase from each other. Because of this, when one end of the SRR is at the peak of the AC cycle, the other will be at a trough; thus the potential difference between the two ends has been doubled. This geometric design allows for the doubling of the strength of the electric field at a constant power.

Astute readers may notice that the ring of the SRR device shown in figure 4.1 is not symmetrical. Instead, the discharge gap appears to be offset towards one side of the device. This is deliberate as the offset position changes the characteristic impedance of the device, allowing for impedance

matching without the need of additional passive components. This offset angle (θ), measured from the very centre of the ring, is chosen using the expression [78]:

$$\theta = \arccos\left(1 - \frac{Z_{in}\pi}{Z_0 Q}\right) \quad (4.2)$$

where Z_{in} is the input impedance of the power supply, Q is the quality factor, and Z_0 is the characteristic impedance of the SRR.

The input impedance of most power supplies is 50Ω , while the quality factor is a parameter given on the data sheet of the substrate used. As for the characteristic impedance, it is governed by four factors:

- the width of the top copper trace, w .
- the thickness of the copper pour, t .
- the thickness (or height) of the dielectric substrate, h .
- the dielectric constant of the substrate, ε_r .

For a thin microstrip, it is typical to use the analytical solution derived by Wheeler [79], as it approximates the characteristic impedance with an error of less than 1%. These are shown in equations 4.3-4.6:

$$Z_0 = \frac{42.4}{\sqrt{1 + \varepsilon_r}} \ln \left(1 + \frac{4h}{w'} (X_1 + X_2) \right) \quad (4.3)$$

$$X_1 = \frac{4h}{w'} \left(\frac{14\varepsilon_r + 8}{11\varepsilon_r} \right) \quad (4.4)$$

$$X_2 = \sqrt{\left(\frac{4h}{w'} \right)^2 \left(\frac{14\varepsilon_r + 8}{11\varepsilon_r} \right)^2 + \pi^2 \frac{1 + \frac{1}{\varepsilon_r}}{2}} \quad (4.5)$$

$$w' = w + \frac{t}{\pi} \ln \left(\frac{4e}{\sqrt{\left(\frac{t}{h} \right)^2 + \left(\frac{t}{w\varepsilon_r + 1.1\pi} \right)^2}} \right) \frac{\varepsilon_r + 1}{2\varepsilon_r} \quad (4.6)$$

4.2 Production

While the SRR device shown in figure 4.1 would generate a microwave plasma, a slight modification is required for the device to be usable as a small jet for this project. To allow the gases to flow through the plasma and exit the device, an orifice needs to be placed in the discharge gap.

While this may be a small alteration to the device, it was an unknown if such a change would effect the behaviour of the plasma formed. To investigate this, several simulations were run to better understand the discharge dynamics. For this research, the author used *Particle-in-cell* (PIC) simulations using the software called *XOOPIC* [80]. Further information on PIC simulations and XOOPIC can be found in the appendices.

4.2.1 Simulations

Multiple different simulations were run to understand the characteristics of the plasma, however they could be broadly broken down into three groups. For all these simulations, a cross sectional plane of the discharge gap of the SRR was modelled. The reasoning for this was that the plasma formed would typically be constrained around the gap [46]. Though the ring of the SRR is a circle, the discharge gap is small relative to the overall device, hence simulating this region is sufficient to understand the plasma characteristics. For all the following simulations, the parameters can be found in table 4.1 unless specified otherwise.

The first of these simulation groups was to simply study the effects of introducing a through hole to the SRR. For this test, all simulation parameters were kept identical, the only difference would be the introduction design of the gap. A visualisation of the simulation domain is shown in figure 4.2. In figure 4.2a, the dielectric substrate (seen in gold) and the bottom electrode (seen in green) is kept intact as a single structure, whereas the top electrode (seen in yellow) is split. However in 4.2b, all three layers of the SRR are split into two.

The results of the simulation after it stabilised (which amounted to approximately 2 μ s in

Table 4.1: Simulation parameters of SRR in XOPIC.

Parameters	Value	Units
Domain x-axis	1.0	mm
Domain y-axis	2.5	mm
Dielectric thickness	500	μm
Dielectric constant	3.66	
Equipotential thickness	40	μm
Gas pressure	780	Torr
Gas temperature	25	meV
Potential Difference	150	V
Frequency	1	GHz
Time step	0.1	ps

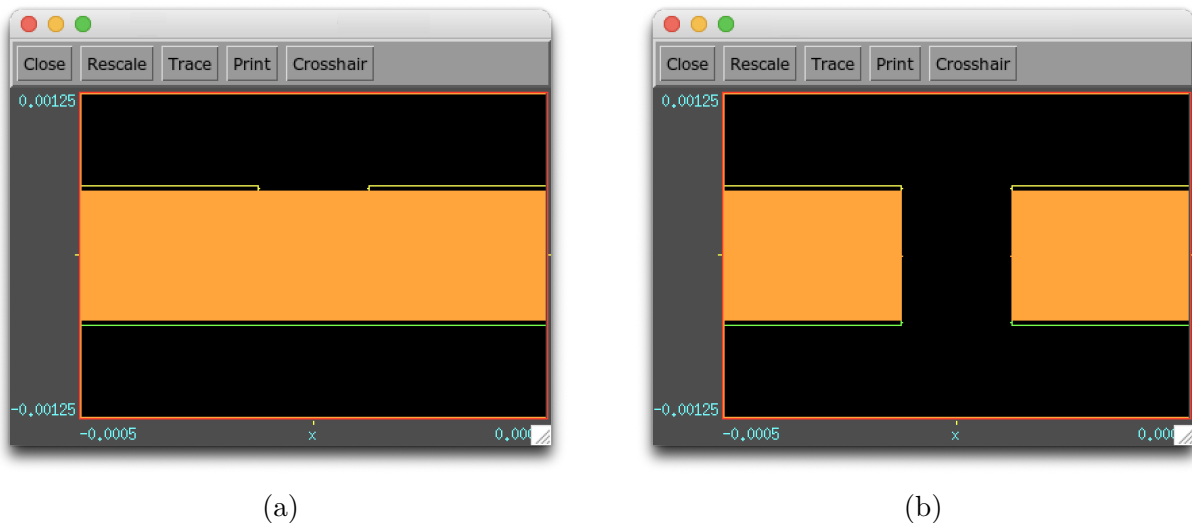


Figure 4.2: A cross section comparison of SRR simulation domain without a hole (a) and with hole (b) in gap.

simulation time) can be seen in figure 4.3. The immediate difference that can be observed is the fact that the ions and electrons, represented as blue and orange dots respectively, tended to ‘sit’ deeper into the gap in the case with the through hole. Intuitively, this would make sense as these particles are not colliding with the substrate. Additionally, it was hypothesised that strength of the electric field between the top electrodes and the ground plane could potentially play an effect in how deep the ions and electrons penetrate in the gap, which is investigated later.

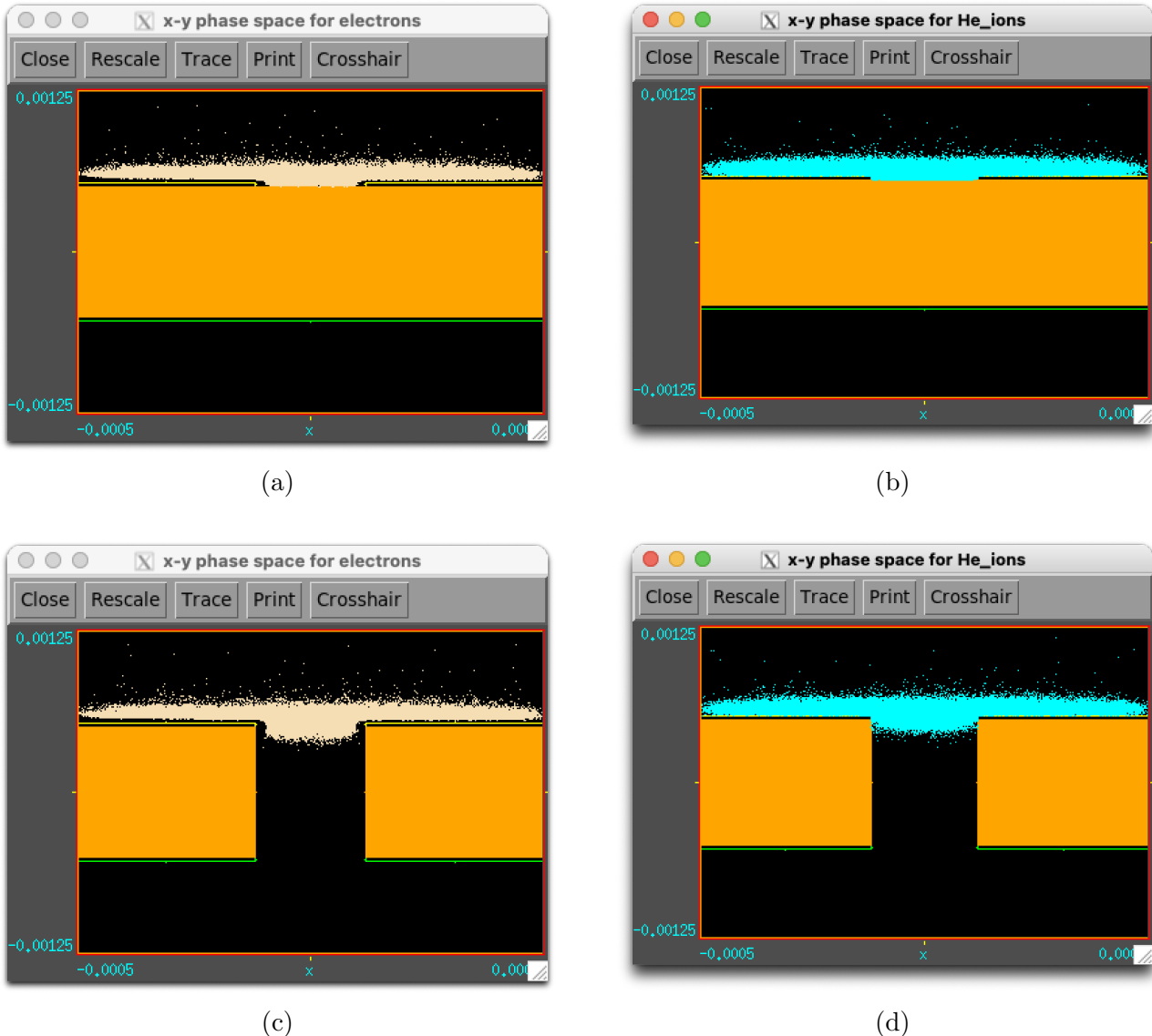
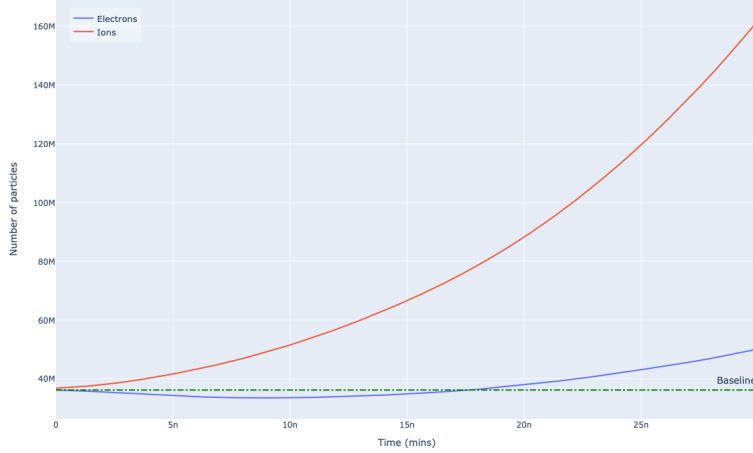


Figure 4.3: A comparison of the distribution of electron (a, c) and ions (b, d) in the discharge of the SRR. The top two subfigures (a, b) show the distribution in an SRR with no hole, while the bottom two (c, d) show the distribution in an SRR with a hole in the gap.
Comparison of SRR with and without hole in gap.

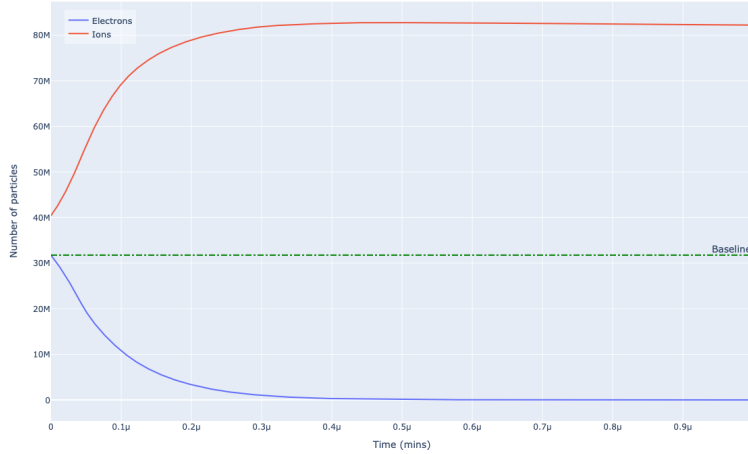
The next set of simulations run were to identify the ideal width discharge gap to be used. As seen in Paschen's law, it is one of the parameters governs to breakdown voltage. Hence selecting the ideal gap width should allow for a lower operating power. In these simulations, the only parameter changed was the gap width, taking the values of 120 μm , 180 μm , 240 μm , 300 μm , 360 μm , 420 μm , and 480 μm .

Rather than observing the steady state characteristics, in these simulations the focus was to obtain the exact breakdown voltage for each gap, forming a very rough Paschen curve. To do

this in simulations, one observes if a given voltage creates the Townsend avalanche resulting in the increase in the number of electrons in the simulation. This is better explained visually as shown in figures 4.4.



(a)



(b)

Figure 4.4: A comparison of the number of particles diagnostic between a simulation potential difference of 150V (a) causing a voltage breakdown and one with a potential difference of 100V (b) which does not cause a breakdown.

In figure 4.4a, the number of electrons initially drop below the baseline but then increases again, meaning that the Townsend avalanche occurred, hence the plasma is said to be ignited. Whereas in figure 4.4b, the number of electrons decreases until it reaches zero, meaning that the voltage set was not sufficient to cause a breakdown. The reason for the baseline number of

electrons is due to seeding the simulations with particles.

This process of varying the simulation voltage was done across all the aforementioned gap widths to form a voltage breakdown curve shown in figure 4.5. From the data, it can be seen that the ideal gap width for the simulated design of the SRR was a $180\mu\text{m}$ discharge gap. However based on the shape of a Paschen curve, a smaller discharge gap could be more optimal, though the gains would probably be marginal.

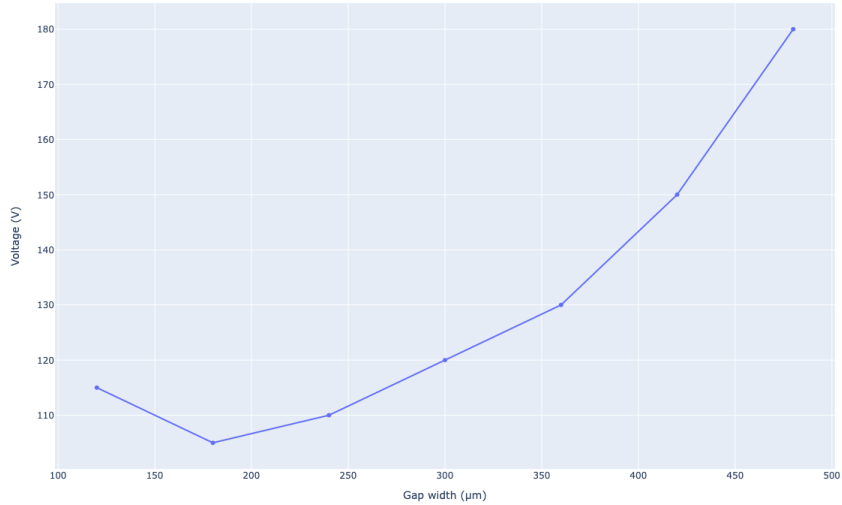


Figure 4.5: Simulation breakdown voltages across the various tested discharge gap widths.

With the optimal gap width identified, another parameter that needed to be looked into for the design of the SRR was the separation distance between the top and bottom electrodes. In other terms, it was to identify the ideal dielectric substrate thickness to be used when manufacturing the SRR. These simulations were split into two parts.

For the first part of the simulations regarding the dielectric thickness, the goal was to observe if changing the thickness would have any effect on the plasma behaviour. For these simulations, the dielectric thickness used were 0.2 mm, 0.5 mm, 1.0 mm, 1.5 mm, and 2.0 mm. The simulations were run until they stabilised, again to around $2\mu\text{s}$ in simulation time. The results of these simulations can be seen in 4.6 in the form of a cross sectional view of the density plot of electrons. From the data, it can be seen that there are ‘hotspots’ of electrons near the top electrodes that vary from tests, however the overall density and shape of the plasma are

almost identical. This implies that changing the dielectric thickness does not play a large role in the plasma behaviour, so other factors would need to be used to determine which dielectric thickness would be chosen for manufacturing the SRR.

The first was to observe if increasing the dielectric thickness had any effect on the plasma characteristics, notably deep the plasma ‘sits’ in the discharge gap. The other characteristic investigated was if changing the dielectric thickness would have any affect on the

The other part of the dielectric thickness simulations was to identify if the thickness chosen would have an impact on the breakdown voltage since reducing the thickness would make the strength of the electric fields between the top electrodes comparable to the electric field between the AC electrodes and the ground plane. A similar approach was taken to simulations run for evaluating the impact of the gap width on breakdown voltage, though in this case the gap width was kept fixed and the only parameter changed was the thickness of the dielectric. The same values were used for the dielectric thickness as before.

The results for these simulations are shown in table ??.

TODO.

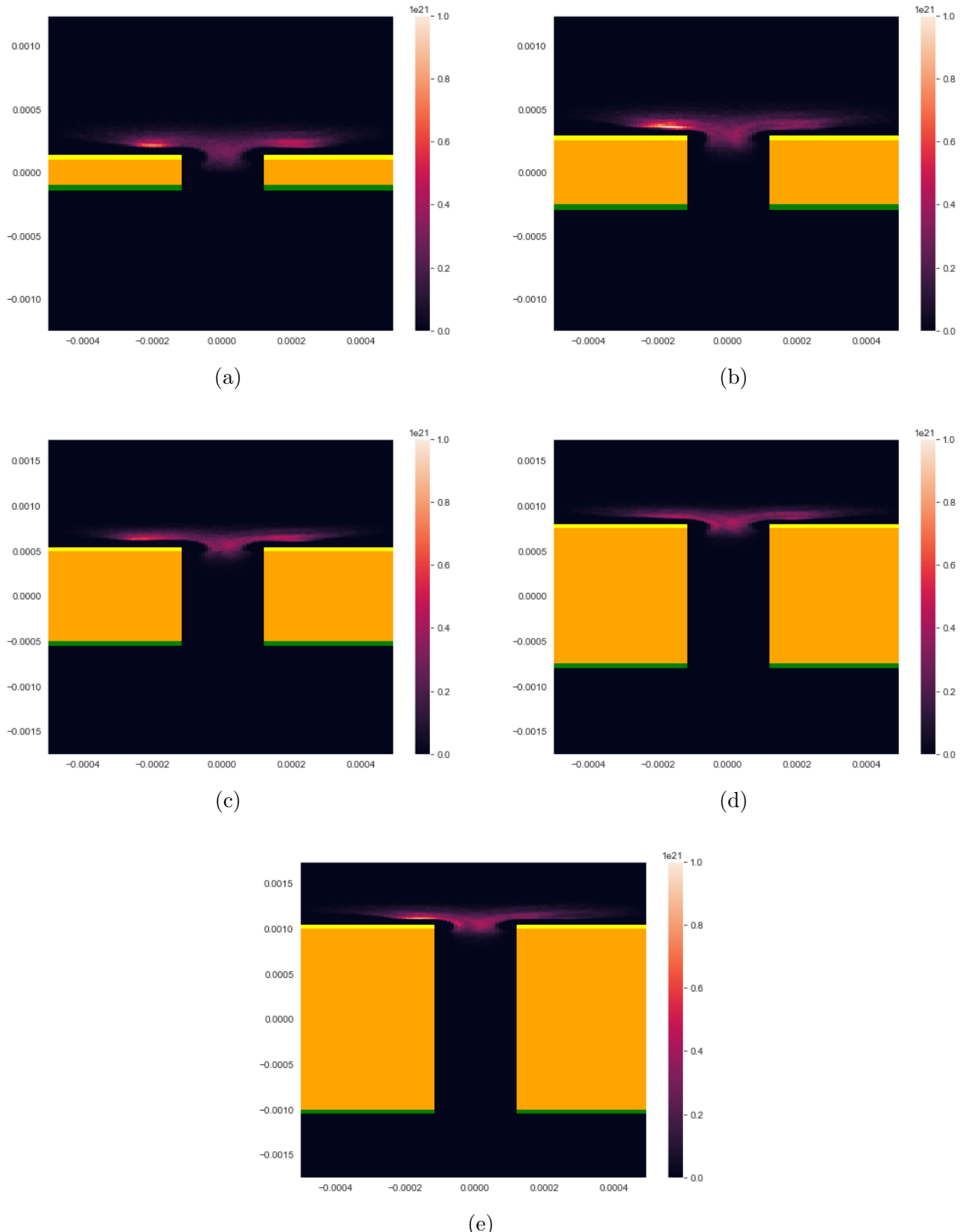


Figure 4.6: Comparison of dielectric thickness of 0.2 mm (a), 0.5 mm (b), 1.0 mm (c), 1.5 mm (d), and 2.0 mm (e) on the SRR.

4.2.2 Design

Using the results from the simulations run, a design of the SRR to be used could be made. The first step was to select the desired operating frequency (also referred to as the resonant frequency). Selecting this frequency for the SRR required striking a compromise. Ideally, a higher resonant frequency would improve the quality factor, reducing power losses and making it more likely that a plasma discharge occurs. However, a frequency that is too high would increase power requirements required to drive the SRR. An additional drawback to using higher frequencies is that as seen in equation 4.1, increasing the frequency causes a decrease in the wavelength, which in turn reduces the size of the SRR. While this is not directly a problem, a smaller ring for the SRR would require significantly tighter manufacturing tolerances which in turn drive up the cost of production. As such, a target frequency of 1 GHz was chosen to strike a balance between these factors.

The next step was to then select the PCB substrate to be used, as its dielectric constant (ε_r) is another central parameter for all other calculations of the SRR. For this, the material selected was the RO4350BTM substrate from Rogers corporation. This material was chosen over traditional PCB substrates, such as FR4, due to its excellent dissipation factor (D_f) at high frequencies. RO4350BTM had a $D_f = 0.0031$ (at 2.5 GHz) whereas FR4 had a $D_f = 0.022$ (at 500 MHz). Though not an apples to apples comparison, the D_f typically increases with frequency. Thus at approximately 1 GHz, the D_f for FR4 would be an order of magnitude over that of the RO4350BTM substrate. In the real world, this translates to a higher insertion loss for FR4 over RO4350BTM, resulting in worse efficiency. Though better performing substrates were available, they came with the tradeoff of manufacturing cost, hence using RO4350BTM was a suitable compromise. Additionally, RO4350BTM did not require any special treatments or procedures to introduce a through hole.

According to its data sheet, the RO4350BTM board has a dielectric constant (ε_r) of 3.66. However, the data sheet also specified that this result was only tested for the frequencies between 8 to 40 GHz; significantly higher than the desired operating frequency. From a previous experiment operating at roughly 500 MHz, it was ascertained that the ε_r was reduced by nearly

25% compared to the stated value, giving a $\epsilon_r = 2.93$. Thus, this was the assumed value of the ϵ_r when designing the SRR.

Feeding the target resonant frequency and ϵ_r into equation 4.1, gives a the wavelength of 0.175 m. since the circumference of the SRR is given as $\lambda/2$, this meant that the design had a circumference of 8.7 cm; which gives the SRR a radius of approximately 1.385 cm.

With the circumference of the ring determined, the next step was to set the parameters that determine the devices characteristic impedance. Again, this value should be as close to the input impedance of 50Ω . As stated previously, the characteristic impedance is governed by four factors, but the most important factor when determining the design requirements of the SRR was the thickness of the dielectric substrate. From the simulations, there was no difference in the plasma behaviour between different substrate thicknesses, but from a mechanical standpoint, a thicker substate would be preferable for structural rigidity. The only issue with this is that a thicker substrate comes with the detriment of additional manufacturing cost. Hence a dielectric substrate thickness of 0.5 mm was selected.

With the substrate thickness and ϵ_r selected, and the thickness of the copper pour being fixed by the manufacture (at $35 \mu\text{m}$), the final step was to tune the width of the ring to give an impedance of 50Ω . By using the equations 4.3-4.6, a trace width of approximately 1.05 mm would produce a characteristic impedance of 50.1Ω .

Finally using equation 4.2, the offset angle of the SRR was calculated. As from the datasheet, the dissipation factor of the RO4350BTM material is 0.0031. The reciprocal of this value was taken to determine the quality factor, which was 323. This would give a gap with an offset angle of 7.99. Again based on the simulations above, the ideal gap width was $180 \mu\text{m}$, however the minimum size drill hole size would be the limiting factor when manufacturing the device, hence the gap width was slightly increased to $250 \mu\text{m}$. Though from the simulations, the gap width of $240 \mu\text{m}$ only increased the breakdown voltage by around 5%.

With these parameters known, the next stage was to create the PCB design. This was done

using the open-sourced PCB design software called *KiCad*¹. One benefit of using KiCad was the output files were natively supported by the PCB manufacturer used, *EuroCircuits*².

An illustration of the final design can be seen in figure 4.7. As seen from the figure, four SRR designs were made. These were done to test various gap designs that could not be replicated using XOOPIIC simulations. These designs could be broken down into two categories: single versus multiple drill hole in the SRR gap; and the presence versus absence of ‘finger-like’ copper pours next to the SRR gap. The permutations of these categories resulted in the four designs, with a close up image of each shown in figure 4.8. All four designs used an SMA connector as the input source.

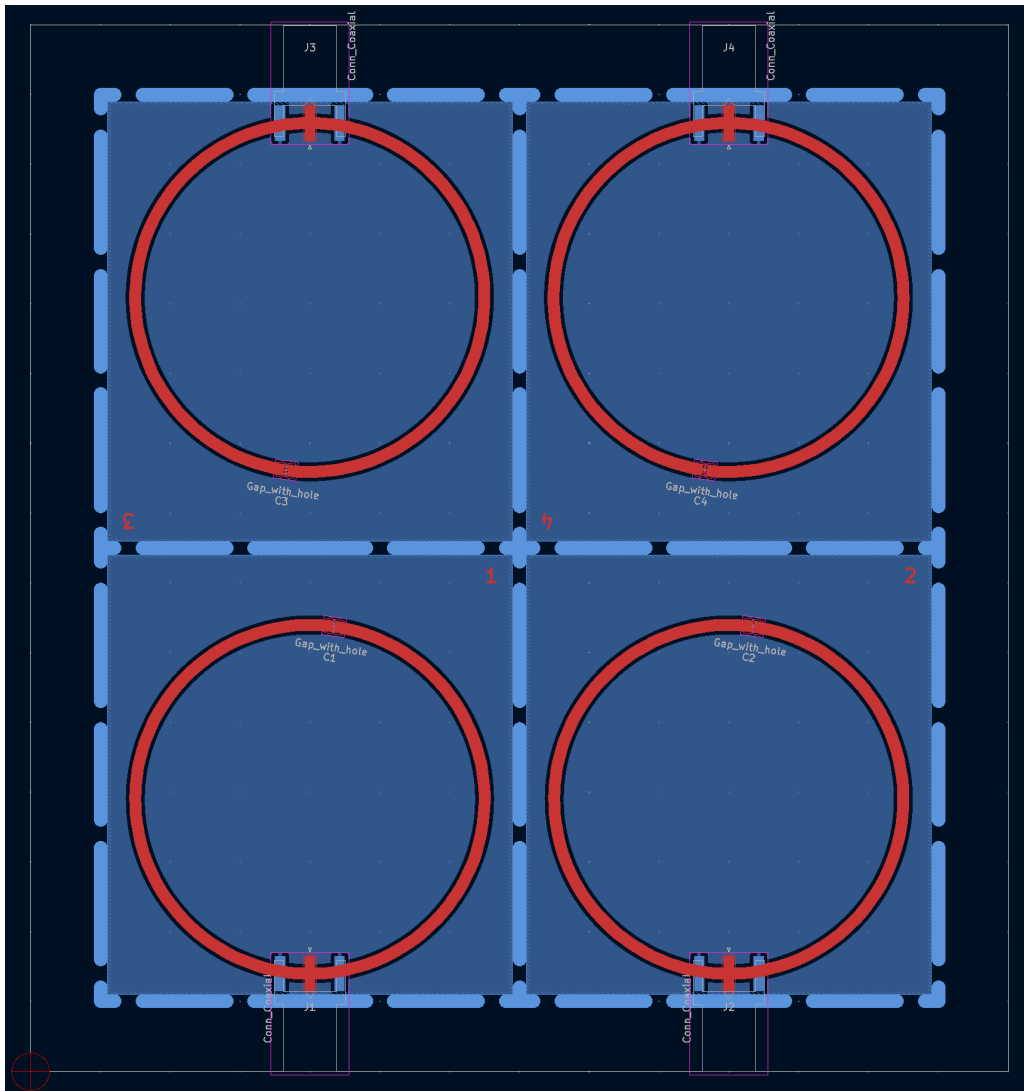


Figure 4.7: PCB schematic of SRR panels in the KiCad software suite.

¹<https://www.kicad.org>

²<https://www.eurocircuits.com>

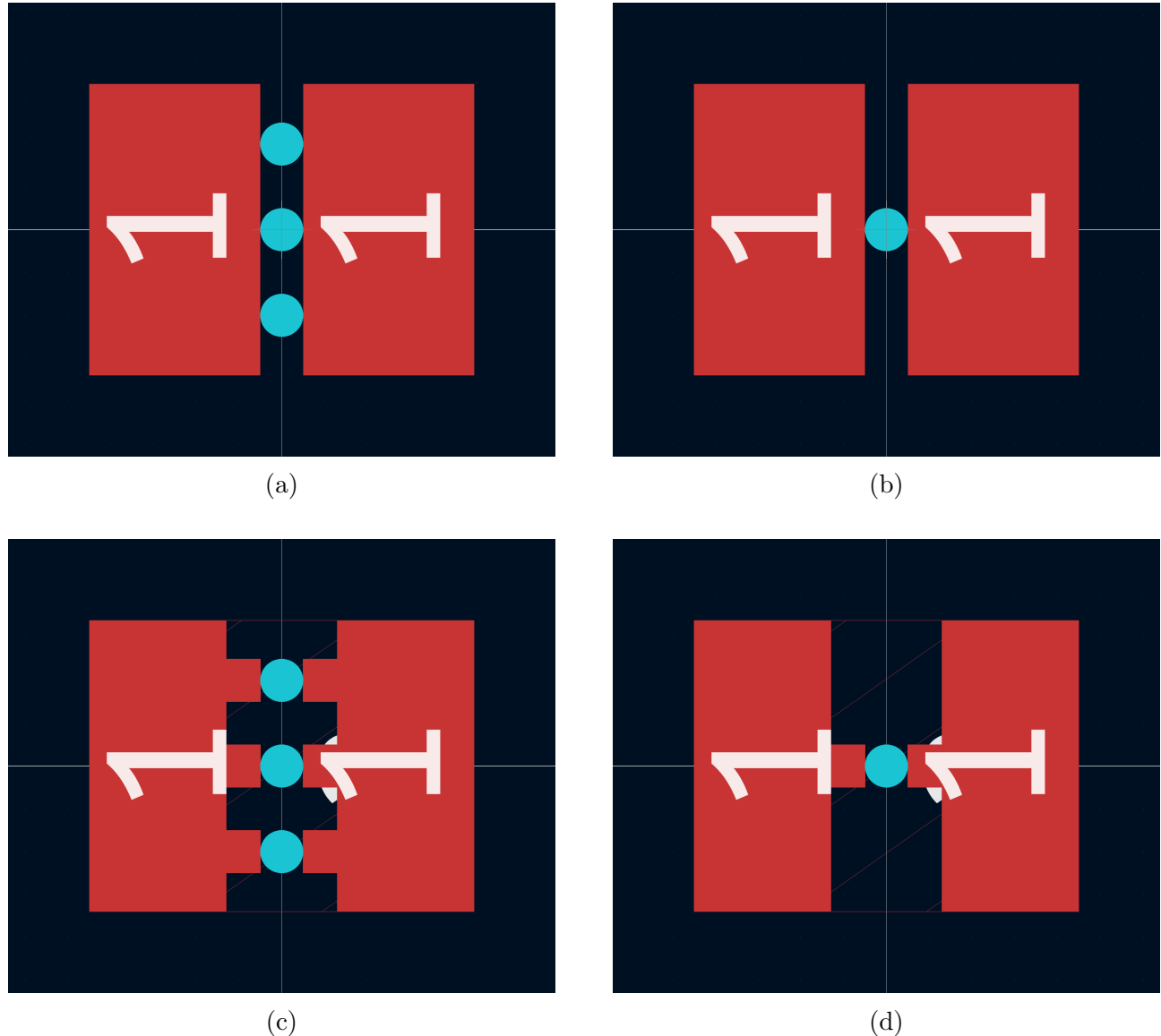


Figure 4.8: SRR gap designs with multiple holes (a, c) versus single holes (b, d). The designs in the lower two subfigures (c, d) have the presence of ‘finger-like’ copper pours next to the holes.

4.3 Testing

4.3.1 Scattering Parameters

The next step was to compare the real-world characteristics of the device to the theoretical calculations. The first of these tests was to evaluate the *scattering parameters* (S-parameters) of the device. The S-parameters are a measurement of the linear characteristics of a device under test (DUT) such as its gain, impedance, and phase delay, as a function of frequency. This test is typically done on high-frequency RF or microwave circuits, ranging with one or more ports; with the results in the form of an $N \times N$ matrix, where N is the number of ports on the DUT. Since the SRR has only a single port, its characteristics are given by a simple 1×1 matrix with the value s_{11} . As such, this s_{11} parameter describes the ratio of the forward power going into the device and the reflected power coming out, and is governed by:

$$s_{11}(dB) = -10\log\left(\frac{P_{forward}}{P_{reflected}}\right) \quad (4.7)$$

The s_{11} characteristics of the SRR were measured using a vector network analyser (VNA), specifically the *PicoVNA*. A sweep between 500 MHz to 1.5 GHz was performed. Since the SRR was designed to resonate at approximately 1 GHz, this should place a single largest peak at roughly the centre of the frequency range, and the broad range would also capture any shifts in the resonant frequency due to manufacturing tolerances.

Figure 4.9 shows the results of the s_{11} parameter tests for a sample of the four designs made, with the y-axis indicating the magnitude of attenuation (in decibels) at a given frequency. From the data, it is immediately obvious that for a given test, there was only one strong attenuation peak. The value of this peak varied from each board tested but they ranged from 1.01 to 1.03 GHz. This equated to an error of roughly 1-3% from the designed resonant frequency, which would be inline with the margin of manufacturing tolerances and design assumptions.

However, the magnitude of attenuation for the devices (i.e. from the depth of the peaks) were much lower than expected. The expected quality factor was in the order of $Q \approx 300$ but the

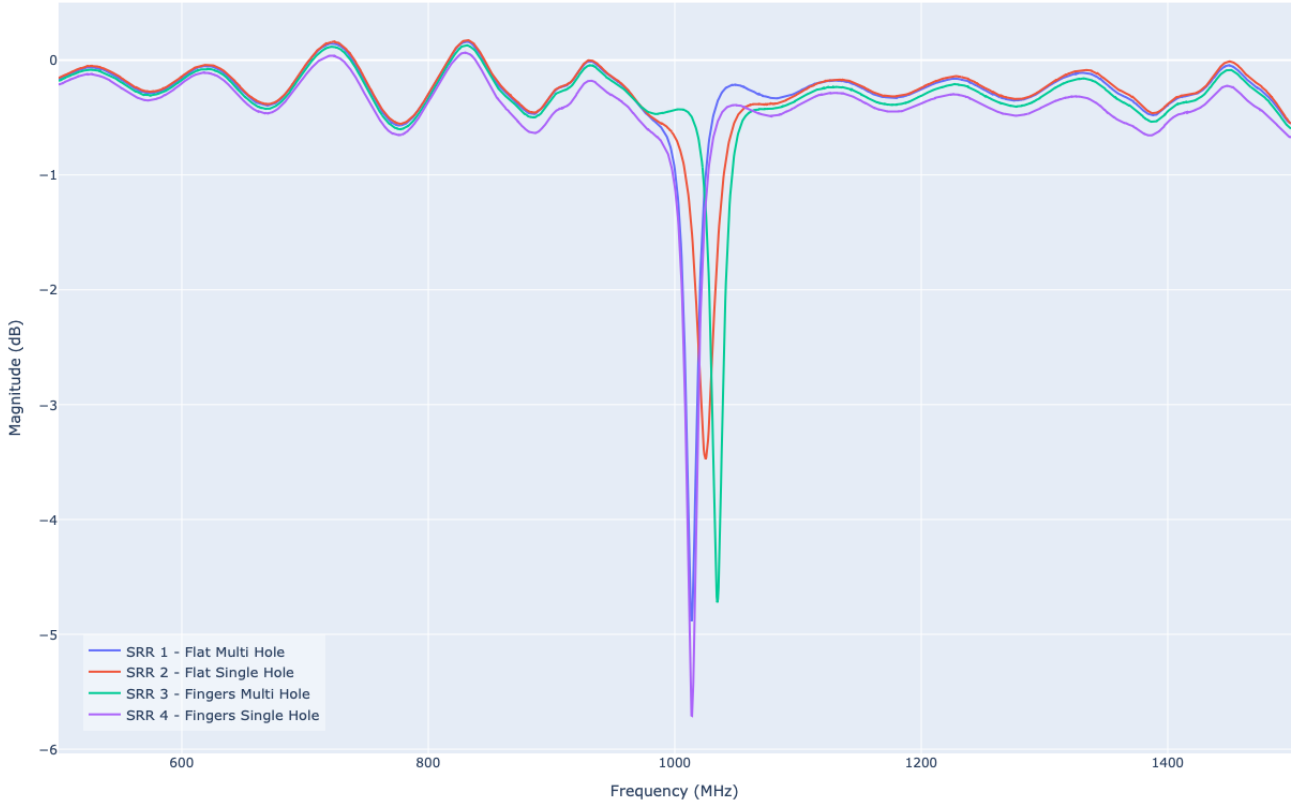


Figure 4.9: Reflection coefficient (S_{11}) of SRR in dB.

quality factor attained was closer to $Q \approx 90$. This implies that the assumption made in the design phase regarding the dielectric constant and dissipation factor were incorrect. While this should not necessarily affect the ability of the device to ignite a plasma and sustain the discharge, it would do so at a higher power thus hurting the power efficiency of the device.

4.3.2 Experimental Setup

Once the true resonant frequency was determined, the next step was to setup the experiment. Note that this is not the final setup to be used for recirculating the gases, instead it was used to reliably ignite a plasma from the SRR in order to characterise it and understand its behaviour. An illustration of the setup is seen in figure 4.10.

In the setup, there are two mass flow controllers by MKS Instruments. For the time being, these are only controlling the flow of helium gas into the setup; the introduction of carbon dioxide gas is discussed in the next chapter. The first one (MFC_1) is positioned on the bottom side of

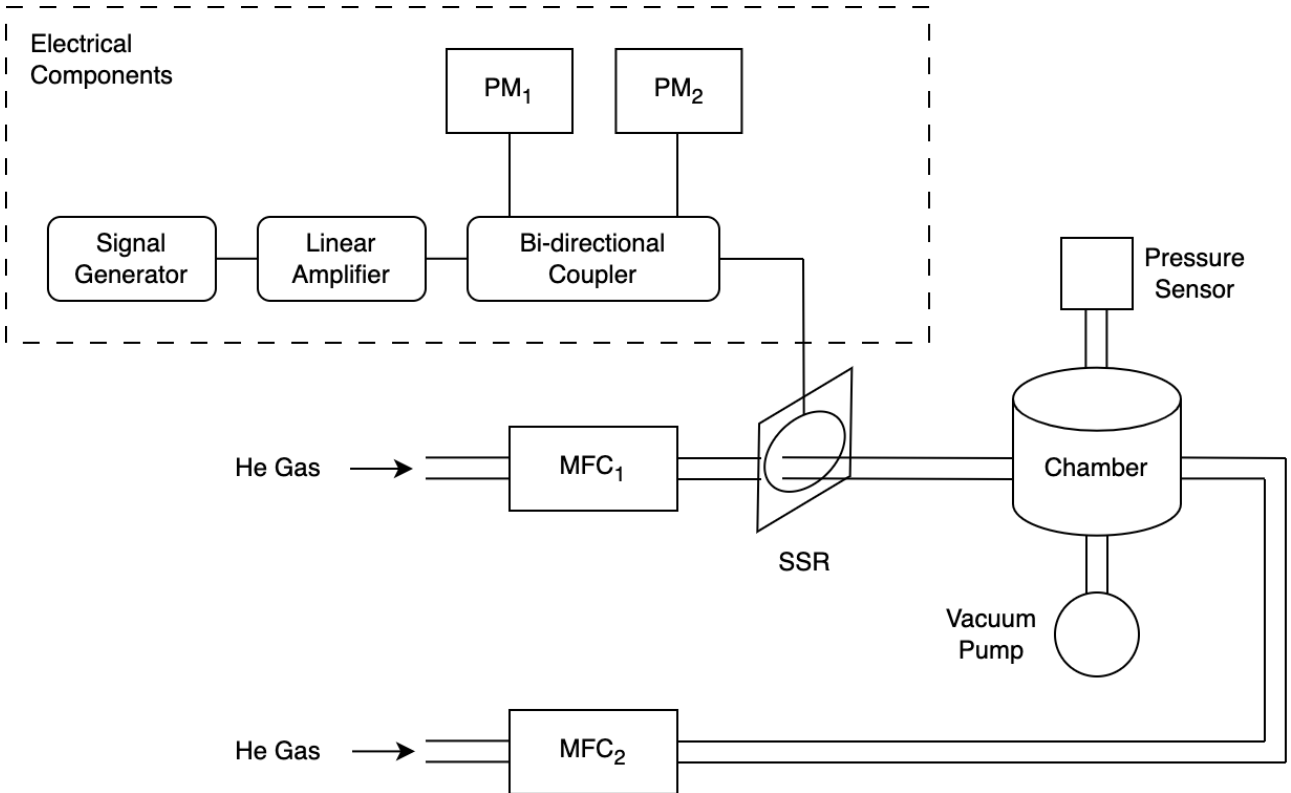


Figure 4.10: Schematic of experimental setup.

the SRR, whilst the second one (MFC₂) controls the flow to the chamber. The reason for two separate mass flow controllers is that the size of the aperture of the SRR is quite small (with a diameter of 0.25 mm), hence only using one controller to pressurise the entire apparatus at 760 Torr (which is one atmosphere) would take a long time. Thus, MFC₂ is used to maintain pressure the pressure of the chamber whilst MFC₁ maintains a flow of Helium through the gap of the SRR.

The SRR device is oriented so that the Helium flows from the bottom (i.e. the ground ring) to top; (i.e. the AC ring). This is because the plasma discharge occurs at the top of the ring, thus when used later in the epoxidation process, this is the side that is going to face the liquid co-reactant. A photographs of the plasma can be seen in figure 4.11.

In terms of the electronics, the the SRR is powered by a signal generator (Aim-TTi TGR2050), capable of generating frequencies up to 2 GHz, and a linear amplifier (Amplifier Research 50W1000A), with a maximum power output of 50 W. This is connected to a bi-directional coupler (Mini-Circuits ZGBCD20-33H-S+) to allow for the accurate measurement of the forward

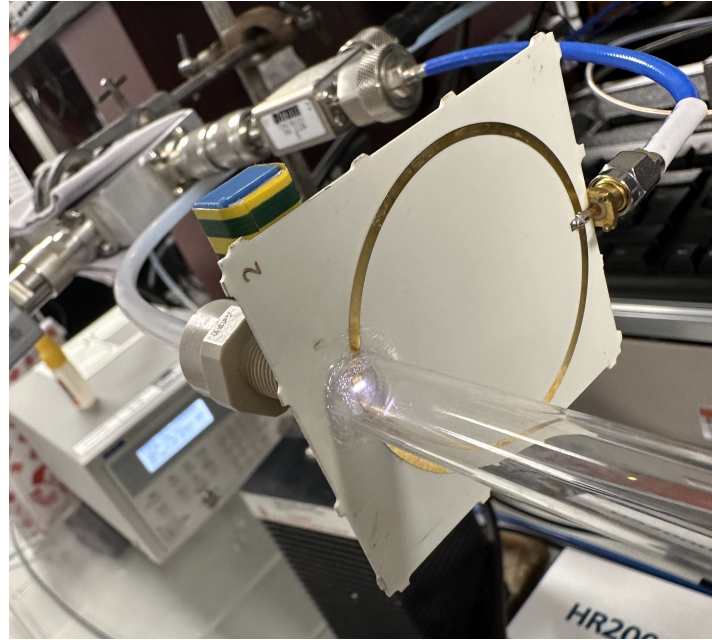


Figure 4.11: Photograph of plasma discharge in the gap of the SRR.

path and the reverse path of the microwave signals from the power supply and SRR respectively. These signals are monitored using a pair of USB power meters (Mini-Circuits PWR-SEN-4GHz, Mini-Circuits PWR-SEN-6LRMS-RC). One note regarding the power meters, the first power meter (PM_1) has a maximum power input of 100 mW, whilst the second one (PM_2) has a maximum reading of 10 mW. This is because, when the SRR is at resonance, only a small amount of signal is reflected back.

4.3.3 Device Performance

Once ignition was achieved, the next steps were to evaluate the performance of the device. This was determined by evaluating was the ignition power of the SRR. This is because, igniting plasma at higher pressures tends to be slightly more inefficient compared to lower pressures. Thus, the ignition power was tested at various pressures to determine the minimum power required to get a plasma to form with the SRR.

To obtain this data, first the pressure of the chamber was fixed. Then input power to the SRR was increased gradually until the self-ignition of the plasma. The power value was noted, and the input power was reduced back to the minimum value and the process was repeated. In

total, there were five power readings taken at each pressure to account for outliers. This data is shown in figure 4.12. Each point in the figure denotes the average ignition power at that pressure, with the error bars denoting the standard deviation in the data collected. Do note that x-axis of this graph was plotted in logarithmic scale.

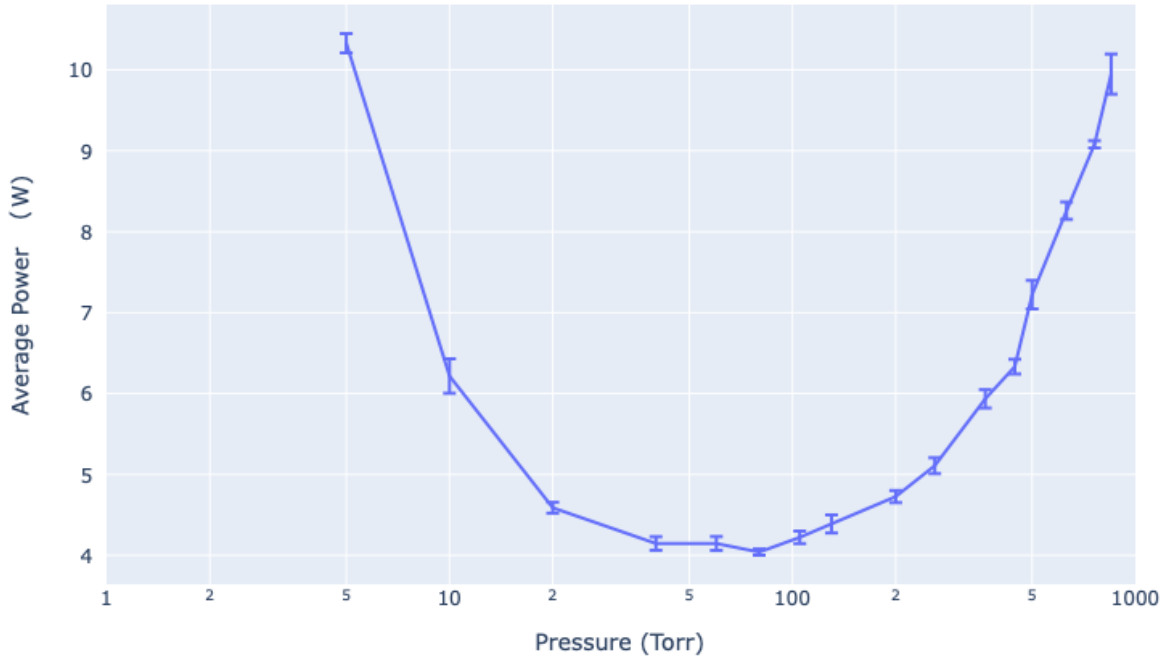


Figure 4.12: Ignition power of SSR, in W, across a pressure range of 5 Torr to 850 Torr.

As seen by the graph, the minimum power required to ignite the plasma was just 4.04 W. While this is fairly small, it could be better as the real world quality factor of the SRR was lower than anticipated. While this minimum ignition power was achieved at 80 Torr, the power remained relatively low across a broad range of pressures, ranging from 40 Torr to 105 Torr, with the ignition power hovering around 4.1-4.2 W. As the pressure decreased below 40 Torr, the ignition power required increased steeply up to a pressure of 5 Torr where the readings maxed out the range of the power meter. It is also important to note that at 5 Torr, while the plasma self-ignited, it did take significantly longer when compared to the ignition at other pressures. As for pressures above 105 Torr, the ignition power also increased, though at a much slower rate. At 760 Torr, the average power required to ignite the plasma was 9.08 W. The testing was carried out past 760 to determine the upper bound pressure that a plasma could

be ignited with the equipment in the setup; this value was at 850 Torr.

From the data in figure 4.12, it can be concluded that the most efficient way to ignite a plasma with this SRR would be to first pressurise the chamber to approximately 100 Torr. Then, once the plasma is ignited, the pressure can be increased back to 760 Torr.

4.3.4 Pressure Drop across Orifice

Another test done was to evaluate the pressure difference between both sides of the SRR. Since the size of the drill hole through the gap of the SRR was quite small, this would restrict the gas flow. This meant that as gas flowed through the orifice, it would accelerate and reach its maximum velocity just after the orifice. This point of maximum velocity is referred to as the *vena contracta*. From Bernoulli's principle, it is known that an increase in a fluid velocity results in a drop in pressure. As the goal of this research to use a co-reactant (trans-Stilbene) at atmospheric pressure in the carbon conversion process, the significance of this pressure drop needed to be known. An illustration of this pressure drop can be seen in figure 4.13. Note that while the pressure drop is at its greatest at the vena contracta, but there is also a net pressure drop well after the orifice.

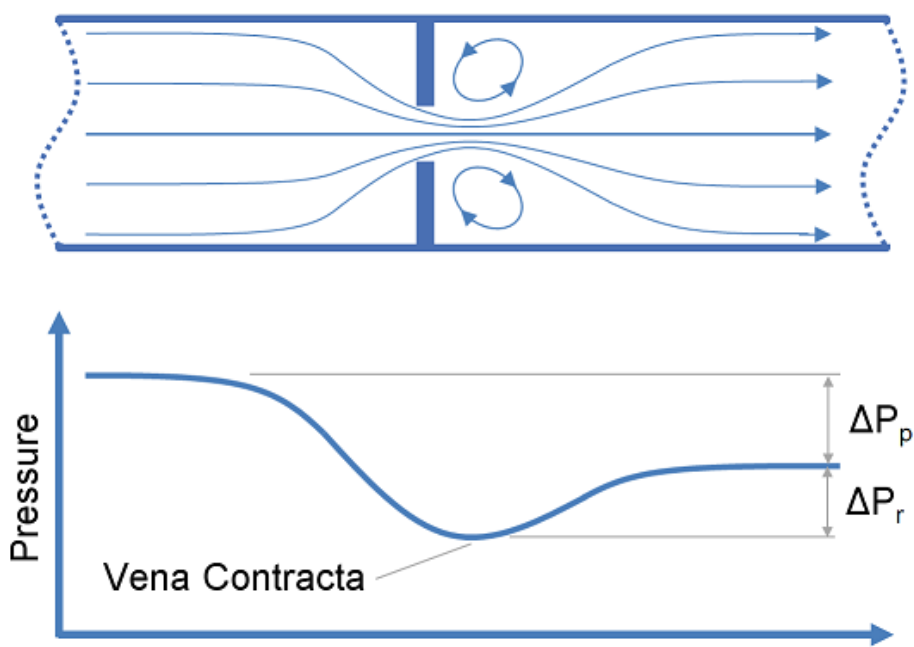


Figure 4.13: Pressure drop across an orifice visualised. [81]

This drop in pressure can be determined analytically by using Bernoulli's equation as shown in equation 4.8. The derivation shown here would be for the case where orifice placed in horizontal pipework, as this is the orientation used in the setup shown in figure 4.10. Though the orientation of the pipework (and thus the orifice) for the final experiment with the co-reactant will be vertical, the impact of this change is minor as shown later in this subsection.

$$P_1 + \frac{1}{2}\rho v_1^2 + \rho gh_1 = P_2 + \frac{1}{2}\rho v_2^2 + \rho gh_2 \quad (4.8)$$

where ρ is the density of the gas, g is the acceleration due to gravity, P is the pressure, v is the gas velocity, and h is the height of the gas. The subscripts denote the positions of the pressure, velocity, and height at different points in the pipework. In this case, point 1 denotes a location just before the orifice and point 2 is just after the orifice of the SRR.

For the case of horizontal flow, it can be assumed that there is a negligible change in elevation. The resulting equation when $h_1 = h_2$ is:

$$P_1 + \frac{1}{2}\rho v_1^2 = P_2 + \frac{1}{2}\rho v_2^2 \quad (4.9)$$

Assuming that the velocity profiles at points 1 and 2 are uniform, the continuity equation can be shown to be:

$$Q = A_1 v_1 = A_2 v_2 \quad (4.10)$$

where Q is the flow rate and A denotes the area of flow at the given points.

Substituting the velocity terms in equation 4.9 with equation 4.10, and rearranging the pressure terms to the same side of the equation results in the expression:

$$\Delta P = P_1 - P_2 = \frac{1}{2}\rho \left(\frac{Q}{A_2}\right)^2 - \frac{1}{2}\rho \left(\frac{Q}{A_1}\right)^2 \quad (4.11)$$

Since the tubing used and the orifice or the SRR are concentric, the areas A_1 and A_2 are simply $\frac{\pi}{4}d_1^2$ and $\frac{\pi}{4}d_2^2$ respectively. Because $d_2 < d_1$, a new parameter can be introduced to describe the relationship between the size of the orifice and the tubing. This parameter, called β , is defined as:

$$\beta = \frac{d_2}{d_1} \quad (4.12)$$

This term can be added to 4.11 as follows:

$$\begin{aligned}
 \Delta P &= \frac{1}{2}\rho \left(\frac{Q}{A_2} \right)^2 - \frac{1}{2}\rho \left(\frac{q}{A_1} \frac{A_2}{A_2} \right)^2 \\
 \Delta P &= \frac{1}{2}\rho \left(\frac{Q}{A_2} \right)^2 \left[1 - \left(\frac{A_2}{A_1} \right)^2 \right] \\
 \Delta P &= \frac{1}{2}\rho \left(\frac{Q}{A_2} \right)^2 \left[1 - \left(\frac{d_2^2}{d_1^2} \right)^2 \right] \\
 \Delta P &= \frac{1}{2}\rho (1 - \beta^4) \left(\frac{Q}{A_2} \right)^2
 \end{aligned} \tag{4.13}$$

The expression above is the *ideal* equation for pressure difference through an orifice in horizontal pipework. However, in practice the flow rate through the orifice will be smaller than the expected flow rate due to the geometry of the hole itself. This can be rectified by adding a discharge coefficient term to the final line of equation 4.13. The discharge coefficient, C_d is the ratio of actual discharge compared to the ideal discharge at the end of the orifice. An intuitive explanation of this is the ratio between the area of flow at the vena contracta compared to the area of the orifice.

Adding this discharge coefficient term results in the final equation:

$$\Delta P = \frac{1}{2}\rho (1 - \beta^4) \left(\frac{Q}{C_d A_2} \right)^2 \tag{4.14}$$

Note that in the equation above, the only independent variable is the flow rate. Thus, it can be said that $\Delta P \propto Q^2$.

To test this relationship, the setup in figure 4.10 was modified by adding a second pressure sensor. An illustration of this setup can be seen in figure 4.14, where PS_1 is the original pressure sensor at the main chamber and PS_2 corresponds to the new pressure sensor. The gas from the mass flow controller is fed through a pressure sensor located before the SRR orifice. The pressure after the orifice was measured from the pressure sensor located in the chamber. These are not the ideal locations to measure the pressure, but should be sufficient to determine the significance of any pressure drop.

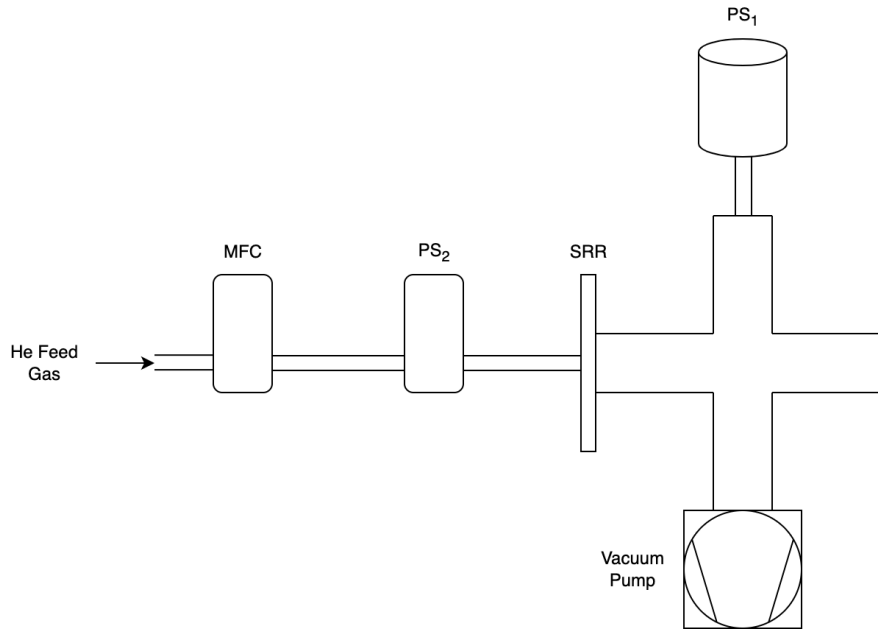


Figure 4.14: Schematic of setup used to determine the pressure drop through orifice.

Both the SRR with a single hole and multiple holes were tested. The mass flow controller used had a range of up to 200 sccm, which determined the maximum flow rate possible. As for the minimum flow rate, values under 20 sccm would cause the valve of the mass flow controller to oscillate open and closed which meant that the flow rate was no longer uniformed. The results of this test can be seen in table 4.2.

Table 4.2: Comparison of pressure drop across single-hole and multi-hole SRR orifices across different flow rates.

Q (sccm)	ΔP - Single hole (Torr)	ΔP - Multi hole (Torr)
30	0.716 ± 0.050	0.348 ± 0.086
50	1.341 ± 0.050	0.504 ± 0.076
70	3.415 ± 0.124	0.601 ± 0.076
100	5.052 ± 0.068	0.928 ± 0.081
120	6.318 ± 0.063	1.210 ± 0.071
150	8.582 ± 0.061	1.615 ± 0.072
180	10.877 ± 0.088	2.000 ± 0.069
200	12.598 ± 0.063	2.275 ± 0.102

Based on equation 4.14, it is possible compare the theoretical results to the ones measured. However, this is only applicable to the SRR with a single hole as the equation is only valid for

simple concentric geometries. The fixed parameters used to model the pressure drop are seen in table 4.3. A discharge coefficient of $C_d = 0.6$ which selected as it was a typical values used to model sharp edged orifices [82, 83].

Table 4.3: Parameters used in equation 4.14.

Parameters	Values	Units
ρ	0.167	g L^{-1}
d_1	4	mm
d_2	0.24	mm
β	0.06	
A_2	0.0452	mm^2
C_d	0.6	

A graph of the the comparison between theoretical and measured pressure drops can be seen in figure 4.15. It can be seen that the measured results are within the same order of magnitude to the theoretical values. However, there are sizeable discrepancies between those numbers.

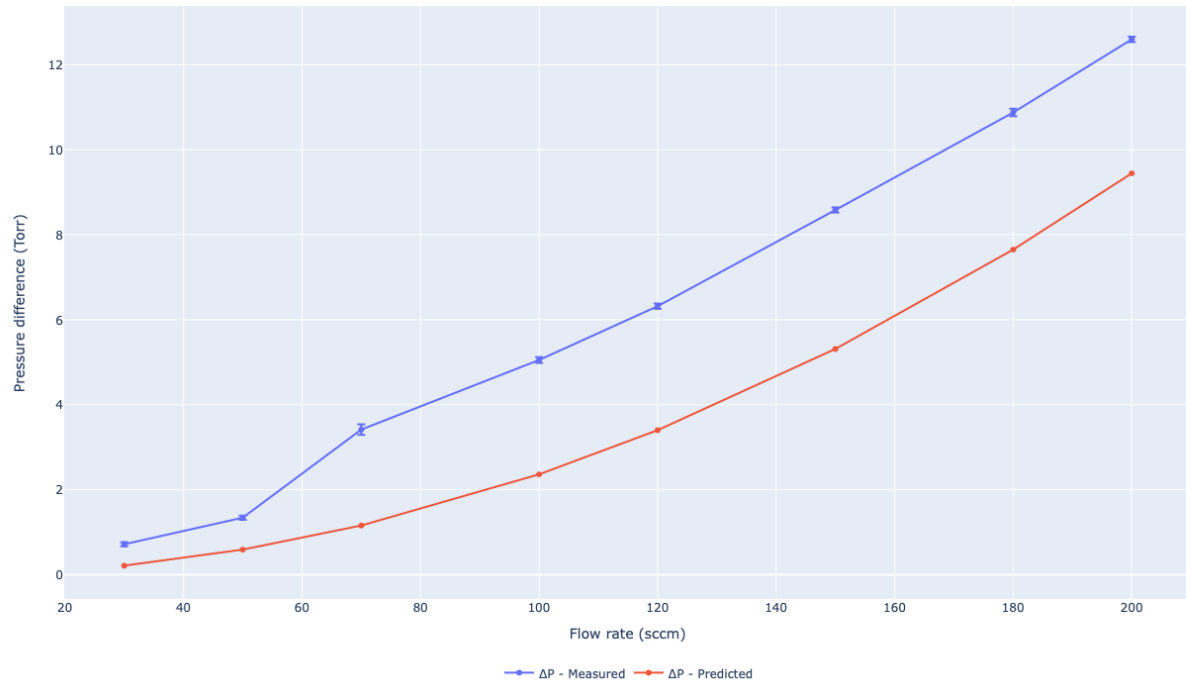


Figure 4.15: Comparison of true and predicted results for pressure drop across SRR with single hole orifice.

The are numerous possible reasons for this, with the largest being that the model in equation 4.14 is incomplete. Adding factors such as the expansion coefficient (to take account the difference between compressible and incompressible flows) and the specific heat ratio (which describes the relationship of the heat capacity of the gas at constant volumes and pressures) could improve model, though the values for these terms need to be determined experimentally. Another possible reason is that the assumed value of C_d is simply incorrect. Finally, as stated previously, the location of the pressure sensors are simply too far from the SRR, thus the readings at the measured locations not correspond to that in equation 4.14. Nonetheless, the model is a sufficient approximation for the purposes of this project.

Another point to note on equation 4.14 was that it was derived for a setup with horizontal pipework. For the case with a vertical gas flow, the change in elevation needs to be taken into account. Modifying the equation to include these terms results in:

$$\Delta P = \frac{1}{2}\rho(1 - \beta^4) \left(\frac{Q}{C_d A_2}\right)^2 - \rho g \Delta h \quad (4.15)$$

where Δh is the height difference between the two points.

However, as the thickness of the SRR is not particularly large and that the device will be located relatively close to the surface of the liquid co-reactant, the impact of the added height term is negligible. To give an example, a 10 mm drop in height would cause the pressure to drop by only 0.0001 Torr. As such, the measured results indicate that the pressure drop across the SRR is not significant, thus should not cause issues when operating with the co-reactant.

4.4 Flow of gases

4.4.1 Helium only

The only variable that could not simulated with XOOPIIC, aside for the geometry of number of orifices on the SRR, was the flow rate through the device. As such, the flow rate through the SRR were tested with the Helium feed gas on both designs.

To evaluate the impact on changing the flow rate, the light intensity of the plasma was used as a proxy for its temperature. The higher the light intensity of the plasma, the more energetic it is, thus the more likely ionising collisions are occurring. The light intensities were determined via optical emission spectroscopy, with the spectrometer located opposite the SRR as shown in figure 4.16.

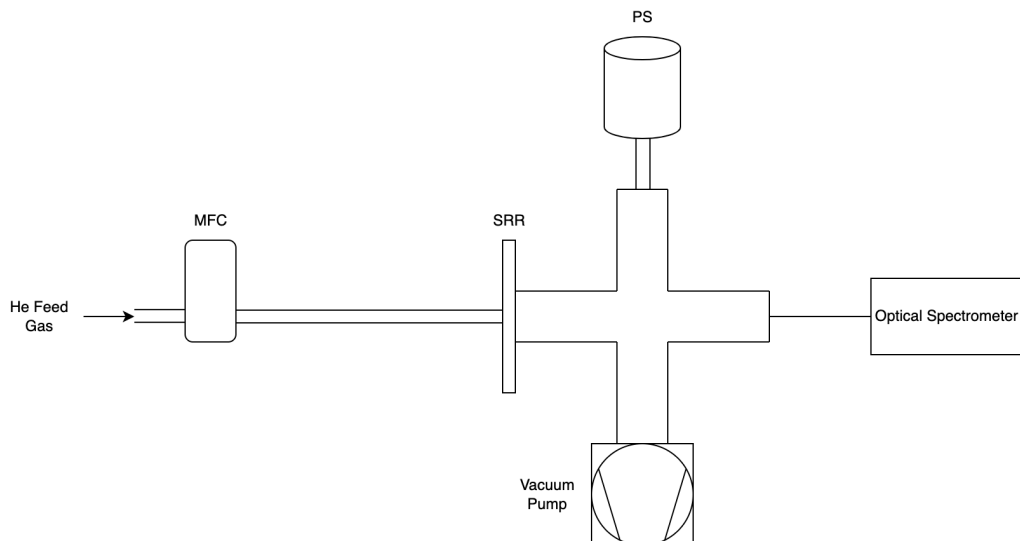


Figure 4.16: Schematic of setup used for He feed gas to ignite SRR.

The spectrometer used was the *Ocean Optics USB2000+ Spectrometer*. These spectrometers work by focusing the light received onto a grating, which spreads the light out into a spectrum. Once spread out, the light is focused onto a detector which is then interpreted by the Ocean Optics software. An illustration of the light path through the spectrometer can be seen in figure 4.17 from the spectrometer datasheet.

The spectrometer used has a range between 200 to 900 nm, with an optical resolution of

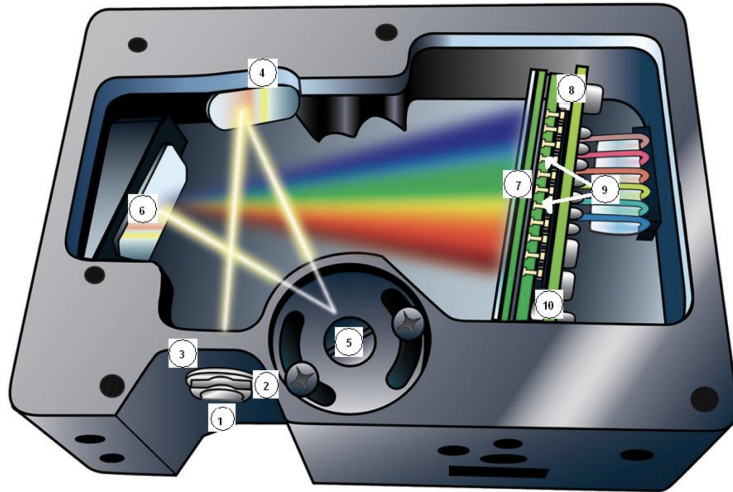


Figure 4.17: Schematic for Ocean Optics spectrometer [84].

roughly 0.5 nm. However, the viewport opposite the SRR used borosilicate glass, which blocks the transmission of light below 300 nm. However, this is not an issue since the wavelengths of light of interest closer to the red part of the spectrum. The emission peaks for Helium are located at 587.5, 667.8, 706.5, and 728.1 nm. The peaks for a control test (where $Q = 50$ sccm and $P = 5$ W) are shown in figure 4.18. The other peaks observed were mainly N₂ impurities in the gas, which are present since they have a much lower ionising potential (approximately 15.6 eV) than that of He (25.6 eV). Additionally, an atomic O peak was present at 777 nm.

To evaluate the impact of flow rate on the light intensity of the plasma, the strong He peak (which was at 587 nm) was taken. Its intensity was measured at flow rates between 20-50 sccm, across both orifice designs. These results are shown in table 4.4.

Table 4.4: The effect of flow rate on the light intensity of the He plasma.

Q (sccm)	Intensity (a.u) - Single hole	Intensity (a.u) - Multi hole
20	3724	4884
30	4222	4810
40	4498	4789
50	4427	4798

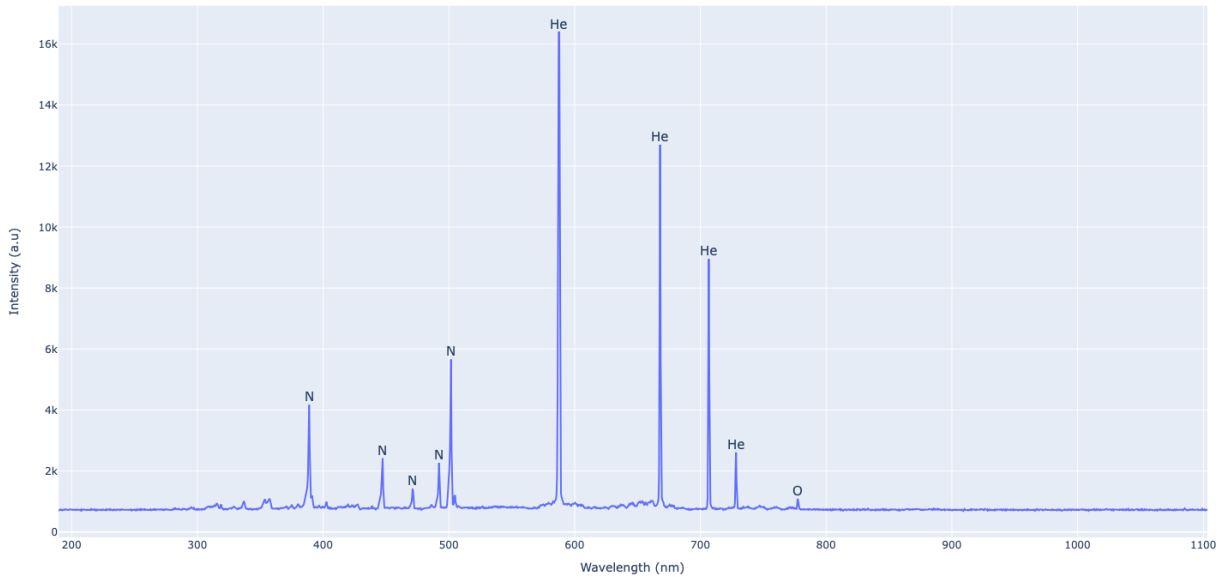


Figure 4.18: Optical emission spectra of He plasma with SRR.

4.4.2 Helium with Carbon Dioxide

As seen in figure 4.19, CO_2 gas was introduced into the system with a second mass flow controller. Since both mass flow controllers were calibrated for their respective gases, this meant that the CO_2 concentration of the gas mixture through the SRR is governed as the ratio of the CO_2 flow rate to the total flow rate.

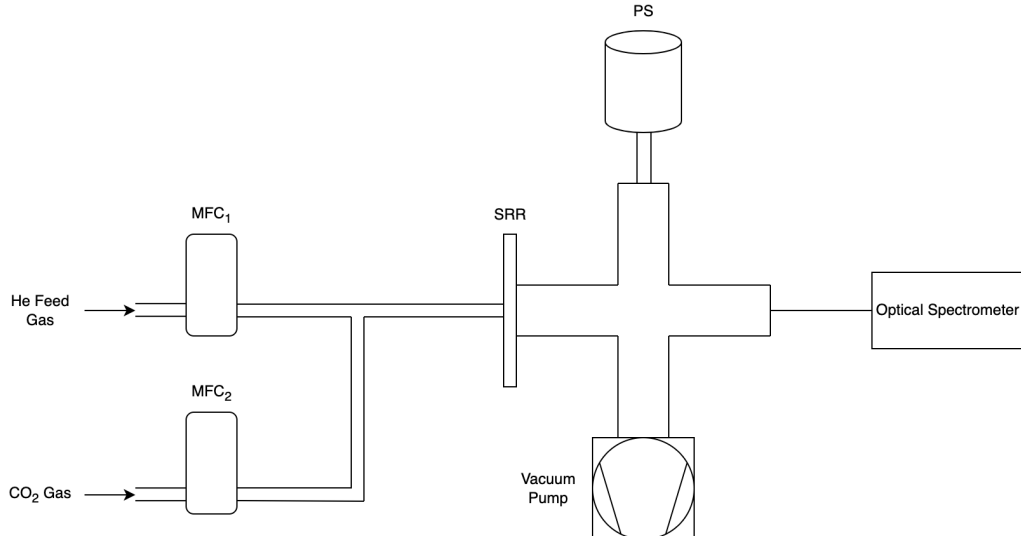


Figure 4.19: Schematic of setup used for He- CO_2 gas mixture to ignite SRR.

To visualise the impact of CO_2 concentration on the plasma, optical spectroscopy was used

again. Keeping the total flow rate through the SRR constant at 50 sccm, the CO₂ concentration was increased from a 0% to a 2.5% gas mixture. These results can be seen in table ??.

It can be seen that as the concentration of CO₂ in the gas mixture increases, the intensity of the plasma drops. At a 2.5% CO₂ concentration, the light intensity of the Helium peaks drop to zero as the plasma is extinguished. One thing to note that was not visible in the figure was that the plasma at 2% CO₂ was quite unstable, in the sense that in some the tests the plasma would extinguish but not in others. As such when determining the ideal concentration of CO₂ to be used, a tradeoff between the amount of CO₂ available to react versus the plasma performance was required. In the end a 1% CO₂ gas mixture was selected.

With the optical spectroscopy, the intention was also to detect the excitation peaks from the CO₂. This could be used later for the control system for regulating the concentration of CO₂ when recirculating the gases (seen in the next chapter). However, the CO₂ molecule itself does not have any excitation peaks in the optical spectrum. Instead, one has to rely on peaks from CO₂⁺ and CO. For the former, these peaks are typically found at 337.0, 354.6, 362.1, and 396.1 nm [85]. However, the issue is that these peaks typically also very similar to nitrogen peaks. As for the CO peaks, these are typically referred to as the Ångström system and can be found at 451.1, 483.5, 519.8, 561.0, and 608.0 nm [85]. The full optical spectra for a 0% and 1% CO₂ concentration can be seen in figure 4.20. In the figure, the intensity of the light (seen on the y-axis) has been normalised to the peaks of Helium. This was done to show the relative changes of the peaks as the flow rate of Helium is effectively constant.

As seen from the figure, there are unfortunately no CO peaks. This could mean one of two possibilities. The first is that there is no CO₂ dissociations occurring in the plasma. However, due to the carbon deposits on the surface of SRR visible in figure 4.21, this is very unlikely. The more likely reason is that there is not sufficient energy to excite the CO molecules in the optical spectra. This is further evident as it can be seen that there is an increase in atomic oxygen, which could only come from the dissociation of the CO₂ molecule.

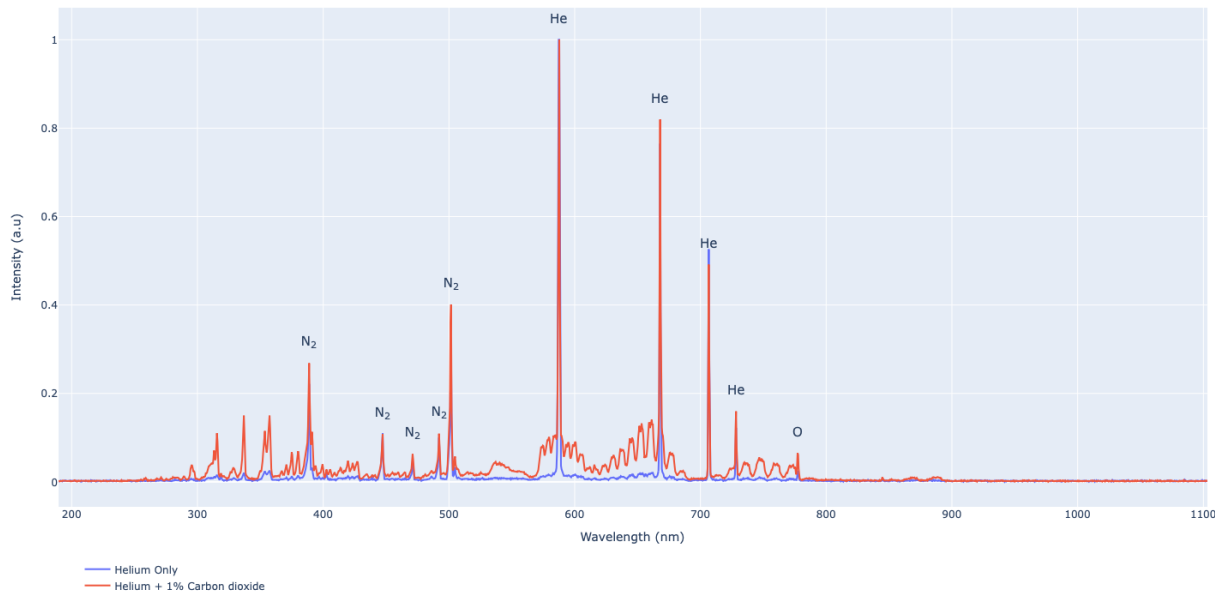


Figure 4.20: Comparison of optical emission spectra of He only plasma and (1%) CO_2 -Helium plasma.

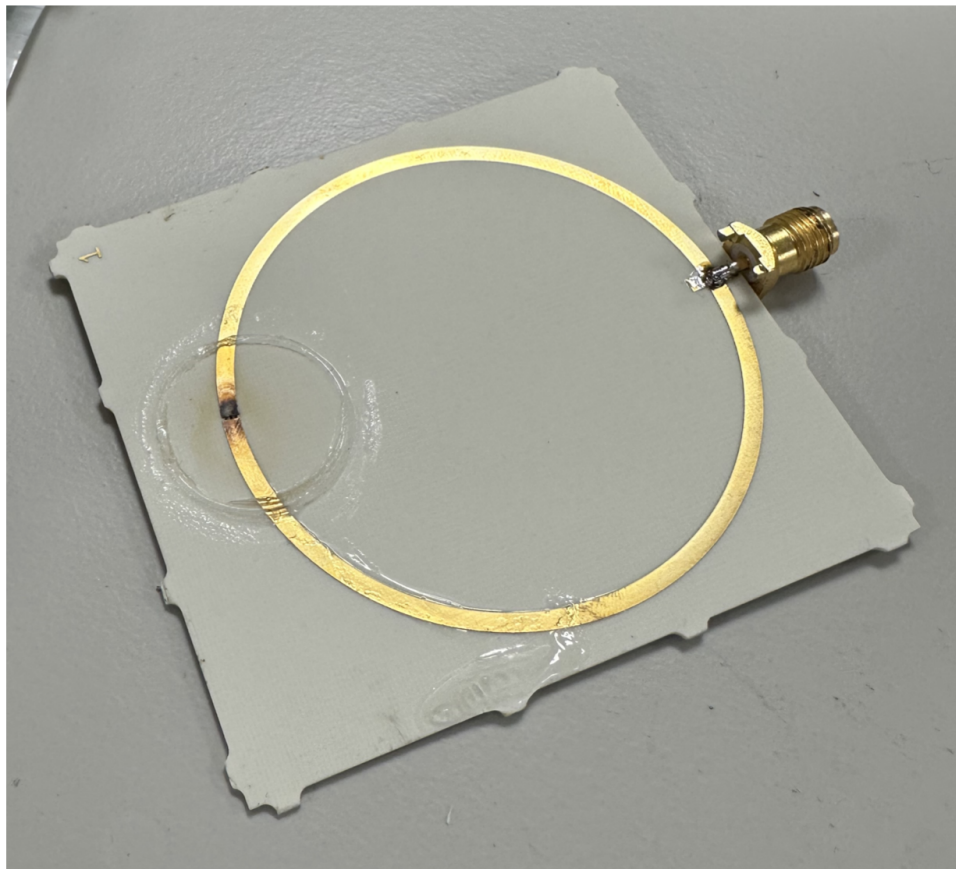


Figure 4.21: Photograph of carbon deposits on SRR.

FTIR Analysis

Because of this, an alternative test was required to ascertain the approximate CO₂ concentration in the system. This was achieved using Fourier-transform infrared spectroscopy (FTIR). The notable difference between the optical spectroscopy used above which measured the emission spectra of molecules and atoms, the FTIR detects the absorption spectra; which as the name suggests is the amount of light at a given frequency that is absorbed by the sample.

An illustration of how the FTIR works can be seen in figure 4.22. In essence, it can be explained as follows. A beam of light that contain many frequencies of light is sent through the sample, and the detector measures the amount of light absorbed. Then the beam is changed to contain a different set of frequencies, and this process is repeated several times over a short period of time. These beams of light are referred to as interferograms. These interferograms are then decoded an algorithm called a Fourier transform. To generate the beam of light going into the sample, a broadband light source is pointed to a beam splitter, which in turn is transmitted to a set of mirrors. By varying the distance of the moving mirror, constructive and destructive interference is observed in the recombined beam which results in the many frequencies.

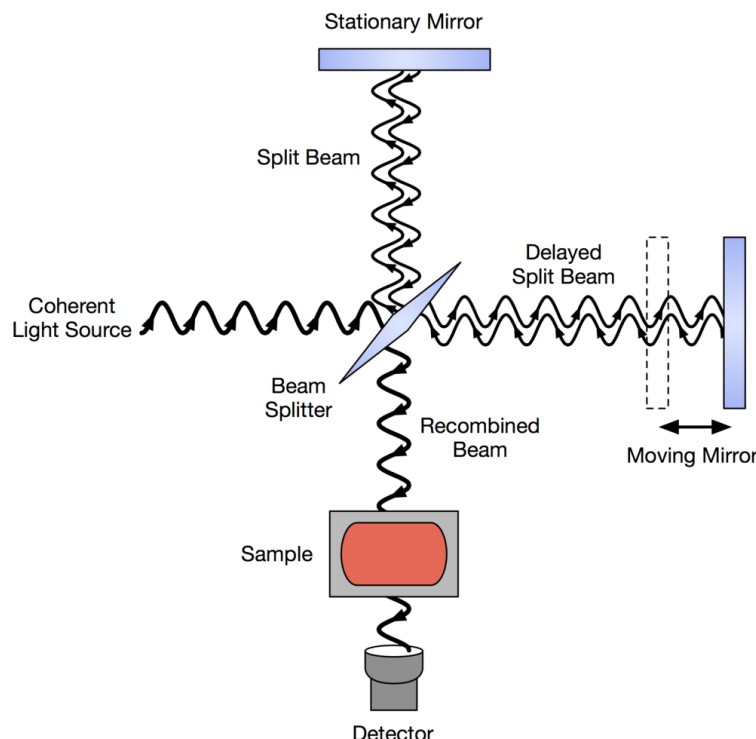


Figure 4.22: Schematic of Fourier-transform infrared spectroscopy (FTIR) interferometer.

To test the gas mixture, a *Jasco FT/IR-4700* was used. The device was set up in-between the primary chamber of the SRR and the pump. In the infrared spectrum, CO₂ has a pair of strong absorption peaks at approximately 4255 nm. Typically when using IR spectroscopy, the measurement of wavenumber is used rather than the wavelength. The wavenumber is usually denoted in the units cm^{-1} , and is simply governed by:

$$\tilde{\nu} = \frac{1}{\lambda} \quad (4.16)$$

Thus, the CO₂ peaks would have a wavenumber at approximately 2350 cm^{-1} . As such the FTIR was set to have a range of 500 to 5000 cm^{-1} to keep the CO₂ peaks roughly in the centre of the test range. This range would also be useful at potentially identifying CO peaks later on, which have absorption peaks at roughly 2100 cm^{-1} . The resolution of this sweep was set at 0.5 cm^{-1} , though the device used could go finer.

In order to measure the components of the gas mixture, a measurement chamber needed to be designed since traditional materials such as glass, plastic, or acrylic tend to block IR light. For this, Potassium Bromide (KBr) is typically used with FTIRs, as they transmit up to 90% of the light through. However these are typically only available as windows to look into the sample. The housing of the viewing chamber, was machined out of a block aluminium. The details of this are not shown here, but a 3D model of the chamber can be seen in figure 4.23

The dimensions of the viewing chamber will govern the fraction of transmitted light detected by the FTIR. This is due to the optical path length (l) of the incident through the sample gas. This relationship is governed by the Beer–Lambert law, seen below:

$$T = \frac{I}{I_0} = \exp(-\mu l) \quad (4.17)$$

where T is the transmittance, I is the intensity of light measured, I_0 is the light intensity of the incidence light, and μ is the attenuation coefficient of the sample. The attenuation coefficient for a given volume is simply the sum of the absorption coefficient (μ_a) and scattering

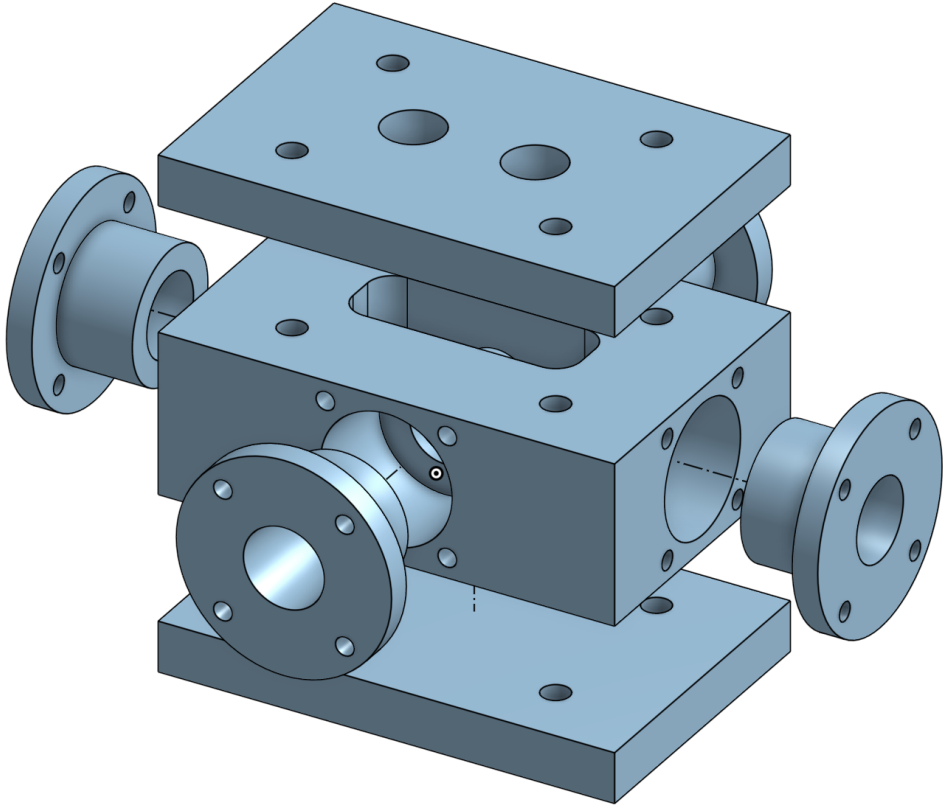


Figure 4.23: 3D CAD model of gas viewing chamber for FTIR.

coefficients(μ_s). However, since the FTIR is only measuring the amount of light absorbed by the sample, the scattering coefficient can be ignored. The absorption coefficient can also be expressed in terms of the absorption cross section, shown in equation 4.18.

$$\mu = \sigma n \quad (4.18)$$

where n is the number density of the sample, i.e. the number of constituent particles per unit volume. The absorption cross section(σ) is best described as the probability that particles within the sample will absorb the light.

Therefore, equation 4.17 can be updated as follows:

$$T = \frac{I}{I_0} = \exp(-\sigma nl) \quad (4.19)$$

The viewing chamber was designed to have two optical path lengths. One along the length with $l = 5 \text{ cm}$, and another along the width where $l = 2 \text{ cm}$. These path lengths were designed to be small to allow greater sensitivity when measuring drop in light intensity.

Typically when using an FTIR, one would first calibrate the device by measuring the background signal. After that, a measurement of the sample can be taken. The FTIR software would then remove the effects of the background signal and return the change in light intensity with sample, called the transmittance (T). The goal would be to continuously take these measurements to detect the change of CO_2 concentration in the sample gas. Luckily, the Jasco software has the ability to take continuous measurements over a set interval.

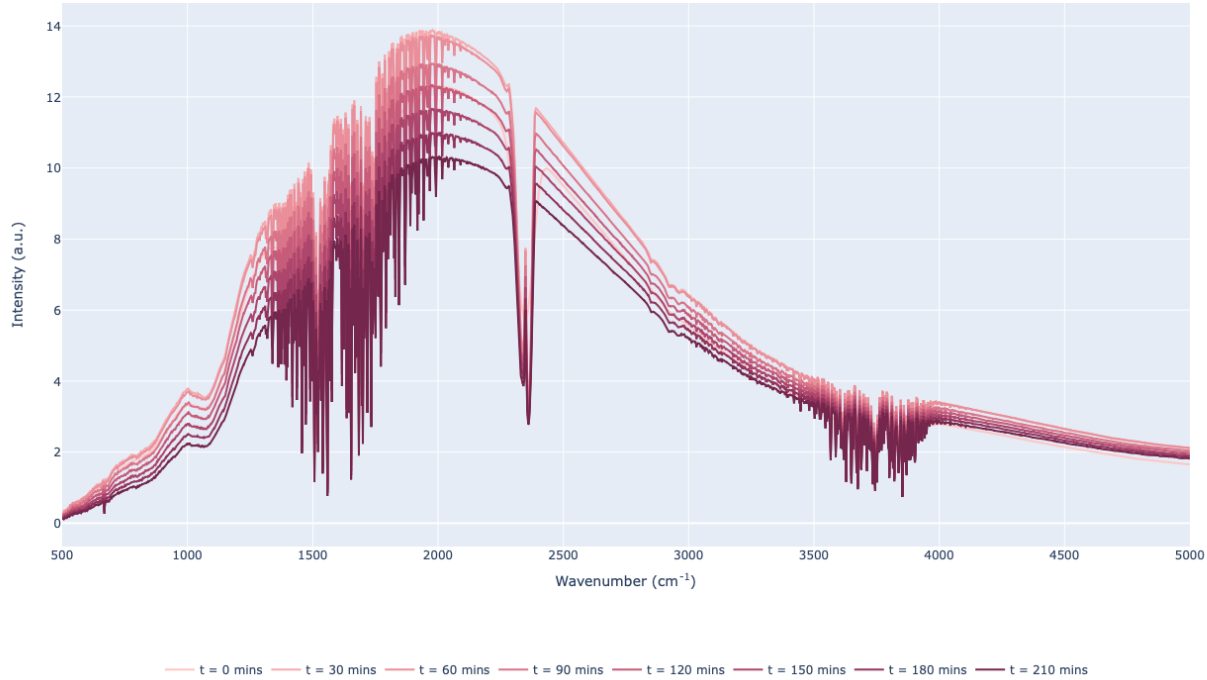


Figure 4.24: Snapshots of raw light data from FTIR across the span of 3.5 hours.

However when the FTIR is set in this mode, it cannot take another background signal. This is an issue because the concentration of background gas changes over time, which would impact the sample measurement. Another issue present with the device being used is that the characteristics of the incident light intensity changes with time. An illustration of this can be seen in figure 4.24, showing snapshots of the raw light data from the FTIR after running continuously for 3.5 hours. Another visualisation of this change can be seen in figure 4.25, high-

lighting the shift of the second moment of area (which can be thought as the centre of mass) of each snapshot over time. Since a 3D plot would be difficult to show in a report form, the change of wavenumber and intensity are shown in separate axis. The cause of this is uncertain, but it most likely stems from the fact that the optics were not designed to operate in such a continuous fashion.

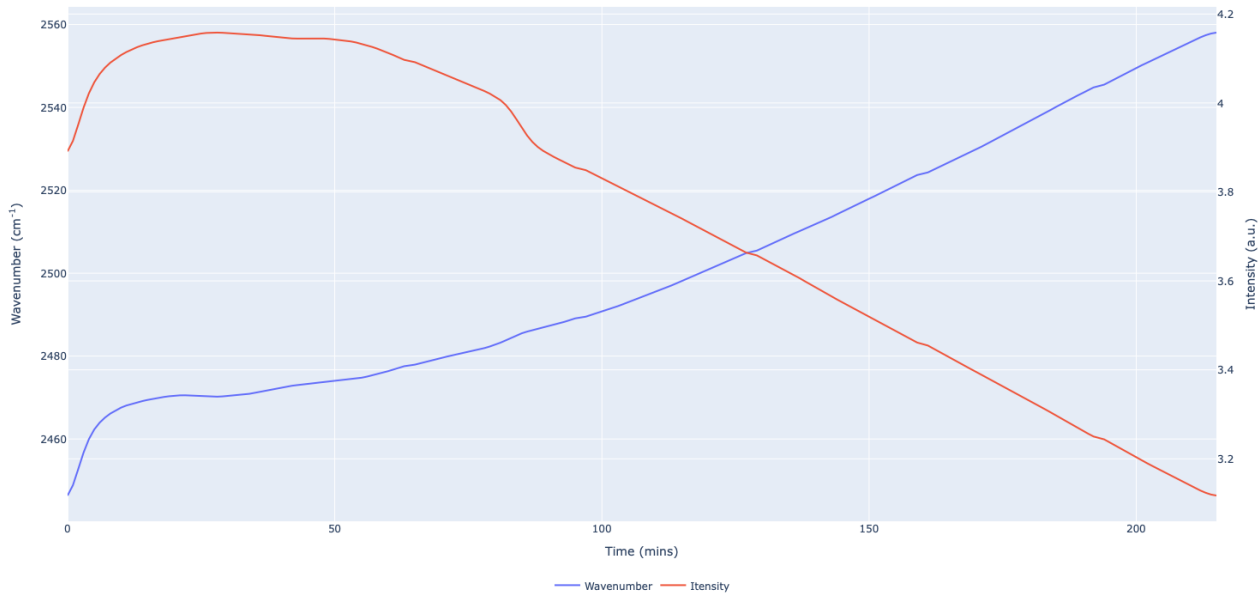


Figure 4.25: The change of the second moment of area over the span of 3.5 hours.

In order to combat both these issues, the computations that would typically be handled by the FTIR software had to be done manually. The first step would be to preprocess the raw light data from the FTIR, shown in figure 4.24. The data, which can be called $f(\tilde{\nu})$, corresponds to an average signal detected by the FTIR detector for a “single beam” of light. The jagged peaks located between $1300\text{-}2000\text{ cm}^{-1}$ and $3000\text{-}4000\text{ cm}^{-1}$ correspond to absorption due to water vapour in the atmosphere, whilst as previously mentioned CO_2 absorption can be seen between $2300\text{-}2400\text{ cm}^{-1}$. The general structure of these peaks can be captured by filtering the signal. After testing a few different filtering functions, it was found that the Gaussian filter produced the cleanest results. The Gaussian function is expressed as follows:

$$g(\tilde{\nu}) = \frac{1}{\omega\sqrt{2\pi}} \exp\left(-\frac{\tilde{\nu}}{2\omega^2}\right) \quad (4.20)$$

where ω is a specified term that determines the width (or mathematically speaking, the standard deviation) of the impulse. Typically this term is denoted with the symbol σ , however this has been replaced to avoid any confusion with the absorption cross section seen in equation 4.18.

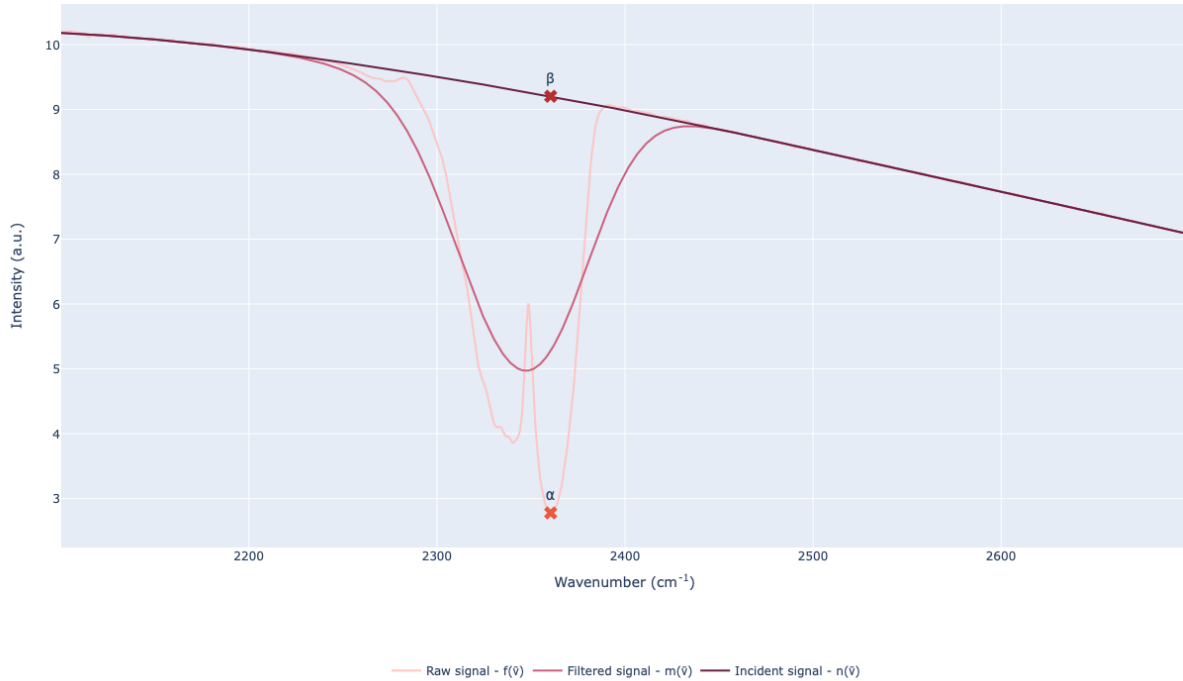


Figure 4.26: Output signals from FTIR preprocessing steps.

Taking the convolution of the raw signal with the filter, $f(\tilde{\nu}) * g(\tilde{\nu})$, produces a cleaned signal that denotes the general characteristics of the absorption spectra. With this cleaned signal, called $m(\tilde{\nu})$, the focus can be placed to the region that corresponds to the of CO₂ absorption. For this, $m(\tilde{\nu})$ can be truncated between 2100-2600 cm⁻¹. A comparison between $f(\tilde{\nu})$ and $m(\tilde{\nu})$ in this truncated region can be seen in figure 4.26. The final step in the preprocessing was to remove the effects of the CO₂ absorption to determine the estimated true incident light signal. This was achieved by first removing the peak from $m(\tilde{\nu})$, then performing a quadratic interpolation of the remaining data points. The interpolation technique used is called spline interpolation and is beyond the scope of this report, however the documentation of the function used can be found in [86, 87]. The estimated incident signal can be referred to as $n(\tilde{\nu})$.

With this preprocessing complete, the transmittance of the light from the FTIR can be determined. First, the intensity at the CO₂ absorption peak needs to taken from $f(\tilde{\nu})$. For

the purposes of this report, the peak of CO₂ absorption is said to be at 2360 cm⁻¹, and is represented as I_m . Next, the incident light intensity is taken from $n(\tilde{\nu})$; also at 2360 cm⁻¹. These are denoted in figure 4.26 as the points α and β respectively. With that, the measured transmittance can be determined using:

$$T_m = \frac{I_m}{I_0} = \frac{\alpha}{\beta} \quad (4.21)$$

Nevertheless, this only solves one part of the problem. The issue of subtracting out the effects of the background CO₂ remains. To solve this, several steps were undertaken during the data gathering stage. First, the region of the FTIR containing the sample and detectors were continuously filled with nitrogen (N₂) gas. This would keep the FTIR in positive pressure, minimising the mixing of gas from the atmosphere. However, it would not eliminate the presence of background CO₂ present. Then, when gathering the data on different concentration of CO₂ in the gas sample, the chamber would be flushed with Helium before the next concentration of CO₂ being tested.

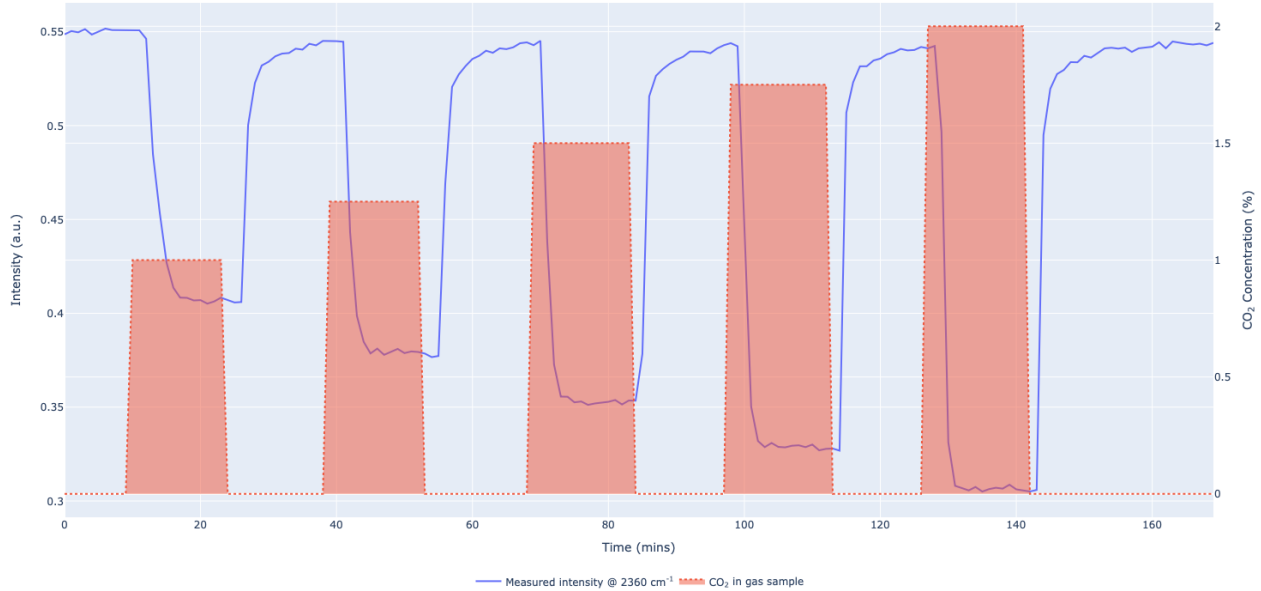


Figure 4.27: Test measured transmittance at 2360 cm⁻¹ across CO₂ concentrations between 1-2%.

A visualisation of this testing process can be seen in figure 4.27. It figures shows the trans-

mittance at 2360 cm^{-1} when evaluating CO_2 concentrations between 1-2%, with increments of 0.25%. Readings from the FTIR were taken approximately every minute, with each test of different CO_2 concentrations in the sample lasting 20 mins. This was down to allow sufficient time for the readings to stabilise. While the transient from background took 5-6 minutes in all tests performed, the settling time depends on the flow rate of the mass flow controllers and the volume of the overall experimental setup.

The reason for flushing the gas in the chamber after every test was to obtain multiple samples of the background transmittance, which can be averaged to determine the reading of the background CO_2 . The measured transmittance is actually a combination of the CO_2 in the gas chamber and the background, which can be expressed as:

$$T_m = T_b \times T_c = \exp(-\sigma n_b l_b) \times \exp(-\sigma n_c l_c) \quad (4.22)$$

where the terms with the subscript b correspond to the signal of the background, while terms with the subscript c corresponds to the signal from the CO_2 gas sample. T_m is expressed in equation 4.21.

By flushing the chamber with Helium, the n_c term goes to zero resulting in the expression for the background transmittance of:

$$T_b = \frac{I_b}{I_0} = \exp(-\sigma n_b l_b) \quad (4.23)$$

This can be substituted into the equation 4.22 giving the an expression for the transmittance due to the sample:

$$T_c = \frac{I_c}{I_b} = \exp(-\sigma n_c l_c) \quad (4.24)$$

The test procedure shown in figure 4.27 was repeated across many different CO_2 concentrations between a 0.25 to 5% CO_2 -Helium mixture, with a greater test frequency placed on values

between 0.25 to 2% since this is the region of operation for the SRR. The results of these test are shown in figure 4.28, which shows the relationship between the CO₂ concentration and the absorbance. The absorbance is a simplification of the terms within the exponential, $A = -\sigma nl$; and can also be defined as $\ln(T_c)$. The absorbance is also directly proportional to the CO₂ concentration, as changing the flow rate of gas changes the number density of CO₂ molecules in the gas sample. This relationship is also shown in figure 4.28, where a line of best fit was plotted using the least-square solution. The rational for using this instead of a traditional regression fit was to force the solution through the origin.

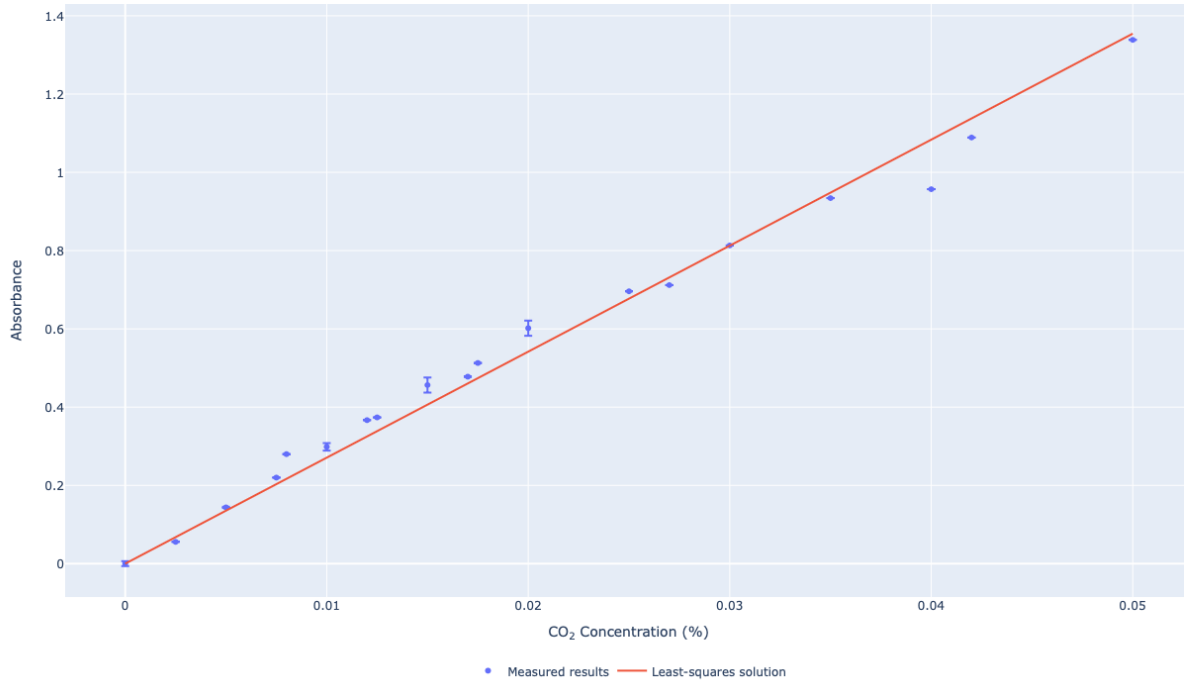


Figure 4.28: Absorbance across CO₂ concentrations between 0-5%.

Chapter 5

Gas recirculation

The primary goals for this project is to recirculate the helium feed gas, instead of exhausting it into the environment as with many other laboratory scaled plasma experiments. For the intended process of carbon conversion, the recirculation process can be divided into two stages. The first was to simply design a control system to recirculate the feed gas whilst maintaining the plasma. Then once that was achieved, a second control system for regulating the concentration of CO₂ was designed. Having these two stages controlled separately was the simplest and most robust way to develop the controller. It also allowed for ease in testing, as each control system is only responsible for one aspect of the system.

5.1 Control System with Helium only

The design for this control problem requires several key components. Firstly, there needs to be an inlet mass flow controller to regulate the inflow of the feed gas which will have two roles: initially pressuring the system to the desired target pressure, and to subsequently top up the system as it begins to lose pressure due to leaks. Next there needs to be a pump to recirculate the gas to ensure a steady gas flow through the SRR. Since most pumps require a large pressure differential between the inlet and outlet to function optimally, it is necessary to install a second mass flow controller between the SRR and the pump to restrict the gas flow into the pump.

Additionally, there needs to be a third mass flow controller to regulate the gas flow to the SRR when the system is in a steady state (i.e when the inflow of the helium gas is stopped). Lastly, a vacuum pump was included to allow the system to be completely depressurised, to ensure the only gas in the system was helium. While strictly not necessary, this allowed time to be saved as the alternative would involve allowing the system to run in open loop for a period of time to allow any residual gas to flush out. An illustration of this setup can be seen in figure 5.1.

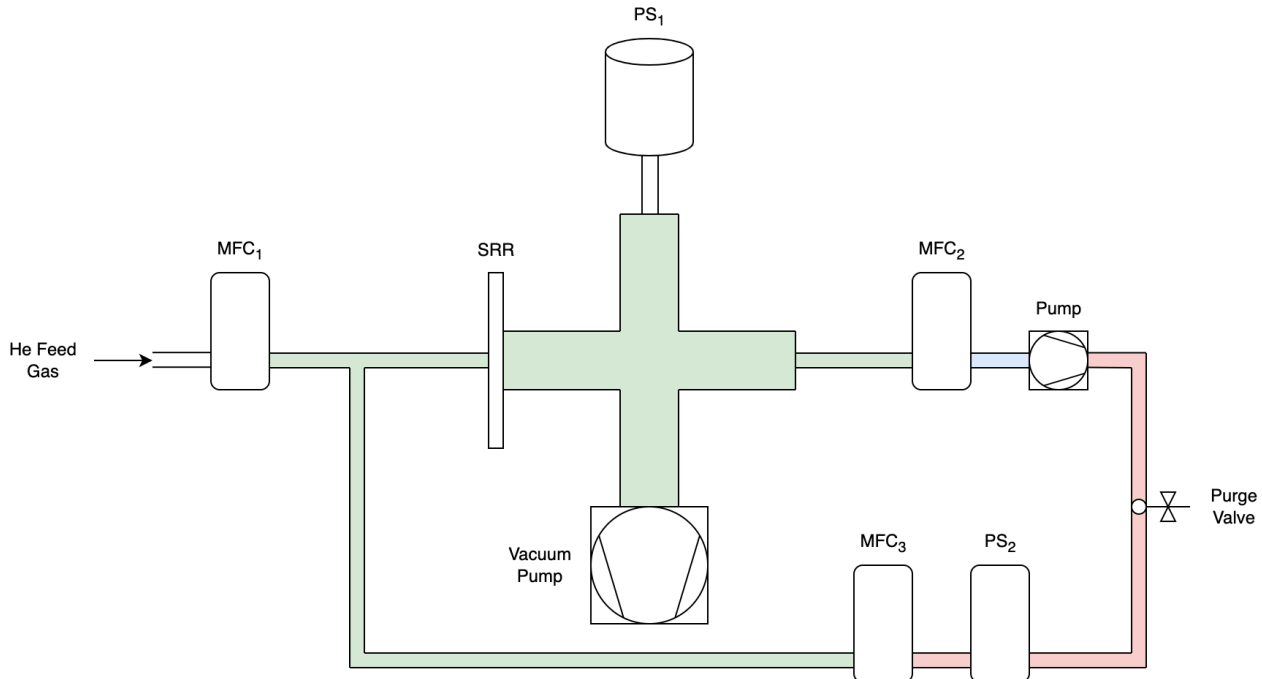


Figure 5.1: Schematic of control system with helium feed gas.

In the aforementioned design, there are three distinct pressurised regions. The first, highlighted in green, is the region where the SRR is located, thus shall be kept at atmospheric pressure. As such a pressure sensor is required to allow the pressure in this region to be controlled. The next region, shown in blue, is just before the inlet to the pump and would be at a much lower pressure, typically close to a vacuum. The final region, noted in red, is before the steady state mass flow controller; to allow a gas to flow through, this region needs to be pressurised slightly above atmospheric pressures. Since this third region is kept above atmospheric pressure, and it is kept on the outlet side of the pump, safety measures are imperative to prevent cases where the pressure continues to build up to dangerous levels. As such, another pressure sensor is required here to notify the controller if the pressure in this region exceeds a certain threshold and to initiate a software abort. Additionally, a mechanical pressure relief valve would be wise

Table 5.1: Name and description of equipment used for recirculation of helium only.

Code	Type	Description
MFC ₁	MKS GE50A, 200 sccm	Mass flow controller for (fresh) feed gas
MFC ₂	MKS GE50A, 200 sccm	Mass flow controller for pump inlet
MFC ₃	MKS GE50A, 50 sccm	Mass flow controller for (recycled) feed gas
PS ₁	MKS 623H, 1000 Torr	Capacitance manometers for pressure in primary chamber
PS ₂	MKS 640B, 1000 Torr	Pressure controller for secondary chamber

in the case that the software abort fails for any reason.

The equipment details used in figure 5.1 has been listed in table 5.1. One point to note is the use of a pressure controller in lieu of the second pressure sensor was due to the fact that only one capacitive pressure sensor available for the project. As such, the pressure controller was set to be normally open and was only used to sample the pressure. It was also calibrated to the capacitive pressure sensor and showed minimal error through the range of pressures used. The mass flow controllers were calibrated from factory, as such the only change made to the devices were to the gas correction factors.

To design this controller, all modelling was done using MATLAB Simulink, however the implementation of the controller in code was done in Python with the use of *simple-pid*, an open sourced PID controller library. A simple GUI was also designed in Python using customtkinter, and open sourced UI-library based on Tkinter, to allow information regarding the controller to be brought up in real time. Communication with the sensors and actuators were achieved via serial, as stated in the previous subchapter. The implementation of the controller can be found in the accompanying GitHub repository for this report.

The control system for a helium only setup can be broken down into two stages. First, there is the depressurising of the system to take it as close to a vacuum as possible. The goal was to remove the residual gas from the system and any gas that has leaked in from the atmosphere which can affect the plasma. This process was primarily done manually as the vacuum pump did not have remote functionality. In the depressurising stage of the controller, all the mass flow

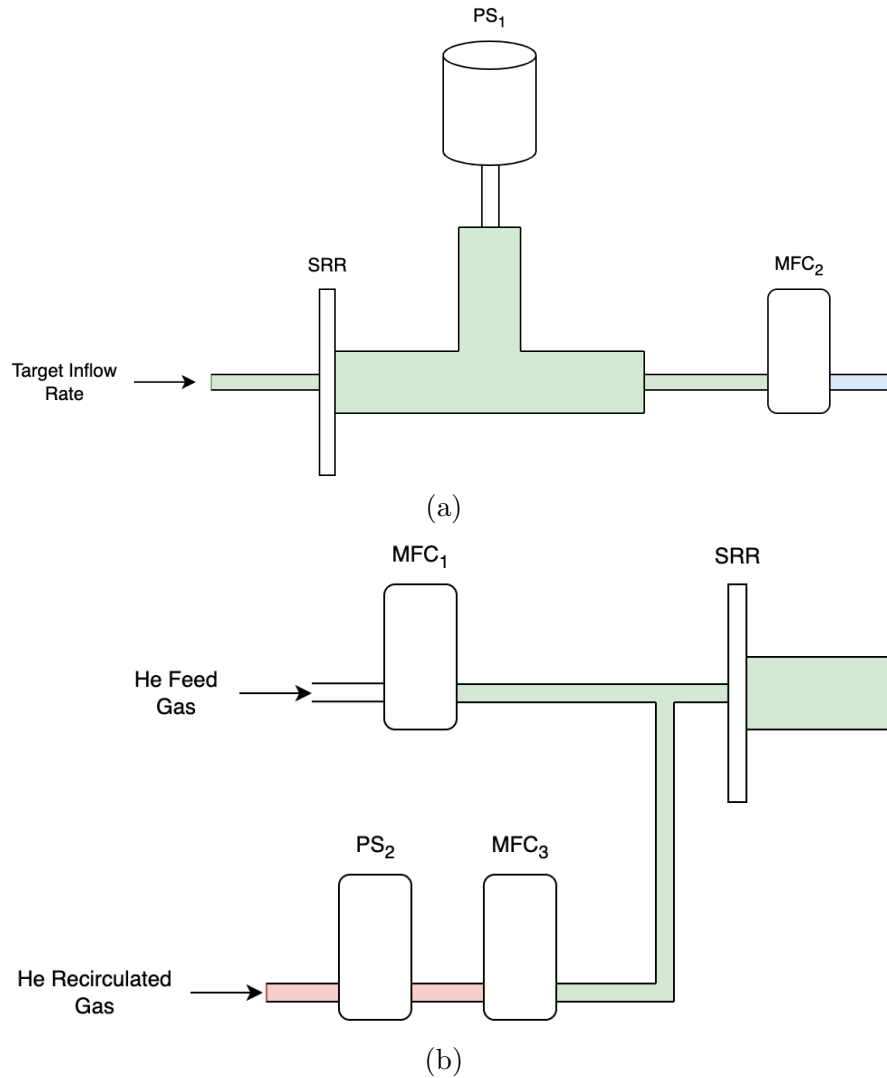


Figure 5.2: Splitting control system into chamber pressure control (a) and target flow rate control (b).

controllers bar the one controlling the feed gas (MFC_1) were set to their maximum rated flow rate. Once this happened, the vacuum pump can be manually run until the pressure sensors read zero Torr.

In the second stage, the helium feed gas can be introduced into system and the controller would recirculate the gas. For this stage, it would be useful the split the setup in figure 5.1 into two disparate control designs. One of this designs is to control the pressure in the chamber housing the SRR, while the other controls the net flow rate through the SRR. These are illustrated in figure 5.2.

5.1.1 Pressure in the SRR chamber

The pressure in the main chamber with the SRR was controlled by only using MFC₂, which controls the outflow of gas from the chamber. As the flow rate into the chamber (through the SRR) was controlled separately, it can be assumed that the flow rate into the chamber is fixed to a particular target; this can be called Q_t . Since the mass flow controllers determine the amount of gas let in and out of the chamber, its pressure can be modelled by the ideal gas law. This is possible because MFC₂ is located before the recirculation pump, which means that pumping speed (which is dependant on the pressure on the inlet) plays no role.

The ideal gas law is:

$$P = \frac{nRT}{V} \quad (5.1)$$

The pressure (P) is a function of the number of moles of gas (n), its temperature (T), and the volume of the main chamber (V). R is simply the gas constant. Both the temperature of the chamber and its volume are constant. Though there is heat generated from the plasma, its area of affect is much smaller compare to the size of the chamber, thus it is effectively constant. Hence the only variable is n . Taking the partial derivative of the pressure with respect to the number of moles gives:

$$\left(\frac{\partial P}{\partial n} \right)_{T,V} = \frac{RT}{V} \frac{\partial n}{\partial t} \quad (5.2)$$

The number of moles can be derived as a product of the net flow rate (Q_{net}) and time, which is expressed as:

$$n = Q_{net}t \quad (5.3)$$

And its derivative with respect to time is:

$$\frac{\partial n}{\partial t} = Q_{net} \quad (5.4)$$

Thus, the rate of change of pressure in the system is governed by:

$$\left(\frac{\partial P}{\partial t} \right)_{T,V} = \frac{RT}{V} Q_{net} \quad (5.5)$$

While this is an analytical solution, the issue is that the volume of the chamber is unknown. While it is possible to get an approximate volume by taking measurements of the chamber and hose lengths, it would be simpler to determine numerically. However rather than just determining the volume, the constant $\frac{RT}{V}$ can be determined instead. To achieve this, the change of pressure with respect to time was measured across several net flow rates from 10 sccm to 50 sccm. This is shown in figure 5.3.

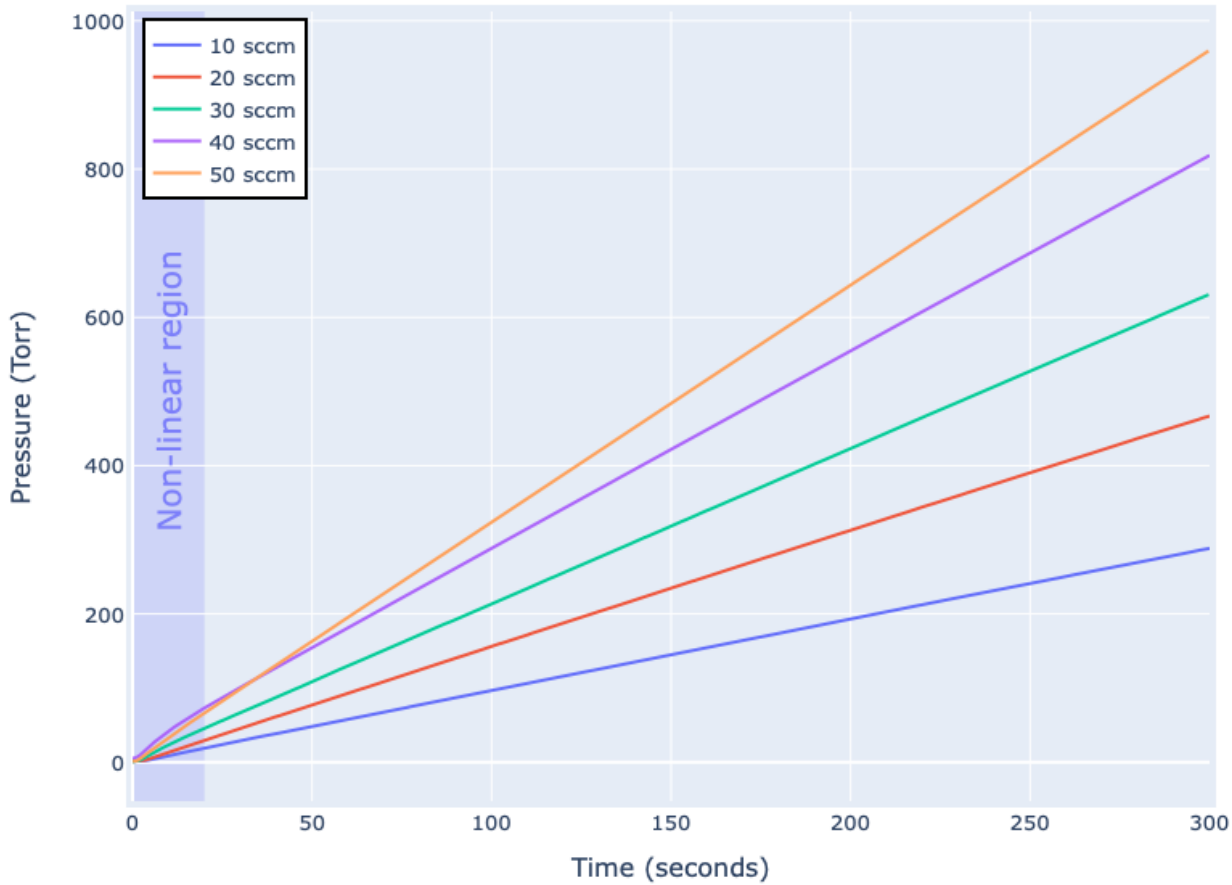


Figure 5.3: Rate of change of pressure in main chamber for flow rates between 10-50 sccm.

The gradient of the slope express the right hand side of equation 5.5. While not visible from the figure, there are some non-linearity in the beginning of the slope when the pressure increases

Flow rate (sccm)	Average rate of change of pressure (Torr/s)
10	0.960 ± 0.237
20	1.558 ± 0.330
30	2.089 ± 0.181
40	2.655 ± 0.116
50	3.189 ± 0.129

Table 5.2: Average rate of change of pressure measured for flow rates between 10-50 sccm.

from zero Torr. This is primarily due to the transients from the mass flow controllers turning on and typically settle after around 15-20 seconds. The average slope across all the flow rates tested from between 20-300 seconds are shown in table 5.2.

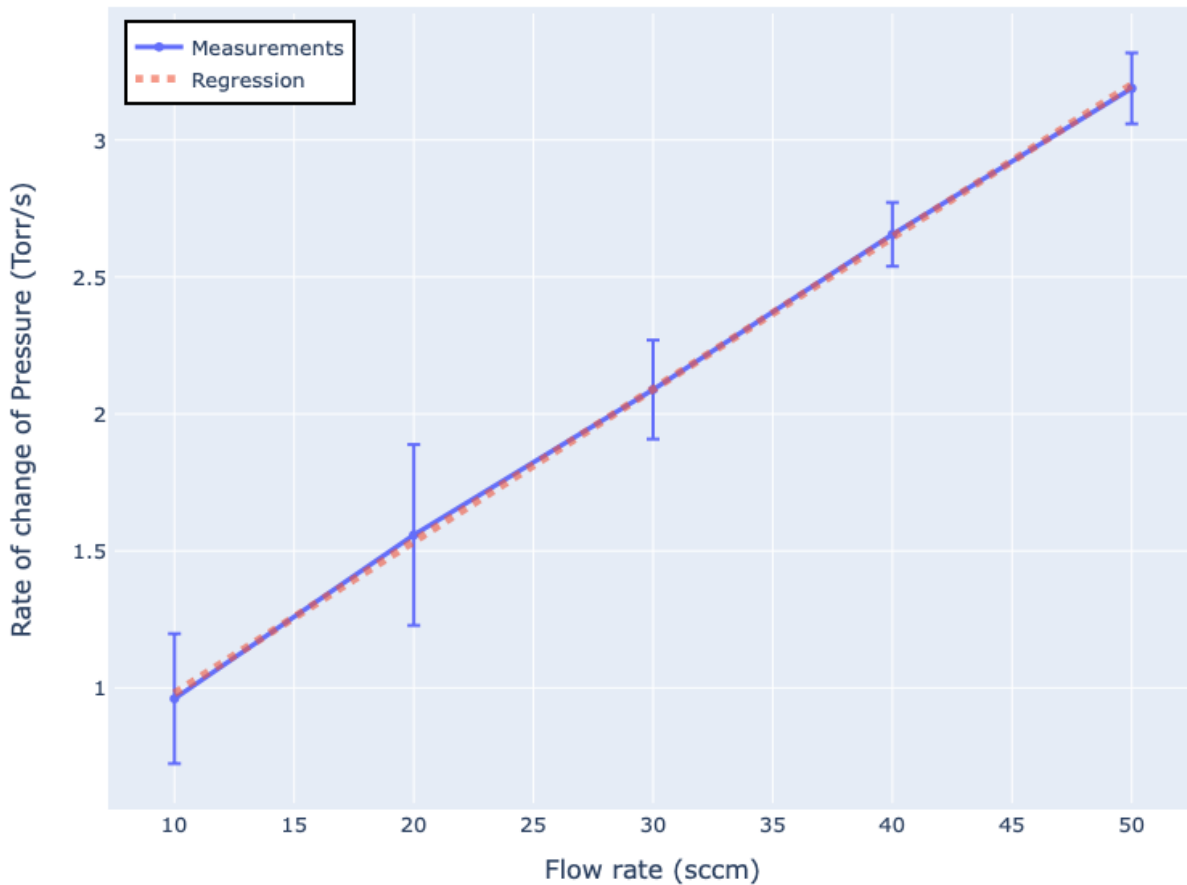


Figure 5.4: Relationship between rate of change of pressure and flow rate.

When graphing the data from table 5.2, a linear relationship is observed; though not a perfect one. This is shown in figure 5.4. A line of best fit can be taken in order to determine the value

of the constant $\frac{RT}{V}$, which would be the slope of the graph. The gradient was determined to be 0.055 Torr min cm $^{-3}_{STP}$. Therefore the solution for the rate of change of pressure is:

$$\frac{dP}{dt} = 0.055Q_{net} \quad (5.6)$$

This new equation can be used as the transfer function to represent the plant for the control system. Applying a Laplace transform gives the plant transfer function:

$$P(s) = \frac{0.558}{s}Q_{net}(s) \quad (5.7)$$

With the plant characterised, the control system can be built. A typical control system has three parts: the sensors, the actuators, and the control algorithm itself (henceforth simply referred to as the controller). The basic control system model for the plant is shown in figure 5.5. The term P_{set} corresponds to the set point pressure, Q_d to the drive flow rate suggested by the controller, and P_m is the measured pressure. In the case without the sensor and actuator blocks, Q_d and P_m correspond to Q_{net} and P respectively. The rational for incorporating the sensors and actuators into the model is to take into account factors that produce errors such noise or bias. However, at first it would be best to simply design a controller assuming ideal circumstances.

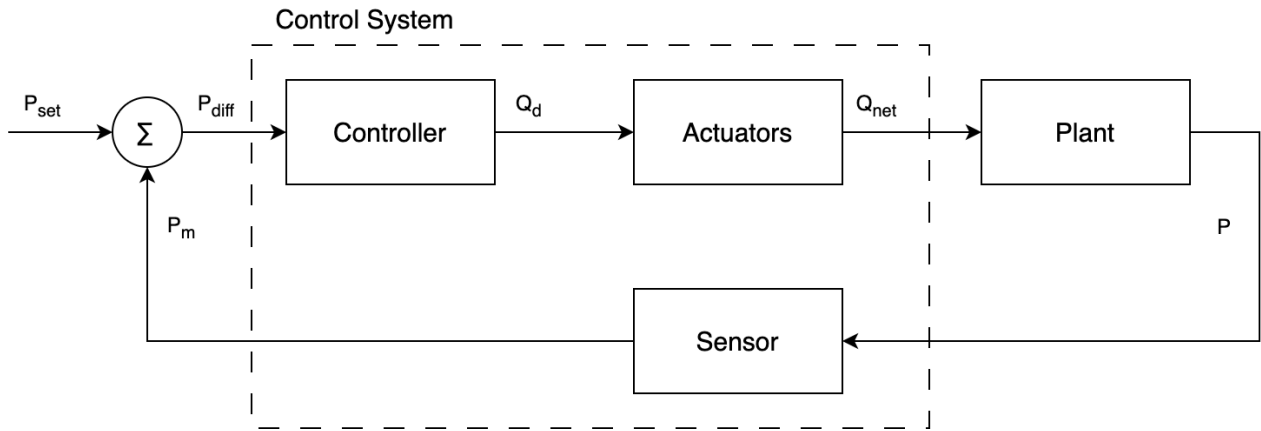


Figure 5.5: Basic schematic of control system.

To start, the proportional controller modelled in figure 5.6 was used. In essence, this controller

adjusts the output based on the error between the set point and measured pressure value (called the process variable). Therefore as the error increases, the correction applied also increases. The correction can be adjusted using a proportional term called K_p , which is simply a fixed gain. The value of $K_p = 5$ was chosen arbitrarily. To evaluate the controller, three test cases were devised. These include:

- **Test case 1** - Bringing the chamber up to 760 Torr from a vacuum, which would simulate the case of flushing the system and re-pressurising it.
- **Test case 2** - Brining the chamber up to 760 Torr from 720 Torr (approximately 95% of the set point), which would simulate a steady state case where there was a small drop in pressure in the system.
- **Test case 3** - Brining the chamber down to 760 Torr from 800 Torr (approximately 105% of the set point), which would simulate a steady state case where there was a build up of pressure in the system.

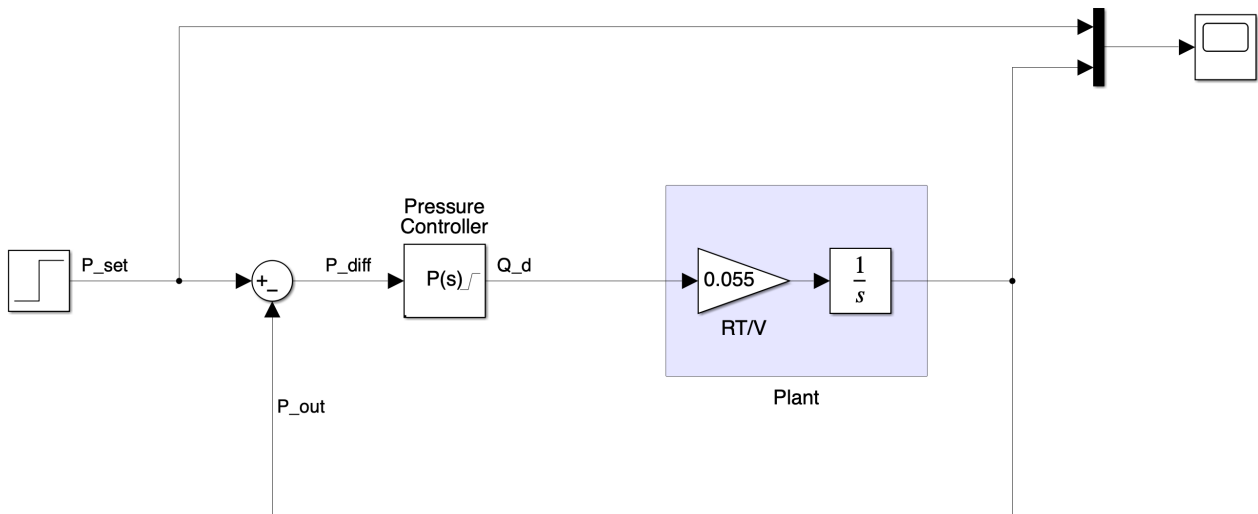


Figure 5.6: Illustration of control system.

The results for the proportional controller can be seen in figures 5.7 (seen as P - No saturation). Note, for the purposes of quantifying the results, the term settling time is defined as the time taken for the controller to settle to within 0.1% of the set value; which is approximately ± 1 Torr for a set value at atmospheric pressure.

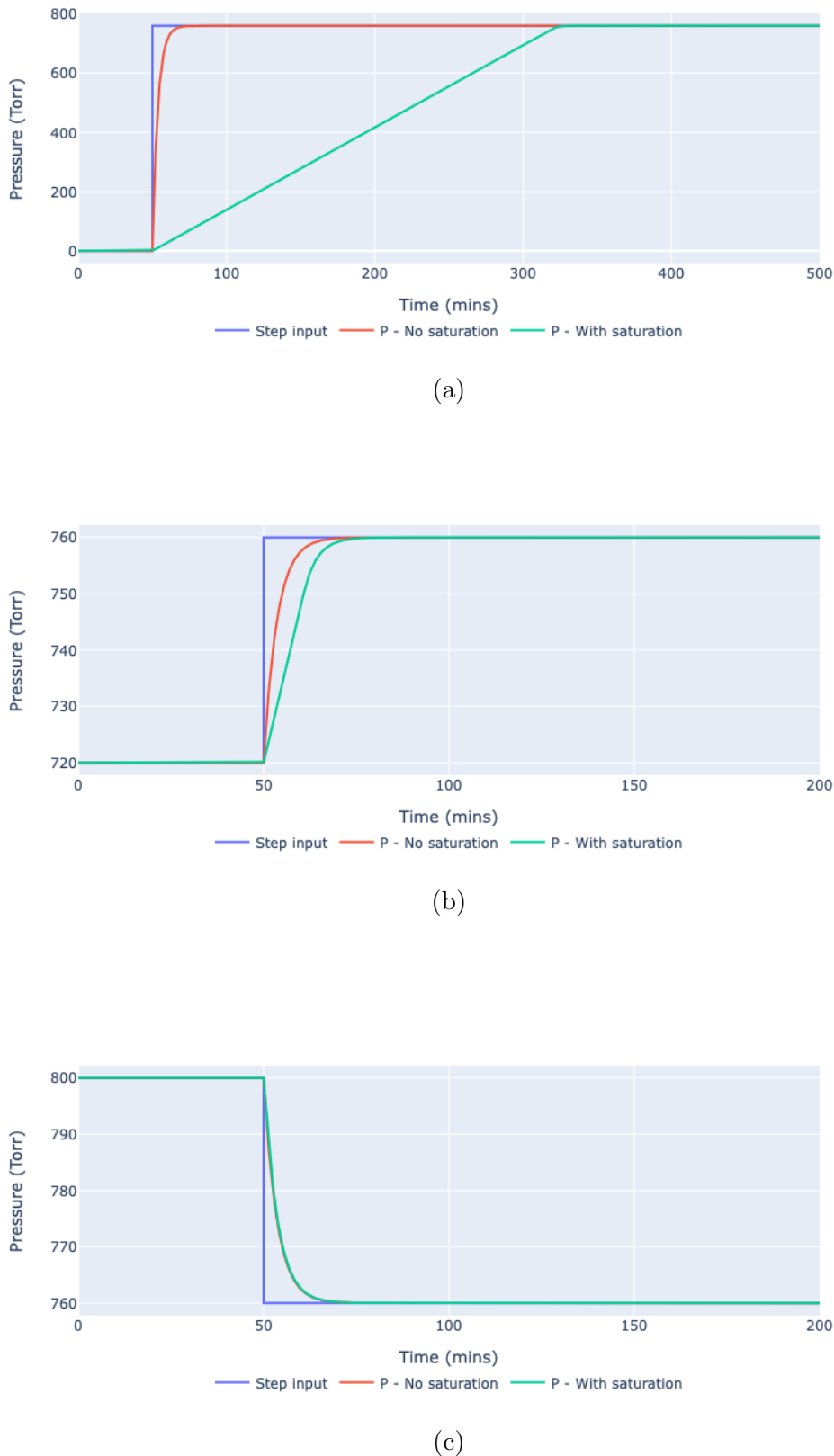


Figure 5.7: Evaluation of proportional controller for test cases 1 (a), 2 (b), and 3 (c).

The basic controller seems to perform well with no overshoot and a settling time of 19 seconds for the first test case, and 8.5 seconds for the second and third test case. However, such performance is unobtainable in the real world as the drive flow rate is beyond the capabilities of the mass flow controllers used. When the drive flow rate is saturated within the constraints of the mass flow controllers used, the settling times increase to 273.5 seconds for the first test case, 14.3 seconds for the second, and 8.6 seconds for third. The saturation values chosen were between a maximum of 50 sccm to a minimum of -150 sccm. This is because the maximum drive flow rate is achieved when the outlet mass flow controller is set to zero, whilst the minimum flow rate is achieved when the outlet mass flow controller is set to its maximum value of 200 sccm. The results with the output saturation of the controller are also shown on figure 5.7 (seen as P - With saturation). Note that the times are noticeably longer for both test 1 and 2, however test 3 only shows a marginal decrease in settling time. This is because of the asymmetry of the drive flow rate, where the controller can more quickly get rid of gas in the chamber than it can fill it up.

Now that a controller was designed for the ideal control system, the sensor and actuator blocks can be reintroduced. Starting with the actuators, the data sheet states that the mass flow controllers have a typical accuracy of “ $\pm 1\%$ of set point for 20 to 100% Full Scale, $\pm 0.2\%$ of Full Scale for 2 to 20% Full Scale” [88]. Based on the equipment used (the details of which can be found in table 5.1), the systematic error for the mass flow controllers would be ± 2 sccm. As for the sensors, the data sheet states that the capacitive pressure sensor used has accuracy of “ $\pm 0.25\%$ of reading” [89] for the pressure sensor; and “ $\pm 0.5\%$ of reading” for the pressure controller [90]. Assuming the worst case, this would mean that the systematic error in the sensor would be ± 3.8 Torr. Errors caused by environmental affects would be difficult to model, thus are ignored in the model.

The updated Simulink model can be seen in figure 5.8, where these errors were modelled as constants. The terms Q_{in} and Q_{out} are the input and output flow rates governed by MFC₁ and MFC₂. Note that the controller is designed to control the net flow rate in or out of the chamber, hence the value for Q_{out} was determined by taking the difference between Q_{in} and Q_d . As for the value of the error constants, these were set to take the maximum possible errors

specified in the previous paragraph.

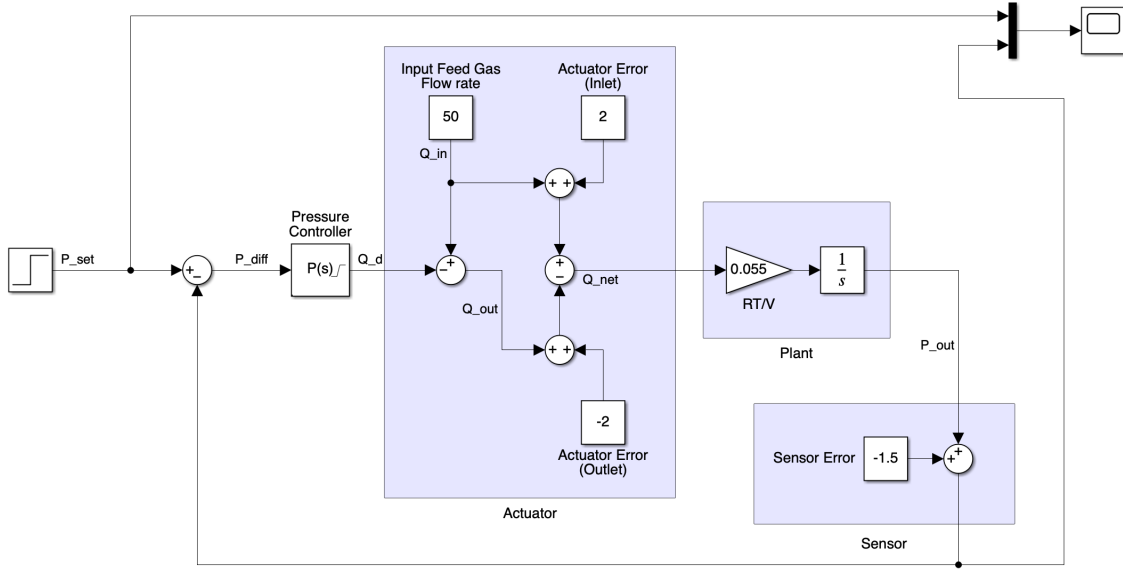


Figure 5.8: Illustration of control system.

Introducing these constant error terms into the model caused a steady state offset to be observed in all three test cases. The magnitude of the offset was the same for each test case, meaning they are independent of the pressure. An intuitive explanation for this is that the controller is attempting to send the correct signal to the plant, but the error from actuator or sensor cancels out the drive signal, hence no change occurs in the plant. A visualisation of these offsets can be seen in figure 5.9, which highlights the effect that varying the systematic error has on the offset. The impact of the errors from the actuators and sensors were compared separately.

In order to get rid of this, the introduction of an integrator component to the controller is needed. The integrator adjusts the output of the controller based on the accumulated error over time. As the duration or magnitude of an error increases, so does the correction factor. Thus, the integral term compensates for any steady state error in the system. One common trade off with the integrator component is called overshoot, where the lag introduced by the integrator causes the controller to not respond fast enough. This results in the controller overshooting the set point. To control this, an integrator term, K_i , can be introduced.

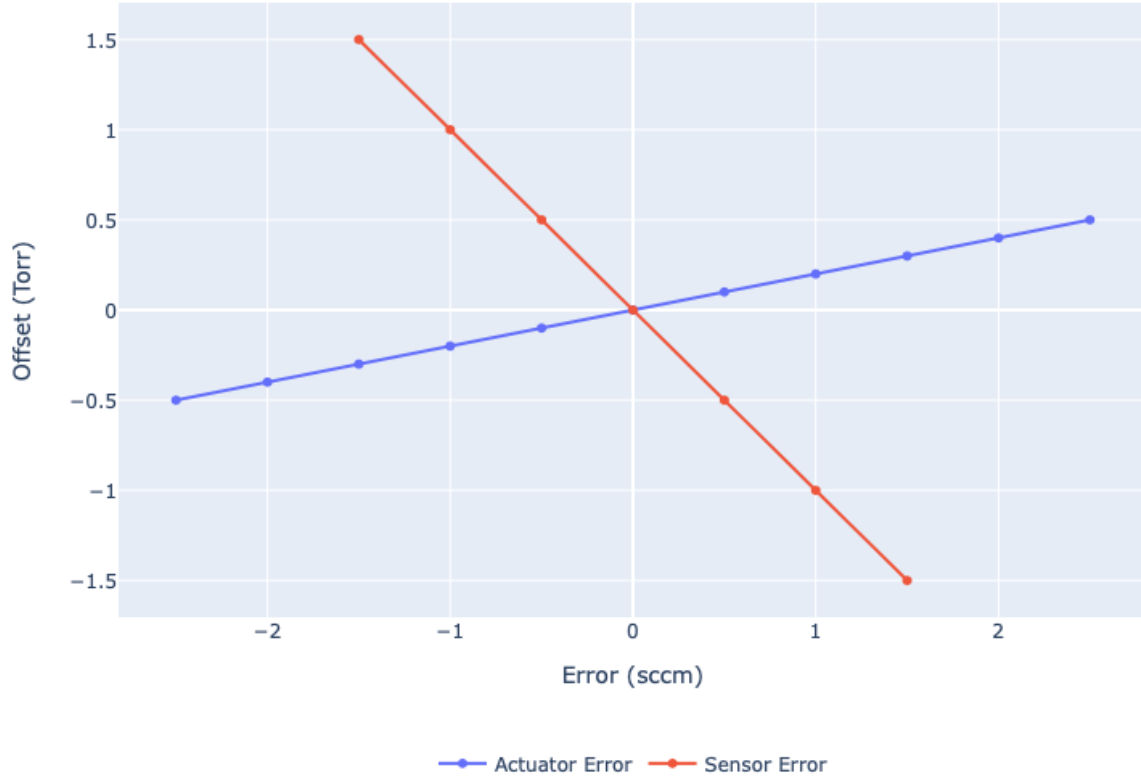


Figure 5.9: Comparison of offset introduced by the actuator and sensor error.

Another limitation with using an integrator component called integral windup. This is especially apparent in a system where the actuators have an upper and lower limit to the amount of drive signal it can produce. Windup occurs due to a large accumulation of error between the set point and process variable, then when the sign of the error is flipped, time is required to unwind the accumulated error. The result is an excessive overshoot, which cannot be eliminated using K_i .

An illustration of can be seen in figure 5.10, shown using test case 1. With $K_i = 0.01$, resulted in an overshoot to 940 Torr (nearly 24% over the set point pressure). The windup is simply the accumulation of the error, shown as the area between the step input and the response in orange. Then as the response overshoots, the integral error drops until it reaches the maximum point. Finally, the error is unwound as shown in the graph as the green area; the error is fully unwound when the green area is equal to the orange area. In order to address

this problem, a process called clamping is used. This is achieved by preventing the integrator component from accumulating error by limiting its value within a certain upper and lower bound.

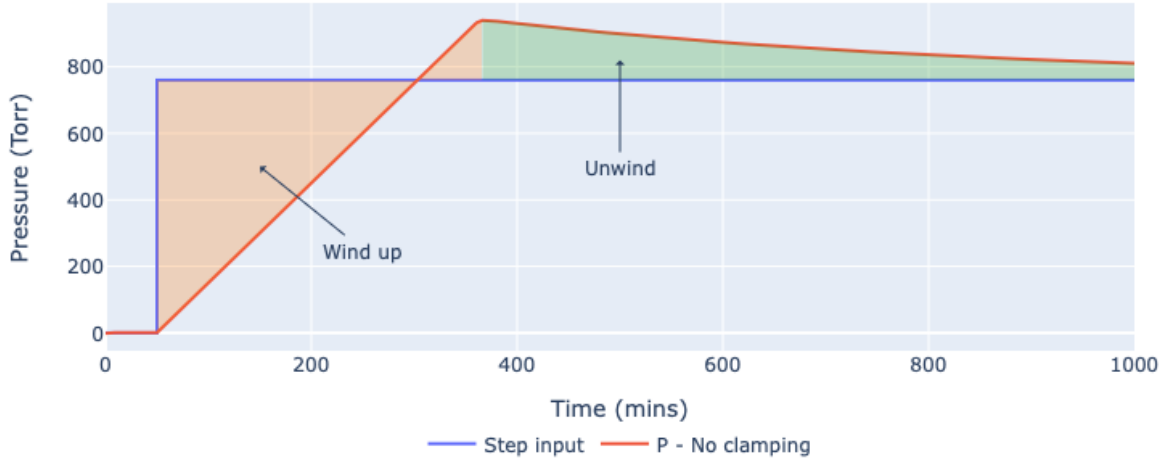
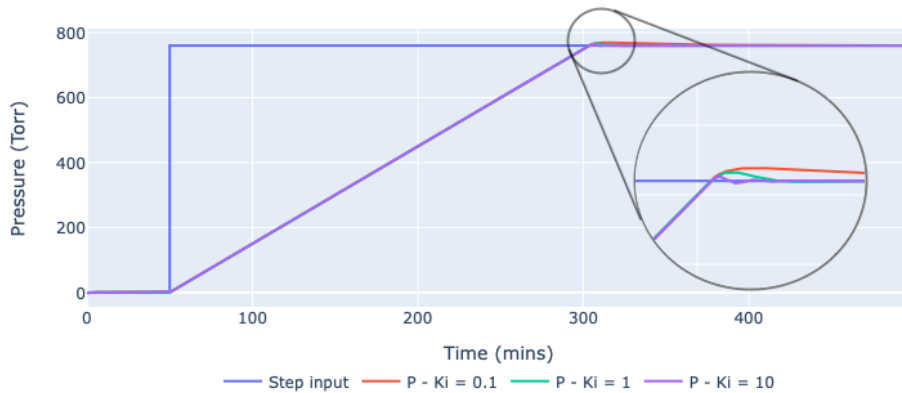


Figure 5.10: Illustration of integral windup for PI controller ($K_p = 5$, $K_i = 0.01$).

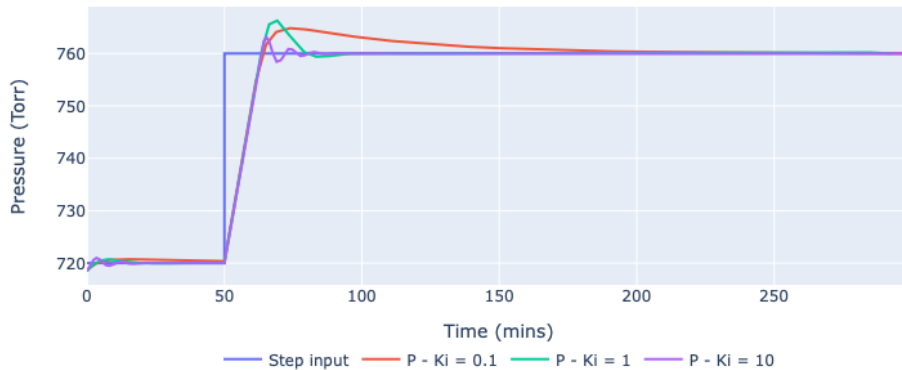
Thus, the resulting controller (with a proportional and integrator component) is known as a PI controller. The final proportional and integral terms selected were $K_p = 5$ and $K_i = 1$, which were determined heuristically. The goal when tuning the controller was to balance settling time and overshoot, whilst avoiding oscillations. The rational for avoiding oscillation was to minimise any disturbances to the plasma that could potentially cause it to die out. A comparison of several K_i values are shown in figure 5.11. Note that the impact of varying the K_i values in test case 1 were minimal in terms of overshoot, with the only observable changes being the settling time.

When modelling, the time step selected was 1 second. This specific value was chosen to allow sufficient time to read data from the sensors and send commands to the actuators. Additional buffer time was included for cases when the sensors or actuators fail to acknowledge the commands sent to it.

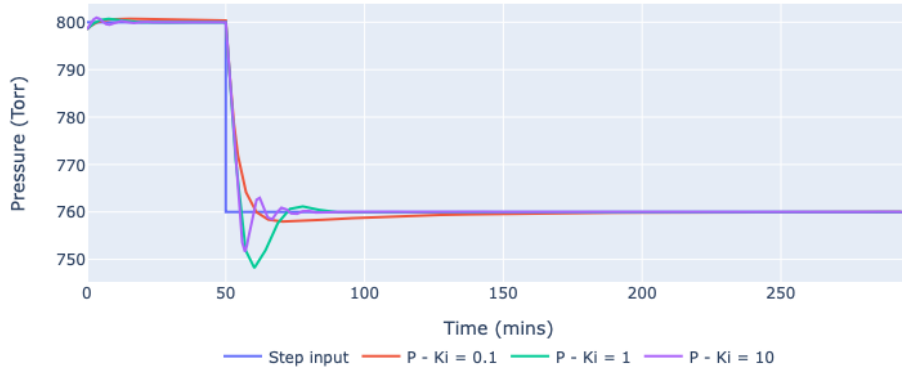
The PI controller in Simulink, was translated into Python code. The controller was expressed



(a)



(b)



(c)

Figure 5.11: Evaluation of PI controller for test cases 1 (a), 2 (b), and 3 (c).

in the following form:

$$Q_d(t) = K_p P_e(t) + K_i \int_0^t P_e(t) dt \quad (5.8)$$

The performance of the real controller was evaluated using the first test case, with the results shown in figure 5.12. When compared to the model, the real controller performed worse when it came to the overshoot but slightly better in terms of settling time. The overshoot value was nearly doubled from 5.8 to 10.6 Torr. However, this overshoot is just over 1% of the set point, which was thought to be an acceptable performance. The settling time of the real controller 261 seconds, about 6 seconds faster than the model but is within the margin of error. The discrepancy observed at the start of the step input are the same non-linearities seen in 5.3.

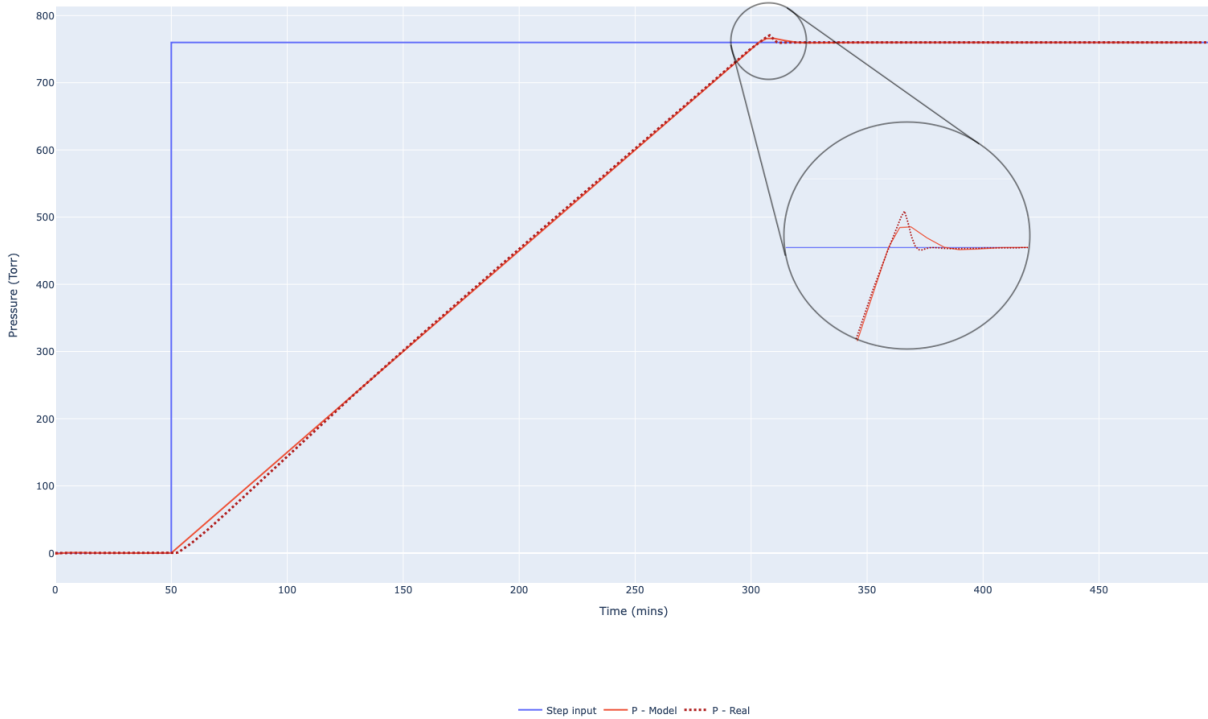


Figure 5.12: Comparison between the performance of the modelled and real PI controllers.

5.1.2 Flow rate to the SRR

With the PI controller designed, the second stage of the control system was to regulate the flow rate to the SRR. After depressurising the system, it needs to be first refilled with Helium

feed gas from the tank, henceforth referred to as *fresh gas*. Then as the main chamber and secondary chamber is pressurised, the dependance on fresh gas can be reduced in favour of the recirculated Helium from the secondary chamber; simply referred to as *recycled gas*. Whilst this is occurring, the net flow rate through the SRR needs to be kept constant at the target flow rate.

The value for target flow rate is limited by the maximum flow rate of MFC₃ which was 50 sccm. So the first step was to determine what level of pressure difference is required between the inlet and outlet of the mass flow controller (MFC₃) to achieve a steady flow rate of 50 sccm. The data sheet for the mass flow controllers state that the normal operating pressure differential was “10 to 40 psid at 10 to 5000 sccm” [88]. This equates to a pressure difference of over 500 Torr between the inlet and the outlet. However from some experimentation, it was found that the pressure difference required ranged from around 100 to 200 Torr, with the difference increasing as the outlet pressure is dropped below atmospheric pressure.

Since the outlet was at atmospheric pressures, the pressure difference of at least 100 Torr is required to ensure that target flow rate is achieved with only using the recycled gas. Based on this, the selected pressure differential chosen was slightly higher at 150 Torr. This was simply to give a slight buffer in the case where the outlet pressure is higher than atmospheric pressure, meaning that the pressure in the secondary chamber would be 910 Torr in the steady state.

Armed with this information, a controller can be designed to regulate the target flow rate to the SRR. Rather than building a second PI controller, these two parameters (fresh gas and recycled gas) can be controlled algebraically. The simplest equation to govern this is:

$$Q_f = Q_t - Q_r \quad (5.9)$$

where Q_t corresponds to the target flow rate at the SRR, Q_f is the flow rate of fresh gas, and Q_r is the recycled flow rate.

Then based on the pressure readings from PS₁ and PS₂ the recycled flow rate can be expressed

as function of pressure and the target flow rate:

$$Q_r = \frac{1}{150} P_{diff} Q_t \quad (5.10)$$

where P_{diff} is the pressure difference between PS₁ and PS₂.

Equation 5.10 is only valid for cases where $P_{diff} \geq 0$ and $P_{diff} \leq 150$, thus a more complete expression would be:

$$Q_r = \begin{cases} 0, & \text{if } P_{diff} < 0 \\ Q_t, & \text{else if } P_{diff} > 150 \\ \frac{1}{150} P_{diff} Q_t, & \text{otherwise} \end{cases} \quad (5.11)$$

Thus, the flow rate of fresh gas (through MFC₁) can be controlled using equation 5.9 and the flow rate of recycled gas through (through MFC₃) can be controlled via equation 5.11.

5.1.3 Complete control system

As mentioned earlier, the detailed implementation of the Python code is not included here. However, the full control system algorithm is expressed in the form of a flow chart seen in figure 5.13.

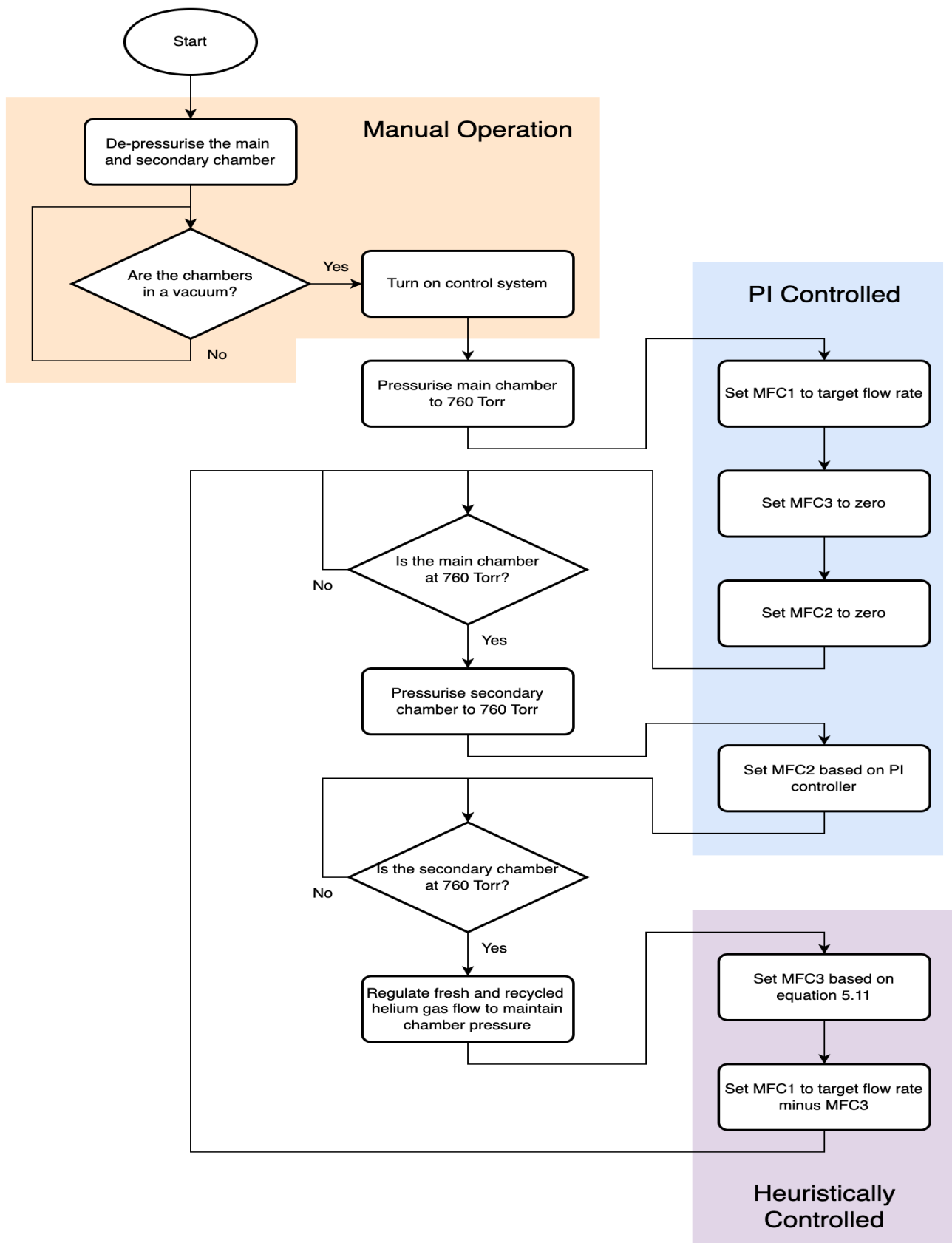


Figure 5.13: Flow chart of Helium only recirculation control system.

5.2 Control System with Helium and Carbon Dioxide

In order to introduce CO₂ into the control system, a fourth mass flow controller (MFC₄) was required. If the system were to be an open gas loop design, the gas composition could simply be measured as a ratio of the flow rates of CO₂ and Helium. Though it is a crude method, this was precisely how the concentration of CO₂ was determined during the characterisation experiments in the previous chapter. However in a closed gas loop design, this method of detection would not be feasible as the CO₂ concentration would build up over time. Instead, the gas composition would be determined using the Fourier-transform infrared spectroscopy (FTIR) spectrometer, using the correlation data of CO₂ concentration with absorbance (seen in § 4.4.2).

These two additional components can be seen in the updated schematic drawing seen in figure 5.14. There are several important points to note about the positioning of these components in relation to each other in the setup.

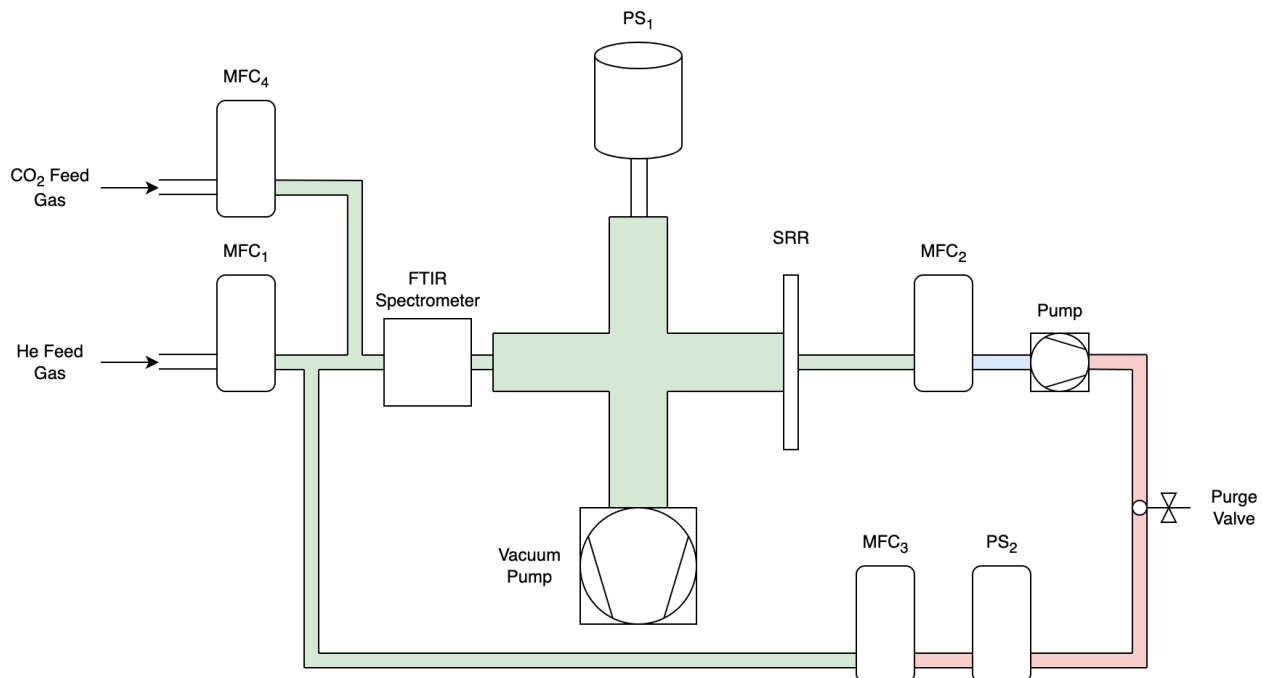


Figure 5.14: Schematic of control system with helium feed gas and carbon dioxide.

Firstly is with regards to the position of the FTIR spectrometer located before the SRR. Initially, the idea was to position the spectrometer after the SRR in order to measure the

gas composition immediately after the plasma, which would be useful in the later experiments involving the trans-stilbene liquid. However from experimentation, it was found that positioning the spectrometer behind the SRR there would cause a relatively large lag time between when the CO₂ was first introduced into the system to when it detected by the spectrometer. This has to do with the fact that the volume of the main chamber is several orders of magnitude bigger than the volume of tubing, and even the FTIR sample chamber would be about one tenth the volume. As such, moving the CO₂ detection before the SRR reduces this lag time, which would be incredibly beneficial when designing the CO₂ controller aspect of the system. Though one loses out on the benefit of detecting the gas composition post the plasma-reaction, positioning the spectrometer before the SRR allows for the detection of aerosolised organic compounds which could potentially interfere with the plasma performance.

Another thing of note is the location of MFC₄ with relation to the other mass flow controllers. Due to the relatively small concentration of CO₂ required in the system, the required flow rates of CO₂ gas are also low. Given that the volumetric flow rate of a gas is:

$$Q = \nu A \quad (5.12)$$

where ν is the flow velocity of the gas and A is the cross sectional area of the tubing. Since all the tubing for the gas is the same size (approximately a 4mm inner diameter), this means that the gas flow rate is proportional to the flow velocity. The associated low flow velocity for CO₂ result in a delay in the mixing of the overall gas composition which is dependant on the length of the tubing. As such, the tubing length for the CO₂ gas (post the mass flow controller MFC₄) should be as short as possible. An illustration of the time delay across two tubing lengths can be seen in figure ???. The short tubing had a length of x cm, while the long tubing was x cm.

5.2.1 Controlling carbon dioxide concentration

In order to ensure only helium and CO₂ are present, the system is first de-pressurised to vacuum (as mentioned in the previous subsection). Thus, there are two possible ways re-pressurise the system with both gases.

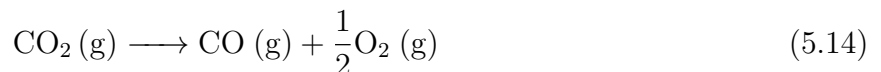
The first method would be to simultaneously turn on both MFC₁ and MFC₄, which control the flow rates of helium and CO₂ respectively. At a first glance, this method would be the simplest and fastest way to fill a system with gas. Additionally, the CO₂ concentration can be set in the same manner as it was set for an open gas loop system, using the expression:

$$c = \frac{Q_{CO_2}}{Q_{He} + Q_{CO_2}} \quad (5.13)$$

where c is the concentration of CO₂ in the system.

One could simply design a control system in the exact manner as the helium only gas controller. The only difference being, instead of topping up the system with just helium, the correct ratio of helium and CO₂ can be used instead.

However, this approach is only viable when the plasma is not ignited. This is because when the plasma is ignited, CO₂ is dissociated into carbon monoxide (CO) by the following reversible reaction:



In an ideal system, where only the two intended gases are present, this would not be a particularly large issue since the ratio of CO₂ and CO would settle to a steady state. However in reality, the presence of impurities are almost a certainty. These impurities (such as nitrogen) would most likely interact with the atomic oxygen, preventing the reverse reaction to take place; thus obfuscating the true CO₂ concentration in the system.

The alternative method for re-pressurising the system would be to first fill up the system with helium. Then once completed, CO₂ can be introduced into the system until the desired concentration is obtained. This approach should be more robust as CO₂ concentration can be measured in real time using the FTIR to keep it a fixed value. However, this improved robustness comes at the cost of complexity.

Previously, when measuring the the CO₂ concentration for the open gas loop configuration, the concentration was expressed using the number of moles:

$$c = \frac{n_{CO_2}}{n_{He} + n_{CO_2}} \quad (5.15)$$

Given that the number of moles of inert gas is significantly larger than that of CO₂ (considering the plasma would be operating at a CO₂ concentration of only 1%), the aforementioned equation for concentration was linearised to:

$$c = \frac{n_{CO_2}}{n_{He}} \quad (5.16)$$

While this linearisation would introduce some error into the model, the reality is that this error is very small; for example, in the case of a 1% CO₂ gas mixture, the error between the true concentration equation and the linearised one is around 1%. The fact is that the sources of error from the mass flow controllers or the reading from the FTIR would be larger than this error, due to both systematic and environmental reasons respectively.

The issue in using this equation for a closed gas loop configuration comes down to the fact that input into the control system will be a given flow rate of inert gas and CO₂. In theory, one could form a new expression to determine the relationship between flow rate and CO₂ concentration, but this would require knowing the exact value of certain parameters of the system which would be difficult to measure, such as its volume and rate of gas leaking out of the system. Additionally, since the pressure in the primary chamber is fixed, gas is being compressed in the system within the secondary chamber which adds another layer of complexity. Instead, the

behaviour of the system can be determined experimentally, then assumptions can be made to simplified the Simulink model.

The following experiment was run to determine this behaviour. First, the system was run as an inert gas only system, where it was drawn to a vacuum then repressurised with inert gas until it reached a steady state. Then after approximately 15 minutes of steady state behaviour, a series of baseline samples were taken on the FTIR, and these values were averaged as the background CO₂. Finally, a fixed flow rate of CO₂ was added into the system, and the FTIR would measure the absorbance every 5 seconds (running the exact settings detailed in § 4.4.2). This test was run across several flow rates of CO₂, between 0.3 to 1.0 sccm. The minimum of 0.3 sccm was set due to the fact that the mass flow controller MFC₄ cannot continuously deliver lower flow rates of gas without resorting to PWM control; which would affect the characterisation of the system.

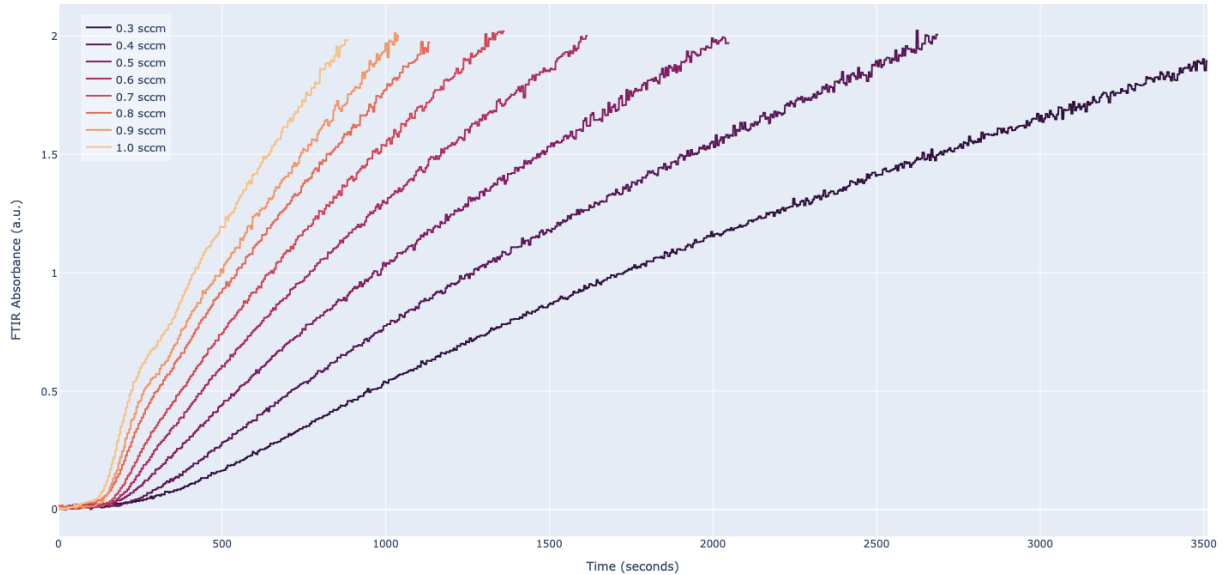


Figure 5.15: Time series response of the system without a CO₂ controller various flow rates of CO₂ gas.

The raw results of this test can be seen in figure 5.15. The origin time, $t = 0$, was set from the moment MFC₄ was turned on to let CO₂ into the system. CO₂ was only added until the FTIR read an absorbance of 2.0, which approximately equate to a 7% CO₂-inert gas composition. The rationale for this is that values above this were too close to the limit of the CO₂ sample

capabilities of the FTIR, meaning that any results would be very sensitive to noise.

The results shown mostly match the expected behaviour, wherein there is a (relatively) short lag time where the CO₂ concentration remains at 0 before the FTIR signal increases. However from the figure, it can be observed that there are some non-linear behaviour in the initial part of the system response before linearising. Possible mechanisms for this are explained later, however for now there are two important characteristics to look at from this data.

The first is the effect of CO₂ flow rate on the lag time of the system. This can be achieved by finding the inflection point of the curves, which simply involves finding the second derivative. However before this can be done, the data needs to be smoothed since derivatives are incredibly sensitive to noise. To achieve this, a gaussian filter was applied before each derivative was taken. An example of this process can be visualised in figure 5.16.

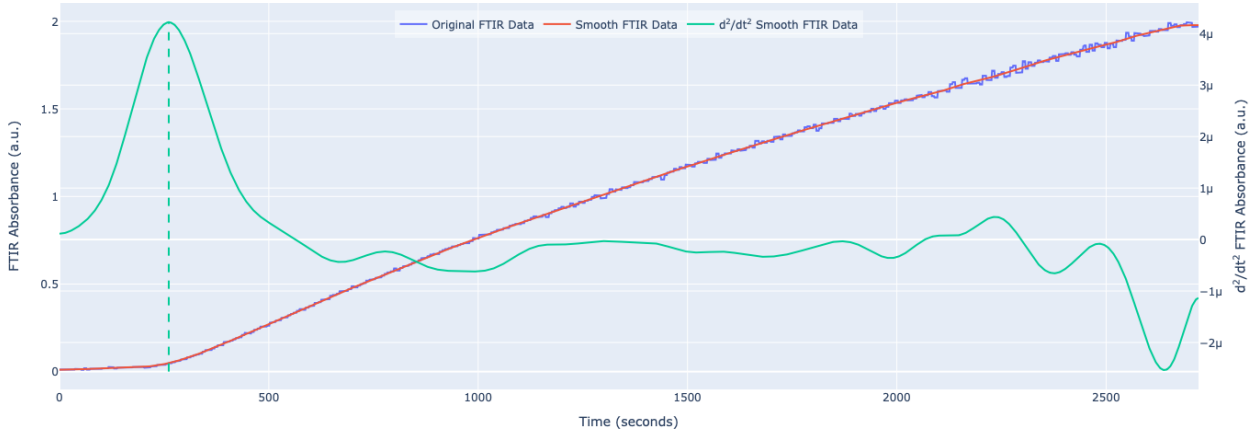


Figure 5.16: Illustration of process used to determine the lag time of the system.

The results of this analysis can be seen in table 5.3. The inflection times measured have to be inversely proportional to the flow rate. This is because, as shown in equation 5.12, the flow rate is governed by the cross sectional area of the tube (A) and the velocity of gas going through it (v). Since the length of the tubing is fixed, the flow rate can be said to be:

$$Q = V_{tube} \frac{1}{t} \quad (5.17)$$

where V_{tube} is simply the fixed volume of the tube.

Table 5.3: Measured lag time across various flow rates of CO₂ gas.

CO ₂ flow rate (sccm)	Lag time (s)
0.3	343.889
0.4	290.050
0.5	263.828
0.6	230.379
0.7	205.384
0.8	179.995
0.9	165.620
1.0	149.341

Using linear regression, a line of best fit can be obtained. This is shown in figure 5.17. The coefficients from the linear regression will be used in the Simulink model shown later.

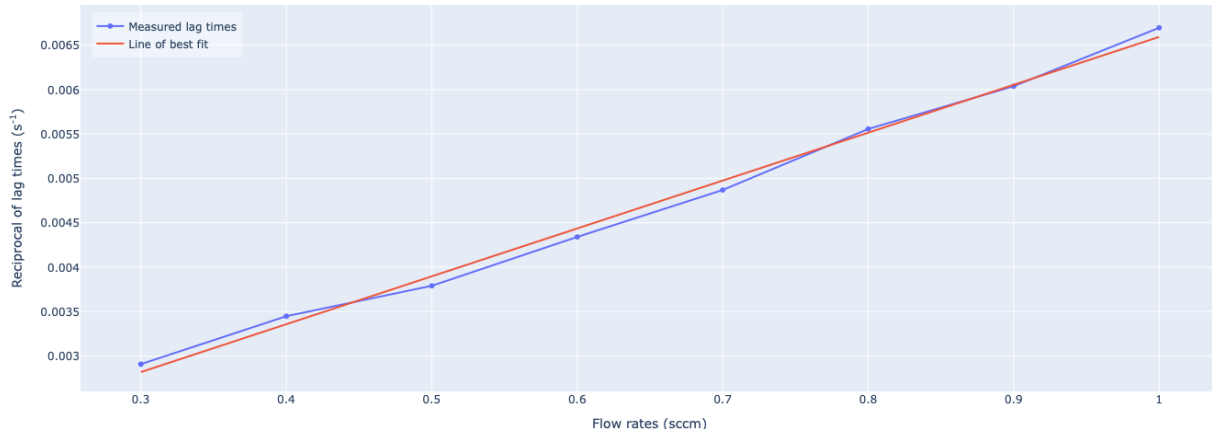


Figure 5.17: The inversely proportional relationship between flow rate and lag time.

With the CO₂ lag times of the system characterised, the other characteristic to be determined is how the rate of CO₂ concentration increases with respect to the flow rate. As stated previously, there appears to some non-linear behaviour in the system when the CO₂ concentration first increases. Hence, this characterisation process will only look at the results for when the FTIR absorbance is between 1.0-2.0.

The expectation here is that the rate of increase of CO₂ concentration should be linear. The reason for this is that MFC₄ feeds a fixed volume of gas into the system, and since its pure CO₂ gas, the number of CO₂ molecules should enter the system at any given moment should be constant. Thus, since the system is a closed gas loop, the accumulation of CO₂ molecules should increase at a linear rate.

To achieve this, a slightly process was taken that in § 5.1.1 where the relationship between flow rate and the rate of increase in pressure were determined. This is because the FTIR data is inherently more noisy than the pressure readings. As such, rather than taking the gradient directly, a linear regression was first performed then the gradient of that line of best fit was used. An illustration of this process can be seen in figure 5.18. Note that the origin times were reset so that $t = 0$ occurs when the FTIR absorbance first crosses 1.0.

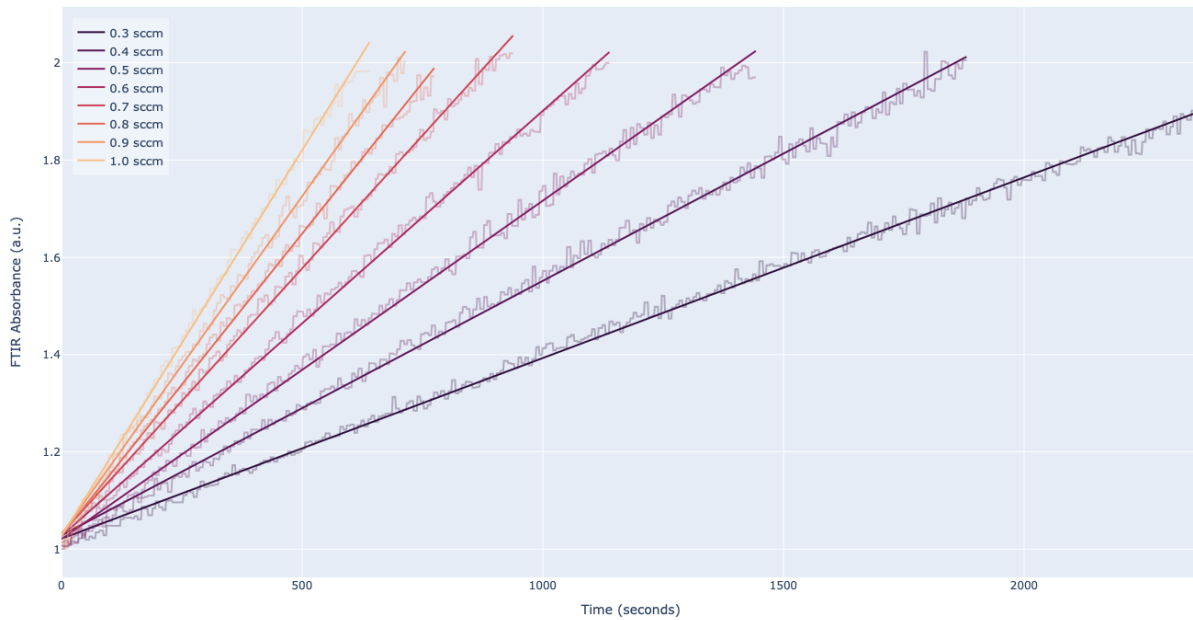


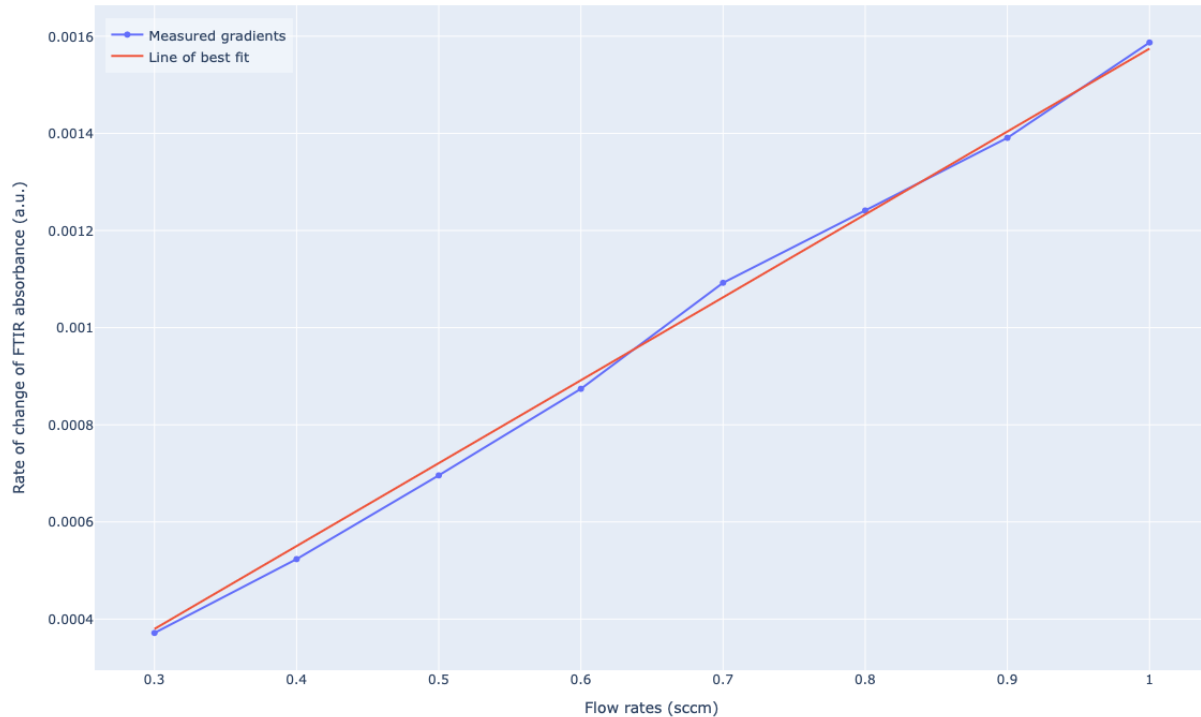
Figure 5.18: Rate of change of CO₂ concentration for CO₂ flow rates between 0.3-1.0 sccm..

The gradient of the rate of change of CO₂ concentrations are shown in table 5.4, along with the corresponding coefficient of determination (R^2) values which denote the fit of the regression lines to the original data. All models have a $R^2 > 0.99$ with the worst values being 0.997, confirming the expected linear characteristic.

Table 5.4: Best fit rate of change of FTIR absorbance across various flow rates.

Flow rates (sccm)	Rate of change of FTIR absorbance (a.u.)	R2 Score
0.3	0.00037	0.99731
0.4	0.00052	0.99672
0.5	0.00070	0.99678
0.6	0.00087	0.99721
0.7	0.00109	0.99734
0.8	0.00124	0.99760
0.9	0.00139	0.99653
1.0	0.00159	0.99754

With the gradients determined, the relationship between those values and the flow rates can be visualised in figure 5.19. The slope of the line will again be used in the Simulink model for the CO₂ controller.

Figure 5.19: Rate of change of CO₂ concentration for CO₂ flow rates between 0.3-1.0 sccm..

With these lag time and rate of change of CO₂ concentration characteristics obtained for var-

ious flow rates, the next step is to take these parameters into Simulink for modelling. The modelled control system can be seen in figure ???. This is simply the ideal plant model (without incorporating errors from the mass flow controllers or the FTIR).

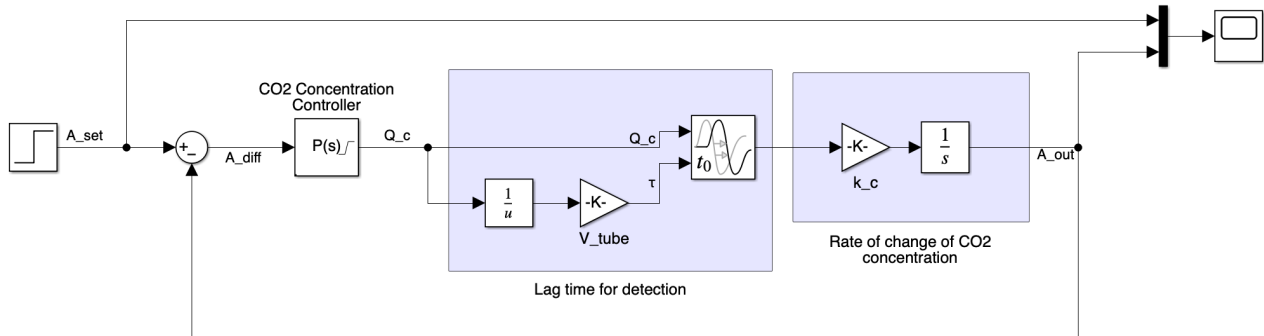


Figure 5.20: Modelled CO₂ gas control system in Simulink.

The lag time is modelled using a variable time delay, based on the set CO₂ flow rate (Q_c) and the volume of the tubing (V_{tube}). It is governed by the equation:

$$\tau = \frac{V_{tube}}{Q_c} \quad (5.18)$$

As for the rate of change of CO₂ concentration, it is modelled identically to equation 5.7 in § 5.1.1. The transfer function for the CO₂ plant is:

$$A(s) = \frac{k_c}{s} Q_c(s) \quad (5.19)$$

where A is the CO₂ absorbance measured by the FTIR and k_c is the linear coefficient for the rate of change of CO₂ concentration; which was $k_c = 0.00171$.

A comparison between this ideal plant model to the results previously gathered for the CO₂

characterisations are shown in figure 5.21, specifically the the case with the flow rate $Q_c = 0.5$ sccm. At a glance, it is very obvious that the real world data and the model do not match. However, it appears that bulk of this error between two graphs occurs during the initial phase of the CO₂ concentration increasing. Then after some time the error plateaus, as the two graphs rise in parallel.

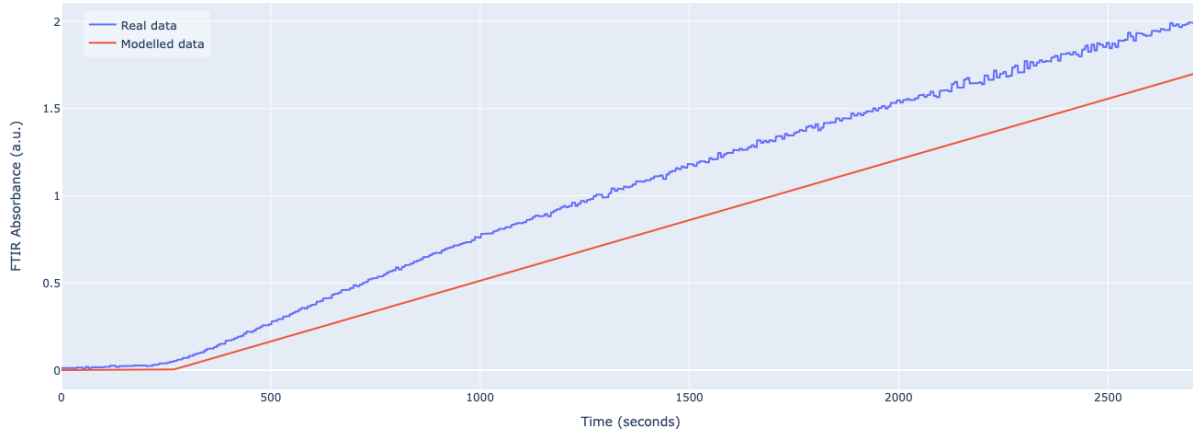


Figure 5.21: Comparison between the (real) measured characterisation data and modelled data for the flow rate $Q_c = 0.5$ sccm.

This behaviour is confirmed for all flow rates by taking the difference between the real and modelled data, shown in figure 5.22. There could potentially be several reasons for this error in the initial phase, though the most likely reason is probably due to the mixing of the inert gases and CO₂. This explains why after a period of time this error plateaus as the gas mixture is fully homogenous.

The other difference in behaviour seen in figure 5.22 is that for the flow rates of 0.9 and 1.0 sccm, there are two plateaus; which implies that there is a separate mechanism occurring here. Indeed, if one refers back to figure 5.15, there appears to be a slight plateau before the FTIR signal continues to increase again. The most likely explanation here is that at higher flow rates, the CO₂ concentration is saturated since there was not sufficient time for the CO₂ gas to complete the closed loop yet and begin accumulating in the system. To confirm this behaviour, additional tests were done with flow rates of 2.0 and 3.0 sccm of CO₂ gas, shown in figure 5.23. From the figure, the plateaus are even more prominent, confirming the hypothesis for this

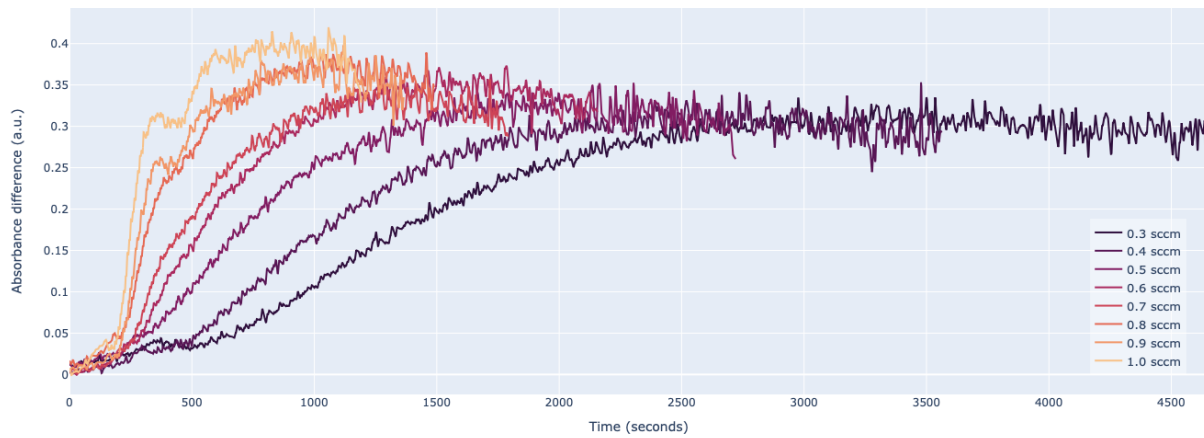


Figure 5.22: Difference between real and modelled data for all flow rates tested.

behaviour.

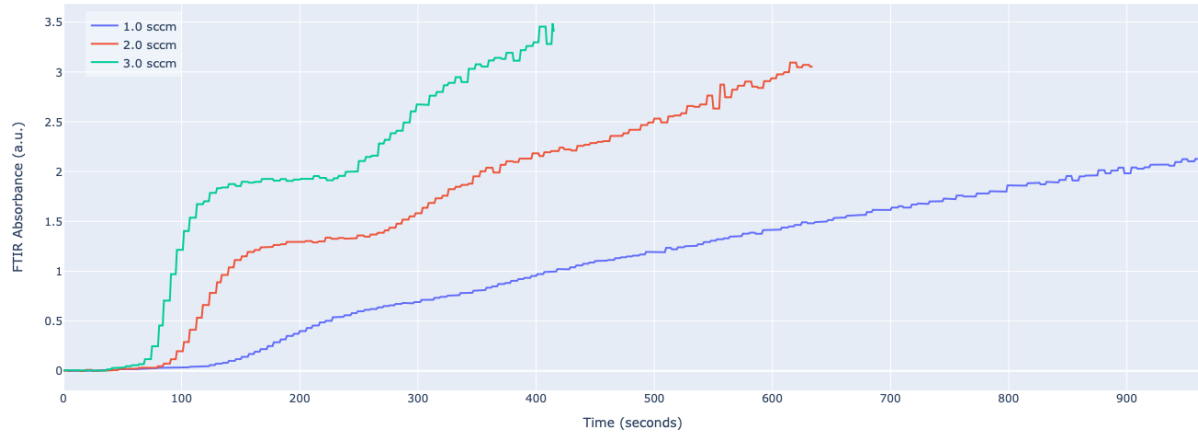


Figure 5.23: Time series response of system (without a CO₂ controller) for larger flow rates.

Nevertheless, even though the model generated does not exactly match the real data, it is sufficient to understand the basic mechanics of the control system and give the author an idea of the type of controller to be used. As such, proportional only controller was chosen. This is because of the large lag time of the system would mean that if a PI controller were to be used, a large integration error would be present which would cause a large but temporary overshoot of the setpoint CO₂ concentration. This was not an issue with the Helium gas only controller since there was effectively no lag in the system, meaning there was minimal overshoot thus

no effect on the plasma. However, a large overshoot in the CO₂ composition of the plasma would result in an increase in the deposition of carbon on the SRR gap itself. This would either extinguish the plasma, or worse block the orifices for the gas to flow through.

A proportional only controller would eliminate this issue, though this comes at the cost of time performance and potentially an offset error. The former is an inconvenience, but seeing as the system is a proof of concept, it is not necessarily a deal-breaker. The offset error would be more of an issue, but this again depends on the severity of the error. The only way to determine this was run the model and evaluate how it performed.

For the proportional controller, a unity gain was set. Setting the gain higher would in theory improve the time taken for the system to reach steady state. However as stated earlier, with the higher flow rates, there is not a sufficient amount of time for the CO₂ gas to complete the closed loop. This could lead to overshoots if the CO₂ concentrations were set to lower values. With this, a comparison of the modelled performance and the real-world performance of this controller was done. The controller was instructed to reach a FTIR absorbance set point of 0.3, which is approximately equivalent to a 1% CO₂ gas mixture.

Figure 5.24 shows the results of this comparison. From the data, it can be seen that the modelled performance quite closely matched the measured results. The measured lag time in this test appears to be slightly shorter, but is still in line with the results seen in table 5.3.

As for the rise of the FTIR absorbance, the real world results seems to indicate a slower rise compared to the model. Though this is explained by the fact that at flow rates below 0.3 sccm, the mass flow controller struggles to continuously output a fixed flow rate, instead relying on PWM. This is more evident when measuring the settling time. In the previous section on the pressure controller, the settling time was measured in terms of 0.1% of the set point. However, due to the relatively small values of the FTIR absorbance, the settling time taken was to 5% of the set point (in this case, an absorbance of 0.29).

The settling time for model was approximately 2300 seconds (\approx 38 minutes) whereas the settling time for the real world controller was around 2800 seconds (\approx 46 minutes). These are relatively

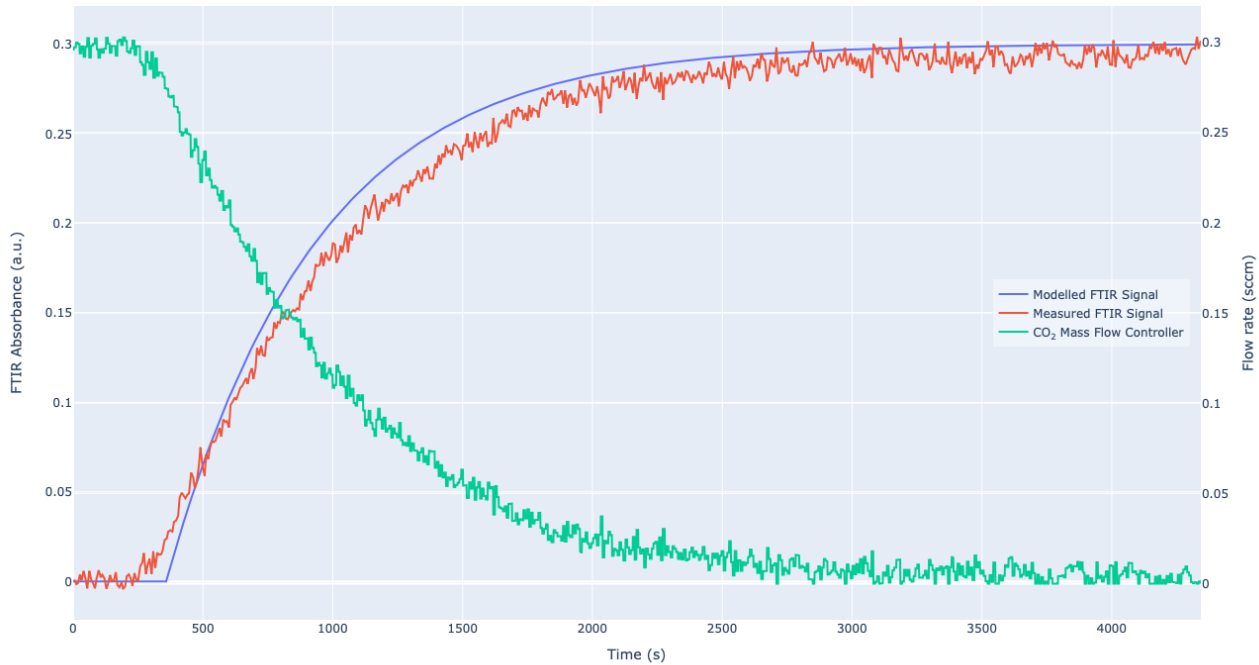


Figure 5.24: Comparison between the modelled and real proportional controllers for regulating CO₂ concentrations.

large wait times, especially when compared to the pressure controller results. However, since the system is designed to intended to be run continuously for several hours at a time, such wait times the start of the process were deemed to be acceptable.

5.2.2 Carbon monoxide concentrations

With the CO₂ controller functioning with the presence of the plasma, an interesting observation can be seen in the FTIR spectra. In addition to the CO₂ peaks (and the peaks due to presence of water vapour), there are strong peaks of CO present in the system. This was also observed in the open gas loop configuration with the FTIR placed after the plasma, but this signal was quite weak due to the fact that only a small amount of CO as formed and all the gas was vented to atmosphere. With the closed gas loop configuration, since the gas is recycled, its concentration can build up resulting in more visible peaks.

For the purposes of this report, the CO concentration will not be quantified simply because

of the lack of access to pure CO to produce a calibration curve (like that performed on CO₂). However, this system could be easily adapted to control the concentration CO instead of CO₂ if needed. Nevertheless, the accumulation of CO in the system adds further proof that the CO₂ is being dissociated, meaning that the epoxidation process will occur.

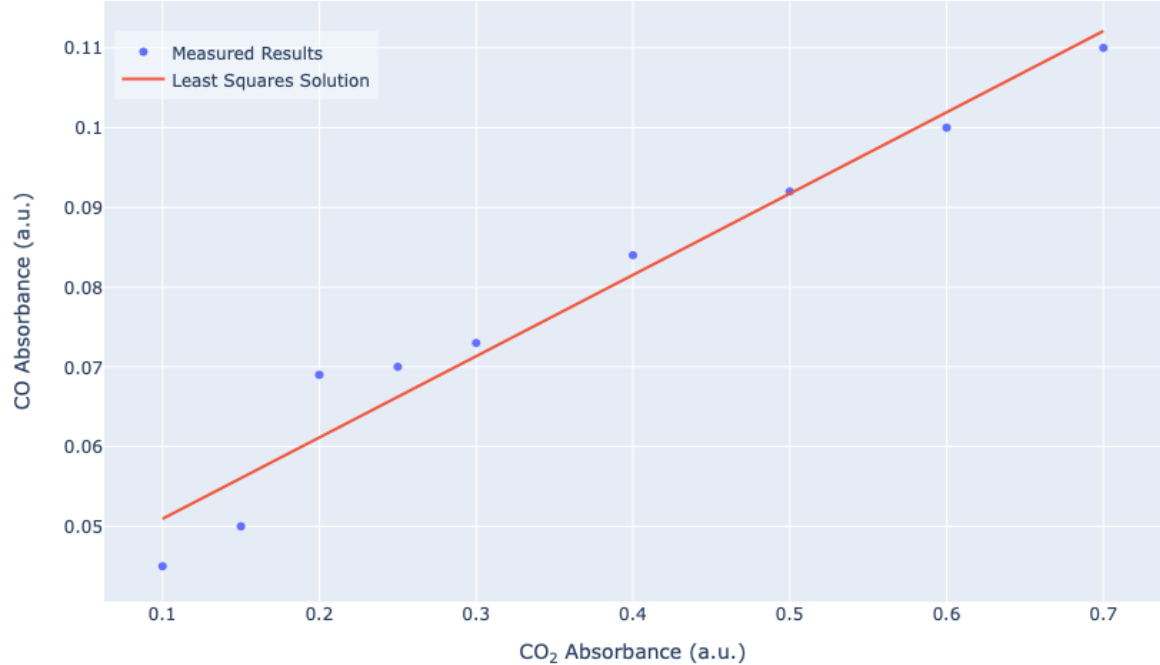


Figure 5.25: Comparison CO₂ and CO absorption in the FTIR spectra.

One observation seen with the CO results in the FTIR is that the absorption peaks settle to fixed value after a period of time. This is to be expected since the CO₂ dissociation reaction is reversible, thus it should settle into a steady state after some time. Since every molecule of CO₂ should produce one molecule of CO, one should expect a linear relationship between the absorption of both these molecules.

To assess this, the CO₂ controller was used to set CO₂ concentration set points between 0.5% to 3%, and the steady state CO absorptions were measured. The results of this test can be seen in figure 5.25.

From the results, a linear relationship was observed though the relationship was not propor-

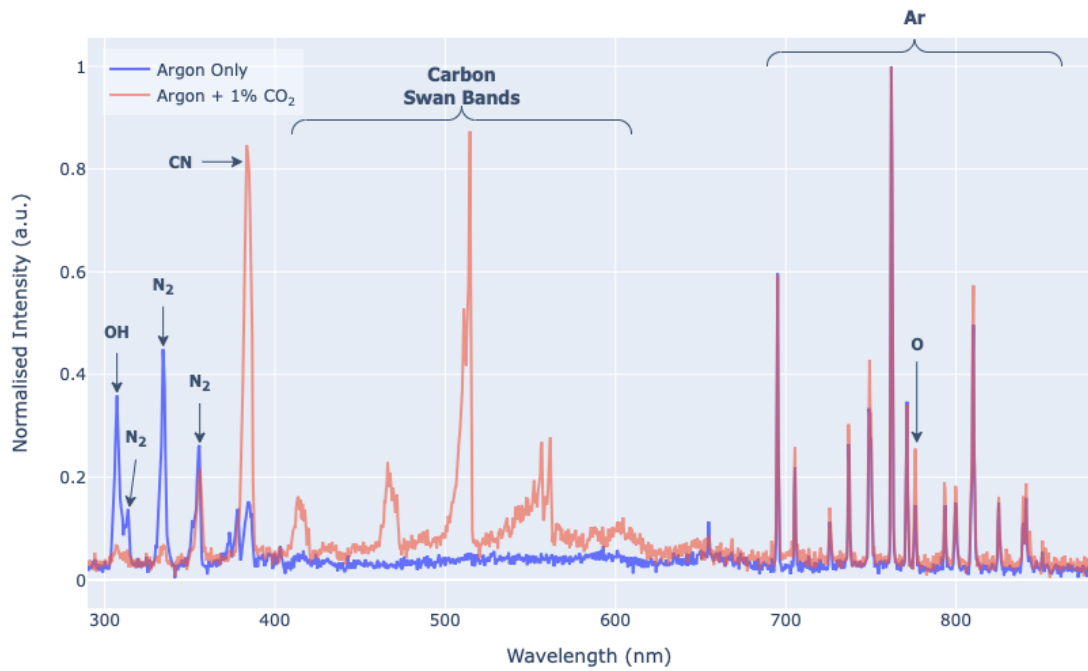


Figure 5.26: Optical spectra between pure Argon plasma and Argon plasma with CO₂.

tional. This is most likely due to the fact that the system does contain some nitrogen gas impurities, which could be reacting with the atomic oxygen producing nitrogen oxides (NO and NO₂), or reacting with the carbon to produce cyanide (CN). Additionally, the carbon deposition on the SRR may play a role in the losses. In the optical spectra, the nitrogen oxides peaks are not particularly visible because they tend to be quite broad. However, the CN peak is strongly visible and also the carbon peaks from the Swan bands. This can be seen in figure 5.26. (Note that test was done using an Argon plasma instead of a Helium plasma, but the results should be the same.)

5.3 Overall Control System performance

With the two parts of the control system functioning as expected when compared to the Simulink models, the next step was to evaluate the long-term performance of the system. This is because the goal is to run this experimental setup for hours at a time, and potentially

even days. While there weren't any issues in the short-term tests when correlating with the models, there could potentially be issues when running for longer periods of time. As such, the control system was left to run over the period of 24 hours. The result of this can be seen in figure 5.27.

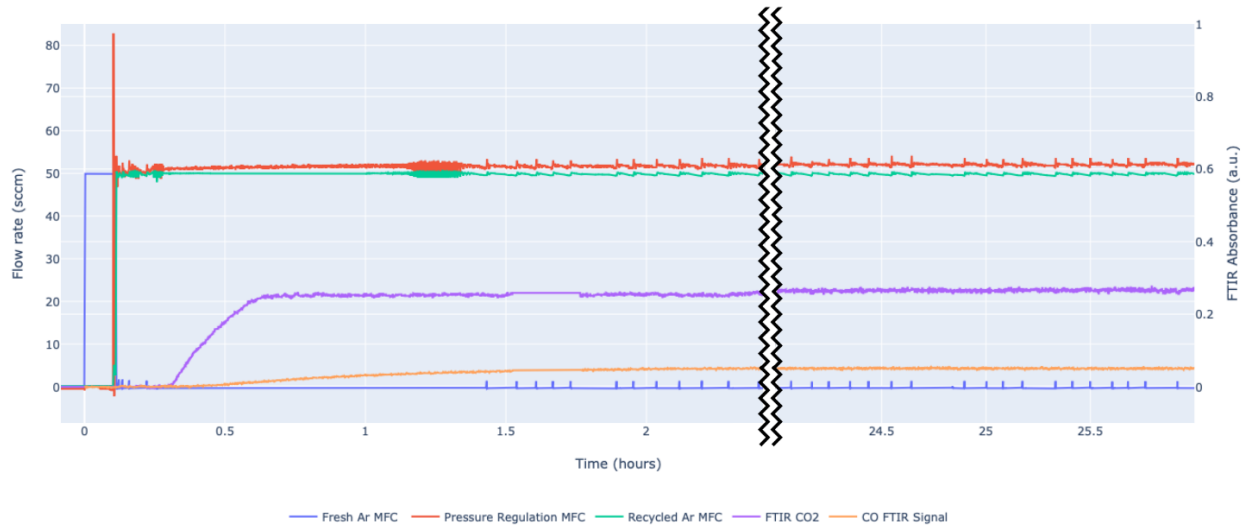


Figure 5.27: Time series plot of the mass flow controller and FTIR traces of the control system operating over a 24 hours.

The test used the typical set points for the control system, which were a main chamber pressure of 760 Torr, a secondary chamber pressure of 910 Torr, and a CO₂ gas concentration of 1%. While figure 5.27 does not show the time series traces from both pressure sensors, both values were kept relatively constant once the system was in steady state. Additionally, figure 5.27 does not show the mass flow controller response of MFC₄ (for the CO₂ gas input) because the traces were not visible due to the scale of the response; the maximum mass flow reading was 0.3 sccm of CO₂ gas.

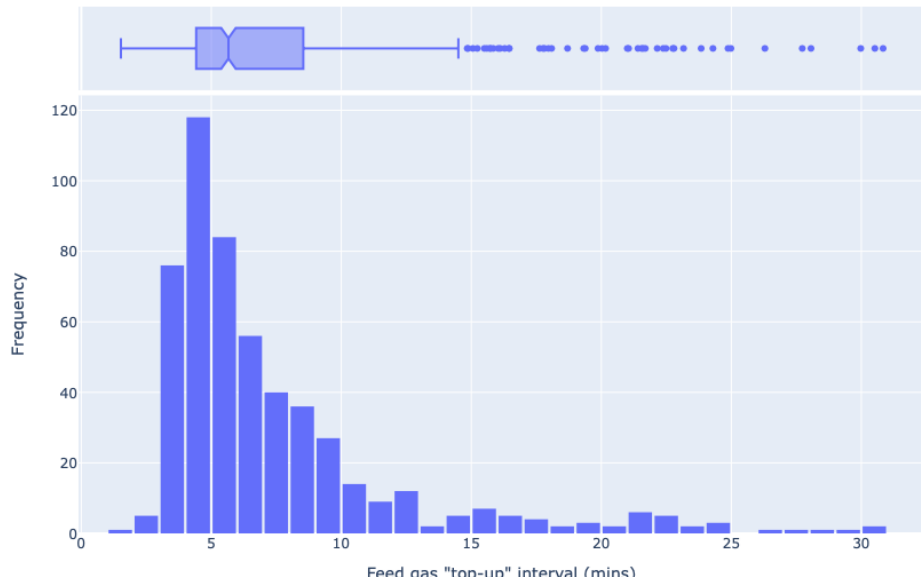
The short-term performance (i.e. the first hour) of the system was inline with previous results. Between the period of 70-80 mins, there was a slight abnormality in the in the MFC₂ and MFC₃ response whereby the signal was quite noisy; though this returned back to normal afterwards. After that, the control system began gradually “topping-up” the main chamber with some additional feed gas. There was another anomaly, this time in the FTIR signal between 90-105 minutes after starting the test, though this was because the FTIR stopped sampling data

periodically and needed to be restarted. However, since the CO₂ concentration of the system was already saturated at 1%, this did not cause any issue. Aside from that, no other issues occurred in the system.

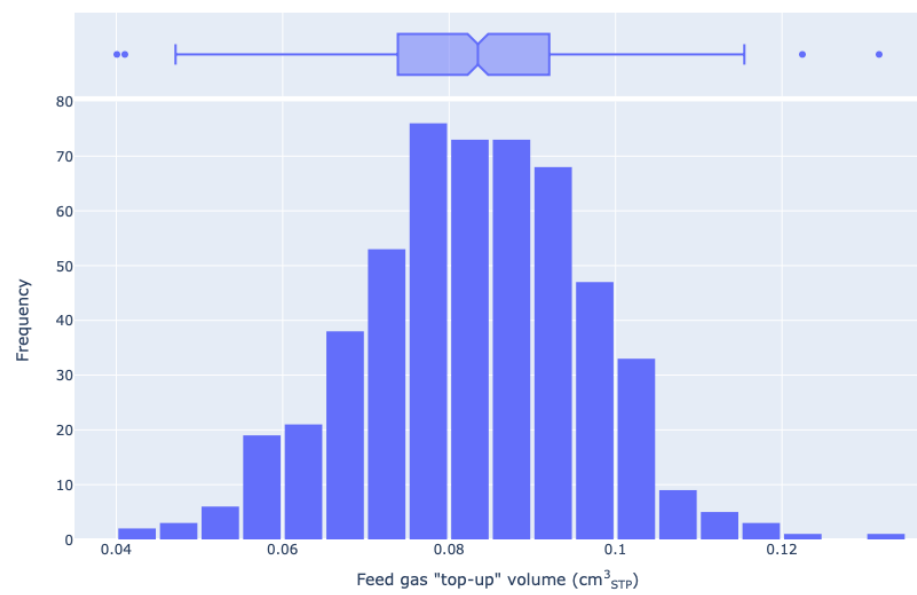
Aside from those two minor issues, the long-term tests show that the system performed satisfactorily. The noble gas usage, once the system was in steady state, was minimal. In the first 20 minutes of the system, when the system was first pressuring and left to equilibrate, the total Helium used was 335 cm³. Then over the next 24 hours, the total fresh gas inputted into the system was only 15 cm³, only 4% of the gas used to originally fill up the system. This gave an equivalent flow rate of approximately 0.01 sccm of Helium gas once in the steady state, which is a 5000 times reduction in gas usage.

In terms of characterisation of the “topping-up” mechanism, figure 5.28 shows the histogram of the “top-up” interval and volume.

The median “top-up” interval of the system was 5.6 minutes, with the mode being between 4-5 minutes and results longer than 15 minutes being outliers. While an ideal system would not require any refilling of the system, this performance is satisfactory. In terms of the “top-up” volume, this was more inline with a normal distribution with the mean (and median) volume being 0.083 cm³.



(a)



(b)

Figure 5.28: "Top-up" interval (a) and gas volume (b) of the system.

Chapter 6

Epoxidation Process

With the previous chapter, it has been shown that the recirculation of the feed-gas was possible for a gas only plasma system (henceforth referred to as the dry plasma system). While the CO₂ dissociation reaction can occur in the previous system, it cannot produce a useful product. As such this chapter will focus on modifying the dry-plasma system to utilise the atomic oxygen from the CO₂ dissociation, by reacting it with a liquid alkene to produce epoxides (henceforth referred to as the wet plasma system).

6.1 Investigation the role of solvent

As stated in the end of chapter 3, the reaction undertaken in this report builds on the work done by Xu et al [75]. The co-reactant used for this reaction would be trans-Stilbene, which utilises the atomic oxygen produced in the CO₂ dissociation to produce the epoxide called trans-Stilbene oxide (which are used interchangeably for the rest of this report).

One thing to note is that trans-Stilbene is a crystalline solid. Thus in the work done by Xu et al [75], it was dissolved in a solvent; specifically acetonitrile. This is a common solvent used in chemistry for organic synthesis due to its high solvent power, especially for dissolving organic compounds. Additionally, its low viscosity and high chemical stability make it very useful when it comes to gas chromatography.

While the aforementioned benefits make it ideal for facilitating the epoxidation process, there are several drawbacks to using it. The most significant drawback is that due to its high solvent power, it tends to attack most plastics, rubbers, and even some types of coatings. The reason this is a problem is that many of the components used for designing the dry plasma system, which include the mass flow controllers and pressure sensors, all use seals that are made from FKM (a fluorocarbon-based synthetic rubber). As such, if those seals are exposed acetonitrile for a prolonged period, it would cause softening and/or swelling of those seals, leading to a potential failure of the part. This tends to be less of an issue in an open gas loop configuration, where most of the gases are vented into atmosphere. However, this issue is particularly significant in a closed gas loop system, where the gases are recycled and any acetonitrile that evaporated into the gas phase would accumulate over time as the system was run.

Another downside with using acetonitrile as the solvent is that is typically classed as a non-green solvent. “Green” solvents is a loose term to describe solvents that minimise the impact on the environment. As such, green solvents are typically expressed on a spectrum as all solvents typically have some impact on the environment throughout its life cycle, and also have potential hazards in the early stages of producing the chemical compounds. The conventional example of a green solvent commonly used in industry is ethanol.

A useful illustration of this concept can be seen in figure 6.1, which shows the environmental assessment of several of the most popular solvents used. This work, done by Capello et al [91], compares the environmental, health, and safety (EHS) score of the solvents (which are assessed on a points basis, where a lower score indicates a safer solvent) against the life-cycle assessment (LCA) score of the solvents (which evaluates the cumulative energy demand for producing a solvent and recycling or incinerating it once used, where a lower score indicates a more energy efficient solvent). As seen in the figure, acetonitrile is one of the worse solvents evaluated.

The relevance of this concept of green solvents is that one of the aims of this research is to assess the feasibility of scaling up this epoxidation process to industry. As such it would be prudent to first investigate the role of the solvent in producing the epoxide, as the feasibility of using a

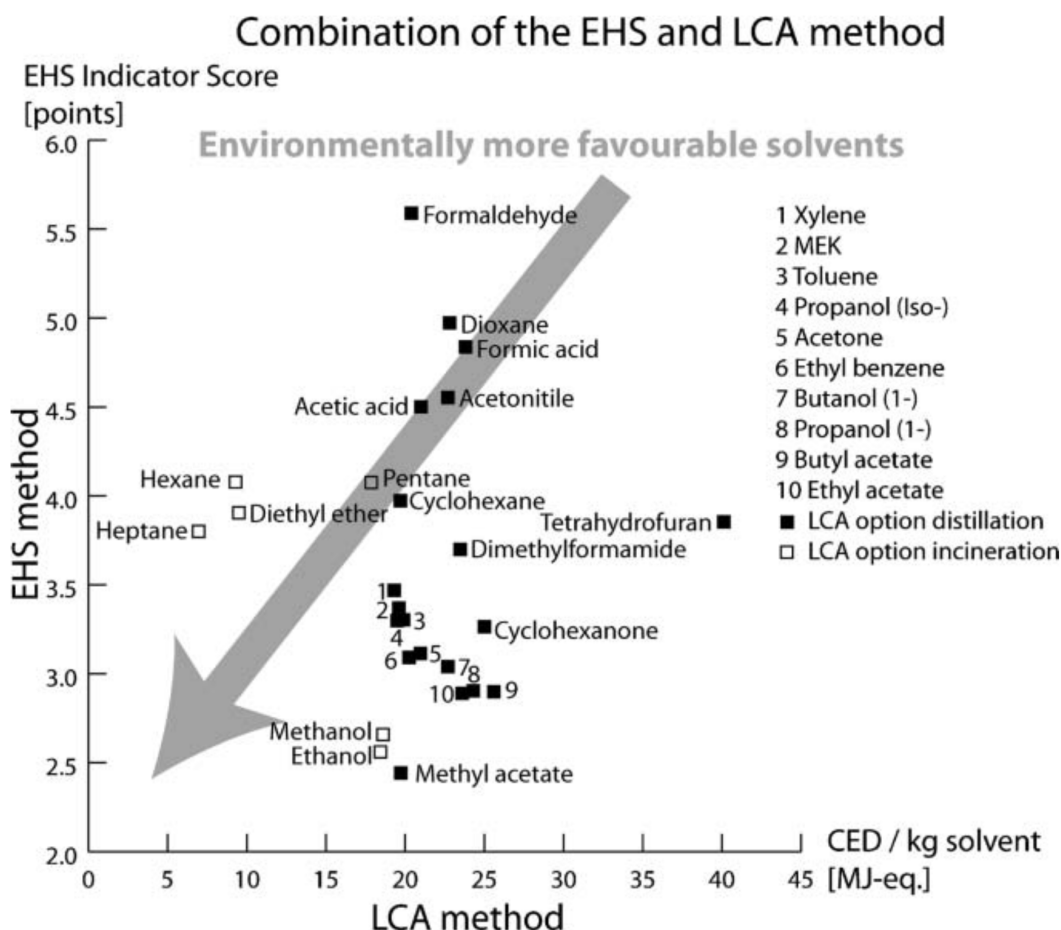


Figure 6.1: Environmental assessment of 26 of the most common organic solvents used done by Capello et al [90].

greener solvent would make a more compelling case for scaling up the process.

For this evaluation, a much smaller set of solvents were tested, simply due to availability of the solvents in the laboratory. In addition to acetonitrile, these include ethanol, iso-propanol, and acetone. The important point to note here is that all the chosen solvents were classed as “greener” than acetonitrile in the assessment criteria developed by Capello et al [91].

To evaluate this, the plasma was generated using COST jet. The reason for reverting to the COST jet over the SRR jet for this experiment was to simply eliminate potential variables. Since the COST jet had been previously used for the epoxidation reaction, this would give a good reference for comparing the solvents used. Additionally, the COST jet could be used a basis to design the reactor for the wet plasma system.

As for the experimental setup, a 1% CO₂+He gas mixture was used. The COST jet was set to

operate at approximately 10 W, which was the minimum power that would sustain the plasma with the chosen gas mixture. The nozzle of the jet was placed approximately 5-10 mm above the surface of the treated liquid. As for the treated liquid, it was a 10 mM solution of trans-Stilbene in the tested solvent, with 10 mL of solvent used. The treated liquid was placed in an ice bath, to keep the temperature at approximately 0 C. The liquid was then treated for a span of 2 hours. These experimental conditions were chosen to mimic the ones done by Xu et al [75] as close as possible.

With these experiments run, four samples were produced. To evaluate the composition of these samples, the method chosen was the gas chromatography–mass spectrometry (GC-MS). As the name suggests, the method combines the techniques of gas chromatography and mass spectrometry to separate different compounds in a sample and identify them.

The first stage of a GC-MS test is the gas chromatography portion, where the injected compounds are vaporised. The vaporised compounds are then moved through the device the aid of a carrier gas, which is typically an inert gas such as helium though other non-reactive gases such of nitrogen can also be used. Regardless of the gas chosen, it carries the vaporised sample through a column. The column is essentially a narrow tube with an inner coating that is called the stationary phase. The substances in the sample interact with the stationary phase differently based on their chemical and physical properties, as such will travel through and exit the column at different rates.

The substances exiting the column (which would typically be a single compound assuming that the procedure for the GC-MS was set up correctly) then enters the mass spectrometer. Once they enter the mass spectrometer, they first gets ionised to give them a charge. These newly formed ions then get accelerated to the same velocity before being deflected by a magnetic field. The amount of deflection of the ions depends on two factors: their mass and charge. The lighter the mass of the ion, the greater the deflection. Similarly, the larger the charge of the ion, the more they deflect. Ions with the same mass-to-charge ration would experience the same deflection, which are then measured by the detector. An illustration of the gas chromatogram and mass spectrometer schematics are shown in figure 6.2 and 6.3 respectively.

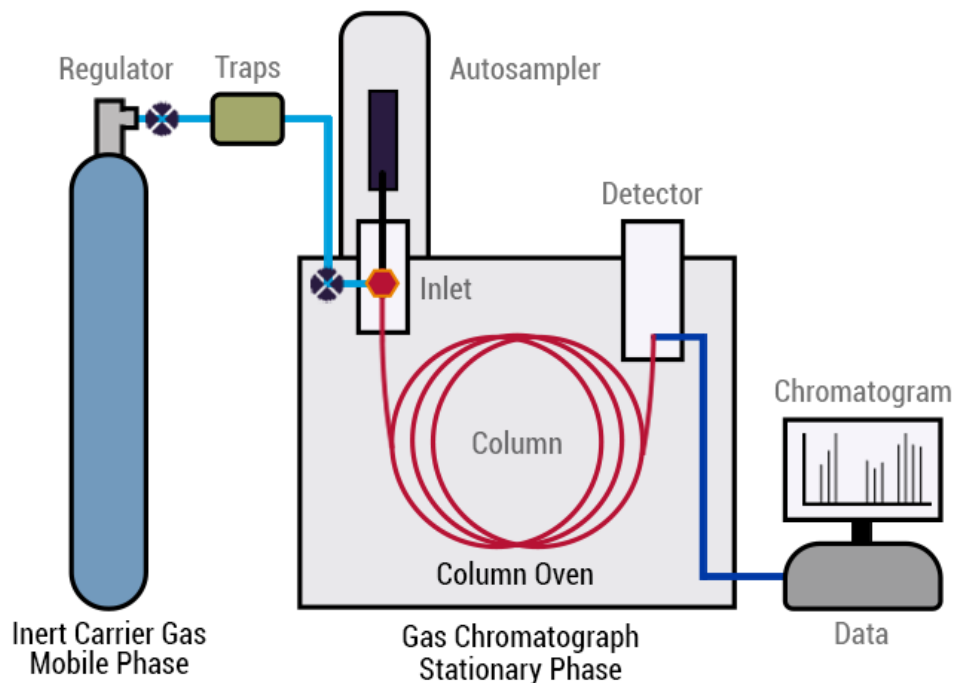


Figure 6.2: A schematic diagram of the gas chromatography method [92].

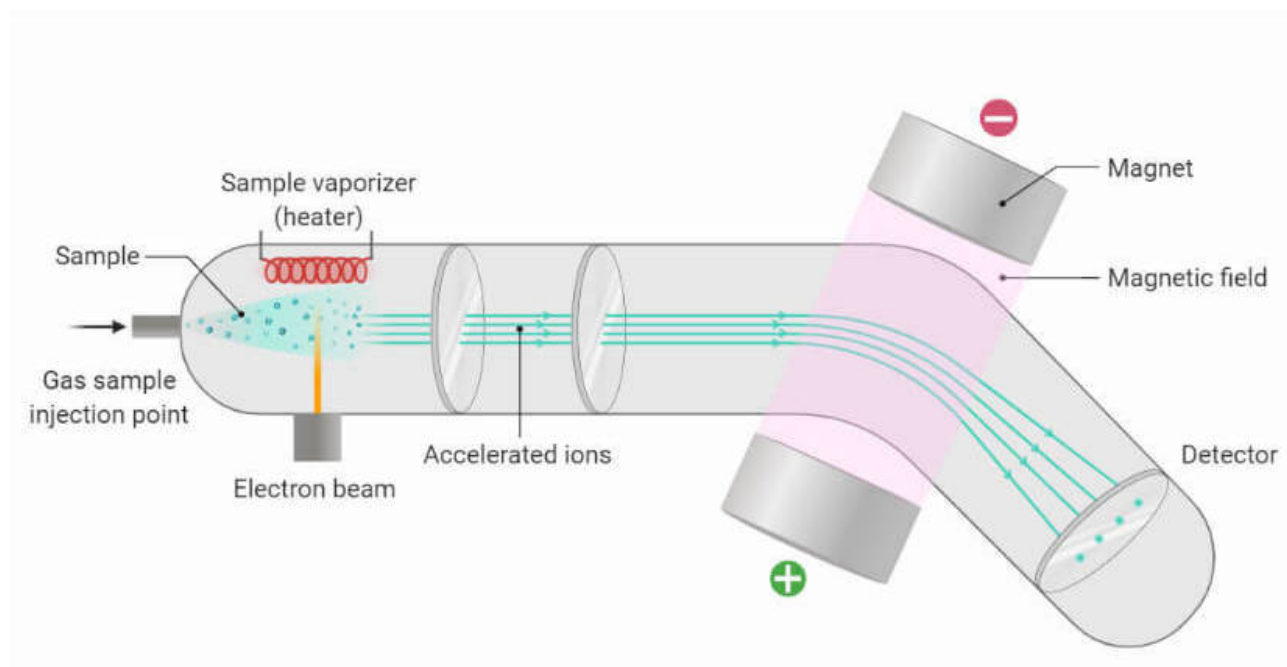


Figure 6.3: A schematic diagram of the mass spectrometry method [93].

The GC-MS used was the Shimadzu GCMS-QP2010 Ultra. It was equipped with a [insert name here] capillary column ($30\text{ m} \times 0.25\text{ mm} \times 0.25\text{ }\mu\text{m}$). The samples were injected into the GC-MS with a configured split ratio of 10:1, and an injected volume of $1\text{ }\mu\text{L}$. A

helium carrier gas used was fed in at a constant flow rate of 65 mL/min. As for the procedure used, the column was at 50 °C for 5 minutes, then increased to 300 °C at a rate of 20 °C/min and finally held there for 5 additional minutes. Thus, the total run time per sample was 23 minutes.

The results of these solvent comparisons are shown in figures 6.4. From the data it was clear that the best performing solvent was in fact acetonitrile, followed by acetone. The possible reason for this is that the vapour pressure for acetone was approximately 3 times larger than that of acetonitrile, meaning that there was significantly more evaporation, which in turn meant that it was difficult to keep a consistent distance between the nozzle of the jet and the surface of the liquid. As for both the alcohols, they performed very poorly with ethanol marginally producing more trans-stilbene oxide over the iso-propanol. The reason for this is unclear, though it is most likely explanation for this behaviour is that the atomic oxygen produced would react with the alcohols, oxidising them. However, preliminary testing with a basic gas chromatography detector failed to find the by products which would be produced from this oxidative reaction. As such further research needs to be undertaken to understand this behaviour, which was unfortunately beyond the scope of this project.

Another thing to note was the large presence of benzaldehyde for the reactions with the acetonitrile solvent. Benzaldehyde is typically only formed when trans-Stilbene reacts with ozone. The source of this ozone had to have come from the surrounding air around the testing container. As such, the container was sealed off and tested again. The results shown in figure 6.5 show a significant reduction in this peak, confirming that a sealed reactor was necessary for the reaction of trans-Stilbene.

From these experiments, the unfortunate conclusion was that acetonitrile had to be used as the solvent of choice for the reactor. This meant that the experiment setup used needed to include some mechanism to remove acetonitrile that was kicked up into the gaseous phase by the SRR jet blowing on the liquid. The design of the reactor and the process of removing the acetonitrile gas are described in the next section.

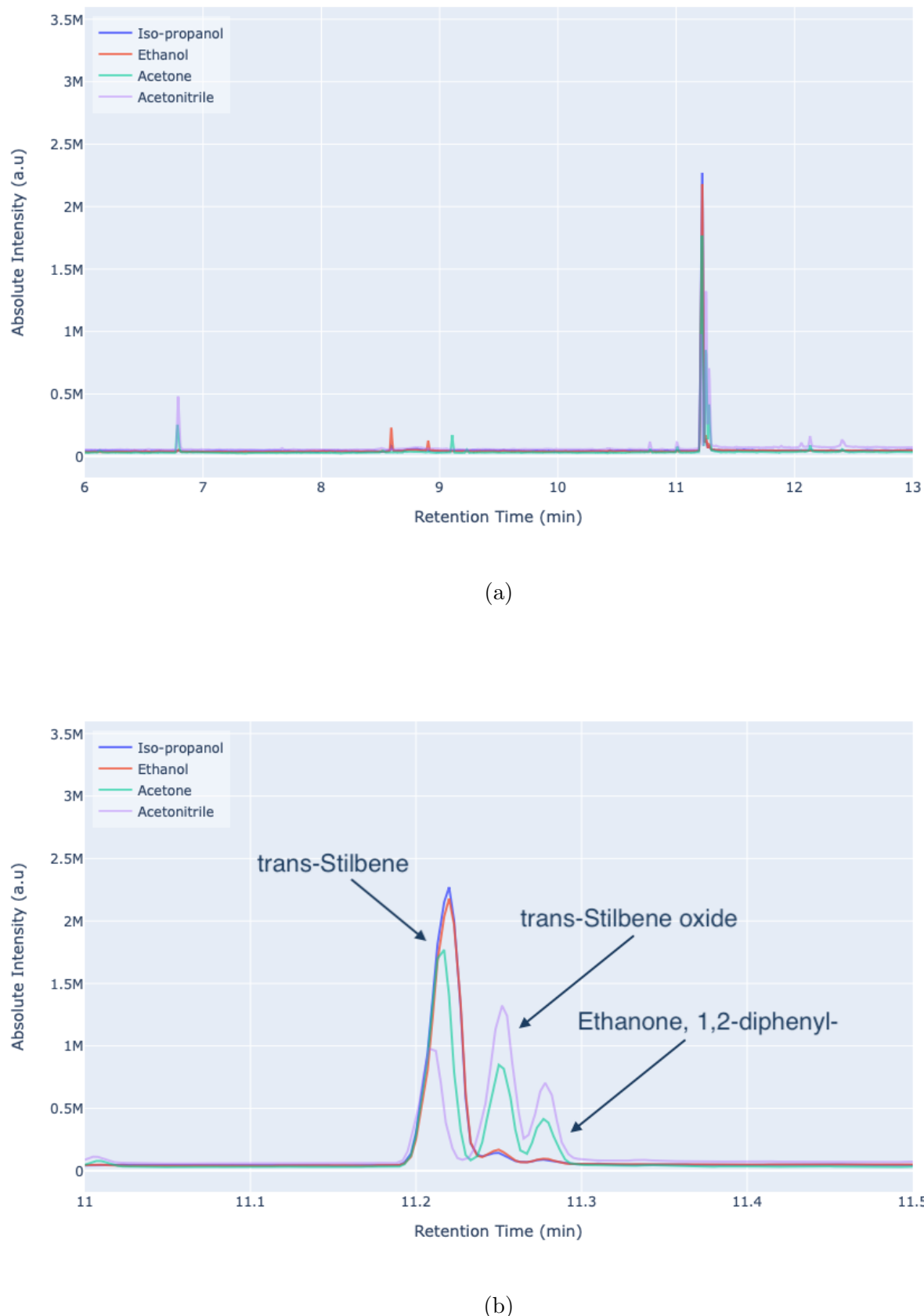
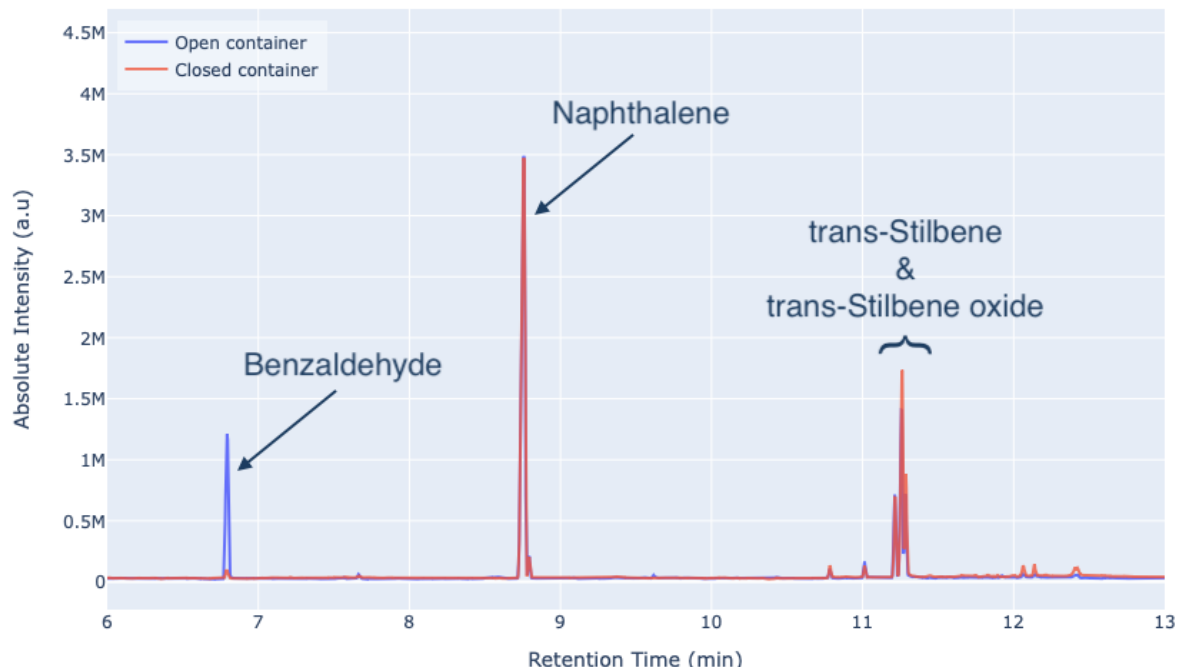
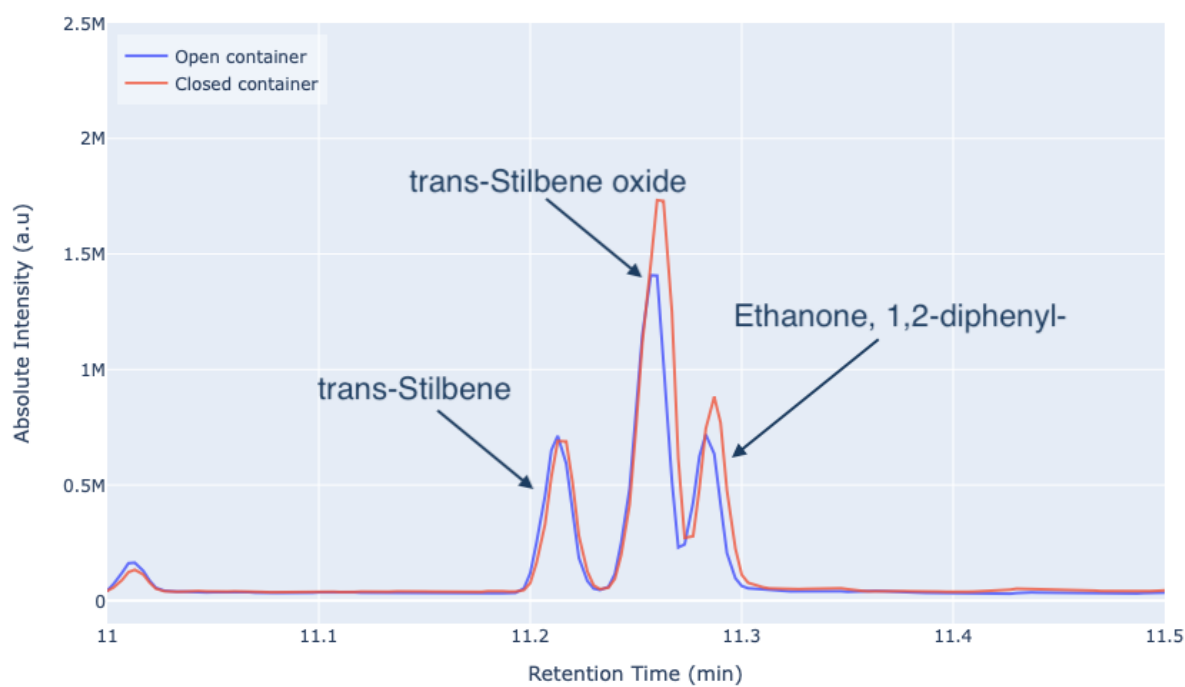


Figure 6.4: A wide (a) and close-up (b) illustration of the GC-MS results from testing the reaction of atomic oxygen with trans-Stilbene dissolved in different solvents.



(a)



(b)

Figure 6.5: A wide (a) and close-up (b) illustration of the GC-MS results from testing an open and closed container of the reaction of trans-Stilbene in acetonitrile. Note, the naphthalene peak was due to its introduction as an internal standard.

6.2 Developing the plasma reactor

6.2.1 Designing the main reactor housing

From the usage of the COST jet, several key design requirements were obtained for the design of the SRR jet reactor. These requirements and the rational for them are detailed in the list below.

- **The reactor housing needed to be completely enclosed:** The main reason for this was that the end goal of the system designed was to function in a closed gas loop configuration. Hence, an enclosed reactor housing that is as leak proof as possible would minimise the feed gas required to top up the system. Additionally, from the previous tests with the COST jet, it was determined that any air present in the system would oxidise the atmospheric oxygen into ozone, in turn reducing the overall yield of the reaction.
- **The surface of the treated liquid needed to be as close as possible to the SRR jet:** This was because the atomic oxygen produced in the decomposition by the plasma is a very short lived species, reacting with anything it comes into contact with. Thus, being able to bring the surface of the liquid as close as possible to the jet would increase the carbon dioxide efficiency of the system, and should also produce an increase in yields. This distance is a key discussion topic in this chapter, and will be henceforth referred to as the *reaction distance*.
- **The gas outlet of the reactor housing needed to be small:** This is a byproduct of the previous requirement of minimising the reaction distance. As such, the tube to allow the gas flow out of the housing needed to be kept small as well.
- **There needed to be an inlet for introducing the liquid into the reactor:** The reason for this was to do with the fact that gas blowing on the surface of the liquid increases the rate of evaporation of the solvent. This mechanism in turn increases the reaction distance over time. As such, there needed to be an inlet to allow for topping up the solvent, ensuring that reaction distance remained constant.

Armed with these requirements, several prototype reactor housings were made. From those designs, several additional findings were learnt. Firstly, the early prototypes designed included a design where the gas from the plasma was bubbled into the liquid rather than simply reacting with the surface of the liquid. The idea was to increase the mixing of liquid and potentially promoting an increase in the the rate of reaction. However, this idea was eventually scrapped because it significantly increased the rate of evaporation of the solvent, meaning that it was more difficult to keep the reaction distance constant. Additionally, the splashing generated would mean that liquid would escape from the reactor and into the gas outlet of the reactor, which would not be easily recoverable at the end of the experiment.

Another learning from the prototypes was with regards to the reservoir of the reactor housing. One of the prototypes made consisted of a multi reservoir design, where the main reactor would contain a small liquid reservoir, while a larger reservoir was kept separate and connected using some tubing and a peristaltic pump. The reasoning for this was that larger volumes of liquid trans-Stilbene could be used, which was inline with how large scale industrial chemical reactions occur. While this idea did work, it was somewhat inconsistent mainly due to the fact that maintaining a constant reaction distance proved challenging with only the use of a single peristaltic pump. This was because the tubing of the inlet and outlet from the larger to the smaller reservoir stretch slightly differently in the pump, meaning that there was very small but noticeable difference in the liquid flow rates. This in turn meant that the liquid volume in the smaller reservoir (within the reactor) would either increase or decrease due to this flow discrepancy. While this is a solvable problem, either with the use of an additional peristaltic pump or a liquid level sensor and some PID controllers, it was decided that this was scope for a future research project and hence was removed.

With those additional findings, the final reactor schematic and build are shown in figure 6.6. The reactor housing is comprised of 4 different parts. The main housing containing the liquid was simply a repurposed glass sample bottle. This was then connected to a short piece of stainless pipe, functioning as a coupler between the glass and the base of the SRR ground plane. The stainless steel coupler also contained two holes to allow for the inlet and outlet glass tubing. The inlet tube was bent 90 degrees and extended to the bottom of the glass sample

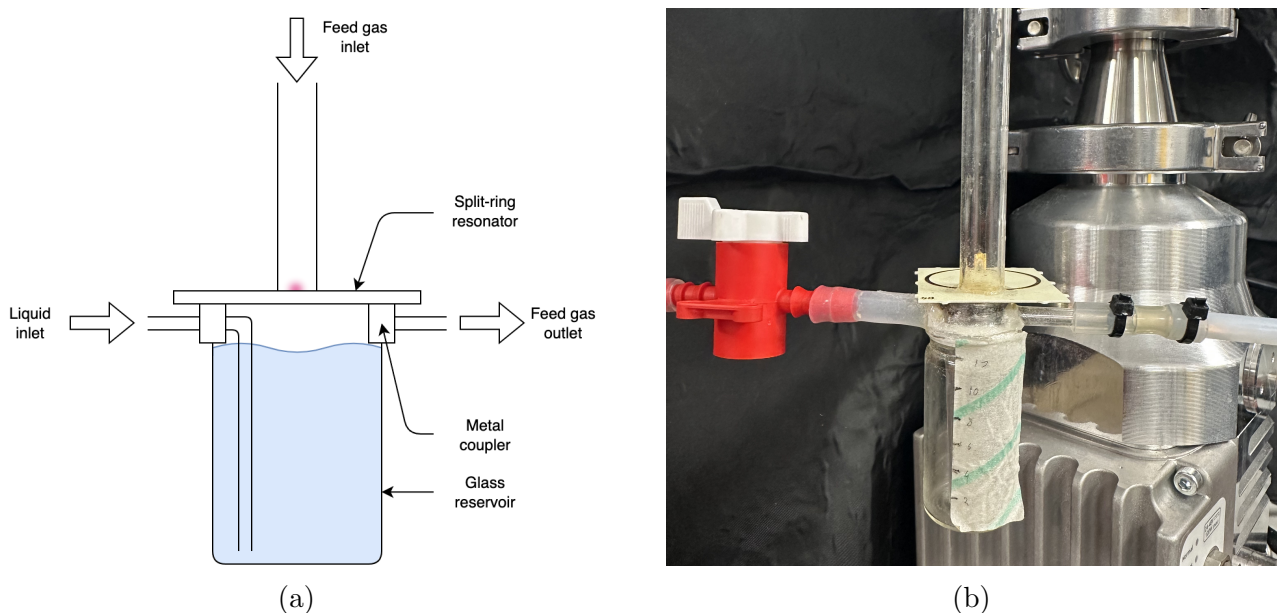


Figure 6.6: An illustration of the schematic design (a) and finished SRR jet reactor build (b).

bottle, while the outlet tube was simply placed at the top of the stainless steel coupler. All the components were then bonded together with the use of Torr Seal® epoxy, which is a two part epoxy designed for low pressure applications. Then the finished reactor housing was attached to the SRR ground plane using superglue. The reason for this was that the epoxy would not attach to the gold plated coating on the ground plane SRR PCB.

Due to the use of acetonitrile as a solvent, there were only three realistic options for designing the housing. These include some form of metal (preferably stainless steel due to its corrosion resistance in the presence of oxygen), a plastic that has a high chemical resistance to acetonitrile (such as PTFE), or glass. Each of these options had their respective benefits and drawbacks. Stainless steel would provide excellent thermal dissipation in order to cool the reactor housing, and would be easy to machine; however it is opaque so observing the reaction distance would not be possible, and stainless steel is quite heavy meaning that the reactor would need additional support. PTFE would also easily machinable and could be made translucent, allowing for the viewing of the reaction distance; but is an insulator and due to its chemical resistance, difficult to bond with other components. Glass is transparent, allowing for easy observations of the reaction distance, and has a thermal conductivity in between stainless steel and PTFE; though it had the disadvantage of being relatively difficult to machine. As such, a compromise was

stuck to use a combination of glass and stainless steel, minimising the shortcomings of each material on their own.

The glass tubing used was the smallest tubing available in the laboratory, with an outer diameter of 4.3 mm. However, in order to make drill holes for the glass tubing through the stainless steel coupler, it needed to be slightly wider than the outer diameter of the tubing. As such, the coupler was designed to be 8mm thick, which would be the theoretical minimum reaction distance. In practice, this distance was slightly longer at approximately 10 mm, due to the tapering walls present the glass bottle. As such, the maximum volume of the reactor was around 12 mL of liquid.

6.2.2 Removing the acetonitrile vapours

As stated earlier in this chapter, the gas blowing from the SRR jet onto the surface of the liquid would increase the rate of evaporation of the acetonitrile solvent. This effect could be minimised by either reducing the flow rate of the SRR jet or decreasing the temperature of the liquid, but neither approach would completely eliminated this phenomenon. The evaporation causes the presence of acetonitrile vapour in the system, which as mentioned previously would have a detrimental effects on various components within the system. As such it was vital to attempt to eliminate as much acetonitrile vapours as possible. In chemistry, this is typically achieved using a condenser to cool the acetonitrile in the gas phase back to a liquid. The general principle of a condenser is the cooling liquid surrounding the condenser has to have a lower temperature than the boiling point of the substance being condensed.

However, the use of a traditional condenser in this application would not be particularly feasible. This was primarily due to the constant circulation of the gas within the system, meaning that the duration the gas spends in the condenser was governed by the flow rate of the gas. Thus depending on the flow rate used, there would be an insufficient amount of time for most of the acetonitrile to condense back into its liquid form. This could be solved in one of two ways. Firstly, one could increasing the duration the gas spends in the condenser by either using a very long condenser tube, a similar concept to the condenser coils on refrigerator; or by increasing

the number of condenser tubes in parallel, a method used in surface condensers typically found in power stations to cool exhaust gases from the turbine. The issue with either of these methods was that they would increase the volume of gas in system. Specifically, it would increase the volume of gas within the main reaction chamber which is kept at atmospheric pressure by the PI controller. The reason this is a problem is that it would increase the lag time of the system, thus the PI controller used would not work to maintain the pressure of the main chamber.

The other solution for the condenser would be to cool the gas as fast as possible, resulting in as much acetonitrile to be drawn out of the gaseous state. The benefit of this method is that the condenser does not have to be particularly large, thus the controller designed in the previous chapter would sufficiently work. However this was where the first issue lied, as acetonitrile has a melting point of -45 °C. This meant that a traditional lab condenser would not work as those rely on circulating water through an ice bath, keeping the condenser at just above 0 °C. The obvious next step was to then use an alternative condenser design, and the one chosen was called the direct-contact condenser. This design directly mixes the gas with the cooling liquid, forcing the gaseous acetonitrile to give up its latent heat and condense with the cooling liquid. Nonetheless, the challenge would be keeping the cooling liquid to -45 °C. The two options for this would be to either changing the pressure of the condenser, thus altering the melting point of acetonitrile; or use solid acetonitrile to cool the cooling liquid. However, the changing the pressure of the condenser was not viable since the reactor has to be at atmospheric pressure, and using large amounts acetonitrile being cooled to its solid state would be quite expensive.

Instead the solution was to take the temperature of cooling liquid beyond the melting point of acetonitrile. This would be much easier achieved by simply using ethanol as the cooling liquid (which has a melting point of -114 °C). The ethanol could be kept cool using some dry ice placed externally to the condenser. The resulting approach would keep the cooling liquid at around -60 to -70 °C. As such, this lead to the direct-contact condenser design used, shown in figure 6.7a. The exhaust gas from the reactor would enter the condenser via a stainless steel tube, then the gas was bubbled directly through the cool ethanol, before it escaped though an outlet to the mass flow controller regulating the pressure in the main chamber.

However, this design introduced a new problem, in which the condenser would perform too well. Due to the extremely cool temperature of the cooling solution, the gaseous acetonitrile does rapidly to a liquid, but then continues to cool to become a solid. Since the gas brought into the condenser entered through the stainless steel tube, this was the first point at which the solid acetonitrile formed (along the walls of the tube). Over time this solid built up, eventually clogging the tube. This resulted in a blockage, thus no gas could enter the condenser; which in turn caused the pressure in the reactor to rise since there was no outlet for the exhaust gas.

To solve this, the tube needed to be kept as warm as possible to prevent the solid build up of acetonitrile, but cool enough that it did not interfere with the temperature of the cool ethanol of the condenser. This was achieved by adding a heating element within the inlet stainless steel tube. The heating element was made from nichrome wire, a component commonly found in hairdryers. The nichrome wire was shielded in some thin PTFE tubing to prevent any contamination of the recirculated gases or the cooling liquid. The wire was connected to an external DC power supply, and the current through the nichrome wire was set to approximately 0.5 A. This number was simply chosen via trial and error, though the exact temperature of the inlet stainless steel tube remained an unknown due to the inability to attach a thermocouple since the design of the condenser needed to be air-tight.

Additionally, a valve was added to the inlet of the condenser to allow a separation between the main reactor chamber and the condenser. This was to allow the reactor to be drawn to a vacuum in order to ignite the plasma and ensure that the gas composition in the reactor is purely Helium. The finalised condenser design can be seen in figure 6.7b.

6.2.3 Complete setup design

With the addition of the addition of the reactor and the condenser, it would be useful to have an updated visualisation of the experimental setup. This is shown in figure 6.8.

On top of the new aforementioned components, an additional mass flow controller was added (shown as MFC₅) for venting the gases into atmosphere rather than recirculation. This was

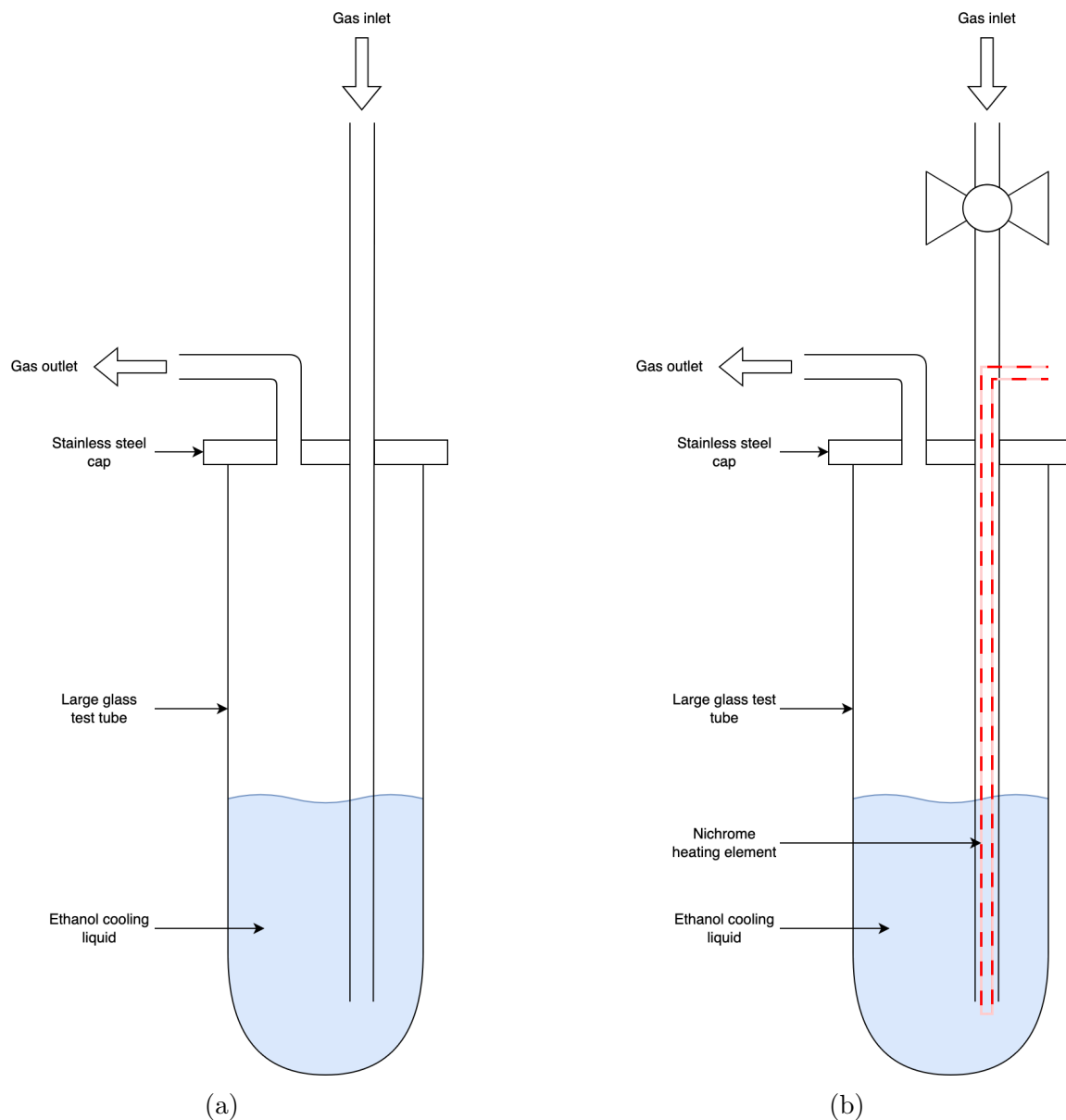


Figure 6.7: An illustration of the schematic design of the direct-contact condenser (a) and the finalised direct-contact condenser with a nichrome heating element (b).

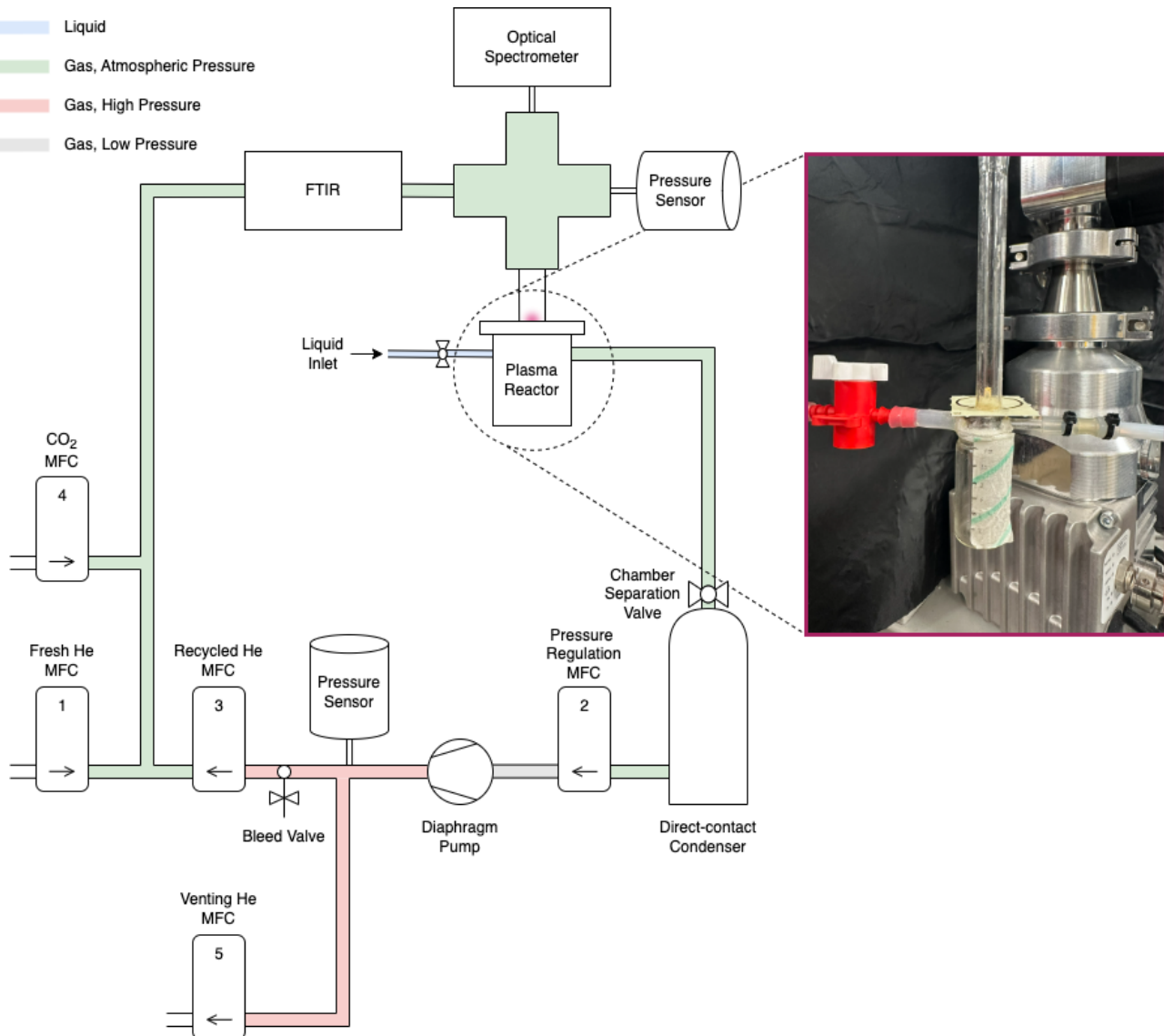


Figure 6.8: An illustration of the completed SSR jet reactor schematic used as the experimental setup.

done for two reasons. Firstly, because of the addition of the condenser, it was no longer possible to pull the entire system to a vacuum. As such, in order to ensure a pure gas composition in the overall system, it is necessary to perform an initial flushing process. The second reason was for a matter of convenience, as most of the characterisation of the SRR jet reactor (seen in the next section) was done in an open loop gas configuration; thus, this allows the system to be run in both an open and closed gas loop configuration. The details for the control mechanism for this additional mass flow control are not necessarily pertinent in this chapter, however it essentially toggles between the venting mass flow controller (MFC₅) or the recirculation mass flow controller (MFC₃) based on an open gas loop or closed gas loop configuration respectively.

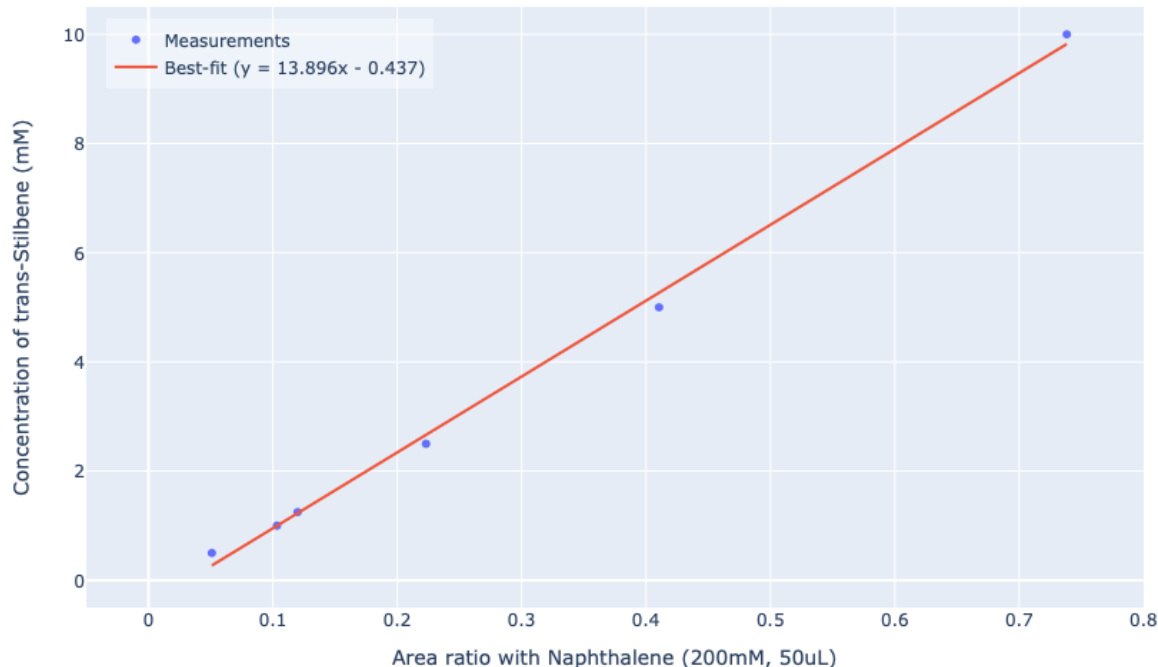
6.3 Characterising the plasma reactor

With the plasma reactor designed, and the full system operational, the next steps were to characterise the reactor to evaluate the best conditions to run it in. This would be done by changing a parameter at a time, then running the plasma over the trans-Stilbene solution a two hour period of time, and finally running the product through a GC-MS for quantification.

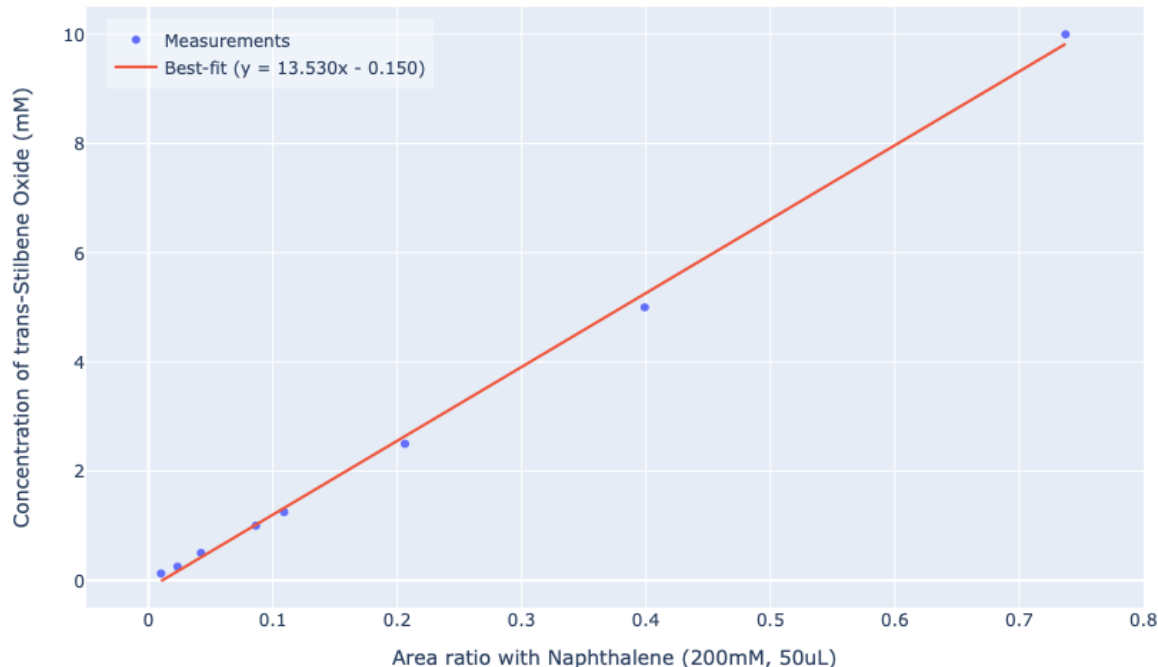
However, in order to obtain quantitative results from the GC-MS, one needs a calibration curve for the starting material (in this case trans-Stilbene) and the final product (which is the trans-Stilbene oxide). To run this, several 0.5 mL solutions of trans-Stilbene and trans-Stilbene oxide were made, each with a different concentration. Then an internal standard was added, which in this case was 50 μ L of Naphthalene with a concentration of 200 mM. The concentrations of trans-Stilbene run were: 10mM, 5 mM, 2.5 mM, 1.25 mM, 1 mM, and 0.5 mM. As for the trans-Stilbene oxide, two additional runs were done so the concentrations were: 10mM, 5 mM, 2.5 mM, 1.25 mM, 1 mM, 0.5 mM, 0.25 mM, and 0.125 mM. The reason for this was because amount of epoxide produced was going to be much smaller than the amount of starting material used.

With these samples run in the GC-MS, the area under the desired peaks were integrated. For the internal standard, the peak was located after 8.75 minutes, with the trans-Stilbene peak located at 11.21 minutes and the trans-Stilbene oxide located at 11.25 minutes. For the calibration curve, the ratio of the reference material (either trans-Stilbene or trans-Stilbene oxide) to the internal standard was taken. These are shown in figures 6.9a and figure 6.9b for trans-Stilbene and trans-Stilbene oxide respectively.

In addition to the calculated ratios, an equation for a regression line was determined based on the provided points. These equations are shown in the figures. Both regression lines fitted strongly to the GC-MS measurements, where the calibration curve of trans-Stilbene had a R² score of 0.997, while trans-Stilbene oxide had a R² score of 0.998. These equation of regression were used to determine the concentration of trans-Stilbene spent and trans-Stilbene oxide produced for all subsequent experiments.



(a)



(b)

Figure 6.9: The calibration curve of trans-Stilbene for molar concentrations between 10 mM to 0.5 mM (a) and trans-Stilbene epoxide for molar concentrations between 10 mM to 0.0125 mM (b).

6.3.1 Evaluating impact of flow rate and reaction distance

The first set of characterisation tests performed were in relation to the flow rate of the gas through the orifice of the SRR jet, which was arguably the most important of the tests to be performed. This is because, the speed at which the atomic oxygen strikes the trans-Stilbene solution, and the frequency of this occurrence are governed by the flow rate.

In the previous chapter, a lot of the initial characterisation of the SRR jet for the controller design of the dry plasma system were done with flow rates of up to 50 sccm. However, the the SRR jet was capable of significantly higher flow rates. As such, for these set of experiments, a range of flow rates between 100 sccm to 2000 sccm or simply 2 slm (which refers to standard litres per minutes) were tested. However there was a slight complication that occurred while running these tests. This is because, as the flow rates were increased, one could no longer continue maintaining the smallest possible reaction distance due to the strong jet essentially splashing the liquid. This splashing was an issue as it allowed the liquid to escape through the gas outlet of the reactor, meaning an irrevocable loss of the yields produced by the epoxidation process. As such, as the flow rates were increased the reaction distance also had to increase. Nonetheless, for the sake of being able to ascertain the impact of reaction distance for the given flow rate, additional runs at said flow rate were performed while varying the reaction distance.

For these runs, there were only two variables being changed were the flow rate and reaction distance, all other parameters were kept constant. These parameters included the pressure being kept at 760 Torr, the CO₂-He concentration being kept at a 1% mixture, the temperature of the liquid being kept at approximately 0 °C using an ice bath, and most importantly the power of the plasma kept at 10 W (the same as the runs with the COST jet).

As for the experimental procedure, the tests were run continuously over the course of two hours. The samples were a 12 mL solution of trans-Stilbene at 10 mM; and as the tests were run, the samples were topped up in the reactor with additional acetonitrile to ensure the reaction distance was kept roughly constant. Once the two hours were up, the sample was extracted from the reactor into a test tubes. The reactor was then flushed with between 2-3

ml of acetonitrile and drained, with the additional re-extracted samples added to the same test tube. Finally, the sample test tubes were topped up to 15 mL to ensure a fair comparison between all tests. For the GC-MS analysis, the same procedure was used with 0.5 mL of the tested sample and 50 μ L of 200 mM of Naphthalene.

Table 6.1: Comparison of trans-Stilbene epoxide produced across flow rates of 100 sccm to 1 slm and reaction distance of 12 mm to 24 mm.

$d_r \setminus Q$	100 sccm	250 sccm	500 sccm	1 slm	1.5 slm	2 slm
12 mm	0.04 mM*	0.08 mM	-	-	-	-
18 mm	-	0.07 mM	0.96 mM	-	-	-
24 mm	-	0.06 mM	0.62 mM	2.54 mM	2.72 mM	2.90 mM

*Extrapolated result from calibration curve

where d_r is the reaction distance and Q is the flow rate.

The results of this multivariable tests are shown in the pivot table seen in table 6.1. The values in the table denote the concentration of the epoxide produced. Do note that there are a number of gaps in the table. For the flow rate values above 250 sccm, the gaps were simply because the tests could not due to the liquid splashing issue as described above. As for the gaps for the flow rate at 100 sccm, this was simply because the epoxide concentration produced was already quite low at the smallest reaction distance, thus there would be no benefit to running it at the increased reaction distances.

From the data, two observations can be seen. The first is that increasing the flow rate does increase the epoxide yields produced by the reactor, which was to be expected. The second is that the reaction distance does impact the epoxide yields produced for a given flow rate, however its impact is minimal relative to the flow rate. The reason for this second observation has to do with the fact that the velocity of any oxygen atoms exiting the orifice is high, thus the time taken for it to travel an extra centimetre is very small; as apposed to doubling the flow rate essentially doubles its velocity, and thus halves the travel time of the atomic oxygen.

Because of this minimal impact of reaction distance for the SRR jet reactor, it is possible to use the bests results for a given flow rate, to plot a curve of the impact flow rate has on the

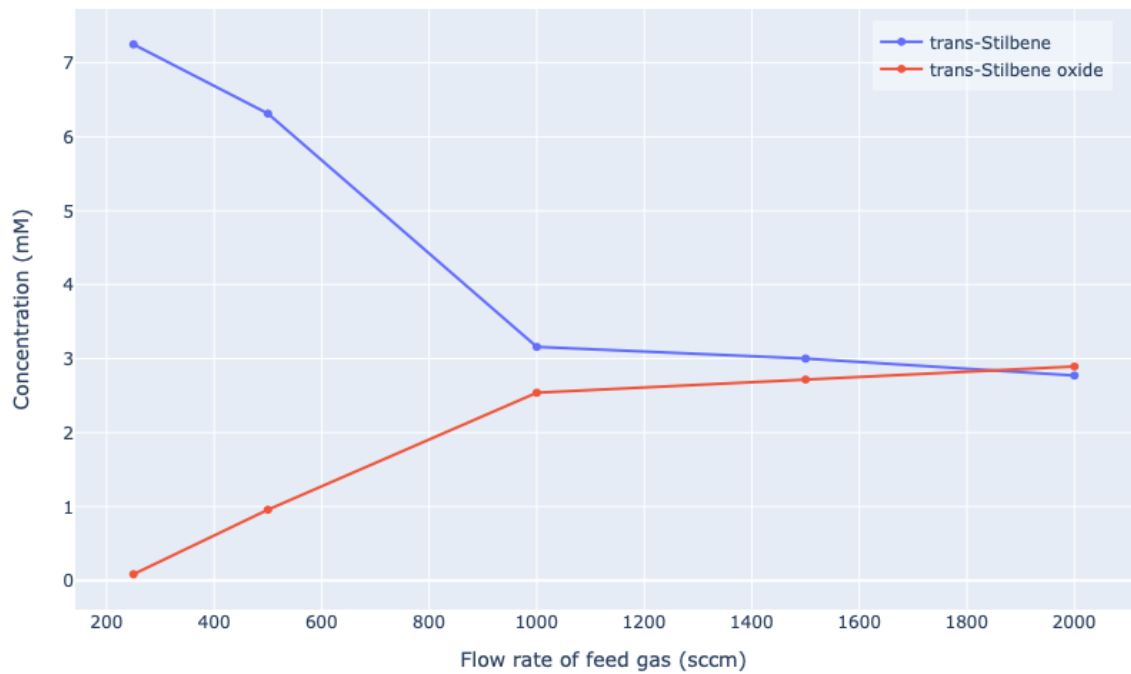


Figure 6.10: The concentration of trans-Stilbene used and trans-Stilbene epoxide produced across a feed flow rate of 250 sccm to 2 slm.

epoxide yields. This is shown in figure 6.10. The results of this graph show that there was a diminishing return for increasing the flow rate after 1 slm.

The reason for this was most likely due to the fact that the plasma produced by the SRR was quite small, with the visible portion of the plasma extending at most 2-3 mm above the electrodes. As such, as the flow rate was increased, the velocity of the CO₂ molecules also increased. This meant that the CO₂ molecules spend less time in the plasma, making it less likely to dissociation to occur.

Another metric to be measured was the epoxide yield and the CO₂ efficiency of the system. The yield was simply expressed as:

$$\text{Epoxide yield (\%)} = \frac{\text{Actual yield}}{\text{Theoretical yield}} \times 100 \quad (6.1)$$

where the theoretical yield was simply the difference in the concentration of trans-Stilbene at the start and end of the experiment.

As for the CO₂ efficiency of the system, the typical equation for CO₂ efficiency is:

$$\text{CO}_2 \text{ efficiency (\%)} = \frac{n_{start} - n_{end}}{n_{start}} \quad (6.2)$$

where n is the number of moles of CO₂.

However, this equation assumes that the number of CO₂ molecules entering and exiting the system are known. Because of the nature of the system built, only the number of CO₂ molecules entering the system are known due to the placement of the FTIR before the plasma. As such, there was no method to determine the CO₂ concentration leaving the system.

Instead, an alternative method to calculate the CO₂ efficiency was required. To achieve this, the epoxide yields were used. This is because, in order to produce an epoxide, one molecule of CO₂ had to be dissociated. Since the pressures were kept at 760 Torr, and the flow rate of CO₂ were kept constant by the mass flow controller, the number of CO₂ molecules entering the system can be determined using the ideal gas law. Thus, the updated equation for CO₂ efficiency, henceforth referred to as the single pass CO₂ efficiency is derived as follows:

$$n_{used} = n_{start} - n_{end} = c_{epoxide} \times V \quad (6.3)$$

where $c_{epoxide}$ is the concentration of epoxide produced and V is the volume of the sample extracted from the reactor.

$$n_{start} = \frac{P}{RT} \times Qt \quad (6.4)$$

where P is the pressure of the system (of 760 Torr), T is the temperature (of 20 °C or 293 K) and R is the gas constant (of 62.364 L Torr K⁻¹ mol⁻¹). Q is simply the flow rate of CO₂ gas and t is the duration of the experiment (which was 2 hours).

$$\text{Single pass CO}_2 \text{ efficiency (\%)} = \frac{c_{epoxide} \times V}{\frac{P}{RT} \times Qt} \quad (6.5)$$

These two additional metrics are shown in figure 6.11. From the results, the yields follow the concentration of trans-Stilbene oxide produced. However, it can be seen that the CO₂ efficiency initially increases as the flow rate increases until 1 slm, then decreases rapidly. This further strengthens the explanation that fewer CO₂ dissociations occur as the flow rate increases past 1 slm.

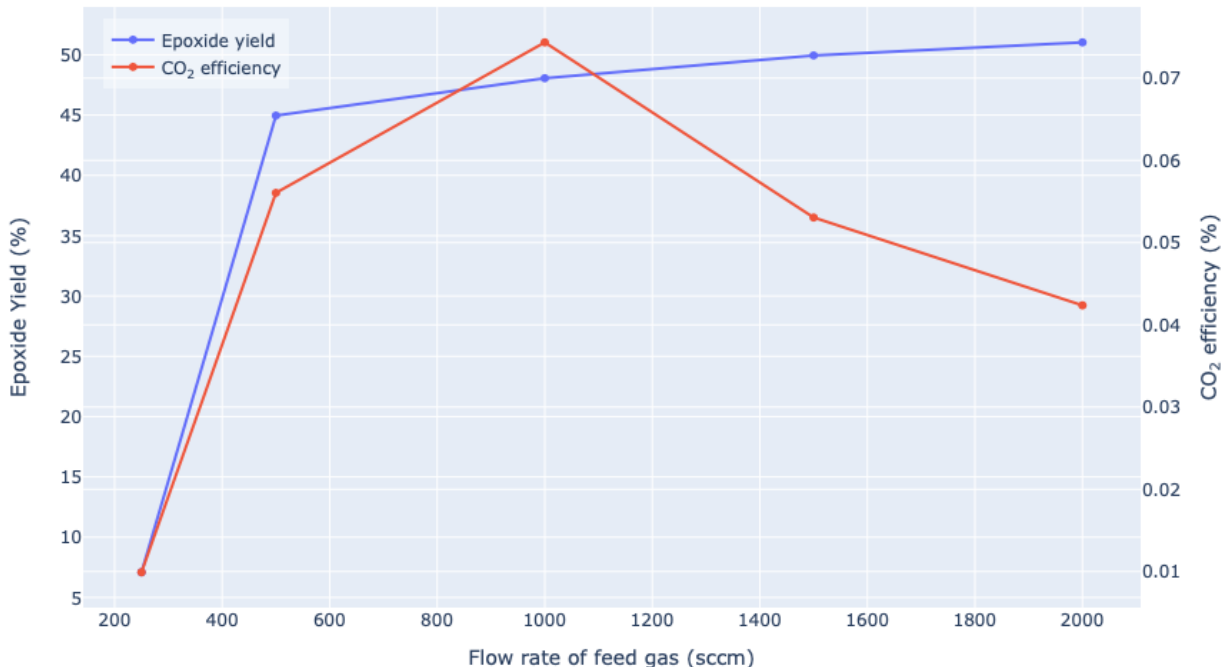


Figure 6.11: The percentage yield of trans-Stilbene epoxide produced and the CO₂ efficiency across a feed flow rate of 250 sccm to 2 slm.

From these results, it is evident that 1 slm would be a suitable flow rate to be used in the system. However, this was not the final selected flow rate. The reasons for this was that the design recirculation system for a closed gas loop configuration was limited by the size of the smallest mass flow controller, which in this case was 500 sccm. As such, the ideal flow rate to be used would be as close to 500 sccm as possible.

6.3.2 Evaluating impact of CO₂ concentration

The next logical test for characterising the system would be assessing the impact of varying the CO₂ concentration in the CO₂-He mixture on the epoxide yields produced. In this set of experiments, the only variable changed was the flow rate of CO₂ into the system, which were a CO₂ percentage between 0.5 to 2.5%. The helium flow rate was kept at 1 slm, the reaction distance was kept at 12 mm, and all other parameters were identical to the first set of experiments. The results of these tests are shown in figure 6.12.

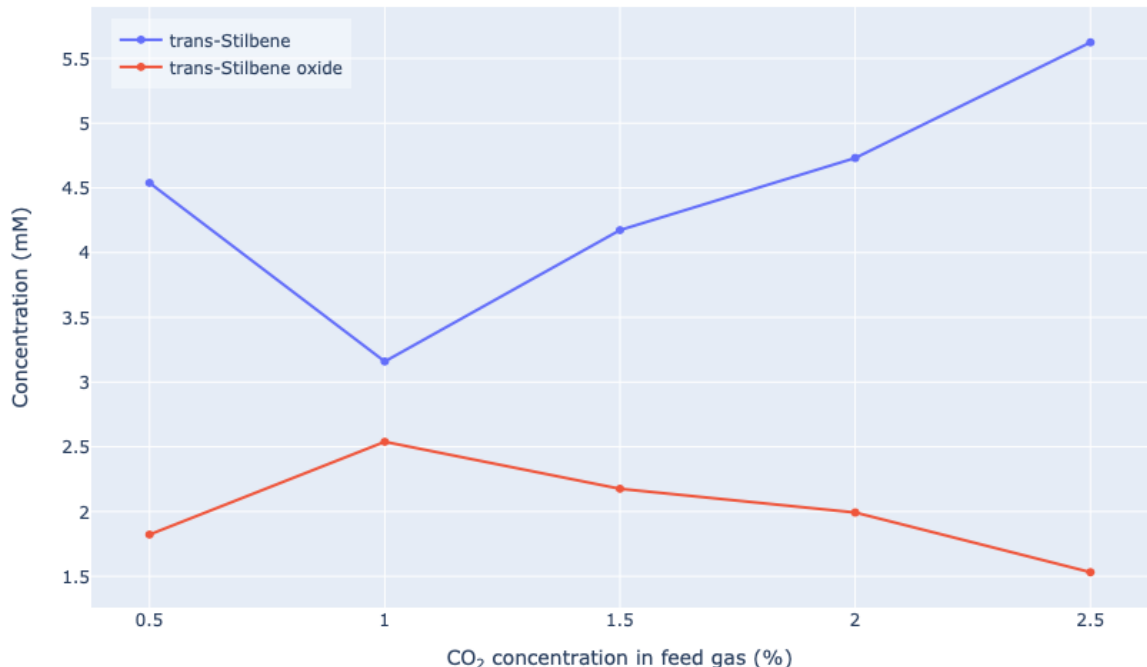


Figure 6.12: The concentration of trans-Stilbene used and trans-Stilbene epoxide produced across a He-CO₂ mixture between 0.5 to 2.5%.

From the results, it can be seen that a 1.0% CO₂-He mixture was the ideal condition for maximising the concentration of epoxide, with a distinct “U-shaped” characteristic where further increasing or decreasing the CO₂ concentration proved detrimental. The reason why a lower CO₂ concentration produced lower epoxide concentrations was quite straight forward; since there were fewer CO₂ dissociations due the lower number of molecules, thus fewer oxygen atoms are available to create the epoxide.

As for why increasing the CO₂ concentration produced lower concentrations of epoxide produced, this was most likely due to the fact that increasing the CO₂ concentration of the gas mixture tends to starve the plasma of electrons. This is because a large number of electrons that would typically undergo elastic collisions in the pure helium plasma now begin colliding with the CO₂ molecules, and start losing energy due to vibrational excitation of the molecule rather than the dissociation. This phenomenon is evident by the reduced light intensity of the plasma that was observed.

In terms of the yields, they showed a upward trend as the CO₂ concentration increased. As for the single pass CO₂ efficiency across the tested concentration, it showed a general downward trend as the concentration of the gas composition was increased.

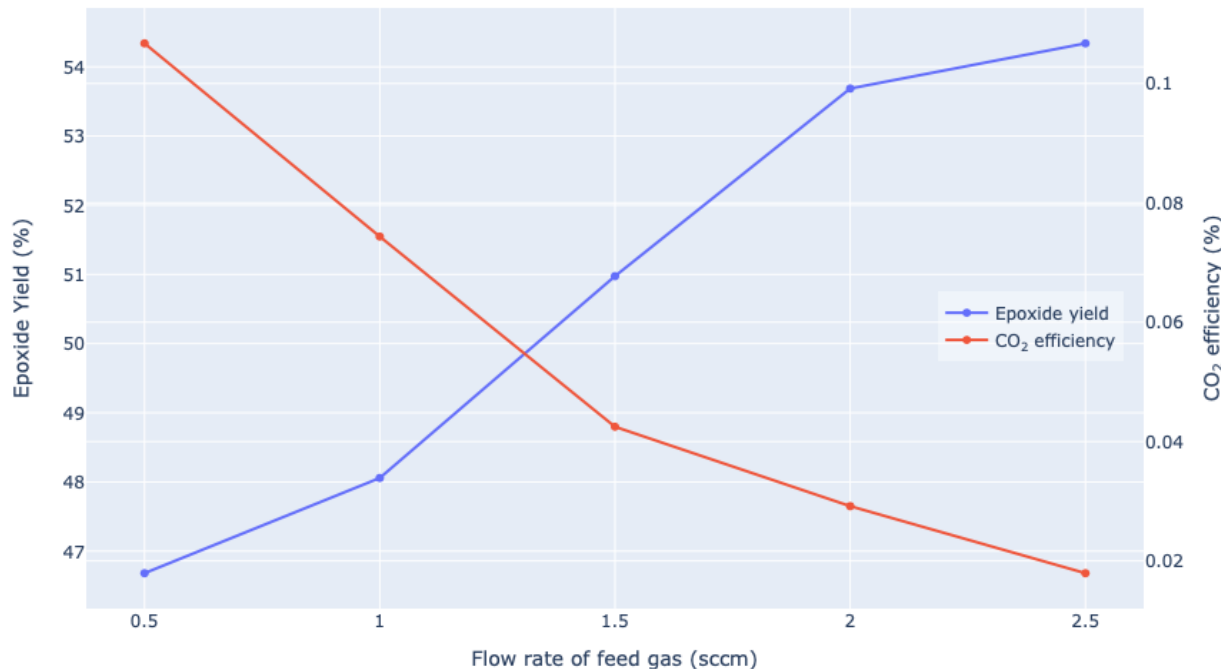


Figure 6.13: The percentage yield of trans-Stilbene epoxide produced and the CO₂ efficiency of the reaction across a He-CO₂ mixture between 0.5 to 2.5%

Based on these findings, the CO₂ concentration to be used would be 1.0%. This was not necessarily because of the yields produced, but because it generated the largest signal in the GC-MS. And since the tested flow rate in the closed gas loop wet plasma system was going to

be lower than the 1 slm flow rate tested in this set of experiments, maximising the signal in the GC-MS was more important.

6.3.3 Evaluating impact of temperature

Another variable to be tested was the temperature at which the liquid trans-Stilbene solution would be kept at. Based on by the work by Xu et al [75], it was already known that decreasing the temperature would improve the epoxide yields. As such, this set of experiments were simply done for the sake of completeness. Three temperatures were tested: one with the reactor an ice bath at approximately 0 °C, one with the reactor at ambient temperature at about 20 °C, and one with the reactor in a cooling bath with a mixture of acetonitrile and dry ice which was around -40 °C. Again, all other parameters were kept the same as the previous two sets of tests.

The results from these runs are shown in figure 6.14. As expected, the cooler the temperature of the liquid in the reactor, the more epoxide produced. The exact mechanism for this behaviour is still unknown but the current hypothesise is that at lower temperatures, less of the atomic oxygen is lost to produce the intermediate adduct with acetonitrile.

However when these results were translated to a percentage of the epoxide yields, they showed a decrease in yields as the temperature decreased, which was the opposite behaviour expected. This is most likely simply due to an increase in concentration of the unwanted byproduct (ethanone, 1,2-diphenyl-). This could be confirmed if a calibration curve for the byproduct was produced, however at the time of writing, this compound was not available in the laboratory.

The only downside of the method in which these experiments were run was that it was not possible to ascertain the exact temperature of the liquid in the reactor due to the enclosed design of the reactor. Instead, several thermal images were captured using a FLIR camera which show the temperature of the glass of the main reactor housing. Since the glass walls were quite thin, the temperature readings should be approximately the temperature of the liquid within the reservoir.

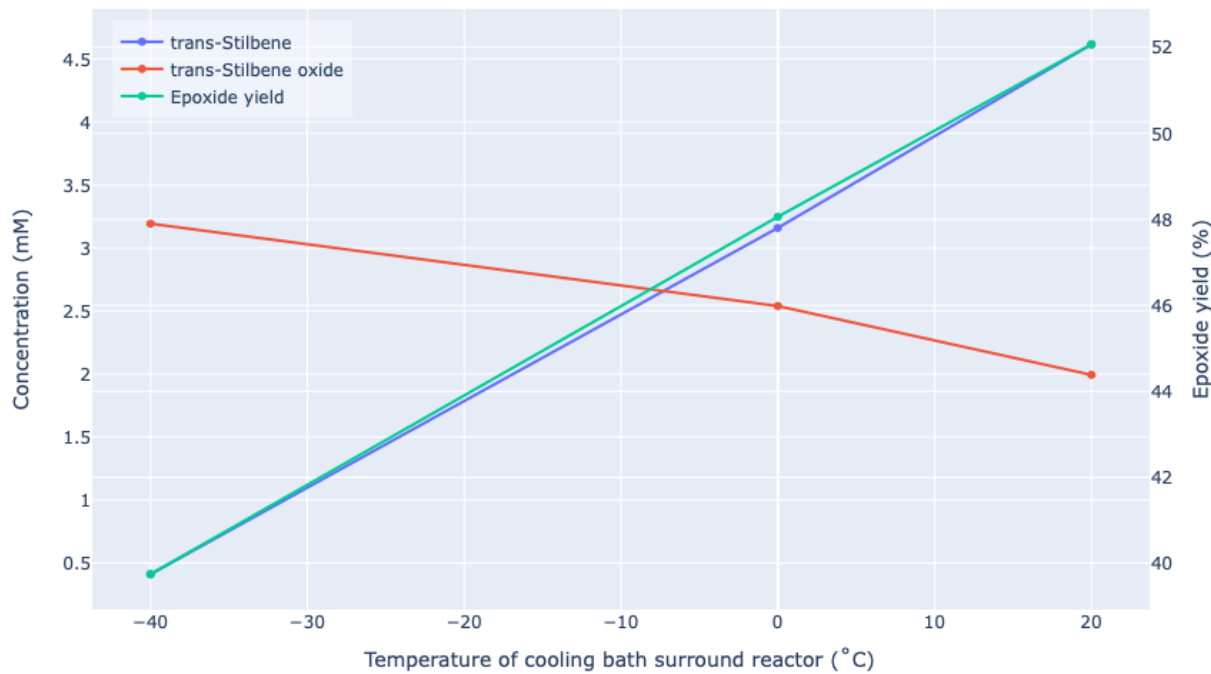


Figure 6.14: The concentration of trans-Stilbene used and trans-Stilbene epoxide produced across range of cooling bath temperatures of $-40\text{ }^{\circ}\text{C}$ to $20\text{ }^{\circ}\text{C}$, along with the epoxide yields produced.

These thermal images are shown in figure 6.15. The value of interest in the images were the sp₂ temperatures. It can be seen that in all three, the temperature of liquid in the reservoir was lower than the ambient temperature of $20\text{ }^{\circ}\text{C}$. The reasons for this behaviour in the ice bath and dry ice baths are obvious. However, the reason for why the setup in figure 6.15a was lower than the ambient temperature was due to jet increasing the evaporation of the liquid, thus decreasing its temperature.

From these tests, it was clear that using a cooling bath at $-40\text{ }^{\circ}\text{C}$ was the best approach to be used for maximising the production of epoxide. Nonetheless, for the rest of the characterisation experiments, the use of the ice bath was continued solely for the purpose of consistency between experiments.

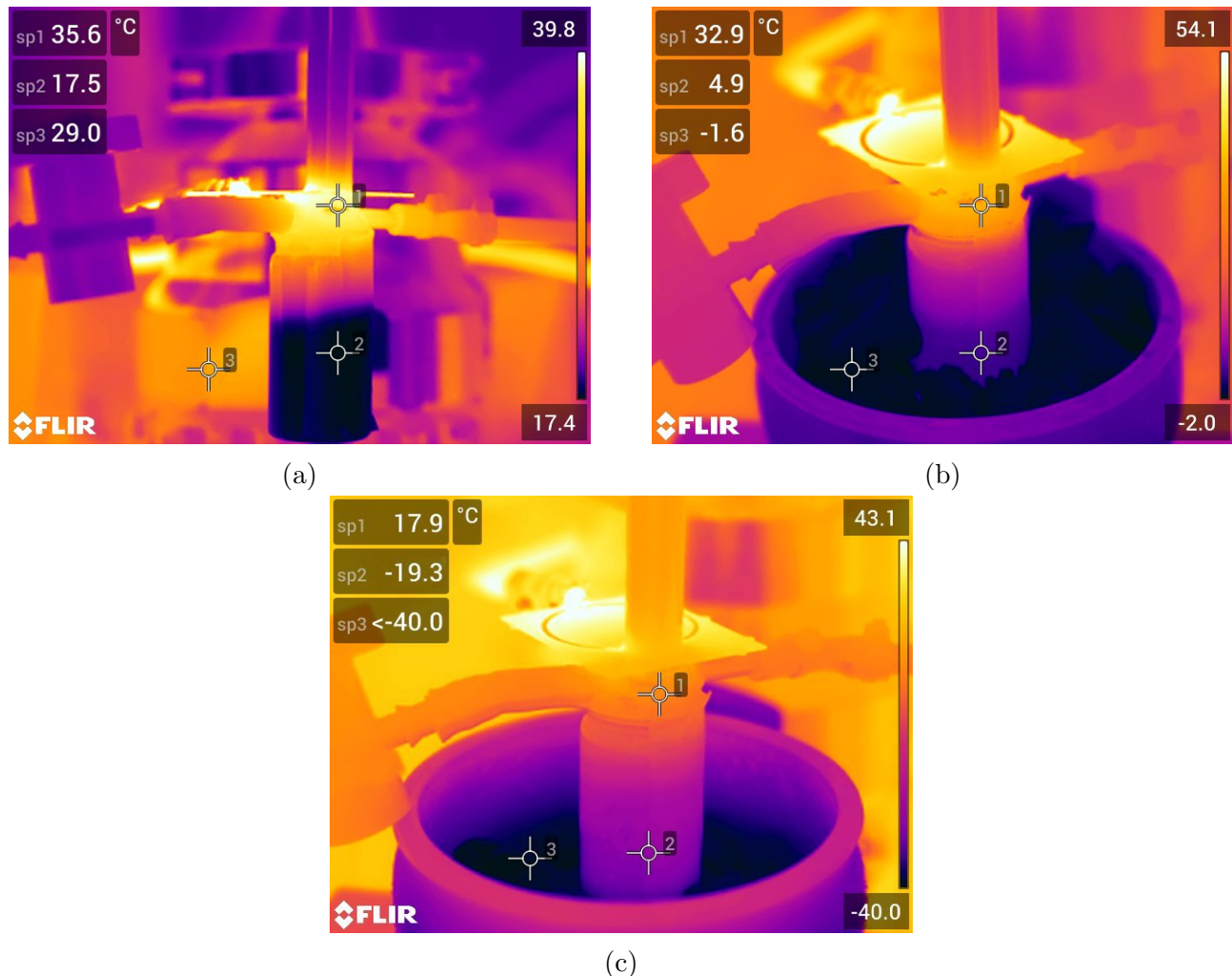


Figure 6.15: Thermal images of the reactor reservoir at ambient temperature (a), with an ice bath (b), and in a dry ice bath with acetonitrile (c).

6.3.4 Evaluating the impact of inert gas used

For most of this report, and all of the characterisation tests, helium has been used as the feed gas of choice. However, helium is significantly more expensive than other inert gases such as argon, which is typically around an order of magnitude less in price. As such, a comparison between helium and argon feed gas was performed.

Based on work by Golda et al [], it has been hypothesised that argon gas should perform identically if not better than helium gas due to the argon plasma having a significantly higher electron density while still having a sufficient electron energy to dissociate the CO₂ molecules. Additionally, Stewig et al [] have shown that the conversion efficiency of CO₂ is higher in an argon plasma compared to a helium plasma.

For this test, the only variable changed was the inert gas used. For both gases, several flow rates were tested. These included flow rates of 250 sccm, 500 sccm, and 1 slm. For each of the respective flow rates, the reaction distance was kept at 12 mm, 18 mm, and 24 mm. All other parameters were kept identical, with the exception of the pressure in the system. This was because argon had a higher density than helium, meaning that there was a build of pressure before the orifice of the SRR jet as the flow rate of argon was increased. So, while the pressure of the system with helium was fairly constant between 760 Torr at 250 sccm to 780 Torr at 1 slm, the pressure of the system with argon ranged from 800 Torr at 250 sccm to 920 Torr at 1 slm. This was why a range of flow rates were tested, simply to eliminate the variable of pressure in the system.

The results of this experiment are shown in figure 6.16. The data clearly showed as the flow rate of the helium feed gas increased, the concentration of epoxide produced (and its yield) increased as well. However, for the argon plasma, the concentration of epoxide produced (and its yield) remained fairly constant even though the flow rate of the argon feed gas was increased. This was quite interesting, given the arguments made in favour of the argon plasma in the previous paragraphs.

To investigate this further, the logical step was to turn to the optical spectra produced by the

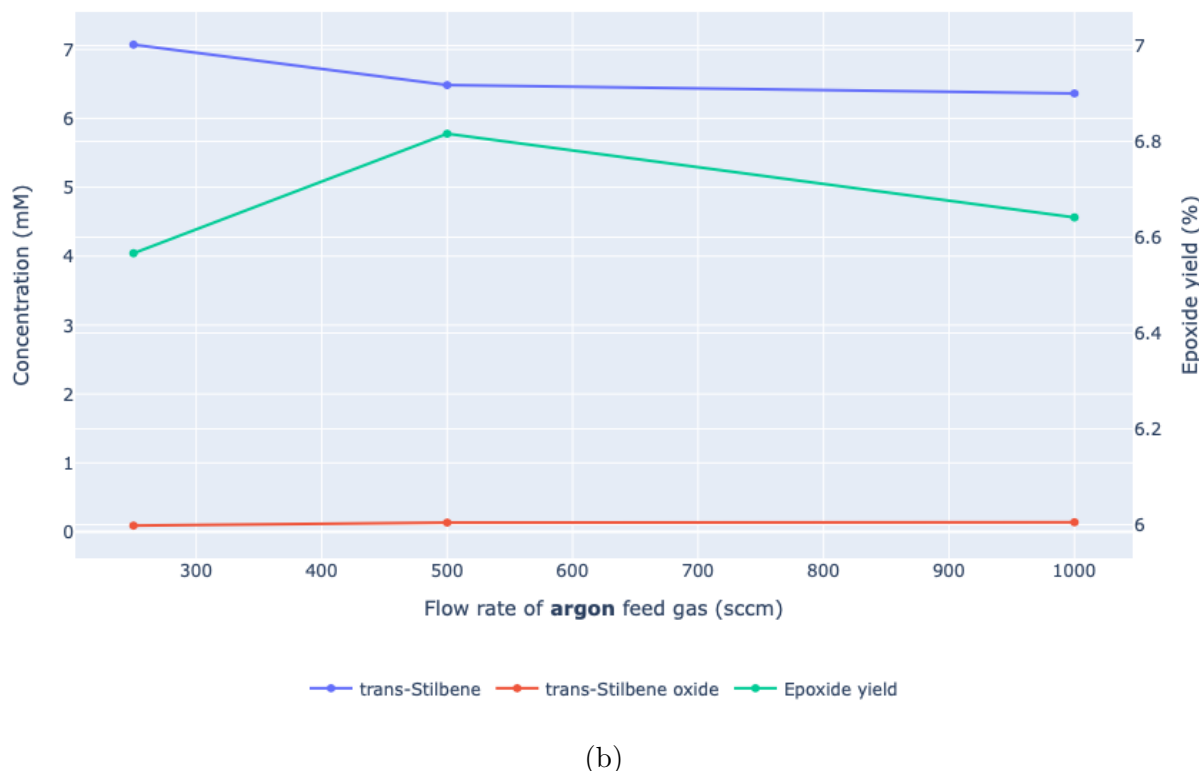
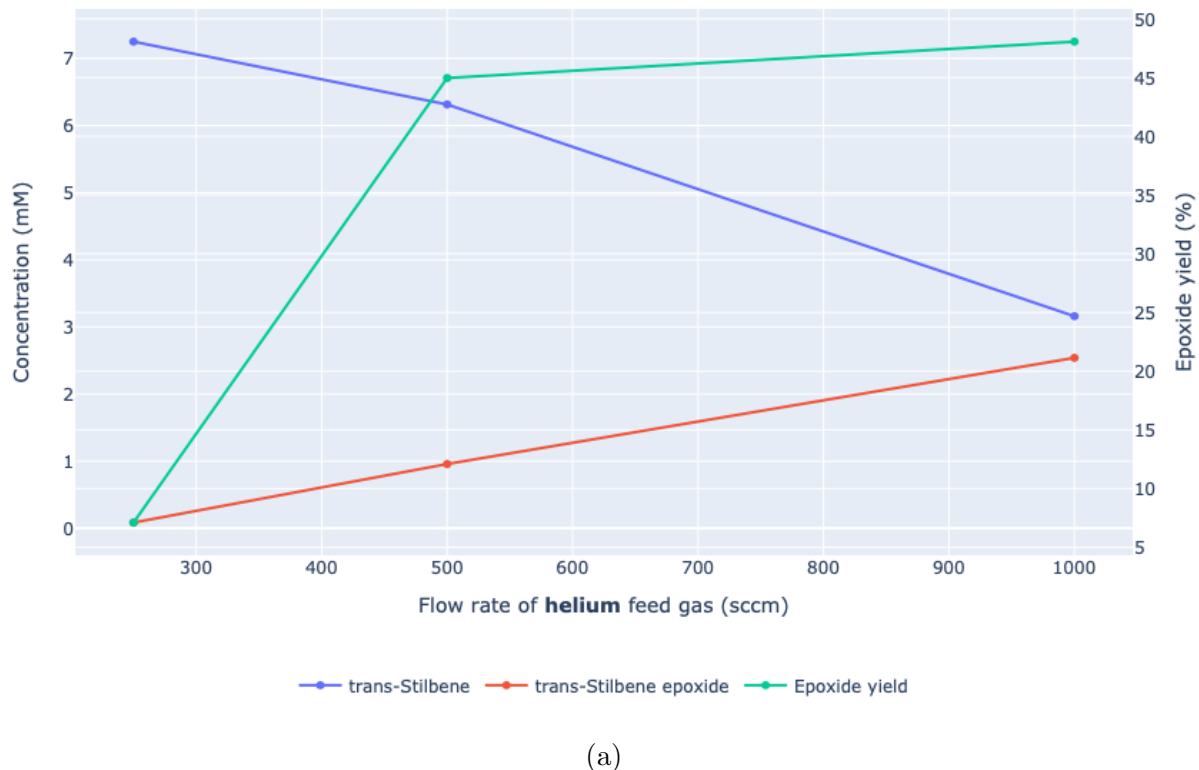


Figure 6.16: A comparison of the concentration of trans-Stilbene used and of trans-Stilbene oxide produced in a helium plasma (a) and an argon plasma (b).

plasma, shown in figures 6.17. From the spectral data, it was can be seen that the light intensity of the pure argon plasma was significantly greater than the pure helium plasma, implying a higher density. This was the expected behaviour since the first excitation potential of argon is much lower than that of helium, of 13.1 eV compared to 24.5 eV respectively.

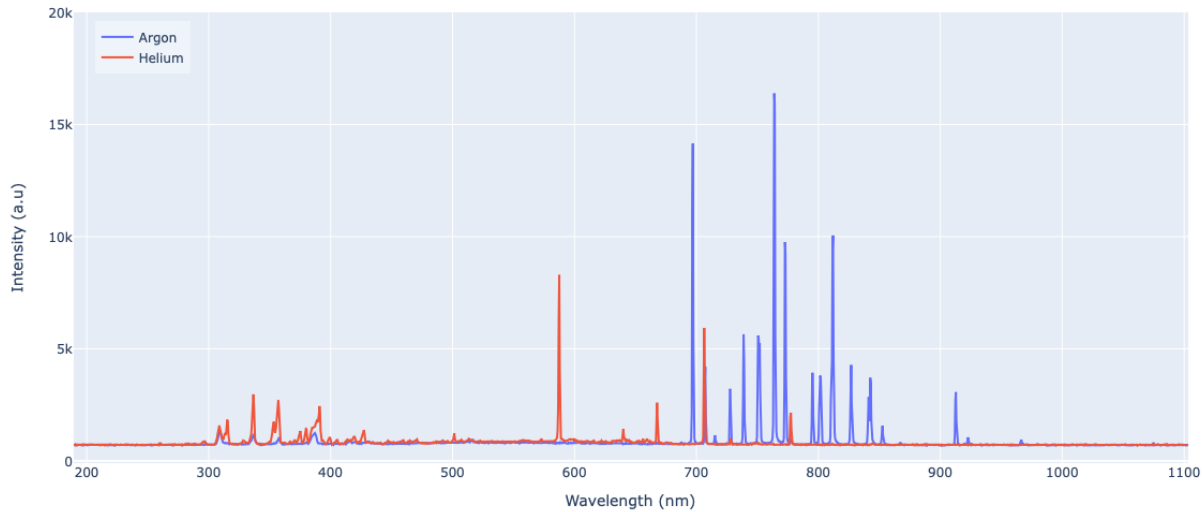


Figure 6.17: Comparison of the optical spectra of a pure Ar and pure He plasma.

Then once the CO₂ gas was introduced, the updated optical spectra can be seen in figure 6.18 and 6.19 for argon and helium respectively. It can be seen that the carbon Swann bands were significantly more present in the argon plasma than the helium plasma. This implied that there was more CO₂ was being dissociated into carbon, and this behaviour was present regardless of reducing the power of the plasma. The interpretation of these results is that for an argon plasma, significantly more of the power goes into the complete dissociation of CO₂ into carbon; whereas in a helium plasma, the typical CO₂ into CO dissociation is more common.

However, in order to definitively say that this is the case, more detailed research is required. This behaviour could simply be the case for this particular plasma source, so the next steps would be to observe if this behaviour if congruent across multiple different plasma sources. Regardless, investigating the exact reason for this behaviour is beyond the scope of report as this test was simply to evaluate which of the two gasses would perform better. In the case of the SRR jet, a helium feed gas was better.

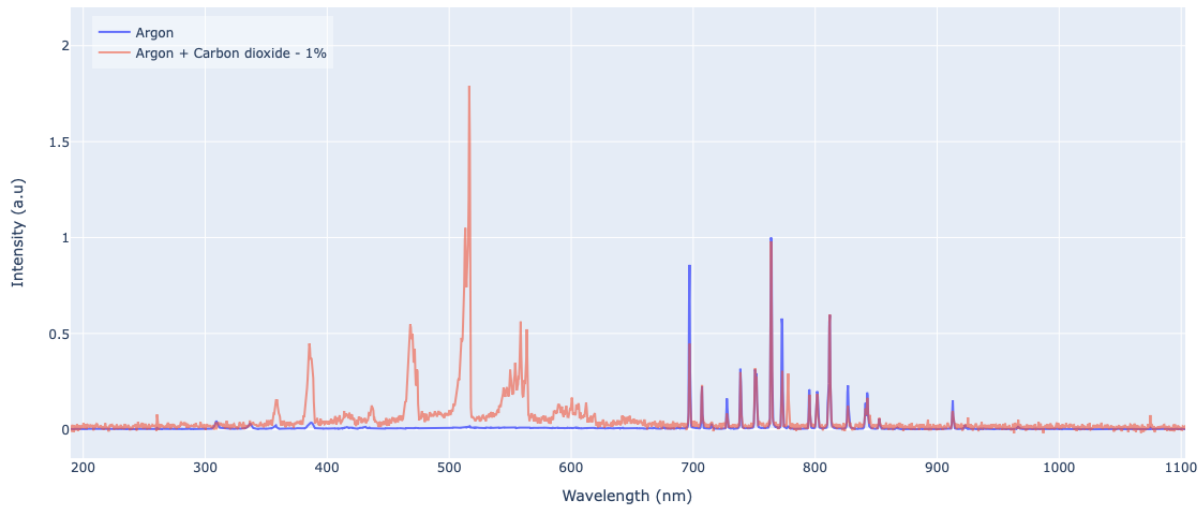


Figure 6.18: Comparison of the optical spectra of a pure Ar and a 1% CO_2+Ar plasma.

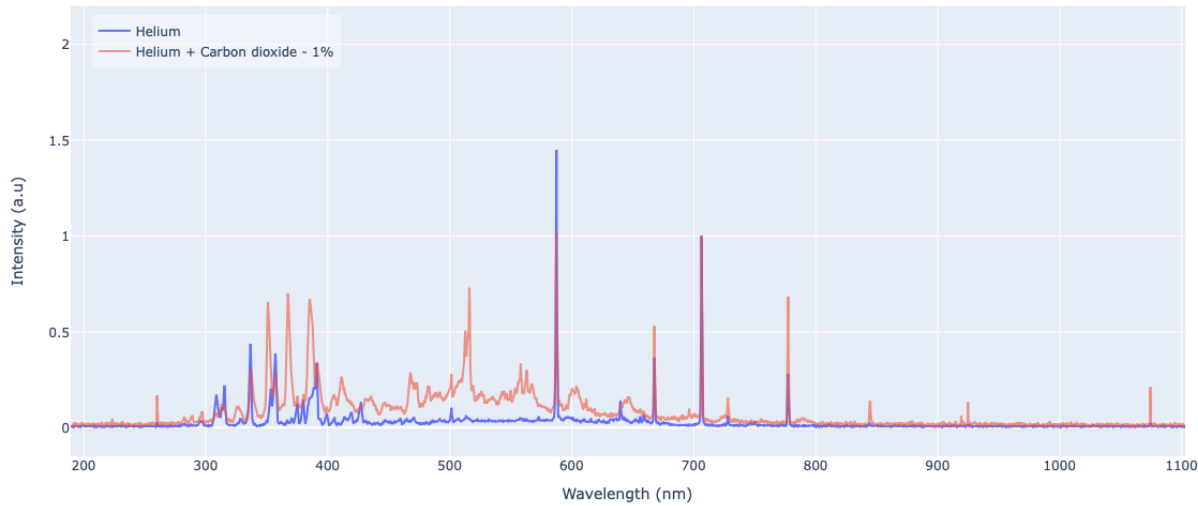


Figure 6.19: Comparison of the optical spectra of a pure He and a 1% CO_2+He plasma.

6.3.5 Comparison with the COST jet reactor

With the optimum operating conditions for the SRR jet established, the next step was to perform a comparison of this jet to the performance of the COST jet. The aim of this was to investigate if such a micro-plasma source has applications outside of the scope of this report.

The first test performed was simply to run both jets with the exact same parameters. Both

jets used a flow rate of 1 slm, with a CO₂ concentration of 1%, and a reaction distance of 24 mm. The results of this test can be seen in figure 6.20. The chart clearly shows that the SRR jet performed better in terms of the concentration of epoxide produced, with around 40% more than that of the COST jet. However, when looking at the percentage yield of the epoxide, the COST jet produced a 54% yield when compared to the SRR jet at 45%. This implies that the SRR appears to be more lossy, though this is something that could be optimised for in the future given that this was the first iteration of such a jet.

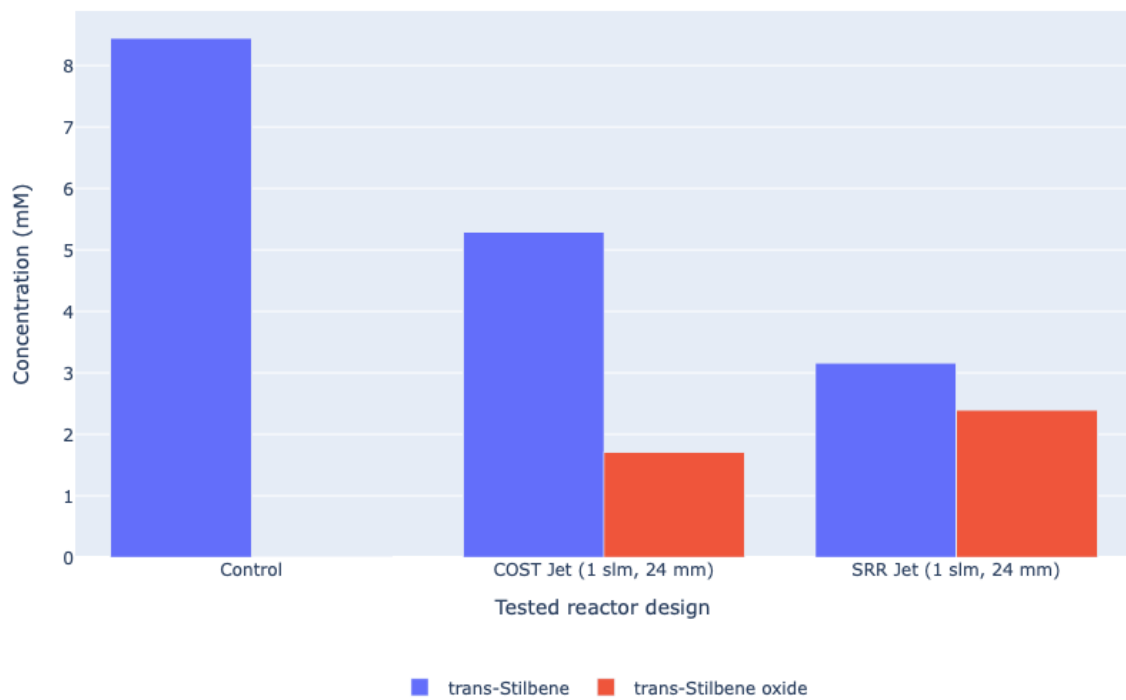


Figure 6.20: A comparison of the concentration of trans-Stilbene used and of trans-Stilbene oxide produced between the COST jet and the SRR jet with equal flow rate (1 slm) and reaction distances (24 mm).

However, the results from these first tests were misleading. This was because while the SRR could only run a 1 slm flow rate at a reaction distance of 24 mm due to the small orifice producing a very strong jet. The COST jet with a larger orifice could actually run a reaction distance closer to the 10 mm range.

Running the tests again with the best possible reaction distance for each jet produced the exact

opposite result, shown in figure 6.21. This time, the COST jet produced a greater concentration of epoxide with a 50% increase compared to the SRR jet. Regardless, the the percentage yield of the COST jet remained the same even with this reduced distance at 55%.

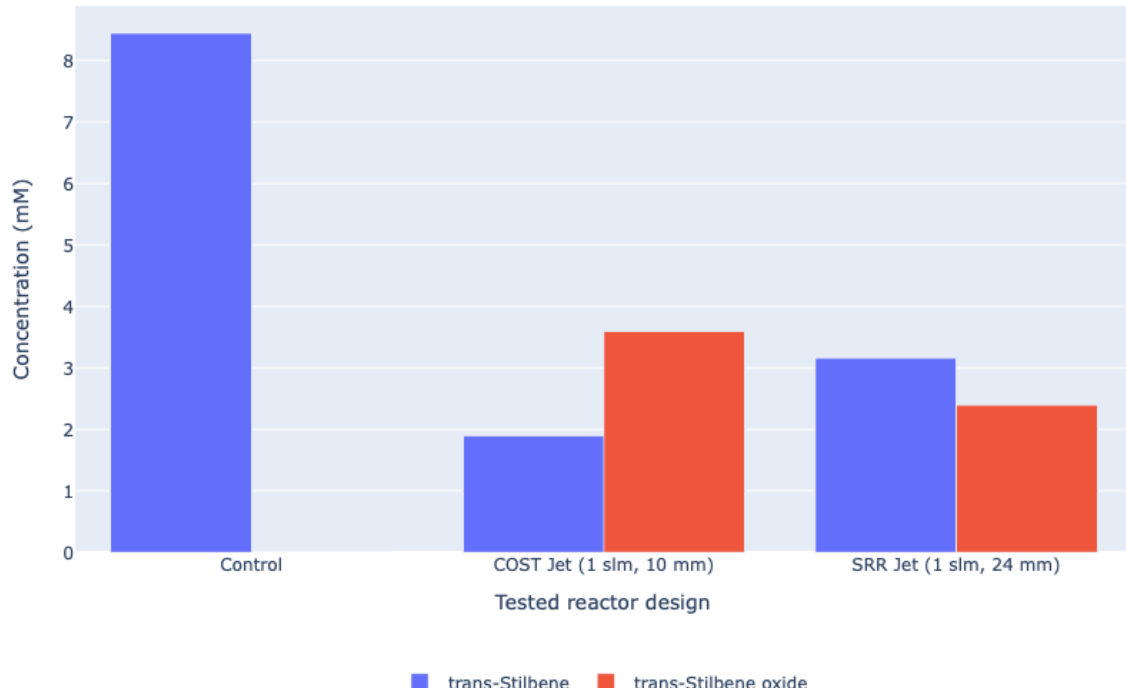


Figure 6.21: A comparison of the concentration of trans-Stilbene used and of trans-Stilbene oxide produced between the COST jet and the SRR jet with equal flow rates (1 slm) but with optimum reaction distances (10 mm for COST jet, 24 mm for SRR jet).

This again though was not a true direct comparison between the two devices. Since the two jets have a different sized orifice, this meant that the velocity of gas exiting the plasma was also different. Thus, the frequency of atomic oxygen hitting surface of the trans-Stilbene solution was going to be higher for a jet with a smaller orifice.

To compensate for this, one could match the approximate velocity of gas exiting the plasma through the orifice. This could be achieved by selecting the gas flow rate for both devices to give the same velocity as it exits the orifice.

The area of the drill hole for the SRR jet is approximately 0.05 mm^2 , and since all the tests were done using the SRR with three drill holes, this gives an area of 0.15 mm^2 . As for

the COST jet, it had an orifice area of 1 mm^2 , which was 6.67 times larger than the SRR jet. Thus if the SRR jet were set to a flow rate of 250 sccm, in order to achieve the same gas exit velocity through the orifice, the COST jet would need a flow rate of 1.67 slm. Even though, the gas velocities are the same for these flow rates, due to the size of the orifice, the COST jet would still have a higher flow rate, meaning more atomic oxygen molecules striking the surface of the liquid. As such, running an experiment with the aforementioned flow rates should produce a result where the COST jet still performs better. However, assuming both jets perform identically, the COST jet should only produce a 6.67 times increase in epoxide concentration than that of the SRR jet.

This exact experiment was run, where the COST jet was set to a flow rate of 1.67 slm whilst the SRR jet was set to 250 sccm. The other parameters were kept constant, including the reaction distance which was set to 12 mm. The results of this test are shown in figure ???. It can be seen that while the COST jet did perform better than the SRR jet, it produced an epoxide yield close to 30 times that of the SRR jet. The percentage yield of epoxide did drop from 54% to 42% with this further increase in flow rate, though this drop was insignificant comparatively to the SRR jet yield of 7% at 250 sccm. Based on these findings, the COST could be said to be the better performing reactor design. The results imply that COST jet was able to generate more atomic oxygen species, though the reason for this is still unanswered. One potential reason could be due to the fact that the electrodes of the COST jet are around 30 mm long, meaning that the residence time of the CO_2 within the plasma was longer, thus there were more dissociations that produced the atomic oxygen species.

Nonetheless, there are still potential applications of using the SRR over the COST jet. First and foremost is the ability for the SRR jet to operate at lower flow rates (something that will become relevant in the next section of this chapter), in comparison to the COST jet which will start to arc if lower flow rates are used. Another benefit of the SRR jet is its cost. Another thing of note is that PCB for the SRR only cost around £25 per device, which makes it a lot more easily replaceable.

Additionally, it may also be possible to eliminate the one drawback of the SRR jet, which is

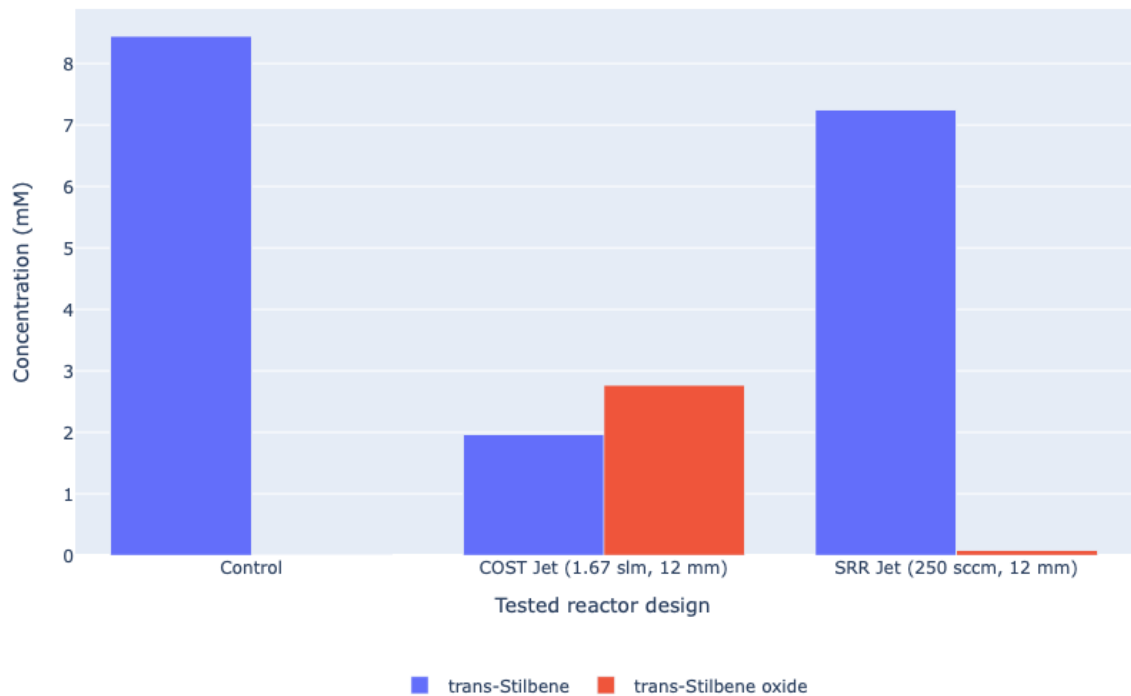


Figure 6.22: A comparison of the concentration of trans-Stilbene used and of trans-Stilbene oxide produced between the COST jet and the SRR jet with equal reaction distances but velocity normalised flow rates (1.67 slm for COST jet, 250 sccm for SRR jet).

the splashing caused when increasing the gas flow rate, by changing the design of the reactor. One of the alternative designs tested was an inversion of the current orientation of the reactor, whereby the treated liquid was located above the SRR PCB, and gas would flow up through the liquid. An illustration of this design can be seen in figure 6.23a, and the prototype designed could be seen in figure 6.23b.

This design would essentially eliminate the gap for the atomic oxygen species to travel, and technically the reaction distance would only be the thickness of the PCB. While this design did successfully run, it relied on an acrylic epoxy to bond the main liquid reservoir the ground plane of the SRR PCB. While this this epoxy was tolerant to many common solvents such as ethanol, it was not chemically resistant to acetonitrile, hence the design was shelved. Nevertheless, it could be possible to create an inverted design that would run with acetonitrile, perhaps with using some acetonitrile resistant seals and custom fabricated parts.

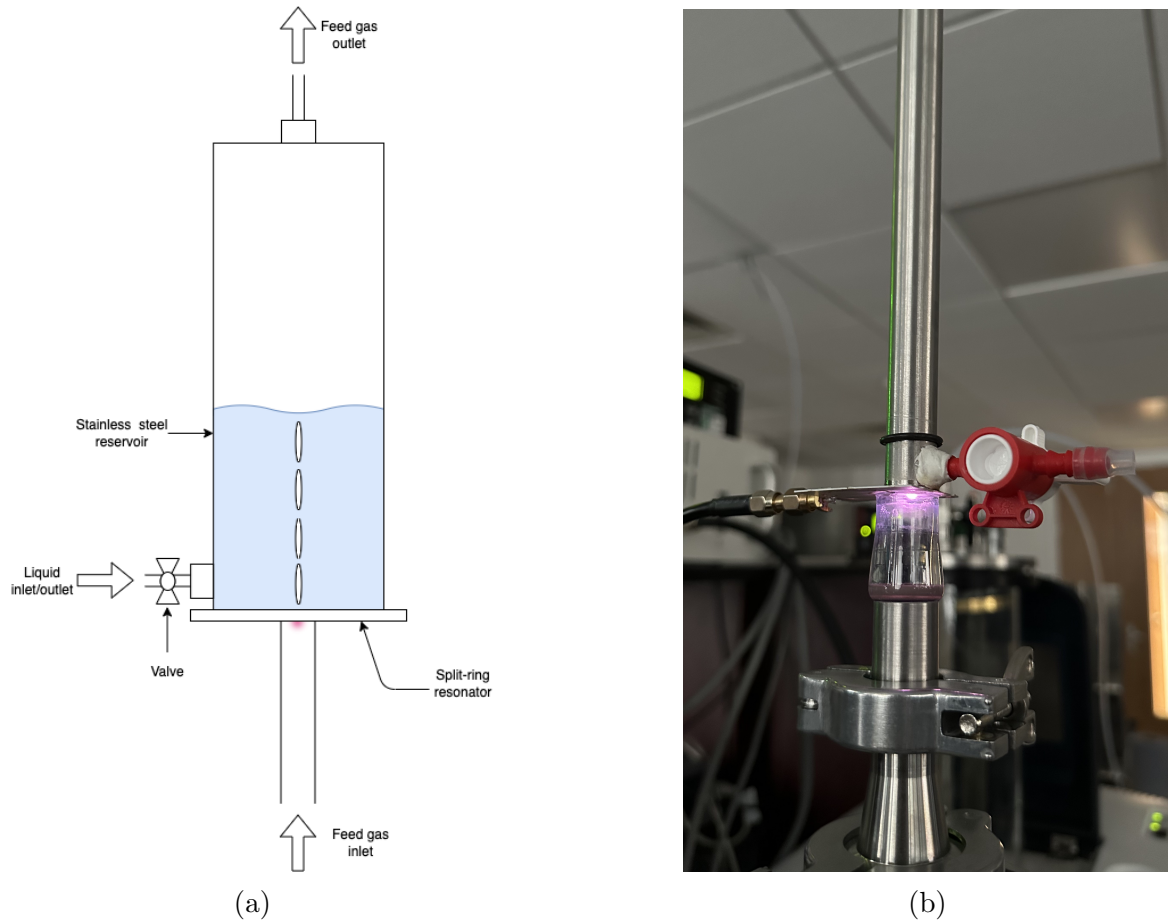


Figure 6.23: An illustration of the schematic design (a) and the prototype (b) of an inverted SRR jet reactor which was scrapped.

6.4 Recirculating the feed gas for the reactor

With the characterisation of the SRR jet complete, the ideal conditions for running the reactor were determined. The conditions could now be used to ascertain the feasibility of running the reactor in a closed gas loop configuration in a wet plasma setting.

In this section, two separate experiments were run. The first one was where the reactor ran in an open gas loop configuration, which served as the control. Then in the second test where the system was switched to the closed gas loop configuration. The intention was to run these experiments for 4 hours, with samples of the liquid within the reactor taken every hour to give a time series plot of concentration of epoxide changes as the reactor was run.

However before running these two experiments, the SRR PCB was changed to a fresh PCB, to ensure that there was no carbon build up on the ring that might hinder the experiments. Then, several integration test runs were undertaken to ensure that the system would function as expected and to also make sure that the system was sufficiently air tight. During these tests, it was discovered that aim of running the system with a flow rate of 500 sccm was not possible. There were two parts to this issue. The first was that the 150 Torr pressure difference for the recirculation mass flow controller, while sufficient for flow rates up to 250 sccm, was too small to sustain a 500 sccm flow rate. The logical step was to increase this pressure difference, which was done to roughly 250 Torr above atmospheric pressure. However, this was where the second issue lied, as the pump used was not capable of maintaining this increased pressure difference. Due to time constraints of obtaining a new pump with custom fabrication for chemical resistance to acetonitrile, it was decided that flow rate to be used was to be reduced.

With this, the new conditions to be used were as follows. The feed gas of choice was Helium, the temperature of the liquid in the reactor was to be kept at -40 °C with a dry ice and acetonitrile cooling bath, 1% CO₂ concentration was to be used for the CO₂-He feed gas mixture, and finally, the desired flow rate to be used was 250 sccm. The plasma power was kept at 10 W, simply for the sake of consistency. As for the pressure of the main reactor, this was increased slightly to 800 Torr. This was done for two reasons, first to ensure a positive pressure in the

overall system so if there were any small leaks, the pressure would force helium out of the system rather than let air into it. The other reason for doing this was to be able to easily identify catastrophic leaks in the reactor from acetonitrile attacking the glues used.

As mentioned earlier, the samples from the liquid within the reactor were to be taken at fixed intervals. However, this meant that procedure of sampling the concentrations of trans-Stilbene and trans-Stilbene epoxide was going to be different compared to the method used in the characterisation tests. This meant that the results of these experiments could not be directly compared to the results from characterisation tests.

The new procedure used is as follows. When preparing the trans-Stilbene solution, a 13 mL sample was made with the same 10 mM concentration. Then, 1 mL was extracted to be used to measure the concentration at $t = 0$. Of the 1 mL extracted sample, only 0.5 mL was used for the GC-MS analysis, with the remainder functioning as a back-up. The rest of the 12 mL of the sample were then put into the reactor to be used over the course of the experiment. Then after every hour, roughly 0.8 mL of liquid was removed from the reactor using a syringe, with the exact volume extracted measured. Again, of the 0.8 mL extracted, only 0.5 mL was used for the quantitative analysis. Once all samples were extracted, the same 50 μ L of 200 mM Naphthalene was added as the internal standard.

The results of the experiments are shown in table x. However, due to the procedure used for periodically sampling the liquid, these values need to be adjusted. The reason for this is due to the fact that the liquid in the reservoir was constantly being topped up with solvent, to ensure that the reaction distance was constant. Since samples were taken every hour, the act of topping up the reservoir with solvent essentially dilutes the concentration of trans-Stilbene and the epoxide. Note that this only applies for the samples taken from $t = 2$ hours onwards, the sample taken at $t = 1$ hour was the first sample taken, hence no dilution took place. The sample at $t = 0$ hours was taken before any reaction took place, thus was also exempt from these corrections.

In order to compensate for the dilution, the formula for molar concentration was used, seen in equation 6.6:

Table 6.2: GC-MS results of periodic samples taken from the wet plasma system running in the open and closed gas loop configurations.

Time (hours)	Concentration of trans-Stilbene oxide (mM)	
	Open	Closed
0	0	0
1	0.123	0.103
2	0.181	0.125
3	0.216	0.124
4	0.243	-

$$c = \frac{n}{V} \quad (6.6)$$

where c is the molar concentration, n is the number of moles of the solute, and V is the volume of the solution.

When the sample at $t = 1$ hour was taken, it can be assumed that the concentration of the sample extracted and the rest of the solution in the reactor reservoir was the same. Therefore, the number of moles remaining once the sample was taken can be expressed by the following equation:

$$\begin{aligned} n_1 &= n_0 - n_{s,1} = c_1 V_0 - c_1 V_1^s \\ n_1 &= c_1 (V_0 - V_1^s) \end{aligned} \quad (6.7)$$

where n_0 is the number of moles originally in the reactor, $n_{s,1}$ was the number of moles in the sample extracted, and n_1 is the number of moles remaining in the reactor. V_0 and V_1^s represent the original (12 mL) volume of the reactor and the volume of the first sample extraction. Finally, c_1 notes the measured concentration from the GC-MS at $t = 1$ hour.

Then when the reactor was topped up back to the original volume after the first sample extraction, this diluted the concentration in the reactor but the number of moles of solute within the reactor remained the same. Hence, this new concentration could be determined by:

$$\begin{aligned} c_1^d &= n_1 V_0 \\ c_1^d &= c_1 \frac{V_0 - V_1^s}{V_0} \end{aligned} \quad (6.8)$$

where c_1^d is the new (diluted) concentration of the reactor, post topping up with the solvent.

Next when the sample at $t = 2$ hours was taken, the measured concentration was c_2 . This measured concentration would be slightly lower than the “true” concentration if the sample at $t = 1$ hour was not taken. As such, it can be corrected as follows:

$$c_2^t = c_2 + (c_1 - c_1^d) \quad (6.9)$$

where c_2^t is the derived “true” concentration. Note that this method assumes that any solute, be it trans-Stilbene or the trans-Stilbene oxide would of remained in the reservoir over the two sample periods. Since, there was a large amount of trans-Stilbene left in the reactor, meaning that the reaction was not limited by the starting material, and that there was very little epoxide in the reactor making it very unlikely to be destroyed during the reaction, it was a fair assumption to make.

The subsequent “true” concentrations for samples taken at $t = 3$ and $t = 4$ hours simply repeated the process of equations 6.7 to 6.9. The results of these calculations are shown in figure 6.24, which shows a time evolution of the open gas loop and closed gas loop configurations.

The graph shows the sample concentrations, which are the direct measurements from the GC-MS; the derived “true” concentrations, which are the corrections from equations 6.7 to 6.9; and the dilution correction factor, which was simply the corrections from equation 6.8.

From the figure, the first thing to be observed was that the open gas loop configuration produced a higher concentration of epoxide than the closed gas loop configuration, with the difference being about 1.7 times the concentration between the two configurations . Another thing to note was that the concentration of epoxide produced in the closed gas loop reduced significantly between $t = 2$ and $t = 3$ hours. With the concentration at $t = 3$ hours of the closed gas

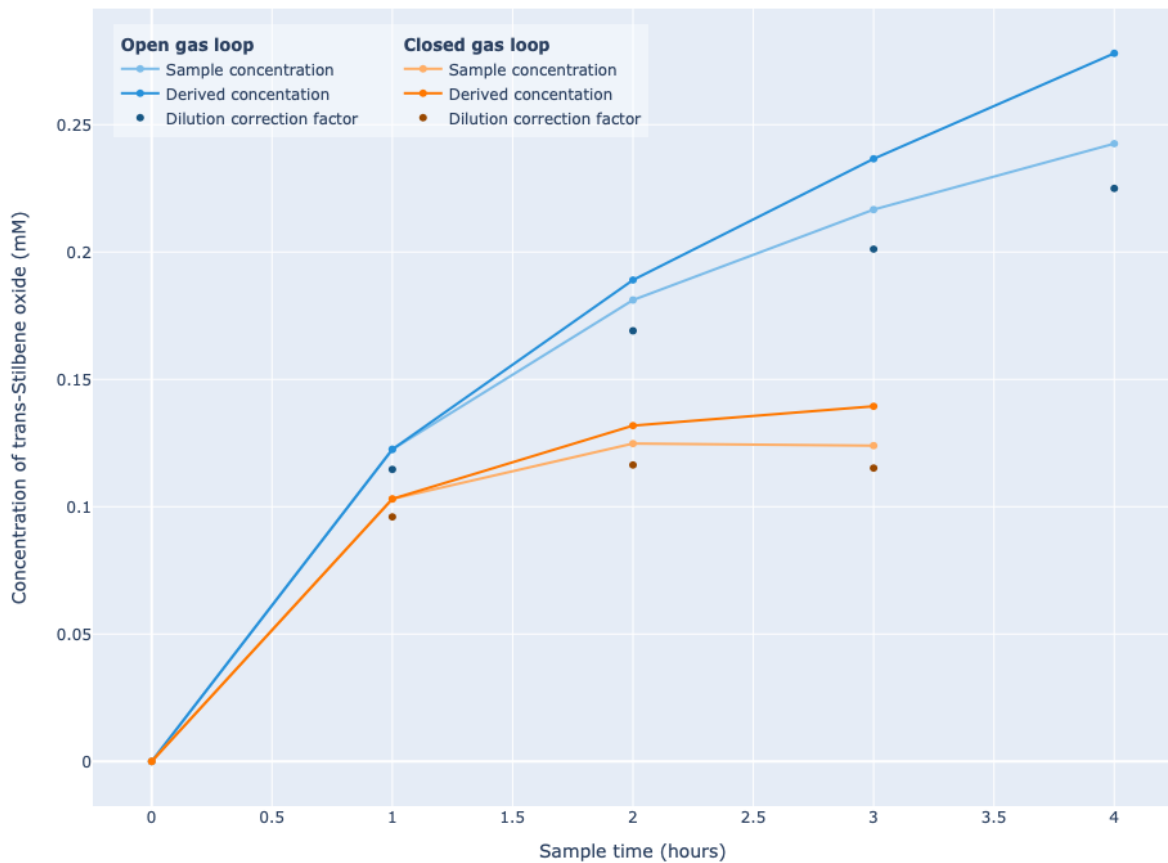
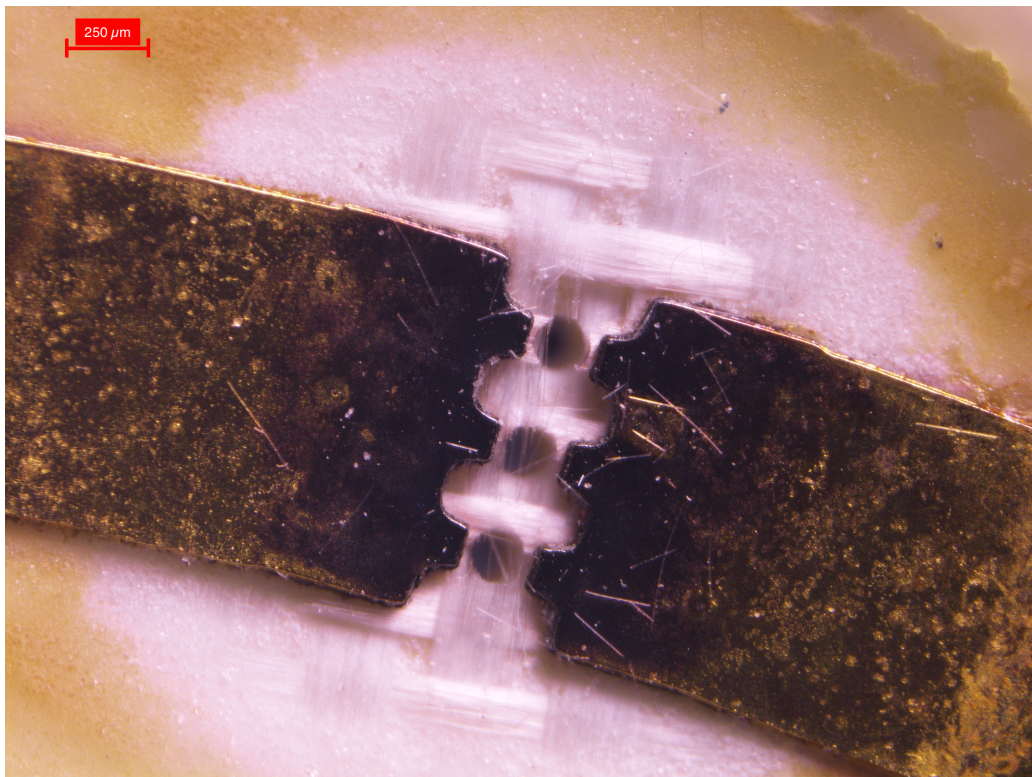


Figure 6.24: The time evolution comparison between the open gas loop and closed gas loop configurations, showing the measured sample concentrations and the corrected concentrations.

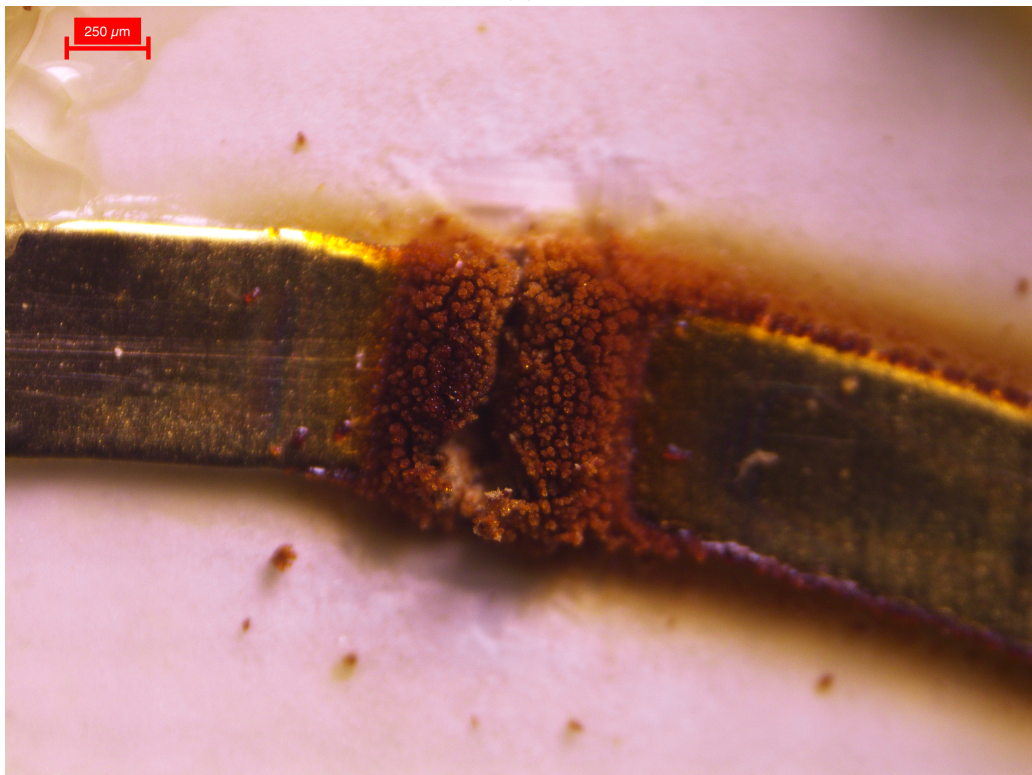
loop configuration equivalent to the concentration at $t = 1.36$ hours of the open gas loop configuration.

This naturally leads to the omission of data for a sample taken at $t = 4$ in the closed gas loop configuration (that some astute readers might have noticed in table 6.2). This was due to the fact that the plasma extinguished shortly after the 3 hour mark of the experiment. The reason for the plasma being extinguished was due to build up of an organic compound on the electrodes of the SRR. However, the exact make up of this organic compound was unknown, and the author lacked the right equipment to perform this analysis in the laboratory; but this build up was most certainly not pure carbon, as shown in figure 6.25.

The explanation for why the closed gas loop configuration performed worst was primarily due



(a)



(b)

Figure 6.25: A comparison between pure carbon deposition (a) and potentially organic solvent deposition (b) on the SRR electrodes.

to contamination of the plasma with the organic solvents used. This included any residual acetonitrile not condensed by the direct-contact condenser and any cooling liquid from the condenser that was kicked up by bubbling the gas through it. This would explain why as time went on, the reactor performed worse in this configuration. This was not necessarily from cumulative accumulation of the organic solvents in the gaseous phase, as this would be limited by the partial pressure of the compound at a given temperature. Instead, this was due to the solvent deposition on the electrodes of the SRR, and as some of the solvent molecules came out of the gas phase, they were immediately replaced by new molecules.

This deposition was detrimental for two reasons. The first is that it obviously blocks the very small orifice of the SRR jet. But the other, more pernicious issue is that the deposited solvent behaves resistively, and since the power going into the SRR PCB remained constant at 10 W, there was less power going into sustaining the plasma. Less power means, fewer ionising collisions, which in turn reduces the amount of atomic oxygen available for creating the epoxide.

Nonetheless, the fact that a closed gas loop configuration works is a massive step forward as it proves that it is possible to recirculate the feed gas to save on the usage of inert helium gas. More on the feasibility, specifically on the cost of this method, is discussed in the next section.

6.5 Cost analysis of recirculating the feed gas

As previously mentioned, the use of helium as a feed gas is quite expensive. At the time of writing, a 300 Bar (which is equivalent to roughly 225,000 Torr) cylinder of A grade helium (which is a 99.996% purity rating) by the supplier BOC¹ cost £1,337. As per the manufacturers data sheet [94], this cylinder would have a gas volume of 12.98 m³ or 12,980 L. Note that this is the equivalent volume at 1 atmosphere of pressure with a gas temperature of 15 °C. Assuming that all the helium gas could be extracted from the cylinder, it would give the helium a cost of 10.3 p/L. Therefore, running an experiment with a steady 250 sccm flow rate of helium in the open gas loop configuration gives a helium usage rate of 15 L/hr and the cost of running this

¹<https://www.boconline.co.uk/>

gas per hour would be 154.5 p/hr.

Over the span of the 3 hour long closed gas loop experiment, the total helium gas usage to top up the system was 240 cm³, or more conveniently 0.24 L. While this value was significantly worse than the results obtained in the end of chapter 5 in the dry plasma system, with a 16 times increase in gas usage over a 1/8 period of original 24 test, it was to be expected. The reason being, there were more parts in the wet plasma system, which simply meant more points at which leaks could occur. Next, looking at the concentration epoxide produced in closed gas loop configuration over the 3 hour run, it took an equivalent of 1.5 hours in the open gas loop configuration to produce the same amount. In that span of time, the open gas loop experiment used 20.4 L of helium. Thus, it can be said that the the closed loop gas configuration saved nearly 94 times the amount of feed gas used in order to achieve the same concentration of epoxide produced. When translated to the cost of helium used, the open gas loop configuration used 210.12p whereas the closed gas loop configuration used 2.47p, which was a saving of £2.08. Note that this was also with the drop off in plasma performance due to contamination, thus could be said to be the worst case scenario. Solving that issue, along with making the total setup more leak proof, would only improve the savings for the closed gas loop configuration.

The same calculations could be performed for the CO₂ gas used. BOC sells a 34 kg CO₂ cylinder (with a 99.8% purity rating) for £63.59. The exact gas volume of the cylinder was not stated on the datasheet [95], but based on the density of CO₂ at room temperature and atmospheric pressure, the calculated gas volume of 17.172 m³ or 17172 L. This meant that CO₂ has a cost of 0.37 p/L, and running a 1% CO₂-He gas mixture would give a CO₂ usage rate of 0.15 L/hr. The cost of running the CO₂ gas per hour would be 0.06 p/hr. Because of how trivial this cost was, it was excluded from the rest of the calculations.

From these calculations, it is obvious that the closed gas loop configuration saves significantly in terms of costs for the feed gas. However, there is a trade off for running these experiments longer which is the cost of electricity. The current price of electricity in the UK is 24.5 p/kWh. Note that this is the cost of electricity for households, businesses would typically pay less though the exact amount varies based on the size of the business and the energy provider. Nevertheless,

this illustrates a worst-case scenario for running the experiments.

While the power required to drive the plasma was only 10 W, in order to drive the plasma, a signal generator and an amplifier were used. The details of the electrical setup can be found in chapter 4, but it is safe to say that the equipment used to drive the plasma certainly used more than 10 W of power. To measure the power consumed by the equipment, a plug-in power monitor was used. The measured power when running the plasma from the signal generator and amplifier were 45 W and 230 W respectively. On top of these two pieces of equipment, there were the MKS mass flow controllers and pressure sensors which drew 168 W in total, the FTIR which drew 80 W, and the pump and heating element for the direct-contact condenser setup that drew 39 W. Thus, the total power usage was 562 W. Running this for 3 hours would equate to 1.686 kWh, which equates to 41.31p of electricity used. Hence, even when factoring electricity usage into the total cost of operation, the closed gas loop configuration saved roughly £1.64.

Moreover, this is with an unoptimised power setup, as the amplifier and signal generator used was designed to operate at a large range of frequencies. If a custom power supply were built, such as the case with the COST jet, the savings would be even larger. For reference, the power usage of the COST jet power supply was measured to be 49 W. Which means, that the total power usage could be brought down to between 50-60 % of the current value. Regardless, with the current setup, it can be said that the closed gas loop configuration operates at 20% the cost of the open gas loop configuration.

Chapter 7

Conclusion

Appendix A

Particle-in-Cell Simulations

Plasmas are complex non-linear systems and contain many unknown variables. Therefore, simplified models are often used to capture major physics of the system whilst ignoring details that can be considered negligible. There are several types of plasma models but the most commonly used methods are fluid description models and kinetic description models [96].

The fluid description method aims to generalise the plasma quantities, such as its density and velocity, by averaging them over a 2D or 3D region . This is achieved by numerically solving the fluid equations; obtained by utilising the velocity components of the Boltzmann equation [96]. Then, the electromagnetic fields are obtained by combining the fluid equations with Maxwell's equations.

In contrast, kinetic description models track the position and velocities of particles within the plasma, taking into account the electromagnetic forces acting on them. As a general rule of thumb, fluid models simulate the plasma behaviour over a macroscopic scale; whilst kinetic models highlight plasma behaviour at the microscopic level.

Particle-in-cell (PIC) simulations are a variant of kinetic description models that tend to be favoured because of its easy formulation. Real-world plasma systems contain a prodigious number of particles, which include electrons, ions, and the background neutral gas; thus, tracking all these particles would be immensely computationally taxing. PIC simulations partially solve

this by tracking so-called *super-particles* [97]. Each super-particle is scaled to represent a number of “real” particles. This scaling factor does not affect the trajectory of the super-particles as the motion of particles within a electromagnetic field are only governed by its mass to charge ratio (see the Newton-Lorentz expression in equation A.3) [97]. For the rest of this chapter, the term super-particle and particles are used interchangeably.

The PIC simulations discussed in this report are known as 2D-3v simulations, i.e. they are 2-dimensional in space but 3-dimensional in velocity. In these simulations, the particle properties (i.e. their position and velocity) are defined in continuous space within the simulation domain. However, the electromagnetic field values are only specified at fixed grid points. Therefore, intermediary steps are required to discretise charges and current densities onto the grid and also interpolation of forces by fields on the particles. These particles and fields are updated sequentially, with time being advanced in small discrete constant steps. An overview of this procedure can be seen in figure A.1 [98]. The rest of this chapter is dedicated to providing an overview of each process in the flow chart.

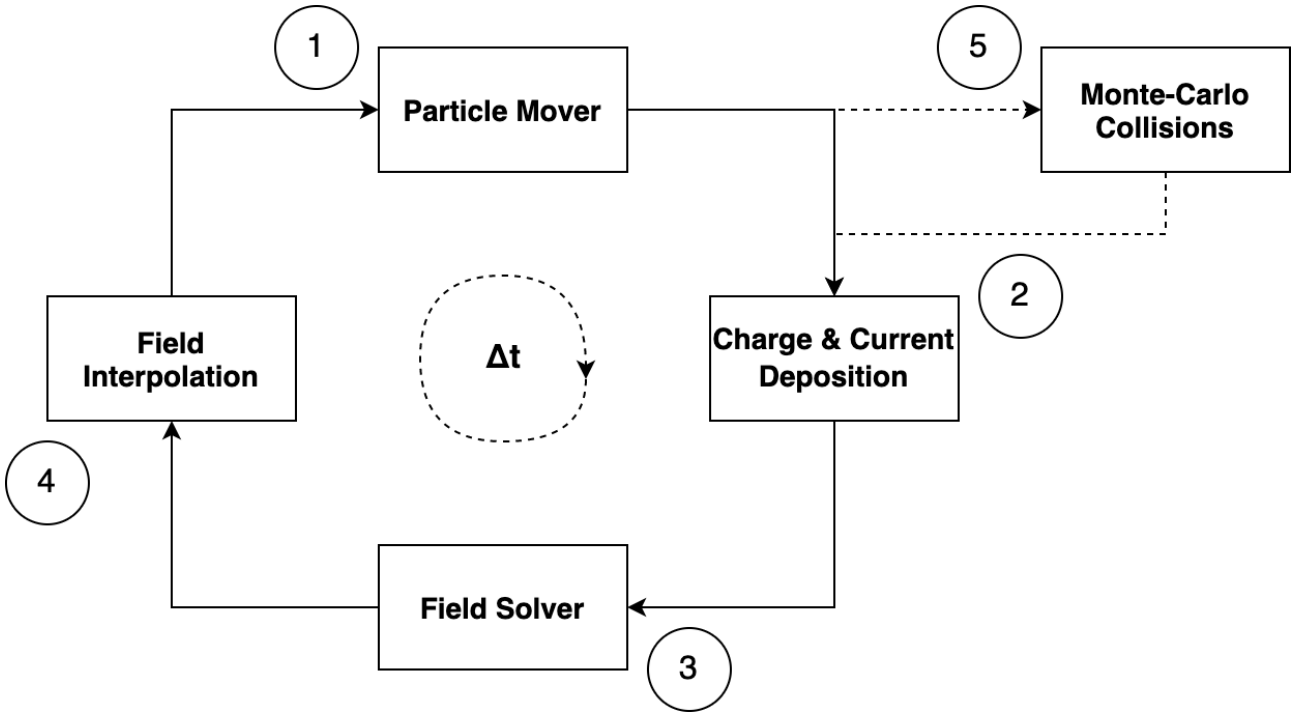


Figure A.1: Process flow of PIC simulations.

A.1 Particle Mover

When first launching the PIC simulation, a random distribution of particle positions and velocities is initialised within the simulation domain. The acceleration of a particle is given by Newton's second law:

$$\frac{d\mathbf{v}}{dt} = \frac{\mathbf{F}}{m} \quad (\text{A.1})$$

The force acting on the particle is determined by the Lorentz force:

$$\mathbf{F} = q(\mathbf{E} + \mathbf{v} \times \mathbf{B}) \quad (\text{A.2})$$

where \mathbf{E} and \mathbf{B} are the electric and magnetic fields respectively, and q corresponds to the charge of the particle.

Combining equations A.1 and A.2 gives the Newton-Lorentz equation:

$$\frac{d\mathbf{v}}{dt} = \frac{q}{m}(\mathbf{E} + \mathbf{v} \times \mathbf{B}) \quad (\text{A.3})$$

As for the particles velocity, it is given by:

$$\frac{d\mathbf{s}}{dt} = \mathbf{v} \quad (\text{A.4})$$

In order to obtain the particle velocity and position, equations A.3 and A.4 have to be numerically integrated with respect to time using the *finite-difference method*; specifically the *leapfrog method* [99]. Thus, the new finite-difference forms of the respective equations are:

$$\frac{\mathbf{v}^{t+\frac{1}{2}} - \mathbf{v}^{t-\frac{1}{2}}}{dt} = \frac{q}{m}(\mathbf{E} + (\frac{\mathbf{v}^{t+\frac{1}{2}} - \mathbf{v}^{t-\frac{1}{2}}}{2}) \times \mathbf{B}) \quad (\text{A.5})$$

$$\frac{\mathbf{s}^{t+1} - \mathbf{s}^t}{dt} = \mathbf{v}^{t+\frac{1}{2}} \quad (\text{A.6})$$

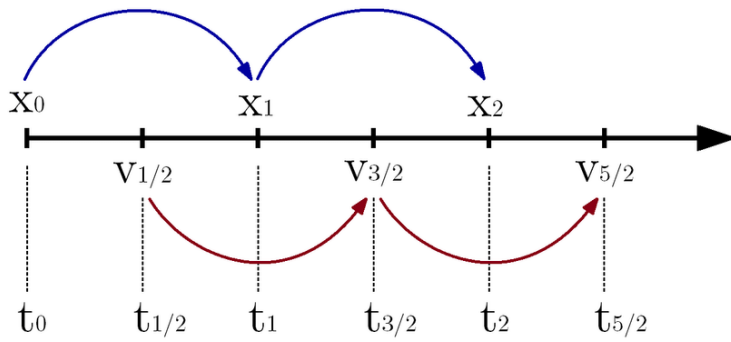


Figure A.2: Illustration of forward-difference and central-difference form [100].

Notice that the particle position is given by the *forward-difference form*, whereas its velocity is given by the *central-difference form*. This is done to conserve the energy of the dynamic system. An intuitive explanation for this is that when solving for the updated position of the particle, its average velocity should be used. Using either the initial or final velocities can result in the particle gaining energy if its accelerating, or losing energy if its decelerating. A visualisation of the difference can be seen in figure A.2.

To solve the Newton-Lorentz equation, the de-facto method used is the *Boris algorithm* [101] for its accuracy, speed, and simplicity. The method first redefines both velocity terms as:

$$\mathbf{v}^{t-\frac{1}{2}} = \mathbf{v}^- - \frac{q\mathbf{E}}{m} \frac{dt}{2} \quad (\text{A.7})$$

$$\mathbf{v}^{t+\frac{1}{2}} = \mathbf{v}^+ + \frac{q\mathbf{E}}{m} \frac{dt}{2} \quad (\text{A.8})$$

When substituted back into the the finite-difference Newton-Lorentz equation (equation A.5), this eliminates the electric field, resulting in an equation that expresses the rotation of the particle's velocity:

$$\frac{\mathbf{v}^+ - \mathbf{v}^-}{\Delta t} = \frac{q}{2m} (\mathbf{v}^+ + \mathbf{v}^-) \times \mathbf{B} \quad (\text{A.9})$$

Because it describes a rotation, it can be solved geometrically. Using the following 2D case seen in figure A.3, it can be determined that the angle through which the velocity rotates is:

$$\tan\left(\frac{\theta}{2}\right) = \frac{\mathbf{v}^+ - \mathbf{v}^-}{\mathbf{v}^+ + \mathbf{v}^-} = \frac{q\mathbf{B}}{m} \frac{\Delta t}{2} \quad (\text{A.10})$$

This angle can also be represented in vector form, referred to as \mathbf{T} . Using this vector form, a bisecting vector \mathbf{v}' can be obtained is parallel to the $\mathbf{v}^+ + \mathbf{v}^-$ vector (the sum of the pre-rotation and post-rotation vector), and perpendicular to both the \mathbf{T} vector (the scaled magnetic field) and the $\mathbf{v}^+ - \mathbf{v}^-$ vector (the difference between the post-rotational and pre-rotational velocity).

$$\mathbf{v}' = \mathbf{v}^- + \mathbf{v}^- \times \mathbf{T} \quad (\text{A.11})$$

Finally to obtain the $\mathbf{v}^+ - \mathbf{v}^-$ vector, this intermediate vector \mathbf{v}' is combined with a new vector \mathbf{S} which can be thought of as a scaled version of vector \mathbf{T} seen in equation A.13.

$$\mathbf{v}^+ = \mathbf{v}^- + \mathbf{v}' \times \mathbf{S} \quad (\text{A.12})$$

$$\mathbf{S} = \frac{2\mathbf{T}}{1 + \mathbf{T}^2} \quad (\text{A.13})$$

Thus, in order to determine the new velocity of the particle:

1. First calculate the velocity of the particle over the first half time step using equation A.7.

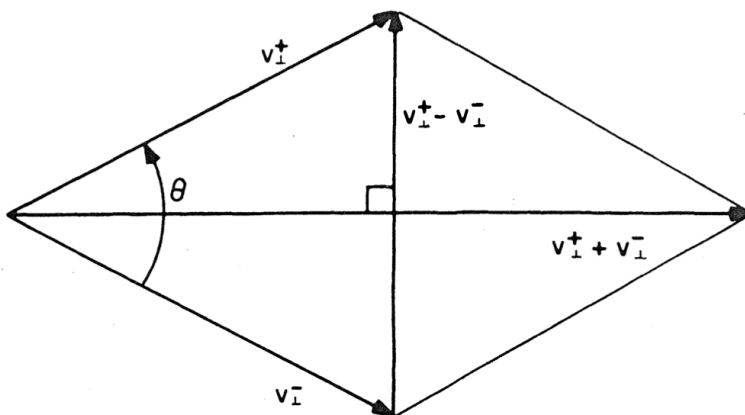


Figure A.3: Visualisation of velocity rotation from the Boris algorithm [101].

2. Then perform the full rotation of the velocity due to the magnetic field using equations A.11 and A.12.
3. Finally, calculate the velocity of the particle over the second half time step using equation A.8.

To obtain the particles new position, substitute the newly calculated velocity of the particle into equation A.6. Once calculated, the positions of each particle in the simulation can be updated.

A.2 Charge and Current Deposition

Once the particles have been moved, their charge and current densities are discretised onto a the specified grid. The exact method of discretising these properties depends on the type of grid for the PIC simulation. The one described in this report is for a uniform 2D rectilinear grid, known as *bilinear interpolation* [102].

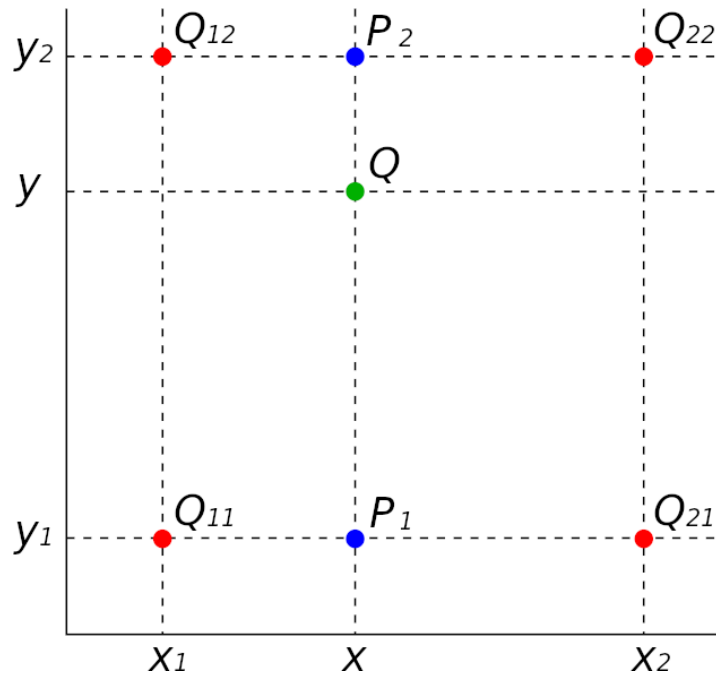


Figure A.4: Interpolation from the grid to the particles [103].

Consider the following case in figure A.4. The charge of the particle within the grid cell is distributed across the four vertices of the cell, called the *nodes*. The total charge experienced

by each node must equal to the charge of the particle, with nodes closest to the particle experiencing the greatest weight. This can be expressed as:

$$\begin{aligned} Q_{11} &= Q \frac{(x_2 - x)(y_2 - y)}{(x_2 - x_1)(y_2 - y_1)} \\ Q_{12} &= Q \frac{(x_2 - x)(y - y_1)}{(x_2 - x_1)(y_2 - y_1)} \\ Q_{21} &= Q \frac{(x - x_1)(y_2 - y)}{(x_2 - x_1)(y_2 - y_1)} \\ Q_{22} &= Q \frac{(x - x_1)(y - y_1)}{(x_2 - x_1)(y_2 - y_1)} \end{aligned} \quad (\text{A.14})$$

Intuitively, the weight of a node corresponds to the ratio of the area of the rectangle opposite (formed by the point of the particle and the point of the opposite node) and the total area of the cell.

Once the (weighted) charges at each node point has been calculated for all particles, the charge density of a node can be determined by summing the total charge on the node from all particles, then dividing by the area of the cell. This node area is typically given as $(x_2 - x_1)(y_2 - y_1)$, with the exception being nodes at the edges or corners of the simulation domain. With such cases, the resulting area is halved and quartered respectively.

A similar process is done to determine the current densities around a node. However, rather than just summing the charges, the total sum of the product between the particles charge and average velocity are taken.

A.3 Field Solver

The field solver utilises the charge and current densities at the grid points to determine their corresponding electric and magnetic field values by solving Maxwell's equations. This report will only consider the electrostatic case and therefore will focus on the process of computing the electric field values.

Gauss's law dictates that the divergence of the electric field in a region is proportional to its

charge density:

$$\nabla E = \frac{\rho}{\varepsilon_0} \quad (\text{A.15})$$

The electric field is determined as the gradient of the electric potential, and by substituting that into the above equation results in Poisson's equation:

$$-\nabla^2 \phi = \frac{\rho}{\varepsilon_0} \quad (\text{A.16})$$

Considering a 2D case with a cartesian coordinate system, Poisson's equation can be rewritten as:

$$\frac{\partial^2 \phi}{\partial x^2} + \frac{\partial^2 \phi}{\partial y^2} = -\frac{\rho}{\varepsilon_0} \quad (\text{A.17})$$

In order to solve Poisson's equation in a discretised domain, the finite-difference method is employed. Specifically using the central-difference, the resulting approximation seen in equation A.18 is produced, which is classed as second order accurate.

$$\frac{\phi_{x+\Delta x, y} - 2\phi_{x, y} + \phi_{x-\Delta x, y}}{\Delta x^2} + \frac{\phi_{x, y+\Delta y} - 2\phi_{x, y} + \phi_{x, y-\Delta y}}{\Delta y^2} = -\frac{\rho}{\varepsilon_0} \quad (\text{A.18})$$

There are several method to solve such an equation numerically. An overview of method used by XOOPIIC (simulation program used in this work, see chapter 4) is described below.

The Poisson equation is classed as an elliptic partial differential equation, which can be written in this form [104]:

$$\mathcal{L}u = \lambda \quad (\text{A.19})$$

where \mathcal{L} is the elliptical operator and λ is the source term.

It is then possible to rewrite this as a diffusion equation (i.e. with respect to time):

$$\frac{\partial u}{\partial t} = \frac{\partial^2 u}{\partial x^2} + \frac{\partial^2 u}{\partial y^2} - \lambda \quad (\text{A.20})$$

which is equivalent since as $t \rightarrow \infty$, $\frac{\partial u}{\partial t} \rightarrow 0$.

Therefore, equation A.20 can be expressed as a diffusion equation in the finite-difference form:

$$\frac{\phi_{x,y}^{t+\Delta t} - \phi_{x,y}^t}{\Delta t} = \frac{\phi_{x+\Delta x,y} - 2\phi_{x,y} + \phi_{x-\Delta x,y}}{\Delta x^2} + \frac{\phi_{x,y+\Delta y} - 2\phi_{x,y} + \phi_{x,y-\Delta y}}{\Delta y^2} + \frac{\rho}{\varepsilon_0} \quad (\text{A.21})$$

From this, a technique known as the *alternating-direction implicit* (ADI) method can be employed. In essence, the ADI method utilises a concept known as operator splitting, wherein the $\frac{\partial^2 \phi}{\partial x^2}$ and $\frac{\partial^2 \phi}{\partial y^2}$ terms can be decoupled, then each can be solved by iterating over half a time step. So for the first half time step, a pass is performed along the x direction; then at the second half time step, a pass is performed along the y direction as illustrated in figure A.5.

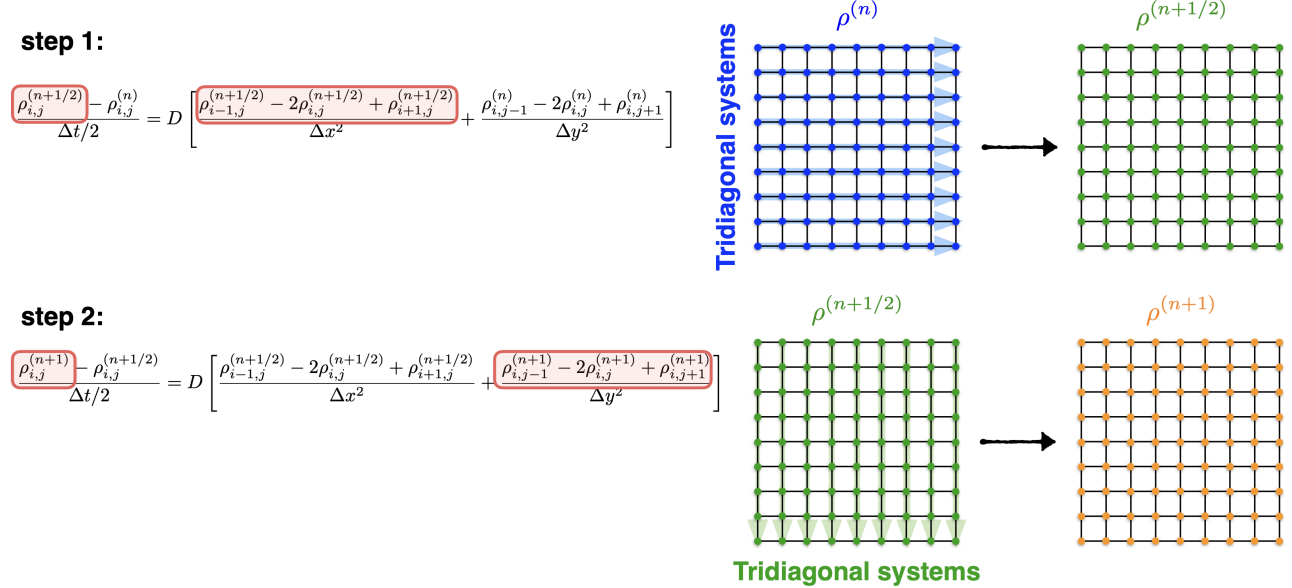


Figure A.5: Illustration of ADI method [105].

The benefit of this method is that rather than solving a large sparse matrix of a 2D system, a set of two independent 1D systems can be solved. These 1D systems can be arranged as a tridiagonal matrix, which can be efficiently solved using the *Thomas algorithm* [106].

Once the Poisson equation is solved and the potentials at the grid determined, the electric field

can be calculated again by the finite difference method. As the electric field is a vector, it needs to be calculated both along the direction of the x -axis and y -axis. Considering only the direction along the x -axis, equation A.22 can be used. For the case of a boundary, equation A.23 should be used instead.

$$E_x^{i,j} = \frac{\phi_{i+\Delta x,j} - \phi_{i-\Delta x,j}}{2\Delta x} \quad (\text{A.22})$$

$$E_x^{i,j} = \frac{\phi_{i+\Delta x,j} - \phi_{i,j}}{\Delta x} \quad (\text{A.23})$$

A.4 Field Interpolation

The interpolation of the electromagnetic field values on the particles is also performed using bilinear interpolation, however the reverse method to that done for the charge and current deposition. Therefore the electric field experienced by the particle is given by the contribution of the electric field vectors at each grid point.

Again, the general case seen in figure A.4 can be used. Here first step is to determine two intermediate points P_1 and P_2 :

$$P_1 = Q_{11} \frac{x_2 - x}{x_2 - x_1} + Q_{21} \frac{x - x_1}{x_2 - x_1} \quad (\text{A.24})$$

$$P_2 = Q_{12} \frac{x_2 - x}{x_2 - x_1} + Q_{22} \frac{x - x_1}{x_2 - x_1} \quad (\text{A.25})$$

Then, interpolate to the point of the particle Q :

$$Q = P_1 \frac{y_2 - y}{y_2 - y_1} + P_2 \frac{y - y_1}{y_2 - y_1} \quad (\text{A.26})$$

Thus for the fields, the variables Q would be replaced with the electric field vectors and the magnetic field vectors respectively. This process is repeated for all particles and the new electromagnetic field values are used in the particle mover for the next time step.

A.5 Monte-Carlo Collisions

Steps 1-4 in figure A.1 are used to simulate collisionless plasma systems, where the charge particles kinetics are governed by magnetic interactions. However, when elastic and inelastic collisions between particles cannot be ignored, an additional step is sandwiched between steps 1 and 2 to account for this.

This is known as the *Monte-Carlo collision* (MCC) method, and it describes the collisions between the particles in a probabilistic fashion [107]. To start, the particles are evaluated for collisions. If a collision occurs, the particle velocity is updated in lieu with the type of collision. One potential downside to using the MCC method is that source particles collide with a target “cloud”, which is not a simulated particle. However, in practice the density of the background is significantly larger than the number of charged species being simulated, so this trade off is acceptable.

Determining if each and every particle in the simulation undergoes a collision can be very computationally expensive, as this requires the computation of each particles kinetic energy and their corresponding collision cross sections. Therefore, a computational trick is employed by adding an artificial collision term. The cross section of this term is chosen to force the total collision frequency for each species to be uniform and independent of the kinetic energy of the particle. This is called the *null collision* [107], which is illustrated in figure A.6.

From this, the portion of particles that should undergo a collision can be determined by the following expression [108]:

$$P(t) = 1 - e^{-\nu \Delta t} \quad (\text{A.27})$$

where ν is the maximum of the sum of all collision frequencies. This can be expressed mathe-

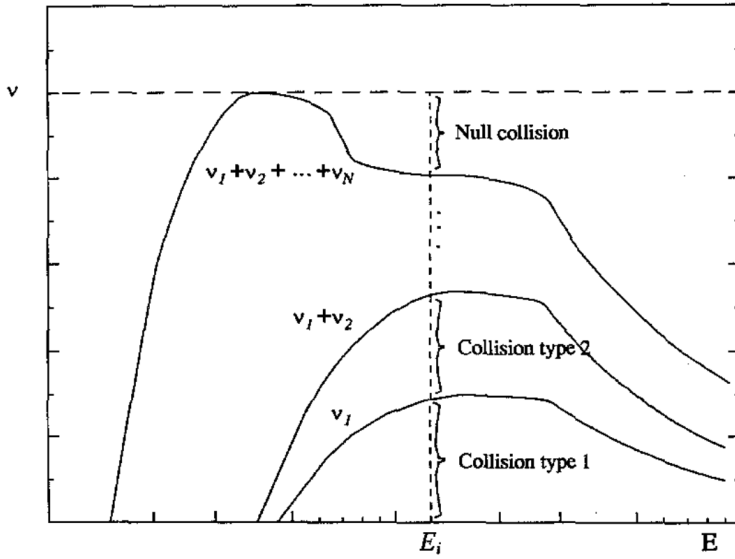


Figure A.6: Addition of null collision to produce a constant collision frequency across all energies [108].

matically as:

$$\nu = n_g \cdot \max(\sigma_{total}, v) \quad (\text{A.28})$$

where n_g is the neutral gas density (which can be assumed to be constant), σ_{total} is the total cross section from all collisions modelled (not including the null collision), and v is the relative speed between the colliding particle and the target.

Once the number of particles that experience collisions has been determined, particles are randomly picked from the population of simulated particles. This way, the kinetic energy of only a small subset of particles from the pool will be determined, making the simulation more efficient. Once a particle has been chosen and its kinetic energy calculated, a random number between $[0, 1]$, called R , is selected. This is used to determine the collision type for the particle, as a function of the value of R , as shown by table A.1.

Table A.1: Determining the type of collision based on the value of R [108].

R	$\leq \nu_1/\nu$	Collision Type 1
$\nu_1/\nu <$	$R \leq (\nu_1 + \nu_2)/\nu$	Collision Type 2
	\vdots	
$(\nu_1 + \nu_2 + \dots + \nu_n)/\nu <$	R	Null Collision

If the collision type selected is a null collision, then it is treated as no collision occurred.

Appendix B

Simulation Software

The PIC simulation program used in this project is called *X11 object-oriented particle-in-cell* (XOOPIC). It is a C/C++ based program that simulates 2D plasma systems. It was originally developed in the 1990s by the Plasma Theory and Simulation Group from the University of California at Berkley [80]. The code base was subsequently forked by the Plasma and Pulsed Power Group at Loughborough University, and improved upon to include additional features and output diagnostics for analysis.

B.1 Overview

XOOPIC is primarily a command-line-interface (CLI) program but support X11 windowing to visualise certain diagnostics in real time. Some examples of these real time diagnostics include: average kinetic energies of the particles, phase-space plots of the position and velocities of the various particle species, and the electric field vectors at the simulation grid. While important for determining the behaviour of the plasma system, running the simulation with these windows does significantly reduce its performance. Therefore, XOOPIC's in-built visualisations are primarily used to observe the snapshot behaviour of the simulated system, whilst any diagnostic information required for further analysis is typically written into output files.

Despite not running with X11 windowing, running these simulations continuously takes a long

period of time (typically on the order of days to weeks) before they settle into a steady state. This is because the simulations have to be run at very small time steps in order to be stable (see section 4.1.2).

B.1.1 Remote Server

Due to this long simulation time, running XOOPIIC simulations continuously on a local machine are just not feasible. Instead, simulations are run remotely on Loughborough University’s high performance servers via *secure shell* (SSH). Typically, multiple simulations are run concurrently in order to test various model parameters.

There are several risks associated with running simulations using a remote server. The first being that if (and when) the connection between the client and the server is severed, the simulations will be killed by the server. This problem can be alleviated with the use of terminal multiplexors, such as *GNU Screen*¹. This allows for the creation of multiple pseudo-terminal sessions that run in the background. Once created, the client is free to attach and detach sessions without the need for an uninterrupted connection to the server.

A broken client-server connection is not the only way a simulation can be terminated. Some others include unexpected server restarts, power outages, or overuse of server resources due to memory leaks. In such cases, the simulation can be resumed using XOOPIIC’s dump files (also referred to as restart files). These files are essentially periodic saves of the simulations and can be used to restart the simulation from the last save point if the need arises. The save interval between dump files is set when starting the simulation. Though tempting to set this interval as small as possible in order to mitigate any data loss, generating these files is very expensive computationally as it involves writing most of the simulation variables onto disk. Thus, the dump file interval are set in the neighbourhood of hundreds of thousands of time steps.

¹<https://www.gnu.org/software/screen/>

B.1.2 Input Files

The parameters for XOOPIC’s simulations are set using an input file. This is simply a custom formatted text file, with a pseudo-JSON-like structure. The input file is divided into three sections: headers, variables, and region. The first two sections are for the user’s benefit, describing the simulation and the parameter values used respectively.

The region section however is where the true simulation parameters are specified. It can be further sub-divided into multiple subsections. The list of all possible subsections is vast, though a typical PIC simulation includes:

- **Grid** where the dimensions of the plasma device are specified, either in cylindrical or cartesian geometry.
- **Control** where the control parameters such as the size of the time step or a flag to use a specific field solver are set.
- **Species** which state parameters of the particle species being simulated, for example its mass and charge.
- **MCC** that determine the collision characteristics of the plasma based on the background gas pressure and temperature. The collisions can also be turned off outright.
- **Load** that establishes the region in which the particle species are loaded.
- **Diagnostic** which as the name suggests extracts the various diagnostic information and saves them to an output file.

The other subsections not listed are the various boundary parameters. The usage of these parameters will vary based on the type of device being simulated. Some examples of boundary parameters include: a grounded boundary, a current source, and a dielectric boundary.

When constructing the input files, care must be taken to ensure that the grid size (within the grid subsection) and the time step (within the control subsection) obey a set of conditions so that the simulation is stable.

The grid size of the simulation, Δx and Δy should adhere to the equation [99]:

$$\Delta x < 3.4\lambda_D \quad (\text{B.1})$$

where λ_D is the Debye length. This is to ensure that the electric fields in the sheath can be resolved.

As for the time step, Δt , it should be able to resolve the plasma oscillations, thus should satisfy the equation [109]:

$$\Delta t < 0.2\omega_{pe}^{-1} \quad (\text{B.2})$$

where ω_{pe} is the plasma frequency. Note, this condition is only valid for electrostatic plasma simulations.

B.2 Improvements

During the course of this project, several improvements were made to XOOPIIC. This primarily included bug fixes, but also the inclusion of a new boundary parameter (within the region section) called the *Circuit* boundary.

B.2.1 Motivation

XOOPIIC previously had two types of (traditional) input source boundaries. An ideal voltage source, known as the *Equipotential* boundary; and an ideal current source, called the *Current Source* boundary.

With the Equipotential boundary, the simulation always keeps the potential at the boundary equal to the source voltage specified in the input file. This has the issue where there are no maximum or minimum bounds for current through the boundary. Thus, theoretically the current through the boundary can grow exponentially to infinity. In practice however, the simulation

simply becomes unstable and crashes. It is also possible for this current to exceed the rated current of the intended power supply to be used.

Likewise with the Current Source boundary, the simulation attempts to keep the current across the boundary at a constant specified value; despite the potential at the boundary. And in practice, it is possible that the potential produced by the simulation exceeds the voltage that can be delivered by the power supply.

Hence, in order to accurately simulate a “real world” power supply, the Circuit boundary was introduced. This boundary represents the configuration of an ideal voltage source with a resistor attached in series. An illustration of this can be seen in figure B.1. The one significant assumption with this boundary is that the circuit shares the same ground plane as the rest of the plasma device being simulated, which is normally the case.

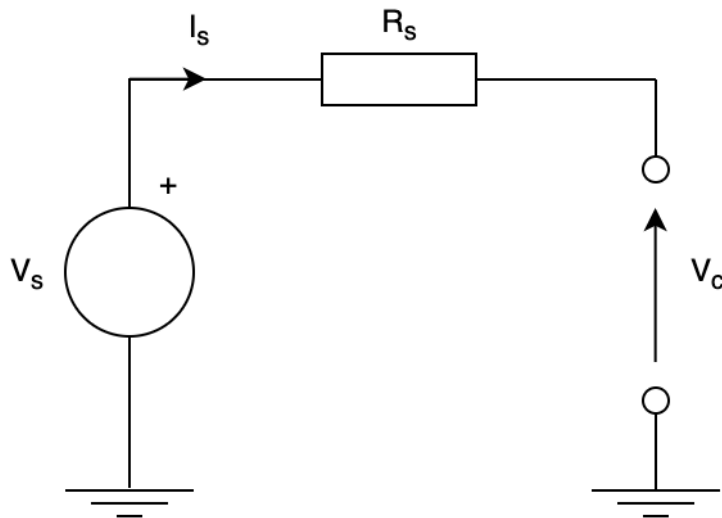


Figure B.1: Illustration of circuit boundary.

By adding the series resistor, in effect the maximum voltage and current across the boundary has been limited. As seen in figure B.2, the maximum voltage is obtained when the simulated device is an open circuit. As for the maximum current, it is achieved when the simulated device behaves as a short circuit. Thus the potential of the Circuit boundary can be given by:

$$V_c = V_s - I_s R_s \quad (\text{B.3})$$

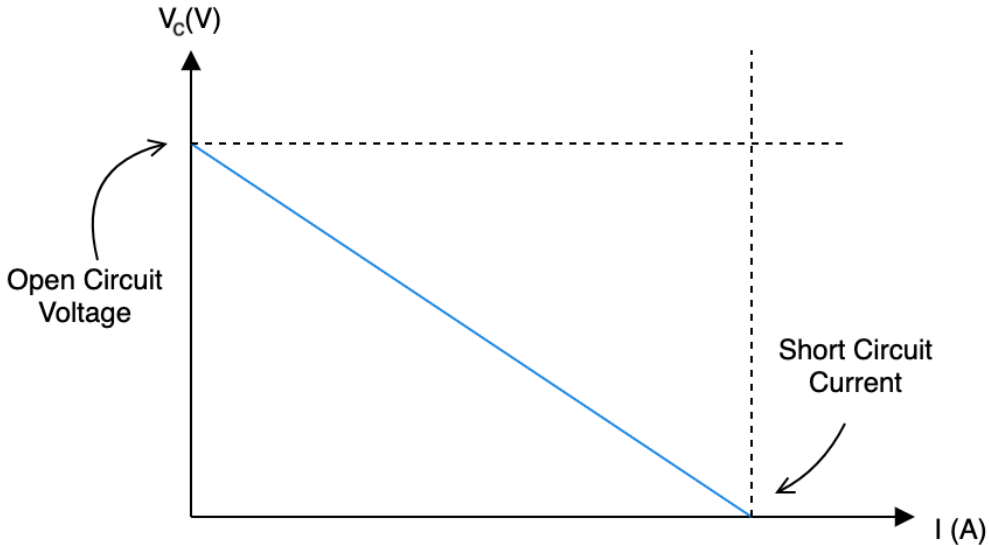


Figure B.2: Voltage-current relationship of circuit boundary.

B.2.2 Methodology

As mentioned previously, XOOPIIC has the capability of performing simulations in cartesian geometry or cylindrical geometry. Hence an implementation was required for both geometry types. For this report, a general solution based on [110, 111] is first described, followed by the specific coefficient values required in either geometry.

General Solution

A case for the Circuit boundary shown in figure B.3. The points represent an arbitrary fixed grid, with grid points labelled i and j that correspond to the relative positions along the horizontal and vertical directions respectively. The boundary itself is represented by the vertical line, placed along the left most grid points, where $i = 0$.

The potential at each grid point that intersects the boundary is first taken, then these values are averaged to give the potential of the overall Circuit boundary. For a given point along the boundary, the potential can be computed using Gauss's law.

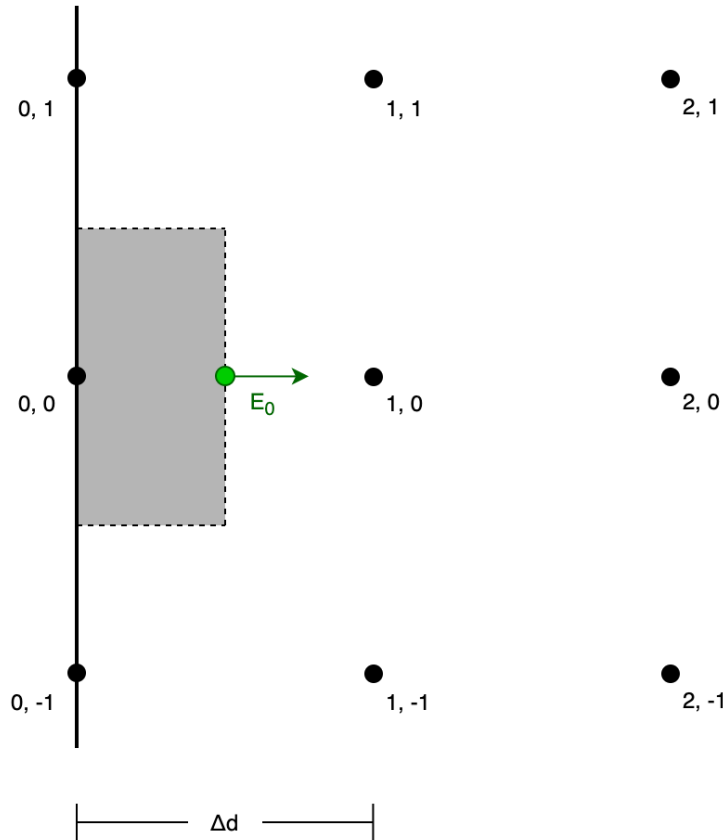


Figure B.3: Illustration of a circuit boundary along a fixed grid.

The expression for a Gaussian pillbox (shown by the dashed line in figure B.3) is:

$$\oint_S E \cdot dS = \frac{Q}{\epsilon_0} \quad (\text{B.4})$$

where Q is the charge enclosed by said pillbox. This charge can be expressed as a sum of the volume charge within the pillbox and the surface charge at the boundary:

$$Q = \oint_V \rho \cdot dV + \oint_S \sigma \cdot dS \quad (\text{B.5})$$

Combining equations B.4 and B.5, then integrating over their respective areas and volumes results in the expression:

$$E \cdot A_1 = \frac{1}{\epsilon_0} (\rho \cdot V + \sigma \cdot A_2) \quad (\text{B.6})$$

Note that there are two different areas produced: one related to the surface charge density along the boundary, A_2 ; and one related to electric field out of the pillbox, A_1 . The values of

these terms depend on the geometry used.

The electric field can be expressed in terms of the potential difference:

$$\mathbf{E} = -\nabla\phi \quad (\text{B.7})$$

Thus, the forward-difference method can be used to determine the electric field of the pillbox seen in figure B.5.

$$\frac{\phi_0 - \phi_1}{\Delta d} \cdot A_1 = \frac{1}{\varepsilon_0}(\rho \cdot V + \sigma \cdot A_2) \quad (\text{B.8})$$

An additional note regarding equation B.8, the term Δd denotes the distance between the grid points. Similarly to the area and volume terms, this value depends on the geometry used.

As explained in chapter 3, the volume charge densities of particles within PIC simulations are discretised onto the grid using bilinear interpolation. This means the the volume charge of the pillbox is known at the at the grid. Therefore, the only unknown term on the RHS of equation B.8 is the surface charge density.

This can be determined using Kirchoff's current law in the circuit shown in figure B.1:

$$\frac{d\sigma}{dt} = J_{cond} + J_{conv} \quad (\text{B.9})$$

Equation B.9 can be expressed numerically using the backwards-difference method. Additionally, the conduction and convection current density can expressed in terms of their charges, eliminating the dt terms on both sides.

$$\sigma^t - \sigma^{t-\Delta t} = \frac{1}{A_2} (Q^t - Q^{t-\Delta t} + Q_{conv}) \quad (\text{B.10})$$

The variables $\sigma^{t-\Delta t}$ and $Q^{t-\Delta t}$ represent quantities determined in the previous time step, thus should be known. Supposing it is the start of the simulation where $t = 0$, they can be simply initialised to zero. Q_{conv} represents the charge deposited onto the boundary by particles since the previous time step. Hence the only unknown term on the RHS of equation is the conduction

charge at the current time step, Q^t .

This conduction charge can be determined using Kirchoff's voltage law (also expressed in equation B.3, though in a slightly different form):

$$\phi_0 = V_s - \frac{dQ}{dt} \cdot R_s \quad (\text{B.11})$$

The derivative term can again be solved numerically using the backwards-difference. However unlike the other equations, a second order difference is used here to provide a better approximation of the charge. This second order backwards-difference is given as:

$$\frac{dQ}{dt} = \frac{3Q^t - 4Q^{t-\Delta t} + Q^{t-2\Delta t}}{2\Delta t} \quad (\text{B.12})$$

Combining equations B.11 and B.12 provides a new expression for the conduction charge, Q^t :

$$Q^t = \frac{V_s - \phi_0 - (\alpha_1 Q^{t-\Delta t} + \alpha_2 Q^{t-2\Delta t})}{\alpha_0} \quad (\text{B.13})$$

where $\alpha_0 = \frac{3}{2} \frac{R_s}{\Delta t}$, $\alpha_1 = 2 \frac{R_s}{\Delta t}$, and $\alpha_2 = \frac{1}{2} \frac{R_s}{\Delta t}$ are constants to simply the expression.

Using equation B.13, a new surface charge density expression can be determined:

$$\sigma^t - \sigma^{t-\Delta t} = \frac{1}{A_2} \left(\frac{V_s - \phi_0 - (\alpha_1 Q^{t-\Delta t} + \alpha_2 Q^{t-2\Delta t})}{\alpha_0} - Q^{t-\Delta t} + Q_{conv} \right) \quad (\text{B.14})$$

This in turn can be combined with equation B.8 from Gauss's law to give the expression:

$$\frac{\phi_0 - \phi_1}{\Delta d} \cdot A_1 + \frac{\phi_0}{\alpha_0 \varepsilon_0} = \frac{1}{\varepsilon_0} \left(\rho \cdot V + \sigma^{t-\Delta t} \cdot A_2 + \left(\frac{V_s - K^t}{\alpha_0} - Q^{t-\Delta t} + Q_{conv} \right) \right) \quad (\text{B.15})$$

where $K^t = \alpha_1 Q^{t-\Delta t} + \alpha_2 Q^{t-2\Delta t}$. Note, that the unknown terms (ϕ_0 and ϕ_1) have been rearranged to the LHS of the equation.

Typically, the coefficients in equation B.15 can then be fed into the field solver to determine the potential of all grid points. However in XOOPIIC, the grid potentials of each boundary

within the simulation are individually computed before the simulation begins. Then at each time step, the overall potential is determined by summing the predetermined potential induced by the individual boundaries via superposition, and adding the potential due to space charges (from the particles). This approach does not necessarily speed up the computation of the field solver, however it does decouple the boundary code from the field solver code; making it easier to implement new boundaries.

Because of this pre-computation, equation B.15 can be simplified by specifying $\phi_1 = c_1\phi_0$, where c_1 is the ratio of ϕ_1/ϕ_0 . Hence, the general solution for a circuit boundary can be given as:

$$\phi_0 \left((1 - c_1)A_1 + \frac{\Delta d}{\alpha_0 \varepsilon_0} \right) = \frac{\Delta d}{\varepsilon_0} \left(\rho \cdot V + \sigma^{t-\Delta t} \cdot A_2 + \left(\frac{V_s - K^t}{\alpha_0} - Q^{t-\Delta t} + Q_{conv} \right) \right) \quad (\text{B.16})$$

Cartesian Geometry

There are two possible orientations for the Circuit boundary for the cartesian geometry: along (or parallel to) the x -axis, or along the y -axis. Therefore, the variables seen in the left most column of table B.1 should be replaced by their values in the given orientation of the Circuit boundary.

Table B.1: Circuit boundary variables for cartesian geometry.

Variables	Along x -axis	Along y -axis
Δd	Δy	Δx
A_1	$\Delta x \Delta z$	$\Delta y \Delta z$
A_2	$\Delta x \Delta z$	$\Delta y \Delta z$
V	$\Delta x \Delta y \Delta z$	$\Delta y \Delta y \Delta z$

When operating in the cartesian coordinate system, the two area terms A_1 and A_2 are identical regardless of the orientation.

Cylindrical Geometry

The two possible orientations for a cylindrical geometry are: along the r-axis, or along the z-axis. However, unlike the cartesian geometry where A_1 always equals A_2 for both orientation, this only holds for the case where the Circuit boundary is along the r-axis. For the case along the z-axis, A_1 and A_2 are distinct.

The terms for a given orientation of the Circuit boundary in cylindrical geometry can be seen in table B.2.

Table B.2: Circuit boundary variables for cylindrical geometry.

Variables	Along z -axis	Along r -axis
Δd	Δr	Δz
A_1	$2\pi r_{i+0.5\Delta r}\Delta z$	$\pi(r_{j+0.5\Delta r}^2 - r_{j-0.5\Delta r}^2)$
A_2	$2\pi r_i\Delta z$	$\pi(r_{j+0.5\Delta r}^2 - r_{j-0.5\Delta r}^2)$
V	$\pi(r_{i+0.5\Delta r}^2 - r_i^2)\Delta z$	$\frac{1}{2}\pi(r_{j+0.5\Delta r}^2 - r_{j-0.5\Delta r}^2)\Delta z$

B.2.3 Validation

The validation for the Circuit boundary was done in two parts. The first was a test case without particles, which was then followed by one with particles. The former was used to evaluate the accuracy of the boundary calculations itself, without the computation from particles (i.e. the discretisation of the volume charge densities or the count of the number of particles colliding with the boundary). The latter was to test the operation of the boundary in a simulation scenario, which almost always has particles.

For both test cases, only simulation of a device in cartesian geometry is shown for the sake of brevity and the fact that the solution to the potential of the circuit boundary is highly dependant on the geometry (as discussed in the previous subsection).

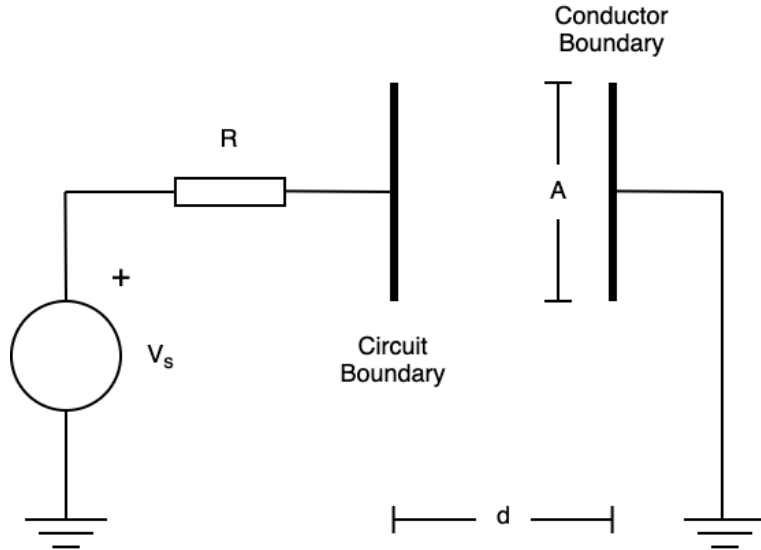


Figure B.4: Illustration of test case for Circuit boundary without particles.

Test Case without Particles

An illustration of the device being simulated can be seen in figure B.4, where the Circuit boundary was placed along the y -axis at the left-most wall and a grounded Conductor boundary placed along the right-most wall. This device, without any particles, essentially behaves as a capacitor with a capacitance given by $C = \frac{\epsilon_0 A}{d}$. The parameters for this test case can be found in table B.3

Table B.3: Parameters for test case of Circuit boundary without particles.

Parameters	Values
V_s	1000 V
R	1000 Ω
A	0.05 m^2
d	0.05 m
C	8.85 pF

Thus, this simulation models the charging of a capacitor in an RC circuit, which can be expressed as:

$$V_c = V_s(1 - e^{-t/\tau}) \quad (\text{B.17})$$

where the time constant is $\tau = RC$.

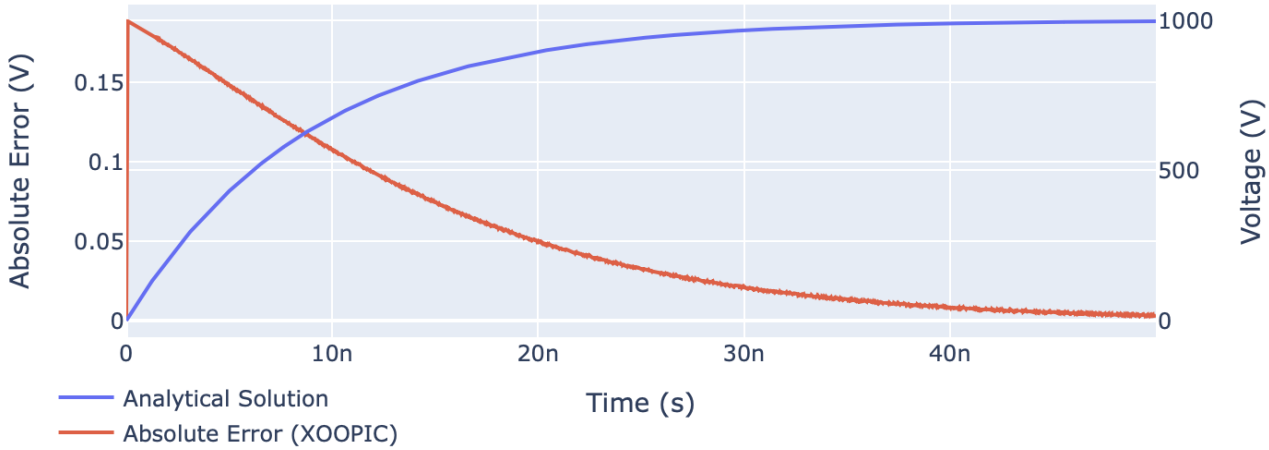


Figure B.5: Comparison between the analytical solution and XOOPIIC, where $\Delta t = 10$ ps.

For the simulated device, $C = 8.85$ pF and $\tau = 8.85$ ns. From this, an analytical solution can be determined, with the RC curve shown in figure B.5. For the XOOPIIC simulation, a run was performed from $t = 0$ to $t = 50$ ns (approximately 5 time constants), with a time step of $\Delta t = 10$ ps. The resulting RC curve overlapped the the one produced by the analytical solution, hence only the absolute error is shown.

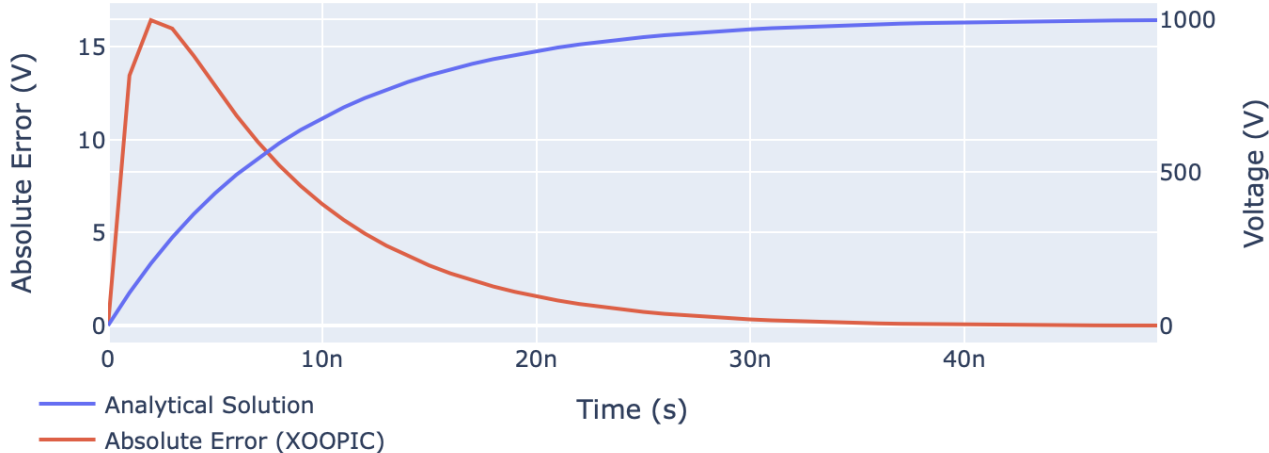


Figure B.6: Comparison between the analytical solution and XOOPIIC, where $\Delta t = 1$ ns.

This error seen is a convergence error, which is due to the conduction charge values requiring a finite number of iterations before they converge to the true value. To illustrate this, the same simulation is run with a larger time step of $\Delta t = 1$ ns (100 times that of the original simulation). These results can be seen in figure B.6. Notice that there is a significantly larger absolute error (nearly 100 times greater). However when observing the percentage error, seen in figure B.7, the differences are quite comparable. Therefore, so long as the time step used is

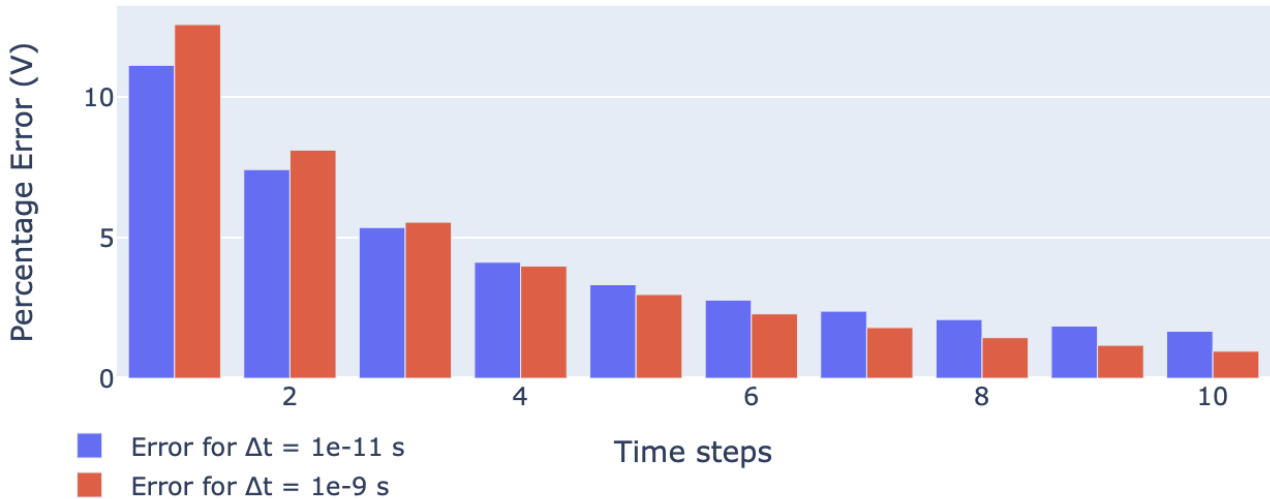


Figure B.7: Comparison of the error from XOOPIIC when $\Delta t = 10$ ps and $\Delta t = 1$ ns.

sufficiently small (to ensure a small absolute error), the simulations can be said to be accurate enough.

Test Case with Particles

Generating a simplified test case to only asses the impact of particles on the Circuit boundary was slightly more challenging. The simulated circuit for this test case can be seen in figure B.8. As for the parameters used, they can be found in table B.4.

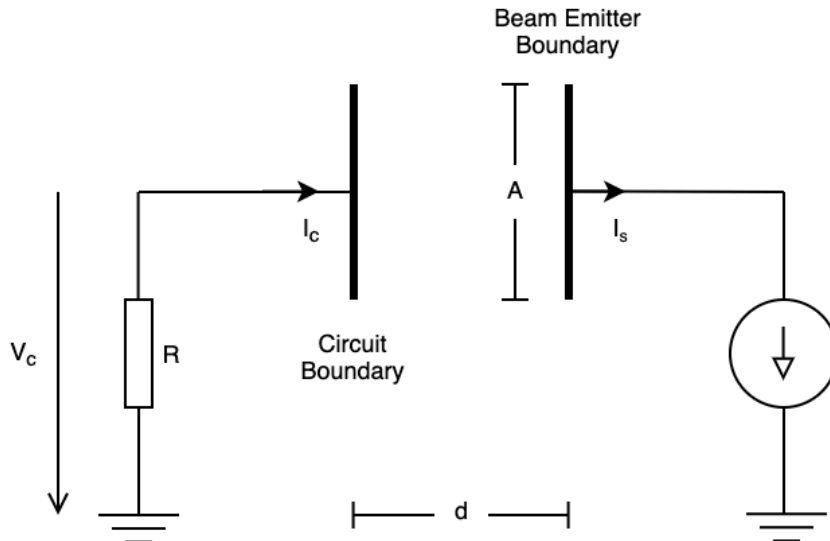


Figure B.8: Illustration of test case for Circuit boundary without particles.

Notice that the grounded Conductor boundary was replaced with a *Beam Emitter* boundary.

Table B.4: Parameters for test case of Circuit boundary with particles.

Parameters	Values
V_s	0 V
I_s	1 A
R	1000 Ω
A	5×10^{-4} m 2
d	5×10^{-4} m
C	8.85 pF
$v_{d,x}$	1000 eV
$v_{d,y}$	0 eV

The Beam Emitter is similar to the Current Source boundary, wherein a steady supply of charge is supplied to the boundary. However, unlike the Current Source which simply deposits the charge at the boundary (which in turn generates a potential), the Beam Emitter releases this charge into the simulation domain in the form of particles. This steady source of particles is what enabled the evaluation of this test case. The particles emitted out of the Beam Emitter (i.e. towards the LHS) in this case were electrons, hence why source current I_s is shown in the opposite direction. To ensure no particle losses, collisions by the MCC were turned off, the simulated device was set to a vacuum, and the drift velocity of the particles along the y -axis, $v_{d,y}$ was set to 0 eV.

As for the Circuit boundary itself, the source voltage V_s was grounded, implying that the potential of the boundary is solely given by the current through the resistor, I_c . Additionally, because the source current must be equal to the circuit current (as there were no losses) and one end of the resistor was grounded, the potential at the Circuit boundary has to be negative.

The analytical solution for this test case is given by the conduction current from electrons colliding with the Circuit boundary, and the displacement current across the capacitor. The conduction current is merely a step from 0 A to the -1 A specified by the source current. It is negative because the current is leaving the boundary. The time at which this step occurs is given by the time taken for the electrons to travel across the device. As the drift velocity of

the electrons along the direction of the x -axis was set to $v_{d,x} = 1000$ eV, thus its true velocity can be determined using the equation for kinetic energy:

$$E_{ke} = \frac{1}{2}mv^2 \quad (\text{B.18})$$

where $1 \text{ eV} = 1.6 \times 10^{-19} \text{ J}$.

This resulted in a velocity of approximately $1.87 \times 10^7 \text{ ms}^{-1}$, hence it crossed the length of the device in roughly 30 ps. Thus this is when the step in conduction current should occur.

As for the displacement current, this is given by:

$$I_{disp} = C \frac{dV}{dt} \quad (\text{B.19})$$

Combining this with the analytical solution of the RC circuit in equation B.17, gives the displacement current of:

$$I_{disp} = \frac{V_{ss}}{R} e^{-\frac{t}{\tau}} \quad (\text{B.20})$$

where V_{ss} is the potential difference across the capacitor when it reaches a steady state, which is given as $V_{ss} = I_s R$. The displacement current is in opposite the opposite direction to the conduction current, hence in this case it is positive. Similiarly to the conduction current, the displacement current at the surface of the Circuit boundary would only occur after the electrons collide with the boundary itself.

The overall potential is obtained by combining the contributions of the conduction and displacement currents with the resistance of the circuit. This is expressed in the equation below, and is illustrated in figure B.9.

$$V_c = \begin{cases} 0 & t < 30 \text{ ps} \\ I_s R (e^{-\frac{t}{\tau}} - 1) & t \geq 30 \text{ ps} \end{cases} \quad (\text{B.21})$$

For the simulation, a similar overall device geometry was used to that of the the previous test,

however the gap distance d was decreased to minimise the time required for the electrons to collide with the boundary. This meant that the area of the boundary plates A also had to be decreased to ensure that the capacitance, and by extension the time constant, remained the same. Again, the simulations were run from $t = 0$ to $t = 50$ ns, with a time step of $\Delta t = 10$ ps. Figure B.9 also shows the absolute error of the Circuit boundary of the simulation as apposed to that of the analytical solution. The error observed is much larger with a maximum error of approximately 26 V; quite a significant error. However, at the time of writing this report, the origin of this error is still unknown.

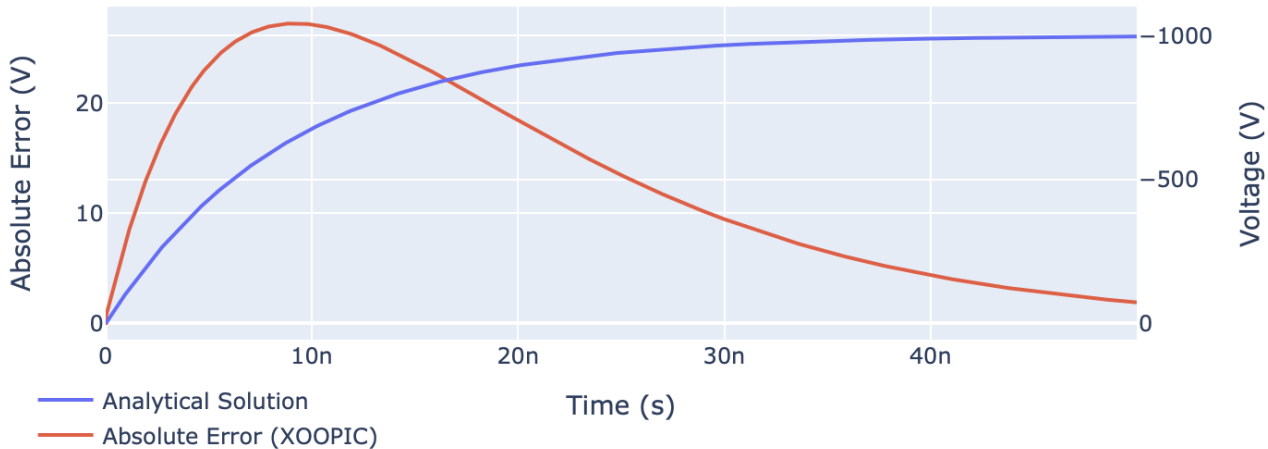


Figure B.9: Illustration of test case for Circuit boundary without particles.

B.2.4 Future Work

Aside from the Circuit boundary simulating a more accurate “real world” voltage source, it can possibly be used in model more complicated circuit networks. This is because, Thevenin’s theorem dictates that any linear circuit network can be represented by an equivalent circuit that contains a voltage source with a series impedance (which is a resistance in this case).

Nonetheless, most circuits also contain some amount of capacitance and/or inductance. Hence, it could potentially be beneficial to add a series inductor and capacitor to the Circuit boundary in addition to the existing resistor. To achieve this, the the RHS of Kirchoff’s voltage law, equation B.11, needs to be modified to include the potential due to the inductor, $V = \frac{d^2Q}{dt^2}L$, and the potential due to a capacitor, $V = \frac{Q}{C}$. This new equation can be rearranged to solve for

the current conduction charge. From there, the same process can be applied to determine the potential of the Circuit boundary.

Bibliography

- [1] IPCC, “Climate change: a threat to human wellbeing and health of the planet. taking action now can secure our future — IPCC,” Feb 2022.
- [2] “Inventory of u.s. greenhouse gas emissions and sinks — US EPA, url=<https://www.epa.gov/ghgemissions/inventory-us-greenhouse-gas-emissions-and-sinks>, journal=US EPA, author=EPA, year=2019, month=Apr.”
- [3] H. Ritchie and M. Roser, “CO₂ and greenhouse gas emissions,” *Our World in Data*, May 2020.
- [4] International Energy Agency (IEA), *CCUS in Clean Energy Transitions*. Paris: IEA, 2020. Licence: CC BY 4.0.
- [5] Heidelberg Materials, “Brevik ccs reaches mechanical completion,” Dec. 2024. Accessed: 2025-02-03.
- [6] K. An, K. Li, C.-M. Yang, J. Brechtl, and K. Nawaz, “A comprehensive review on regeneration strategies for direct air capture,” *Journal of CO₂ Utilization*, vol. 76, p. 102587, 2023.
- [7] D. Khunda, S. Li, N. Cherkasov, M. Rishard, A. Chaffee, and E. Rebrov, “Effect of temperature on the co₂ splitting rate in a dbd microreactor,” *Reaction Chemistry and Engineering*, vol. 8, pp. 2223–2233, May 9 2023.
- [8] L. Mahy, “Basic stellar observables,” 2024.

- [9] K. Chaudhary, S. Z. H. Rizvi, and J. Ali, "Laser-induced plasma and its applications," in *Plasma Science and Technology* (T. Mieno, ed.), ch. 11, Rijeka: IntechOpen, 2016.
- [10] M. A. Lieberman and A. J. Lichtenberg, *Principles of Plasma Discharges and Materials Processing: Second Edition*. Wiley-Interscience, 2005.
- [11] J. P. Molnar, "Studies of γ -processes of electron emission employing pulsed townsend discharges on a millisecond time scale," *Phys. Rev.*, vol. 83, pp. 940–952, Sep 1951.
- [12] I. Sorokin and N. Sergeev, "Measurements of secondary electron emission yield in the linear plasma simulator bpd-psi," *Vacuum*, vol. 217, p. 112528, 2023.
- [13] J. T. Gudmundsson and A. Hecimovic, "Foundations of DC plasma sources," vol. 26, p. 123001, nov 2017.
- [14] C. F. Gallo, "Coronas and Gas Discharges in Electrophotography:A Review," *IEEE Transactions on Industry Applications*, vol. IA-11, no. 6, pp. 739–748, 1975.
- [15] A. Bogaerts, E. Neyts, R. Gijbels, and J. Van der Mullen, "Gas discharge plasmas and their applications," *Spectrochimica Acta Part B: Atomic Spectroscopy*, vol. 57, pp. 609–658, apr 2002.
- [16] J. C. Eijkel, H. Stoeri, and A. Manz, "A molecular emission detector on a chip employing a direct current microplasma," *Analytical Chemistry*, vol. 71, pp. 2600–2606, jul 1999.
- [17] M. Ueda, L. A. Berni, G. F. Gomes, A. F. Beloto, E. Abramof, and H. Reuther, "Application of a dc glow discharge source with controlled plasma potential in plasma immersion ion implantation," *Journal of Applied Physics*, vol. 86, pp. 4821–4824, oct 1999.
- [18] K. H. Becker, K. H. Schoenbach, and J. G. Eden, "Microplasmas and applications," *Journal of Physics D: Applied Physics*, vol. 39, p. R55, jan 2006.
- [19] R. R. Arslanbekov, A. A. Kudryavtsev, and R. C. Tobin, "On the hollow-cathode effect: Conventional and modified geometry," *Plasma Sources Science and Technology*, vol. 7, pp. 310–322, aug 1998.

- [20] A. Watson and J. W. Gewartewski, *Principles of Electron tubes*. Van Nostrand, 1965.
- [21] F. Iza, G. J. Kim, S. M. Lee, J. K. Lee, J. L. Walsh, Y. T. Zhang, and M. G. Kong, “Microplasmas: Sources, Particle Kinetics, and Biomedical Applications,” *Plasma Processes and Polymers*, vol. 5, pp. 322–344, jun 2008.
- [22] V. I. Kolobov and A. S. Metel, “Glow discharges with electrostatic confinement of fast electrons,” vol. 48, p. 233001, may 2015.
- [23] H. Eichhorn, K. H. Schoenbach, and T. Tessnow, “Paschen’s law for a hollow cathode discharge,” *Applied Physics Letters*, vol. 63, pp. 2481–2483, aug 1993.
- [24] M. E. Pillow, “A critical review of spectral and related physical properties of the hollow cathode discharge,” *Spectrochimica Acta Part B: Atomic Spectroscopy*, vol. 36, pp. 821–843, jan 1981.
- [25] S. Y. Kornilov, I. V. Osipov, and N. G. Rempe, “Generation of narrow focused beams in a plasma-cathode electron gun,” *Instruments and Experimental Techniques 2009 52:3*, vol. 52, pp. 406–411, jun 2009.
- [26] I. Yu Bakeev, A. S. Klimov, E. M. Oks, and A. A. Zenin, “Generation of high-power-density electron beams by a forevacuum-pressure plasma-cathode electron source,” *Plasma Sources Science and Technology*, vol. 27, p. 075002, jul 2018.
- [27] D. M. Goebel, G. Becatti, I. G. Mikellides, and A. Lopez Ortega, “Plasma hollow cathodes,” *Journal of Applied Physics*, vol. 130, p. 050902, aug 2021.
- [28] P. Chabert and N. Braithwaite, *Physics of radio-frequency plasmas*, vol. 9780521763. Cambridge University Press, jan 2011.
- [29] T. D. Chu, “High Frequency Breakdown Voltage,” Tech. Rep. March, Superconducting Super Collider Project Office, mar 1992.
- [30] J. Pim, “The electrical breakdown strength of air at ultra-high frequencies,” *Proceedings of the IEE - Part III: Radio and Communication Engineering*, vol. 96, pp. 117–129, mar 1949.

- [31] S. Sharma, N. Sirse, A. Kuley, and M. M. Turner, "Electric field nonlinearity in very high frequency capacitive discharges at constant electron plasma frequency," *Plasma Sources Science and Technology*, vol. 29, p. 045003, mar 2020.
- [32] Y. Ohtsu, "Physics of High-Density Radio Frequency Capacitively Coupled Plasma with Various Electrodes and Its Applications," *Plasma Science and Technology - Basic Fundamentals and Modern Applications*, nov 2018.
- [33] "Ccp reactor for semiconductor materials processing," May 2017.
- [34] K. Denpoh, "Effects of driving frequency on plasma density in Ar and H₂/Ar capacitively coupled plasmas at Torr-order pressure," *Japanese Journal of Applied Physics*, vol. 60, p. 016002, dec 2021.
- [35] J. Lee and S. Hong, "Dual-frequency RF impedance matching circuits for semiconductor plasma etch equipment," *Electronics (Switzerland)*, vol. 10, p. 2074, aug 2021.
- [36] N. Yu, R. Jourdain, M. Gourma, F. Xu, A. Bennett, and F. Fang, "Power Dissipation of an Inductively Coupled Plasma Torch under E Mode Dominated Regime," *Micromachines 2021, Vol. 12, Page 834*, vol. 12, p. 834, jul 2021.
- [37] Y. Sakamoto, S. Maeno, N. Tsubouchi, T. Kasuya, and M. Wada, "Comparison of plasma parameters in ccp and icp processes appropriate for carbon nanotube growth," 2009.
- [38] J. Hopwood, O. Minayeva, and Y. Yin, "Fabrication and characterization of a micro-machined 5 mm inductively coupled plasma generator," *Journal of Vacuum Science and Technology B: Microelectronics and Nanometer Structures Processing, Measurement, and Phenomena*, vol. 18, pp. 2446–2451, 09 2000.
- [39] J. Hopwood and F. Iza, "Ultrahigh frequency microplasmas from 1 pascal to 1 atmosphere," *Journal of Analytical Atomic Spectrometry*, vol. 19, pp. 1145–1150, sep 2004.
- [40] F. Krüger, M. J. Kushner, S. Shim, H. Lee, and S.-K. Nam, "Icp vs ccp in high aspect ratio etching of sio₂ using ar/c₄f₈/o₂ gas mixtures," in *2020 IEEE International Conference on Plasma Science (ICOPS)*, pp. 88–88, 2020.

- [41] U. Kogelschatz, “Dielectric-barrier discharges: Their History, Discharge Physics, and Industrial Applications,” *Plasma Chemistry and Plasma Processing*, vol. 23, pp. 1–46, mar 2003.
- [42] S. J. Tingay, D. L. Kaplan, E. Lenc, K. M. J Alards, P. J. Bruggeman -, C. Constans, P. Mateo, R. Bazinette, R. Subileau, J. Paillol, and F. Massines, “Identification of the different diffuse dielectric barrier discharges obtained between 50 kHz to 9 MHz in Ar/NH₃ at atmospheric pressure,” *Plasma Sources Science and Technology*, vol. 23, p. 035008, may 2014.
- [43] R. Brandenburg, “Dielectric barrier discharges: progress on plasma sources and on the understanding of regimes and single filaments,” *Plasma Sources Science and Technology*, vol. 26, p. 053001, apr 2017.
- [44] H. Toyoda, “Microwave plasma,” in *RF Power Semiconductor Generator Application in Heating and Energy Utilization*, pp. 181–194, Springer Singapore, jan 2020.
- [45] J. Pollak, M. Moisan, and Z. Zakrzewski, “Long and uniform plasma columns generated by linear field-applicators based on stripline technology,” *Plasma Sources Science and Technology*, vol. 16, p. 310, mar 2007.
- [46] F. Iza and J. A. Hopwood, “Low-power microwave plasma source based on a microstrip split-ring resonator,” *IEEE Transactions on Plasma Science*, vol. 31, no. 4 I, pp. 782–787, 2003.
- [47] M. Surendra and D. B. Graves, “Capacitively coupled glow discharges at frequencies above 13.56 MHz,” *Applied Physics Letters*, vol. 59, p. 2091, jun 1998.
- [48] J. Pollak and M. Moisan, “Device and method for inactivation and/or sterilization using plasma,” U.S. Patent US7460225B2, January 2008.
- [49] V. Karanassios, “Miniaturized source devices for optical and mass spectrometry,” E.U. Patent EP2109467A1, March 2005.

- [50] Z. Jiang, T. Xiao, V. L. Kuznetsov, and P. P. Edwards, “Turning carbon dioxide into fuel,” *Philosophical Transactions of the Royal Society A: Mathematical, Physical and Engineering Sciences*, vol. 368, p. 3343–3364, Jul 2010.
- [51] R. Snoeckx and A. Bogaerts, “Plasma technology-a novel solution for CO₂ conversion?,” oct 2017.
- [52] G. Centi, S. Perathoner, and G. Papanikolaou, “Plasma assisted CO₂ splitting to carbon and oxygen: A concept review analysis,” *Journal of CO₂ Utilization*, vol. 54, p. 101775, dec 2021.
- [53] K. Shin, L. Zhang, H. An, H. Ha, M. Yoo, H. M. Lee, G. Henkelman, and H. Y. Kim, “Interface engineering for a rational design of poison-free bimetallic CO oxidation catalysts,” *Nanoscale*, vol. 9, pp. 5244–5253, apr 2017.
- [54] D. Pakhare and J. Spivey, “A review of dry (co₂) reforming of methane over noble metal catalysts,” *Chem. Soc. Rev.*, vol. 43, p. 7813–7837, Feb 2014.
- [55] M. Rezaei, S. M. Alavi, S. Sahebdelfar, and Z. F. Yan, “Syngas Production by Methane Reforming with Carbon Dioxide on Noble Metal Catalysts,” *Journal of Natural Gas Chemistry*, vol. 15, pp. 327–334, dec 2006.
- [56] J. R. Rostrup-Nielsen and J. H. Bak Hansen, “CO₂-Reforming of Methane over Transition Metals,” *Journal of Catalysis*, vol. 144, pp. 38–49, nov 1993.
- [57] J. Ma, N. Sun, X. Zhang, N. Zhao, F. Xiao, W. Wei, and Y. Sun, “A short review of catalysis for CO₂ conversion,” *Catalysis Today*, vol. 148, pp. 221–231, nov 2009.
- [58] E. GmbH, “Industrial 6.3 mw ptg plant (audi e-gas plant),” 2017.
- [59] 2011.
- [60] U. Kogelschatz, “Dielectric-barrier discharges: Their history, discharge physics, and industrial applications,” *Plasma Chemistry and Plasma Processing*, vol. 23, no. 1, p. 1–46, 2003.

- [61] A. Bogaerts and G. Centi, “Plasma Technology for CO₂ Conversion: A Personal Perspective on Prospects and Gaps,” *Frontiers in Energy Research*, vol. 8, p. 533985, jul 2020.
- [62] G. Chen, L. Wang, T. Godfroid, and R. Snyders, “Progress in plasma-assisted catalysis for carbon dioxide reduction,” in *Plasma Chemistry and Gas Conversion* (N. Britun and T. Silva, eds.), ch. 4, Rijeka: IntechOpen, 2018.
- [63] D. Hegemann, “Plasma activation mechanisms governed by specific energy input: Potential and perspectives,” *Plasma Processes and Polymers*, vol. 20, p. 2300010, may 2023.
- [64] A. Ozkan, T. Dufour, G. Arnoult, P. De Keyzer, A. Bogaerts, and F. Reniers, “CO₂–CH₄ conversion and syngas formation at atmospheric pressure using a multi-electrode dielectric barrier discharge,” *Journal of CO₂ Utilization*, vol. 9, pp. 74–81, mar 2015.
- [65] W. A. Bongers, S. Welzel, D. van den Bekerom, G. F. W. M. Frissen, G. van Rooij, A. P. H. Goede, M. F. Graswinckel, P. W. C. Groen, N. den Harder, B. van Heemert, T. Minea, M. van de Sanden, M. Leins, J. Kopecki, A. D. Schulz, and M. Walker, “Developments in co₂ dissociation using non-equilibrium microwave plasma activation for solar fuels,” 2015.
- [66] T. Silva, N. Britun, T. Godfroid, and R. Snyders, “Optical characterization of a microwave pulsed discharge used for dissociation of CO₂,” *Plasma Sources Science and Technology*, vol. 23, p. 025009, mar 2014.
- [67] Y. Qin, G. Niu, X. Wang, D. Luo, and Y. Duan, “Status of CO₂ conversion using microwave plasma,” *Journal of CO₂ Utilization*, vol. 28, pp. 283–291, dec 2018.
- [68] M. Ramakers, I. Michielsen, R. Aerts, V. Meynen, and A. Bogaerts, “Effect of Argon or Helium on the CO₂ Conversion in a Dielectric Barrier Discharge,” *Plasma Processes and Polymers*, vol. 12, pp. 755–763, aug 2015.
- [69] J. Jonkers, M. van de Sande, A. Sola, A. Gamero, and J. van der Mullen, “On the differences between ionizing helium and argon plasmas at atmospheric pressure,” *Plasma Sources Science and Technology*, vol. 12, p. 30, dec 2002.

- [70] G. Chen, N. Britun, T. Godfroid, M.-P. Delplancke-Ogletree, and R. Snyders, “Role of plasma catalysis in the microwave plasma-assisted conversion of co₂,” in *Green Chemical Processing and Synthesis*, IntechOpen London, UK, 2017.
- [71] S. M. Chun, Y. C. Hong, and D. H. Choi, “Reforming of methane to syngas in a microwave plasma torch at atmospheric pressure,” *Journal of CO₂ Utilization*, vol. 19, pp. 221–229, may 2017.
- [72] P. J. Bruggeman, M. J. Kushner, B. R. Locke, J. G. Gardeniers, W. G. Graham, D. B. Graves, R. C. Hofman-Caris, D. Maric, J. P. Reid, E. Ceriani, D. Fernandez Rivas, J. E. Foster, S. C. Garrick, Y. Gorbanev, S. Hamaguchi, F. Iza, H. Jablonowski, E. Klimova, J. Kolb, F. Krcma, P. Lukes, Z. MacHala, I. Marinov, D. Mariotti, S. Mededovic Thagard, D. Minakata, E. C. Neyts, J. Pawlat, Z. L. Petrovic, R. Pfleiger, S. Reuter, D. C. Schram, S. Schröter, M. Shiraiwa, B. Tarabová, P. A. Tsai, J. R. Verlet, T. Von Woedtke, K. R. Wilson, K. Yasui, and G. Zvereva, “Plasma-liquid interactions: A review and roadmap,” *Plasma Sources Science and Technology*, vol. 25, p. 053002, sep 2016.
- [73] Y. Gorbanev, D. Leifert, A. Studer, D. O’Connell, and V. Chechik, “Initiating radical reactions with non-thermal plasmas,” *Chemical Communications*, vol. 53, pp. 3685–3688, mar 2017.
- [74] J. Golda, J. Held, B. Redeker, M. Konkowski, P. Beijer, A. Sobota, G. Kroesen, N. S. J. Braithwaite, S. Reuter, M. M. Turner, T. Gans, D. O’Connell, and V. Schulz-Von Der Gathen, “Concepts and characteristics of the ‘COST Reference Microplasma Jet’,” *Journal of Physics D: Applied Physics*, vol. 49, p. 084003, jan 2016.
- [75] H. Xu, M. Shaban, S. Wang, A. Alkayal, D. Liu, M. G. Kong, F. Plasser, B. R. Buckley, and F. Iza, “Oxygen harvesting from carbon dioxide: simultaneous epoxidation and CO formation,” *Chemical Science*, 2021.
- [76] Y. Gorbanev, J. Golda, V. S.-v. der Gathen, and A. Bogaerts, “Applications of the COST Plasma Jet: More than a Reference Standard,” *Plasma 2019, Vol. 2, Pages 316-327*, vol. 2, pp. 316–327, jul 2019.

- [77] R. A. Dextre and K. G. Xu, “Effect of the Split-Ring Resonator Width on the Microwave Microplasma Properties,” *IEEE Transactions on Plasma Science*, vol. 45, pp. 215–222, feb 2017.
- [78] F. Iza and J. A. Hopwood, “Split-ring resonator microplasma: Microwave model, plasma impedance and power efficiency,” *Plasma Sources Science and Technology*, vol. 14, pp. 397–406, may 2005.
- [79] H. Wheeler, “Transmission-line properties of a strip on a dielectric sheet on a plane,” *IEEE Transactions on Microwave Theory and Techniques*, vol. 25, p. 631–647, Aug 1977.
- [80] J. P. Verboncoeur, A. B. Langdon, and N. T. Gladd, “An object-oriented electromagnetic PIC code,” *Computer Physics Communications*, vol. 87, pp. 199–211, may 1995.
- [81] Neutrium, “Calculation of flow through nozzle and orifices,” 2015.
- [82] E. Buckingham, “On the orifice meter; the expansion factor for gases,”
- [83] J. Woodward, “Source modeling – discharge rates,” in *Reference Module in Chemistry, Molecular Sciences and Chemical Engineering*, Elsevier, jan 2014.
- [84] O. Optics, *USB2000+ Fiber Optic Spectrometer Installation and Operation Manual*. Ocean Optics, 2010.
- [85] R. W. B. Pearse and A. G. Gaydon.
- [86] W. H. Press, S. A. Teukolsky, W. T. Vetterling, and B. P. Flannery, *Numerical Recipes in C*. Cambridge, USA: Cambridge University Press, second ed., 1992.
- [87] SciPy, “Univariate spline in the b-spline basis.,” 2023.
- [88] MKS Instruments, *GE50A Elastomer Sealed, Digital Mass Flow Controller*, 10 2021.
- [89] MKS Instruments, *623H Unheated Absolute Baratron® Capacitance Manometer with Trip Points*, 11 2021.
- [90] MKS Instruments, *640B/641B Electronic Pressure Controller*, 12 2021.

- [91] C. Capello, U. Fischer, and K. Hungerbühler, “What is a green solvent? a comprehensive framework for the environmental assessment of solvents,” *Green Chemistry*, vol. 9, no. 9, p. 927, 2007.
- [92] PerkinElmer, “Gas chromatography explained: What it is and how it works,” 2022.
- [93] S. Aryal, “Mass spectrometry (ms)- principle, working, parts, steps, uses,” 2022.
- [94] BOC Ltd, *Helium CP Grade (N5.0)*, 2022.
- [95] BOC Ltd, *Carbon Dioxide*, 2024.
- [96] H. C. Kim, F. Iza, S. S. Yang, M. Radmilović-Radjenović, and J. K. Lee, “Particle and fluid simulations of low-temperature plasma discharges: benchmarks and kinetic effects,” *Journal of Physics D: Applied Physics*, vol. 38, p. R283, sep 2005.
- [97] D. Tskhakaya, K. Matyash, R. Schneider, and F. Taccogna, “The Particle-In-Cell Method,” *Contributions to Plasma Physics*, vol. 47, pp. 563–594, dec 2007.
- [98] C. K. Birdsall, “Particle-in-Cell Charged-Particle Simulations, Plus Monte Carlo Collisions With Neutral Atoms, PIC-MCC,” *IEEE Transactions on Plasma Science*, vol. 19, no. 2, pp. 65–85, 1991.
- [99] R. Hockney and J. Eastwood, *Computer Simulation Using Particles*. CRC Press, mar 1988.
- [100] A. T. Gisbert and N. Piovella, “Multimode collective atomic recoil lasing in free space,” *Atoms*, vol. 8, p. 93, Dec 2020.
- [101] C. K. Birdsall and A. B. Langdon, *Plasma physics via computer simulation*. CRC Press, 1st ed ed., oct 2004.
- [102] W. H. Press, B. P. Flannery, S. A. Teukolsky, and W. T. Vetterling, *Numerical Recipes in C: The Art of Scientific Computing*. Cambridge University Press, 1988.
- [103] S. V.-U. Ha, T.-A. Vu, and H. M. Tran, “An Extended Occlusion Detection Approach for Video Processing,” *REV Journal on Electronics and Communications*, vol. 8, jan 2019.

- [104] W. H. Press, B. P. Flannery, S. A. Teukolsky, and W. T. Vetterling, *Numerical Recipes in C: The Art of Scientific Computing*. Cambridge University Press, 1988.
- [105] F. Wermelinger, “Diffusion with Alternating Direction Implicit (ADI) and Particle Strength Exchange (PSE) methods.”
- [106] W. H. Press, B. P. Flannery, S. A. Teukolsky, and W. T. Vetterling, *Numerical Recipes in C: The Art of Scientific Computing*. Cambridge University Press, 1988.
- [107] F. Iza, S. H. Lee, and J. K. Lee, “Computer modeling of low-temperature plasmas,” *Transworld Research Network*, vol. 37, no. 2, 2007.
- [108] V. Vahedi and M. Surendra, “A Monte Carlo collision model for the particle-in-cell method: applications to argon and oxygen discharges,” *Computer Physics Communications*, vol. 87, pp. 179–198, may 1995.
- [109] D. Tskhakaya, K. Matyash, R. Schneider, and F. Taccogna, “The particle-in-cell method,” *Contributions to Plasma Physics*, vol. 47, p. 563–594, Dec 2007.
- [110] J. P. Verboncoeur, M. V. Alves, V. Vahedi, and C. K. Birdsall, “Simultaneous Potential and Circuit Solution for 1D Bounded Plasma Particle Simulation Codes,” *Journal of Computational Physics*, vol. 104, pp. 321–328, feb 1993.
- [111] V. Vahedi and G. Dipeso, “Simultaneous Potential and Circuit Solution for Two-Dimensional Bounded Plasma Simulation Codes,” *Journal of Computational Physics*, vol. 131, pp. 149–163, feb 1997.